U N I V E R S I T E D E L I E G E

Aerospace and Mechanical Engineering Department

Multibody Modelling of Mechanical Transmission Systems in Vehicle Dynamics

PhD Thesis Dissertation
submitted in partial fulfillment
of the requirements for the degree of
'Docteur en Sciences de l'Ingénieur'

by

Geoffrey Virlez
Ingénieur Civil Mécanicien

June 2014

Members of the Examination Committee

Olivier Brüls (Co-supervisor)
Professor - University of Liège

Frédéric Cugnon
PhD, Research Engineer - Siemens PLM Software

Wim Desmet
Professor - Katholieke Universiteit Leuven

Pierre Duysinx (Supervisor)
Professor - University of Liège

Michel Géradin
Emeritus Professor - University of Liège

Gaëtan Kerschen (President of the Committee)
Professor - University of Liège

Robert Seifried
Professor - Universität Siegen, Germany

Olivier Verlinden
Professor - University of Mons

Abstract

Automotive drivetrain devices are subjected to complex phenomena, e.g., backlash between gear teeth or contact with friction, which significantly influence the dynamic behaviour of the vehicle. Because of the current requirements in the automotive industry to make lighter vehicles and improve the comfort of the passengers, these phenomena can no longer be neglected during the design proces. However, the modelling of these nonlinear and discontinuous effects is not trivial and can lead to numerical problems during simulation. Therefore, the development of specific formulations is needed in order to manage these particular effects.

This thesis is dedicated to the development of new methodologies to simulate efficiently the dynamics of mechanical transmission devices. The various contributions are formulated within the framework of the nonlinear finite element method for flexible multibody systems. The latter allows the modelling of complex mechanisms composed of rigid and flexible bodies, kinematic joints and force elements.

The modelling of TORSEN differentials has been selected as representative industrial application to demonstrate the developments. In the first part of the thesis, global models of the TORSEN differential have been constructed in the flexible multibody software SAMCEF/MECANO and validated with experimental data. The modelling assumptions introduced and the drawbacks observed during the numerical simulation of this complex industrial application have guided the further developments to be performed to achieve the work.

The modelling of contact conditions is a central question in this work. The contact models developed are formulated following a global approach with the aim to include the transmission component into a vehicle model and perform integrated simulations of the vehicle dynamics. They are based on a continuous approach so that a smooth solver of the generalized-α family can be used.

The second part of the thesis addresses the modelling of contact conditions between rigid bodies. A general kinematic description is proposed to model the contact between two nodes rigidly attached to the contact surfaces. The magnitude of the contact forces is computed by a continuous impact law which uses a restitution coefficient to represent the loss of kinetic energy inherent to impact. The geometric shapes of the contacting surfaces are particularized to the contact between two planar rings and to a non-ideal cylindrical joint where the clearance and the tilting are accounted for. A squeeze film model is also proposed to represent the damping effect produced by the presence of lubricant between approaching bodies. Thanks to this new element, the resulting TORSEN differential model has gained robustness and computational efficiency so that it can be included in a full vehicle model in order to simulate various manoeuvres.

Finally, a new contact formulation is developed between flexible components modelled as superelements. A major originality of the model lies in the determination of the spatial configuration of the potential contact zones from the superelement generalized coordinates. The contact forces computed in the 3D space are reformulated and directly applied upon the superelement generalized coordinates. This approach leads to very compact models of contacting bodies. The primal and the dual versions of the Craig-Bampton method are investigated to formulate the superelement model which includes in both cases a mixed set of static and vibration modes. The relevance of this contribution is demonstrated through the simulation of 3D flexible gear pairs.

Acknowledgements

The achievement of my PhD thesis could not have been possible without the support and advice of numerous persons.

First of all, I wish to thank my advisors Professors Pierre Duysinx and Olivier Brüls for offering me the opportunity to start this research work. I could benefit from their constant guidance and encouragements. They found time on their overbooked diaries to follow the evolution of my research work, answer to my questions and give me some guidelines.

I have enjoyed my stay with Professor Alberto Cardona at the National University of the Littoral, Santa Fe, Argentina. He helped me great deal with his valuable advice and suggestions. Our technical discussions have inspired and motivated me for the various topics broached in my thesis. I also thank the members of his research group for their warm welcome.

Many thanks to Professor Michel Géradin for his great experience about the dynamics of multibody systems as well as for the meticulous reading of the thesis dissertation.

I would like to express my gratitude to Professors Gaëtan Kerschen and Olivier Verlinden for their relevant remarks during the thesis follow-up committee meetings. The other members of the examination committee, Professors Wim Desmet, Robert Seifried and Dr Frédéric Cugnon are also acknowledged for accepting to attend to the dissertation presentation.

I gratefully thank the Belgian National Fund for Scientific Research (FNRS) for its financial support through the F.R.I.A grant. I wish to acknowledge my industrial partners, SAMTECH and JTEKT TORSEN EUROPE, for their technical support. I also thank the University of Liège for the logistical support and the grants allowing me to take part in several conferences.

Last but not least, I would like to thank all the researchers of the Aerospace and Mechanical Engineering Department (LTAS) of the University of Liège. They have contributed to the good working and friendly atmosphere and are too numerous to be cited. A special thank to the Automotive Engineering Research group for their cheerfulness, support and encouragements along all these years.

Contents

Nomenclature

Acronyms

ABS	anti-lock braking system
CB	Craig-Bampton
CPL	coupling gear
DAE	differential-algebraic equation
DOF	degree of freedom
EG	element gear
ESP	electronic stability program
FE	finite element
IG	internal gear
MBS	multibody system
ODE	ordinary differential equation
PG	planet gear
SG	sun gear
TDR	torque distribution ratio
TORSEN	torque sensing

General conventions

d	total spatial derivative
Δ	finite increment

δ infinitesimal spatial variation

$\dot{a}$ time derivative of variable a

∂ partial spatial derivative

$\mathbf{0}$ empty matrix

$\boldsymbol{\nabla}$ nabla symbol $\left(\boldsymbol{\nabla} = \boldsymbol{u}_x \frac{\partial}{\partial x} + \boldsymbol{u}_y \frac{\partial}{\partial y} + \boldsymbol{u}_z \frac{\partial}{\partial z}\right)$

$\overline{\boldsymbol{A}}$ matrix of a reduced model (superelement)

$\widetilde{\boldsymbol{a}}$ skew-symmetric matrix defined defined with the components of vector $\boldsymbol{a} = \begin{Bmatrix} a_1 & a_2 & a_3 \end{Bmatrix}$

$$\widetilde{\boldsymbol{a}} = \begin{bmatrix} 0 & -a_3 & a_2 \\ a_3 & 0 & -a_1 \\ -a_2 & a_1 & 0 \end{bmatrix}$$

$\boldsymbol{A}$ matrix

$\boldsymbol{a}$ vector

$\boldsymbol{A}^*$ intermediate matrix

$\boldsymbol{a}^T$ transposed vector

$\boldsymbol{I}$ identity matrix

$\boldsymbol{x}_{IJ}$ distance vector between node I and J ($\boldsymbol{x}_{IJ} = \boldsymbol{x}_J - \boldsymbol{x}_I$)

A geometrical point or constant numerical parameter

a scalar variable

Operators

$\left(\boldsymbol{I} - \boldsymbol{n}\boldsymbol{n}^T\right)\boldsymbol{b}$ projection of vector $\boldsymbol{b}$ onto the plane orthogonal to $\boldsymbol{n}$

vect($\boldsymbol{A}$) vectorial part of a skew-symmetric matrix $\boldsymbol{A}$

$$\text{vect}(\boldsymbol{A}) = \frac{1}{2}\begin{Bmatrix} A_{32} - A_{23} \\ A_{13} - A_{31} \\ A_{21} - A_{12} \end{Bmatrix}$$

$\boldsymbol{\nabla}\boldsymbol{a}$ divergence of vector $\boldsymbol{a}$ $\left(\boldsymbol{\nabla}\boldsymbol{a} = \frac{\partial \boldsymbol{a}_x}{\partial x} + \frac{\partial \boldsymbol{a}_y}{\partial y} + \frac{\partial \boldsymbol{a}_z}{\partial z}\right)$

$\boldsymbol{\nabla} a$ gradient of function a $\left(\boldsymbol{\nabla} a = \frac{\partial a}{\partial x}\boldsymbol{u}_x + \frac{\partial a}{\partial y}\boldsymbol{u}_y + \frac{\partial a}{\partial z}\boldsymbol{u}_z\right)$

$\widetilde{\boldsymbol{a}}\ \boldsymbol{b}$	product between a skew-symmetric matrix and a vector: equivalent to a cross product
$\boldsymbol{a} \cdot \boldsymbol{b}$	scalar product
$\boldsymbol{a} \times \boldsymbol{b}$	cross product
$\boldsymbol{A}\ \boldsymbol{B}$	matrix product

Multibody systems

$\delta\mathcal{W}$	virtual work
$\delta\boldsymbol{\Theta}$	material angular variation vector
$\delta\boldsymbol{\theta}$	spatial angular variation vector
λ	Lagrange multiplier
$\mathbf{res}$	residual vector
$\mathcal{K}$	kinetic energy
$\mathcal{L}$	Lagrangian ($\mathcal{L} = \mathcal{K} - \mathcal{V}$)
$\mathcal{V}$	potential energy
$\boldsymbol{q}$	vector of generalized coordinates
$\ddot{\boldsymbol{q}}$	vector of generalized accelerations
$\dot{\boldsymbol{q}}$	vector of generalized velocities
$\boldsymbol{\Omega}$	material angular velocity vector
$\boldsymbol{\omega}$	spatial angular velocity vector
$\boldsymbol{\Phi}$	vector of kinematic constraints
$\boldsymbol{\Phi}_{\boldsymbol{q}}$	constraint gradient ($\partial\boldsymbol{\Phi}/\partial\boldsymbol{q}$)
$\boldsymbol{\Psi}$	vector of rotation parameters
$\boldsymbol{\Psi}_{inc}$	increments of rotation parameters
$\boldsymbol{C}$	damping matrix
$\boldsymbol{C}_t$	tangent damping matrix
$\boldsymbol{E}_i$	unit vectors representing the three directions of a absolute inertia frame
$\boldsymbol{g}$	force vector

$\boldsymbol{K}$	stiffness matrix
$\boldsymbol{K}_t$	tangent stiffness matrix
$\boldsymbol{M}$	mass matrix
$\boldsymbol{R}$	rotation matrix
$\boldsymbol{R}_1$	rotation matrix at the initial configuration ($t = 0$ s)
$\boldsymbol{R}_{ref}$	rotation matrix at the reference configuration; i.e. rotation from the initial configuration to the previous converged time step
$\boldsymbol{S}_t$	iteration matrix
$\boldsymbol{T}(\boldsymbol{\Psi}_{inc})$	tangent operator computing the material variation of rotations $\delta\boldsymbol{\Theta}$ from the variation of the incremental cartesian rotation vector $\delta\boldsymbol{\Psi}_{inc}$ ($\delta\boldsymbol{\Theta} = \boldsymbol{T}(\boldsymbol{\Psi}_{inc})\ \delta\boldsymbol{\Psi}_{inc}$)
h	time step size
k	scaling factor
n	total number of generalized coordinates for some element: structural component (finite element, superelement, rigid boody), kinematic constraint, force element,...
p	penalty factor
t	time

Contact modelling

ℓ	penetration length
μ_r	regularized friction coefficient
μ_{dyn}	dynamic friction coefficient
ν	Poisson's ratio
$\boldsymbol{f}_c$	contact force vector
$\boldsymbol{f}_{fr}$	friction force vector
$\boldsymbol{n}$	unit vector representing the normal direction
$\boldsymbol{t}$	unit vector representing the tangential direction
c	damping coefficient

E	Young's modulus
e	restitution coefficient
f	contact force magnitude
k_p	contact stiffness, penalty factor
w	participation factor of contact on nodes of master faces

Squeeze film

μ_{vis}	dynamic viscosity
ρ	mass density
f_{sf}	normal force produced by the squeeze film
h_{sf}	squeeze film thickness
p	lubricating fluid pressure in the squeeze film
p_{atm}	atmospheric pressure

Superelement

$\boldsymbol{d}$	elastic displacement field
$\overline{\boldsymbol{K}}$	reduced stiffness matrix
$\overline{\boldsymbol{M}}$	reduced mass matrix
ω	eigenpulsation ($\omega = 2\pi f$ with f the eigenfrequency)
$\overline{n_f}$	number of free-free vibrations modes included in the modal basis
$\overline{n_I}$	number of internal vibration modes retained in the superelement reduction basis
$\overline{\boldsymbol{\Psi}}_f$	subset of free-free vibration modes
$\overline{\boldsymbol{\Psi}}_I$	subset of internal vibration modes (primal Craig-Bampton method)
$\overline{\boldsymbol{\Psi}}$	mode matrix containing the global shape functions of the reduced model
$\boldsymbol{R}_0$	rotation matrix of the body reference frame (corotational or floating)
$\boldsymbol{\alpha}_i$	nodal rotation parameters in the absolute frame
$\boldsymbol{\eta}$	vector of superelement local coordinates

$\boldsymbol{\eta}_f$	influence coefficient vector of free-free vibration modes (dual Craig-Bampton method)
$\boldsymbol{\eta}_I$	influence coefficient vector of internal vibration modes (primal Craig-Bampton method)
$\boldsymbol{\gamma}_i$	displacement of node i in rotation compared to the undeformed configuration expressed in the reference frame (corotational or floating frame)
$\boldsymbol{\mu}$	diagonal matrix with modal masses
$\boldsymbol{\omega}$	diagonal matrix with eigenpulsations
$\boldsymbol{\Psi}_B$	static boundary modes (primal Craig-Bampton method)
$\boldsymbol{\Psi}_r$	set of residual attachment modes
$\boldsymbol{\tau}$	vector of velocities expressed in the corotational frame
$\boldsymbol{A}_f$	filter of free-free vibration modes
$\boldsymbol{A}_{rig}$	filter of rigid body modes
$\boldsymbol{P}$	kinematic tangent relation ($\delta\boldsymbol{\eta} = \boldsymbol{P}(\boldsymbol{q})\ \delta\boldsymbol{q}$)
$\boldsymbol{r}$	vector with the intensities of residual attachment modes
$\boldsymbol{R}(\boldsymbol{\gamma}_P)$	rotation matrix associated with the three independent rotation variables $\boldsymbol{\gamma}_P$
$\boldsymbol{u}_i$	displacement of node i in translation compared to the undeformed configuration expressed in the reference frame (corotational or floating frame)
$\boldsymbol{U}_{rig}$	rigid body modes
$\boldsymbol{v}$	vector of velocities expressed in the absolute frame
$\boldsymbol{X}_i$	position of node i in the undeformed configuration expressed in the body reference frame (corotational or floating frame)
$\boldsymbol{z}_{C_i}$	deformed position of the contact point C_i in the reference frame
$\boldsymbol{x}_0$	absolute position of the origin of the reference frame (corotational or floating)
n_B	number of boundary degrees of freedom, number of boundary modes
n_I	number of internal degrees of freedom of the non-reduced model
n_{Bnode}	number of boundary nodes

Chapter 1

Introduction

1.1 General context

Nowadays in the automotive industry the requirements to reduce fuel consumption and environmental pollution are greatly increasing. Reducing the weight of the vehicle, lowering the mechanical losses and developing new hybrid electric propulsion systems are needed in order to reach this goal. Nevertheless, these new vehicle designs should not downgrade the security and the comfort of the passengers. For instance, electronic control systems such as ABS or ESP involve additional automotive components and therefore tend to increase the global weight, but they highly improve the vehicle handling and allow to avoid accidents in a lot of situations. The mass reduction of structural parts can also lead to higher flexibility, which can generate vibrations and alter the driving pleasure. Moreover, the comfort in the passenger cell can be affected by the reduction of acoustic isolation due to thinner structural panels.

In order to find a compromise between these antagonist criteria, the current trend addresses the development of reliable simulation tools to enhance the automotive design process. The virtual prototyping approach is very useful during the pre-design phase since it allows to get numerous data about a mechanical device without having to construct a costly real prototype. Numerical simulations can also be used to detect the origin of problems occurring on a car already on the market. It is indeed often difficult to proceed by measurements especially with the increasing complexity and interdependence of automotive components. Once the problem is understood, various modifications in the system can be easily tested thanks to the numerical model in order to find a solution to it.

Usually, in mechanical engineering, two types of numerical studies are carried out. On one side, the multibody system simulations allow studying the kinematics of mechanisms made of rigid bodies and evaluate dynamic loads. On the other side, the structural analyses are performed to compute the stresses and strains in individual

flexible components. These models are often based on the finite element method and allow to verify that the magnitude of strains and stresses have a reasonable magnitude even locally.

However, due to the alleviation requirements, the flexibility effects become a major concern in the design of many automotive components as it has always been the case for aeronautical structural parts. Therefore, the flexible behaviour can no longer be neglected in dynamic multibody simulations. Indeed, if large deformations appear, the rigid body assumption adopted in the MBS model leads to unrealistic prediction of the dynamic response of the system. The interconnection loads between the various bodies are computed with a significant error which will affect the detailed structural analyses if these forces are used as load cases for the finite element model.

Multibody simulation techniques are frequently used to model complex automotive systems [76, 141]. For instance, dynamic simulations of crankshaft or connecting rods have been carried out in [107] to analyse the mechanical losses. Refs. [25, 90] deal with deformations and stresses in multicylinder engines. The suspensions are also widely modelled using multibody tools [11]. Their models are composed of a mixed set of rigid and flexible bodies and enable to analyse the vehicle dynamic behaviour in case of manoeuvres or braking (see for example [30] and [49]).

Models of transmission components are less mature because several complex physical phenomena are involved such as stick-slip, backlash between gear teeth, contact with friction, impact or hysteresis. The modelling of these nonlinear and discontinuous effects is not trivial and can lead to numerical problems during simulation. The development of specific formulations is needed in order to manage these particular effects.

The driveline devices such as the clutch, the gear box or the differential highly interact together. They influence the driveline behaviour but also the whole vehicle performance. For instance, the differential features can have a direct influence on the sizing of the anti-roll bar and the suspensions. The vibrations generated by the backlash between gear teeth can be transferred to the car body and induce noise in the passenger cell if they are not enough damped. Therefore, individual models of transmission components are often not sufficient and there is a need to have global drivetrain or even full vehicle models. Indeed, some physical phenomena can hardly be captured with isolated device models. In this way, the development of efficient formulations dedicated to transmission devices would enable to close the loop between the engine and the suspension models. Besides, the driveline modelling enhances the performance not only of the transmission devices, but also of the other subsystems of the vehicle. Such global vehicle models are currently conceivable owing to the huge computational resources available but were unthinkable a few decades ago.

Modern vehicles include new technologies such as electric motors, active suspensions, electronic active safety systems. Thus, there is also a need to develop multiphysic modelling methods. In addition to the mechanical behaviour, the other physical effects

(e.g. electric, thermal, acoustic) have to be taken into account whereas they were ignored in the past. For instance, the very compact assembly structure in the engine compartment or high voltage in battery systems can lead to a high temperature environment and the thermal expansion can no longer be neglected. The coupling between these different sources of energy has to be managed with care since their respective characteristics can be very different. For instance, the dynamics of the electric part is generally much faster than the dynamics of the mechanical system. Co-simulation techniques can then be considered to adopt different time scales to describe each physical phenomenon.

1.2 Objectives of the thesis

The present thesis is dedicated to the development of new methodologies to simulate efficiently the dynamics of automotive transmission devices. The various models developed have been formulated within the framework of the nonlinear finite element method for flexible multibody systems [42]. The latter allows the modelling of complex mechanical systems composed of rigid and flexible bodies, kinematic joints and force elements. Based on absolute finite element coordinates, the description of flexible structural components naturally accounts for large rigid-body motions and elastic deflections.

In a first step, an industrial drivetrain component is fully modelled by using the tools available in the commercial software SAMCEF/MECANO. This preliminary study has the objective to point out the needs for enhanced or new modelling capabilities in the field of automotive driveline.

TORSEN differentials, which are representative driveline components, have been selected for that numerical study. Their models have been developed with the support of the car part manufacturer JTEKT TORSEN. These limited slip differentials are fully mechanical devices in which the locking effect and the torque transfer are only due to friction inside the differential. The TORSEN differentials are mainly composed of a set of gear pairs and thrust washers (see Fig. 1.1). The frictional contacts occurring between the latter are fundamental to their working principle.

The modelling assumptions introduced and the drawbacks observed during the numerical simulation of this complex industrial application have inspired the further developments achieved in this PhD thesis. However, all claimed contributions are formulated with a sufficient level of generality to be applied to other transmission mechanisms in the automotive industry or even in other fields of mechanics (energy, robotics, etc).

The contact modelling is a central question in this thesis. The finite element software SAMCEF allows to perform dynamic analysis of multibody systems including

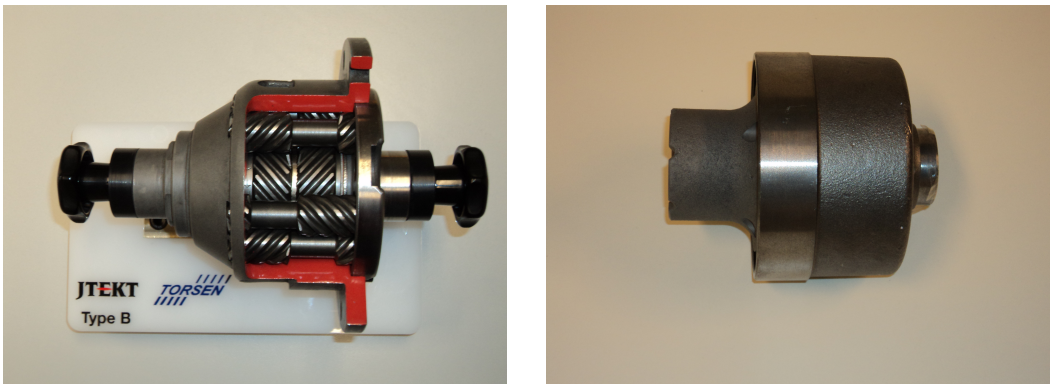

(a) type B (b) type C

Figure 1.1: Main application: TORSEN differentials.

contact conditions. Nevertheless, the contact models available are only suited to study the local effects between detailed 3D finite element meshes. Therefore, more global contact modelling techniques are proposed in this research work to formulate unilateral contact conditions between rigid bodies or superelements. A major characteristic of the developed contact models is related to the fact that they are formulated in a finite element context. A special attention is put on the modelling of impact and friction forces because these phenomena significantly influence the dynamic response of the full drivetrain but they are rarely accounted for in standard models of kinematic joints. All the contact models presented in this dissertation are based on a continuous approach so that a smooth solver of the generalized-α family can be used.

The final goal is to include the transmission component in a vehicle model in order to perform integrated simulations with the vehicle dynamics. Thus the various models are developed by keeping in mind this requirement. For instance, the number of generalized coordinates needed to model each contact condition has to remain small in order to keep the computational time and the memory allocation in a reasonable range.

Although the first TORSEN differential models exhibit numerical results in good agreement with experimental data, we propose to replace the rigid/flexible contact conditions by purely rigid contact models in order to reduce the model size. Based on the same contact modelling method, a non-ideal cylindrical joint is developed where clearance and friction are accounted for.

A squeeze film model is also proposed to represent the damping effect produced by the presence of lubricant between approaching bodies. Thanks to this new element, the resulting TORSEN differential model is more robust and computationally efficient and can be included in a full vehicle model in order to simulate various manoeuvres.

The last contribution of this thesis addresses the development of a new contact modelling approach defined between superelements. This innovative formulation enables to account for the flexibility of the contacting bodies while keeping a model size much smaller than a 3D finite element model. The main application of this contact model is the 3D simulation of gear pairs with meshing defects. The contact model between superelements is implemented in MATLAB whereas the others models are implemented in the software SAMCEF/MECANO.

1.3 Outline of the dissertation

The present manuscript is divided into eight chapters as follows. After this introductory chapter, the Chapter 2 starts with the state of the art in multibody system dynamics (Section 2.1). The nonlinear finite element method for flexible multibody systems is presented (Section 2.2) since all the models developed in the present thesis are formulated following this modelling approach. A brief review of the various topics tackled in the next chapters is given in Sections 2.3-2.6: the model reduction techniques, the modelling of contact, the non-ideal kinematic joints, the squeeze film modelling and the gear pair models.

Chapter 3 presents the TORSEN differentials models constructed by using only tools already available in the software SAMCEF/MECANO. First of all, in order to clearly understand the working principle of TORSEN differentials, a technical description is given in Section 3.1. Afterwards, the formulations used to model the two main kinematics joints are looked over: a global gear pair element (Section 3.2) and an unilateral contact condition (Section 3.3). The modelling assumptions introduced are listed in Section 3.4 where the numerical results are presented too. This chapter enables to emphasize the difficulties inherent to simulate the dynamics of driveline mechanisms.

The modelling of contact between rigid bodies is studied in Chapters 4 and 5. The continuous impact modelling method is described in section 4.2. This continuous contact approach is assessed by means of the simulation of the bouncing ball benchmark (see Section 4.2.2). Then, the kinematic description of a 3D contact element is proposed for frictional contacts between two planar rings (Sections 4.3-4.4). This new element is used to model the contact between the thrust washers and the lateral faces of gear wheels (Section 4.4.1). Using the same kind of contact force law, a cylindrical joint with defects is developed (Section 4.5). This joint accounts for the clearance, the tilting and the friction and is applied to represent the connection between the planet gears and the housing of the type C TORSEN differential (Section 4.5.3).

In Chapter 5, the film of lubricant between two planar bodies is considered. The proposed squeeze film model is based on a set of simplifying assumptions which enables to keep a compact formulation (Section 5.2). After having introduced this simple squeeze film contribution in the TORSEN differentials models, the latter become more

robust during the transient phases between two different working modes (Section 5.4). In the second part of the chapter (Section 5.5), the TORSEN differential models have been included in three different vehicle models in order to analyze the interactions between the differential and the vehicle dynamics. Several manoeuvres have been reproduced.

A new contact formulation defined between two superelement is detailed in chapters 6 and 7. Firstly, the basic principles of the Craig-Bampton's substructuring technique are reminded in Sections 6.2-6.3. The corotational formulation of a superelement based on this linear reduced model is presented in Sections 6.4-6.5. Then, the various steps of a simple contact detection algorithm are summarized (see Section 6.6). The formulation of the internal force vector related to each point in contact is described in Section 6.8 and is the major originality of the proposed model. Finally, the relevance of the approach for the dynamic analysis of transmission devices is demonstrated through simulation results of simple examples first, and then on a gear pair model (Sections 6.9-6.11).

Chapter 7 is also focused on a compact contact formulation between superelements. The main difference with the previous chapter lies in the superelement model used (Section 7.3). The latter is based on the dual Craig-Bampton method which is detailed in Section 7.2. The expression of the kinematic constraints needed to connect the dual superelement to its environment are described in Section 7.4. The chapter ends with the presentation of numerical results for the simulation of flexible gear pairs.

Finally, the conclusions of the PhD thesis and the perspectives for future works are summarized in Chapter 8.

Chapter 2

State of the art

Contents

In order to position the various contributions of the present work against the state of art of their research field, a brief review of the main leading methodologies is presented is this chapter. We do not intend to provide an extensive survey of all the theories available in the literature, but the objective is rather to give an overview of existing methods and explain the choices adopted for the developments of this work.

At first, the principles of the multibody system formalism are introduced in section 2.1 where the different types of coordinates, reference frames and rotation variables are reminded. Then, the nonlinear finite element method for flexible bodies is presented in section 2.2 because it is the basic framework for all claimed contributions of this PhD dissertation. The contact modelling being the core of several developments of this thesis, an overview of frequently encountered contact models is given in section 2.4. The main methods to represent the defects in kinematic joints are looked over in section 2.5. Finally, Chapters 6 and 7 address a novel gear pair model taking advantage of contact between superelements. To this end, model reduction techniques and gear pair models are reviewed in sections 2.3 and 2.6 respectively.

2.1 Multibody systems

A multibody system (MBS) is an assembly of several elements such as bodies (rigid or flexible), joints or force elements (see Fig. 2.1). The relative motion between interconnected structural components is restrained by force elements (e.g., spring, damper, actuator) whereas joints (hinge, prismatic, etc) enable a relative motion in a given direction and prevent the other degrees of freedom. The motion of a multibody system can also be influenced by externally applied forces or torques as well as motion-dependent forces developed through specific elements such as tyre models or controllers.

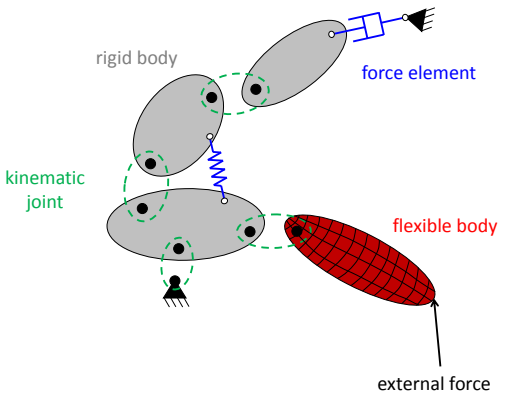

Figure 2.1: Block diagram of a basic multibody system.

The simulation of simple rigid multibody models is based on the fundamental principles of Classical Mechanics (e.g., Newton-Euler equations, Lagrange equations, Hamilton principle). Owing to the spectacular growth of computational resources, reliable and accurate simulations of large and complex industrial system composed of flexible bodies have become feasible over the last decades.

Multibody systems appear in numerous fields of mechanical engineering. Articulated mechanisms are typical applications of multibody systems. For instance, the trajectory of single or multiple arm robots [27] as well as the performance of machine tools [148] can be efficiently simulated using multibody models. As described in Ref. [11], detailed multibody models of automotive suspension systems are developed to study the dynamics of vehicles. One can also find many other application fields of MBS in aeronautics (e.g., landing gear mechanism [78]), spacecrafts (e.g., deployment of solar panels and antennas [84]), railway systems (e.g., wheel-rail contact [94], pantograph dynamics), etc. For a couple of years, the biomechanics expands dramatically the research works based on multibody system theory, see for instance Ref. [117] where the dynamics of the human walking is simulated or Ref. [110] in which the shoulder kinematics is modelled in order to develop new artificial prostheses. More recently, the call for sustainable energy systems also motivates accurate multibody models of wind turbines [55].

The literature mentions various formalisms to describe mathematically a multibody system (see Refs. [7, 143] for a detailed review of existing formulations in flexible multibody dynamics and Ref. [119] for rigid mechanisms). However, no matter the adopted approach, the analysis of a multibody system can be decomposed into a few steps (Fig. 2.2):

1. definition of modelling assumptions;
2. formulation of behaviour laws for components;
3. generation and integration of motion equations;
4. visualisation and interpretation of the results.

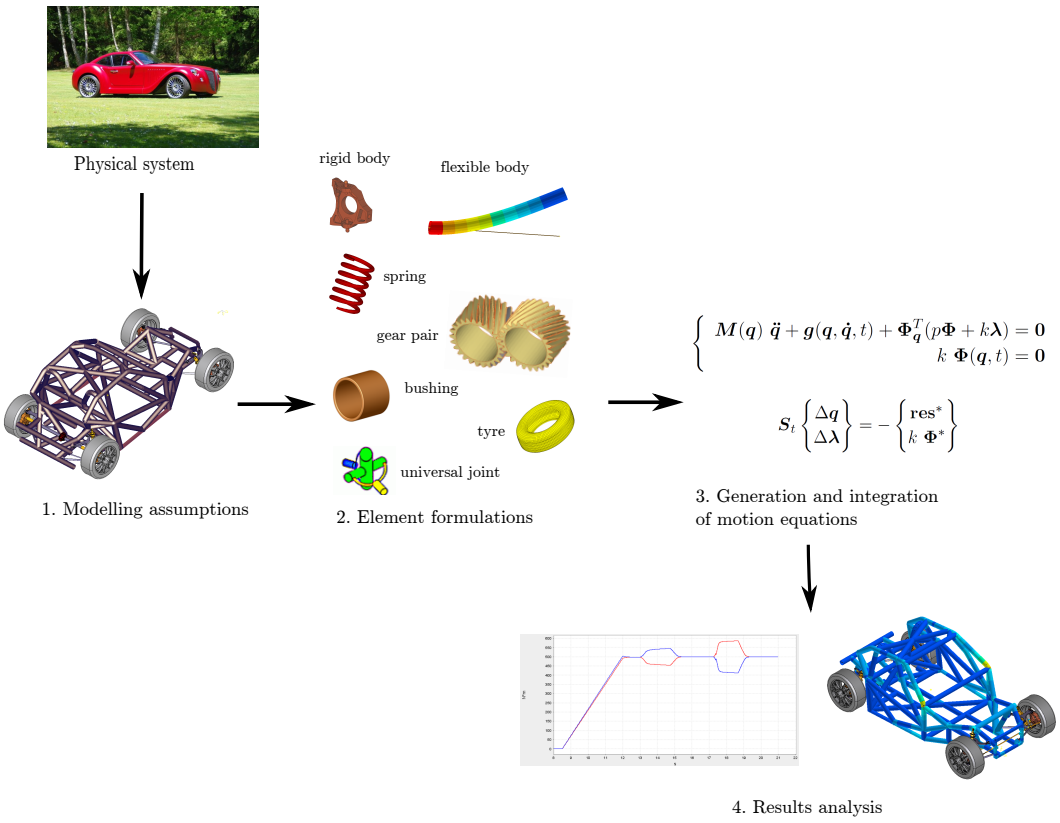

Figure 2.2: Various steps of a MBS analysis.

Modelling assumptions

Firstly, the mechanism under study has to be examined in order to determine the elements to be used in the model and the related assumptions. The model designer has to consider a couple of questions according to the application considered. Can

the system be represented as a planar mechanism or should the 3D spatial motion be accounted for? For each individual body, is the rigidity assumption acceptable? Are the strains in flexible structures sufficiently small to allow using a linear reduced order model (see section 2.3)? Can the kinematic joints be described with an idealized model in which friction and defects such as clearance are neglected?

Element formulations

This step consists in describing the kinematics of each element (body, joint, etc) with a set of coordinates. All the forces generated inside an element have to be expressed as functions of these coordinates and their time derivatives. In case of external forces or elements such as actuators, the forces can explicitly depend on time.

The type of coordinates adopted to define the system has a strong influence on the element formulation. The main types of coordinates will be briefly presented in section 2.1.1.

Generation and integration of motion equations

Once all elements are defined, the equations of motion are constructed using the classical equations and principles of mechanics: Newton-Euler, Lagrange, d'Alembert, Hamilton, etc. The number of differential equations of motion is equal to the total number of coordinates. If the system includes kinematics constraints, a set of equations is added to the ordinary differential equations (ODE) and leads to a differential-algebraic equation (DAE) system. Either symbolic or numerical methods can be used to formulate the equations of motion. The symbolic tools allow generating automatically and efficiently the equations in a symbolic format, which has the advantage of portability as well as avoiding the computation of some expressions by the model designer. Their use is, however, limited to systems of low to medium complexity. The numerical methods enable to build the equations of motion in a more systematic way for large and complex dynamic models including flexible bodies and are suitable for all types of systems.

Because of large amplitude body motions and joint kinematic constraints, most multibody models are nonlinear. Moreover, the equations of motion are often *stiff*, especially in the presence of flexible bodies which introduce a wide range of eigenfrequencies [42] or for multiphysic problems generally exhibiting dynamic time constants of different orders of magnitude between the various physical subsystems (hydraulic, electronic, structure, etc). To ensure the stability of the time integrator, an implicit integration scheme is required to solve constrained flexible multibody systems in a DAE form. Numerical damping is also often needed to avoid the amplification of high frequency numerical noise.

The nonlinear equations resulting from in single step or multistep implicit numer-

ical integrator such as Newmark, generalized-α [23], Adams, BDF, Runge-Kutta [96], are generally solved using a Newton-Raphson iterative process.

Result analysis

At the end of the simulation, the model analyst has to verify the consistency and accuracy of the mechanical response provided by the numerical model. The acceptability of the modelling assumptions adopted has also to be checked. For example, if a slender structural component has been modelled as a rigid body, it cannot be submitted to a high speed motion neither to significant loads. Otherwise, the simulation results can experience significant discrepancies compared with the actual physical system behaviour. The numerical results can sometimes be validated by comparison with experimental results or with more detailed numerical models or analytical models.

Much information can be acquired from a FE based multibody simulation, for instance: stress and strain in flexible bodies, contact pressures, constraint forces in kinematic joints, wear, ... These numerous valuable pieces of data are stored during the computation and can be figured out after the simulation during the post-processing phase.

The various simulation steps presented hereabove are not completely independent. Indeed, the choice of the type of coordinates describing the system strongly influences the formulation of all elements and the procedure to generate the equations of motion. The form of the equation system as well as the characteristics of the integrator scheme also depend directly on the type of coordinates. In order to get a computationally efficient simulation of a multibody system, the different steps have to follow each other in a natural way.

The multibody system approach enables to achieve static, kinematic or dynamic simulations of mechanical systems. Simulation is a *direct problem* which means that the time evolution of the position and the orientation of all bodies is computed from given applied forces/torques or a set of prescribed positions/velocities. Nevertheless, *inverse problems* can also be solved with the help of multibody models. The latter consist in finding a set of driving forces and torques in actuated joints allowing to yield a given global motion. Feedforward control and trajectory tracking in robotics are typical applications of inverse problems, see Ref. [6].

2.1.1 Main types of coordinates in MBS

The number of degrees of freedom is an intrinsic feature of a multibody system and can be interpreted as the minimal number of independent coordinates needed to describe unequivocally the spatial configuration of the whole model. The generalized coordinates are a set of variables allowing to express the position and the orientation of each body of

the system. They often represent positions or displacements in translation or rotation but other kinds of variable can also be used, e.g., the modal amplitudes of superelements (see Section 6.2). These coordinates are not necessarily independent, which means that an arbitrary variation does not automatically induce an admissible configuration of the system. In this case, kinematic constraints are needed to express the dependence between some coordinates so that the MBS model still has the correct number of degrees of freedom (see for instance the Grübler formula in Ref. [13]).

Several approaches are available to select the vector of coordinates describing each element of a multibody system. A global overview of the common type of coordinates is given in the sequel of this section and the differences are illustrated in Figure 2.3 for the modelling of a planar slider-crank mechanism. This simple 2D multibody system is composed of three rigid bodies (crank, connecting rod, piston), three hinges and one prismatic joint.

The choice of the type of coordinates is fundamental because it determines the form and the dimension of the equation system that describe the physical system and therefore influences the computational efficiency and the simplicity of the implementation. However, there is no universal choice: the most appropriate type of coordinates depends on the application considered, each approach having its own advantages and drawbacks.

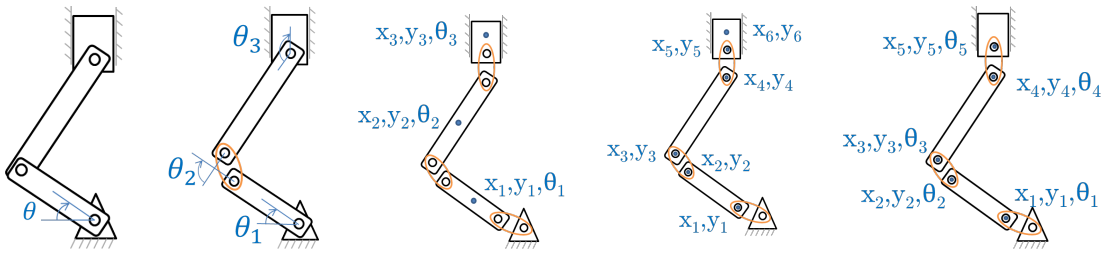

(a) minimal coordinates (b) relative coordinates (c) reference point coordinates (d) natural coordinates (e) finite element coordinates

Figure 2.3: Description of the slider-crank mechanism with different types of coordinates.

Minimal coordinates

With the minimal coordinates approach, the number of generalized coordinates corresponds to the number of physical degrees of freedom of the mechanism. Therefore, all coordinates are independent and no algebraic constraint is needed. The equation system has a minimal dimension and only includes ordinary differential equations (ODE), which an important advantage. For instance, a unique equation of motion enables to simulate the one DOF slider-crank mechanism (Fig. 2.3(a)). The sole coordinate θ

represents the angular position of the crankshaft.

However, the kinematic description of the system and the generation of the motion equations can be quite complicated even though symbolic tools allow an automatic processing. Moreover, for some closed-loop systems such as the well-known four-bar mechanism, multiple configurations may arise for the same numerical values of the generalized coordinates, and singular configurations may also occur.

The minimal coordinates are not commonly used in commercial softwares because this method is not sufficiently systematic to treat a large range of applications. Nevertheless, very efficient simulations of complex rigid multibody systems have been performed using minimal coordinates as presented in Ref. [58].

Relative coordinates

The relative coordinate method is based on the concept of kinematic chains. The position and orientation of each body is computed from the position and orientation of the previous body in the kinematic chain. Hence, the generalized coordinates correspond to the relative DOFs between interconnected bodies. Relative coordinates are particularly well adapted for open-tree mechanisms, i.e., systems for which each joint can be submitted to an arbitrary relative motion without restriction due to the other kinematic joints. Indeed, this choice has the advantage to account for the kinematic joints in an implicit way, i.e., no algebraic constraint is needed to represent the joints. In the case of a closed-loop system, at least one joint has to be cut in order to get a virtual open kinematic chain. The loop closure is then imposed by kinematic constraints which add algebraic equations to the equations of motion.

The slider-crank (Fig.2.3(b)) includes one kinematic loop. The three coordinates $(\theta_1, \theta_2, \theta_3)$ express the relative rotation angle of the three hinges. Consequently, two constraints are needed to impose the correct kinematics of the system. For example, the first constraint can consist in avoiding the displacement of the piston in the x-axis, while the second constraint could express the fixed orientation of the piston.

The use of relative coordinates leads to a small number of differential equations of motion and even to a minimal ODE-system matching the number of degrees of freedom in case of open-tree structures. Nevertheless, the computation of velocities and accelerations is far from being trivial. Recursive algorithms allow to construct a full kinematic description of the system and the generation of motion equations in a symbolic form enables many simplications in the expressions in order to obtain compact and efficient models [118].

However, for complex systems, the choice of loop closure constraints and their formulation can be complicated. Moreover, the modelling of flexible bodies often requires to decompose the motion into rigid body motion and elastic local deformation, which

leads to a complex and non compact form of inertia forces which can hardly capture nonlinear phenomena such as geometric stiffening.

The relatives coordinates, also called Lagrangian or joint coordinates, were the first kind of coordinates adopted since the early applications of multibody models were dedicated to robot manipulators and spacecraft systems. Many research works (see Refs. [31, 74, 100, 146]) have proven the efficiency and reliability of the method which is now used in several commercial software packages (SIMPACK, RECURDYN,etc).

Reference point coordinates

The reference point coordinates enable a highly systematic formulation of multibody systems. This approach is extensively described in the scientific literature [40, 54] for the modelling of large systems including numerous rigid bodies and is often referred to absolute or cartesian coordinates. The software MSC ADAMS, frequently used in the automotive industry, is based on this type of coordinates.

With this approach, each body is considered as an independent entity whose spatial motion is described by the position and orientation variables of the center of mass expressed in an inertial frame. In 3-dimensional analysis, each rigid body is represented by 6 coordinates: 3 in translation and 3 in rotation (only 3 coordinates in 2D models). All joints are modelled by separate elements and are accounted for by adding algebraic constraints to the set of differential equations of motion. In contrast to relative coordinates, even open-tree structures involve kinematic constraints.

The main drawback of reference point coordinates results from the large number of equations in the DAE-system. For instance for the simple 2D slider-crank mechanism (Fig. 2.3(c)) no less than 17 coordinates are introduced. In addition to the 9 coordinates (3 per body), 8 Lagrange multipliers related to the kinematic constraints are needed (2 contraints for each of the 3 hinges and 2 constraints for the prismatic joint as well).

However, the equations take a simple form and the resulting system of equation is sparse. Besides, unlike relative coordinates, it is not needed to reformulate the equations in case of modification of the topology of the system and the pre-processing work to determine the cutting of closed-loops is avoided. Therefore, even if a large set of equations are generated, efficient simulations can be performed with this choice of coordinates.

Initially developed to simulate the dynamics of rigid bodies, this approach has been extended to the modelling of flexible bodies, see Ref. [123] where the absolute motion is decomposed into a global rigid body motion and small elastic deformations in a frame attached to the rigid motion. The nonlinear finite element method presented hereafter permits a more accurate modelling of the flexible and nonlinear effects and can be seen as an extension of reference point coordinates.

Natural coordinates

The concept of natural coordinates has been developed by Garcia de Jalón [39, 40]. It can been seen as a variant of reference point coordinates in order to reduce the dimension of the equation system. The generalized coordinates represent the absolute nodal positions of some specific points (e.g., interconnection nodes between bodies) and the direction of unit vectors attached to the elements (bodies, joints,...). In contrast to the pure reference point coordinates method, it is not necessary to have a node located at the center of mass of each body. Moreover, only translation coordinates are used and therefore the difficult choice of angular coordinates with their inherent singularities is avoided (see Section 2.1.3). The rotation matrices are expressed by means of the unit vectors which can be computed from the position of two arbitrary points.

The formulation of kinematic joints is simplified and often consists in a trivial identification of nodes or unit vectors attached to the bodies constrained by joints. For example, a 2D revolute joint does not involve any algebraic constraint if a node is located on the rotation axis and is shared by the two bodies. Another advantage of natural coordinates is the constant nature of the mass matrix and the absence of Coriolis and centrifugal forces. Nevertheless, to model a rigid body, algebraic constraints have to be introduced to enforce the non-deformability conditions between its various points.

As illustrated in Figure 2.3(d), 12 coordinates are used to describe the planar slider-crank system. However, fixing the mechanism to the ground is achieved by introducing 3 boundary nodal constraints which allows to impose the value of three coordinates (x_1, y_1, x_6) and transform these variables into constant parameters. Moreover, the hinge joints defined between the connection points attached to the bodies permit to eliminate 4 more coordinates (x_3, y_3, x_5, y_5). Since this mechanism has one DOF, the 5 active coordinates (x_2, y_2, x_4, y_4, y_6) are constrained by 4 algebraic constraint equations: 1 constraint for each of the three rigid bodies and 1 constraint for the prismatic joint.

Finite element coordinates

The finite element coordinates can be considered as an evolution of reference point coordinates particularly suited to model flexible structural components. The vector of generalized coordinates is composed of position and/or angular absolute coordinates of various nodes. As for the natural coordinates, some nodes are located at the attachment points between bodies, that allows to simplify the expression of kinematics joints, e.g., simple boolean identifications are sometimes sufficient. Rigidity constraints are prescribed between the various nodes of rigid bodies to satisfy the undeformability assumption. In case of flexible bodies, the absolute coordinates of the nodes of the finite element mesh are included in the set of coordinates. The displacement field of any point of a flexible body is computed according to shape functions defined from the nodal coordinates.

With finite element coordinates, the generalized coordinates are often numerous which leads to large systems of differential-algebraic equations. However, the matrices describing the latter are generally sparse. Fifteen coordinates are introduced in a first step to describe the spatial configuration of the 2D slider-crank system (Fig. 2.3(e)). The boundary nodal constraints and the assembly nodal constraints enable to eliminate several coordinates (x_1, y_1, x_3, y_3, x_5, y_5) through Boolean identification of node components located at the connection point with the ground or with another body. The rigid body constraints involve two additional identifications ($\theta_1 = \theta_2$, $\theta_3 = \theta_4$). The active set of generalized coordinates is reduced to 7 coordinates which are submitted to 6 kinematic constraints: 4 constraints to ensure the rigidity of the crank and the connecting rod, 2 constraints for the prismatic joint of the piston.

The nonlinear finite element method for multibody systems is described in Ref. [42] and is implemented in the module MECANO of the commercial software SAMCEF [88]. The models developed in this doctoral thesis are based on this method. More details about the simulation of flexible multibody systems with the finite element approach are given in section 2.2.

The Absolute Nodal Coordinate Formulation (ANCF) described in [123] is also based on finite element coordinates but replaces the angular variables by slope variables to represent the rotations. That allows to avoid the singularities inherent to the parameterization of large angular motion in 3D (see section 2.1.3) but leads to others drawbacks such as locking or accuracy problems (see Ref. [114]).

Mix of various coordinates

A disadvantage of the natural coordinate method is the absence of coordinates describing explicitly the relative motion of the joints (e.g., relative rotation angle in hinge joint). Therefore, driving actuated joints is more complicated than with the relative coordinate approach. To circumvent this drawback, translational or rotational relative coordinates associated with the DOFs of joints can be added to the vector of natural coordinates. Obviously, the same number of algebraic constraints needs to be introduced. This hybrid set of coordinates is described in [40] and is commonly called *mixed coordinates*. Two different types of coordinates can also be used to model efficiently a system including a mix of rigid and flexible bodies as described in Ref. [38]. The natural coordinates stand for the rigid bodies whereas the absolute nodal coordinates are used to describe the flexible bodies. The formulation of kinematics joints benefits from the common characteristics of both types of coordinates.

The computational efficiency of each multibody system formulation is not only dependent on the dimension of the equation system to be solved. The nature of the equation system has a strong influence: ODE or DAE solver, sparse or full matrices. For instance, a system described with absolute coordinates is often represented by more

equations than using relative coordinates. However, the generation of the equations of motion is easier with absolute coordinates, the computation of the iteration matrix involves more compact and simpler expressions and the matrices are sparse. Consequently, a simulation based on absolute nodal coordinates is not necessarily less efficient than one based on relative coordinates since the numerical implementation has a strong influence on the computational efficiency of the solution.

2.1.2 Reference frame of flexible bodies

The simulation of multibody systems including flexible bodies requires to compute simultaneously their global motion and their deformation at each time step. The deformation field of each flexible body is determined by means of shape functions (vibration modes or finite element shape functions) associated with a finite set of coordinates (amplitude of modes, position of nodes) arising from the spatial discretization of the flexible body. Several approaches are available according to the reference frame used in which the deformations are computed.

The **floating frame** of reference method is a frequently used approach (see for instance Refs. [101, 118, 142]). The motion of a flexible body is decomposed into a global rigid body motion represented by the floating frame and a deformation with respect to this reference frame. Rigid body coordinates correspond to the position and the orientation of the floating frame. A set of flexible coordinates allows to determine the deformations in this floating frame.

In case of small deformations, a linear elastic model can be used in the floating frame and leads to compact and simple expressions of elastic forces. Nevertheless, the computation of inertia forces is not trivial because the rigid and elastic coordinates are coupled by nonlinear terms. Furthermore, geometric stiffening phenomena due to high velocities can not be captured unless a non-constant geometric stiffness matrix is taken into account.

The nonlinear finite element method (see Ref. [42] and section 2.2) is based on an **inertial frame** to describe the position and rotation variables of each node. When this approach is adopted, the motion is not decomposed into global rigid body motion and deformations. The coordinates of a flexible body are absolute nodal coordinates expressed in a unique inertial frame. Even if the deformations are small, a nonlinear elastic model is needed owing to the geometric nonlinearities involved by large amplitude motions. However, the expression of inertia forces is more compact and easier to obtain than with the floating frame of reference approach.

The **corotational frame** approach can be seen as a mix between the floating frame and the inertial frame ones. The absolute position of all the nodes of a flexible body is used to determine its spatial configuration. Nevertheless, a reference frame, called corotational frame, is attached to each element of the finite element mesh and

follows its gross motion.

This intermediate frame at the element level enables to use a linear elasticity model in case of small deformations but large displacements of flexible bodies. In this way, the computation of elastic forces is greatly simplified compared with the nonlinear finite element method based on an inertial frame. Unlike in the floating frame approach, the set of generalized coordinates is not explicitly partitioned in rigid body coordinates on one hand and flexible coordinates on the other hand. Besides, the position and orientation coordinates of the corotational frame are not necessarily generalized coordinates but are intermediate variables which can be interpreted as the gross motion of the flexible body. The corotational frame variables are determined according to the absolute coordinates of body nodes. The superelement formulation presented in section 6.4 of this document uses a corotational description of a linear reduced-order model.

Multibody simulation software packages initially developed to model rigid bodies and thereafter enhanced to account for body flexibility often use a floating frame of reference. The corotational and inertial frame simulation codes generally come from the finite element community.

2.1.3 Rotation representation

In the general case of 3-dimensional motion, the representation of large rotations is intricate because finite rotations are not additive quantities. It is one of the delicate aspects of multibody system theory which has lead to numerous discussions in the scientific community.

The first MBS models were limited to small rotation angles and velocities in order to avoid the singularities due to large amplitude motion as well as the complex expressions of geometric stiffness or centrifugal and gyroscopic forces. During the last decades, on the one hand, specific formalisms have been elaborated to efficiently and rigorously manage finite rotations and, on the other hand, methods such as the ANCF [123] or the natural coordinates approach have been developed to circumvent the problems by excluding the rotation variables from the set of generalized coordinates.

The orthogonality property of the rotation matrix allows to fully describe this 3×3 matrix with only 3 independent variables. The **geometric parameterization** of rotations consists in expressing the rotation around an arbitrary axis as a sequence of three rotations along particular axes. *Euler angles* and *Bryant angles* have both the advantage to provide a convenient physical interpretation of rotation parameters but they are subject to singularities due to the trigonometric functions involved.

The literature also mentions various **vector parameterizations** (e.g. Ref. [8, 43]) which are based on the rotation invariants (rotation angle and direction of the rotation

axis). The well known *Euler parameters* have been successfully used for the simulations of large rotations in rigid or flexible multibody systems. They consist of 4 parameters linked by a normalization constraint leading to a quadratic expression of the rotation operator. The redundancy in the Euler parameters prevents from the singularity problems encountered with geometric parameterization and with the other vector parameterization methods such as the *cartesian rotation vector*, *Rodrigues parameters* and the *conformal rotation vector*.

Each approach for the representation of rotations has its own advantages and drawbacks. The best set of rotation parameters depends on the system modelled and on the formalisms adopted for the other modelling stages (type of coordinates,...). An enhanced version of the Cartesian rotation vector (section 2.2.1) is used in the nonlinear finite element method [42] which is the basis of the models presented in this dissertation. As an exception, in the superelement formulation described in Chapter 6, the rotations are not parametrized but rather considered as objects belonging to a non-linear manifold: a *Lie Group* (see Ref. [15, 125, 127]).

2.1.4 Kinematic joints

Kinematic joints are one of the main distinctive features of computer-aided analysis of multibody systems. These joints permit to connect the various bodies of the system modelled. Owing to the large range of applications of multibody systems, numerous effective joint formulations are available in the scientific literature. No matter the type of coordinates used to describe the system (Section 2.1.1), a library of kinematic joints is embedded in each multibody simulation software.

A distinction can be made between *lower pairs* and *higher pairs* kinematic joints. The lower pairs are limited to a set of six joints which can be expressed from the coordinates of one node and the direction of one axis. These basic joints (hinge, prismatic, cylindrical, screw, spherical, plane) detailed in Ref. [42] are characterized by contacts occurring over a surface. In contrast, the higher pairs present point or line contacts such as in bearings, universal joints, gear pairs, etc. The relative motion in higher pairs is more complicated so that the latter can sometimes be replaced by a superposition of lower pair joints.

The displacements prevented or prescribed by kinematic joints are often expressed by means of **algebraic constraints** added to the differential equations of motion. A **Lagrange multiplier** related to each algebraic equation allows to couple the constraints with the motion equations through the constraint forces. The algebraic equations have to be satisfied at each time step to get the equilibrium of the system.

The kinematic constraints are usually implicit nonlinear expressions of the coordinates of the bodies connected by the kinematic joint. Holonomic kinematic constraints are generally expressed as $\boldsymbol{\Phi}(\boldsymbol{q}, t) = \mathbf{0}$. If other variables than the coordi-

nates are needed to formulate a constraint, this constraint is called *non-holonomic* ($\boldsymbol{\Phi}(\boldsymbol{q}, \dot{\boldsymbol{q}}, t) = \mathbf{0}$). This occurs, e.g., in joints with friction, rolling motion without slipping where velocities coordinates have to be used. In unilateral contact problems, the equality constraint is replaced by an inequality constraint ($\boldsymbol{\Phi} \geqslant \mathbf{0}$). If a constraint is explicitly time dependent, it is qualified as *rheonomic*, otherwise, it is qualified as *scleronomic*. Additional coordinates are sometimes introduced to simplify the constraint formulations, e.g., relative rotation angle of the gear pair model described in section 3.2).

The kinematic constraints can be expressed at different levels: position level, velocity level or acceleration level. This choice strongly influences the index of the DAE system which corresponds to the number of differentiation with respect to time needed to transform the DAE into a ODE system. The integration schemes required to compute the numerical response are different if the initial DAE system is solved (*direct methods*) or if the system is transformed into a lower index DAE or an ODE system (*index reduction methods* [4]).

As described in Ref. [42], various methods are available to formulate a constrained problem: the *Lagrange multiplier* method, the *penalty function* method, the *augmented Lagrangian* method or the *perturbed Lagrangian* method. The *constraint elimination* method enables to transform the constrained problem into a unconstrained one. To this end, the coordinates are split in dependent and independent coordinates. The equations of motion can be expressed in function of the independent coordinates only and have the advantage to form an ODE system rather than a DAE system. Nevertheless, the identification of independent coordinates is not always easy even if symbolic tools are used. Moreover, this approach is not systematic. In contrast, the generality of the finite element coordinates sometimes allows to reduce some constraint equations by simple boolean identification of node coordinates at the joint location.

The kinematic joints are often confused with force elements by misuse of language. Indeed, purely kinematic joints, such as hinge or prismatic joints, prevent any relative motion between bodies in some directions whereas force elements as springs, bushings or the contact model developed in section 4.5 oppose a resistance to relative motions. Elements such as tyre models [135] or the gear pair model presented in section 3.2 rely on a mixed formulation including constraint equations and internal forces.

2.2 Nonlinear finite element method for flexible multibody systems

The contributions proposed in this doctoral dissertation have been developed in the framework of the nonlinear finite element method for flexible multibody systems as described in Ref. [42]. In order to set the context of this approach, the basic principles

are briefly presented in this section.

The nonlinear finite element representation adopted here emerged from the finite element community. The classical finite element theory extensively used for the analysis of individual components has been generalized to nonlinear dynamic systems composed of flexible bodies interconnected by kinematic joints. Unlike the floating frame approach, the motion is not decomposed in a global rigid body motion and local deformation. **The absolute position of each node of the finite element mesh is expressed in a unique inertial frame, that involves a nonlinear formulation of elastic strains**. In this way, the flexibility and the resulting nonlinear effects are accounted for in a natural way. Various types of flexible components can be represented and combined: beams, shells, membranes, volumes.

The inertia forces have simple expressions due to the adoption of finite element coordinates. Moreover, the topology of the system is implicitly included in the model, which is convenient in case of a structural optimization process based on the model.

The kinematics of each element and its contribution to the equations of motion are expressed independently, and a systematic process enables to assemble all elements whatever their type (bodies, joints).

Within this nonlinear finite element formulation of flexible multibody systems, the algebraic constraints are expressed at position level using the Augmented Lagrangian method. The set of equations is necessarily large since numerous generalized coordinates are involved, but the global system matrices are sparse. In order to reduce the size of the equation system, substructuring methods such as the *superelement* method (see Section 6.2) can be used to simplify the detailed finite element mesh of a flexible body. The finite element coordinates allow mixing finite element modelling, superelement formulation and rigid body representation in a same global model in order to get the best compromise between accuracy and computational efficiency.

2.2.1 Rotation parameterization

With vector parameterization of rotations, the rotation of each body in a multibody system is completely represented by two invariants: the rotation axis $\boldsymbol{n}$ and the rotation angle ϕ about this axis. Both quantities are invariants under a frame transformation. According to [42], the rotation matrix is parameterized using the Cartesian rotation vector. The rotation matrix is thus expressed as the exponential of the **Cartesian rotation** vector which is simply defined as the product of the two invariants ($\boldsymbol{\Psi} = \phi\, \boldsymbol{n}$):

$$\boldsymbol{R} = \exp(\widetilde{\boldsymbol{\Psi}}) \tag{2.1}$$

However, such rotation parameterization is only valid in the range $]-2\pi, 2\pi[$ and it encounters a singularity whenever the rotation angle passes through a multiple of 2π.

One solution to circumvent the singularity and allow rotations larger than two complete revolutions consists in combining the Cartesian rotation vector with an **updated Lagrangian approach**. This method is based on a decomposition of the global rotation into the rotation describing the reference configuration corresponding to the previous converged time step, and the increment with respect to this reference configuration.

The rotation matrix is thus split in three contributions (Fig. 2.4):

$$\boldsymbol{R} = \boldsymbol{R}_1 \; \boldsymbol{R}_{ref} \; \boldsymbol{R}_{inc} \tag{2.2}$$

where $\boldsymbol{R}_1$ is the rotation matrix at initial time ($t = 0\,\mathrm{s}$), $\boldsymbol{R}_{ref}$ and $\boldsymbol{R}_{inc}$ are the rotation matrices associated with the reference configuration and with the increment respectively. The resulting set of generalized coordinates $\boldsymbol{q}$ consists thus of the nodal position coordinates $\boldsymbol{x}$ and the increments of rotation parameters $\boldsymbol{\Psi}_{inc}$.

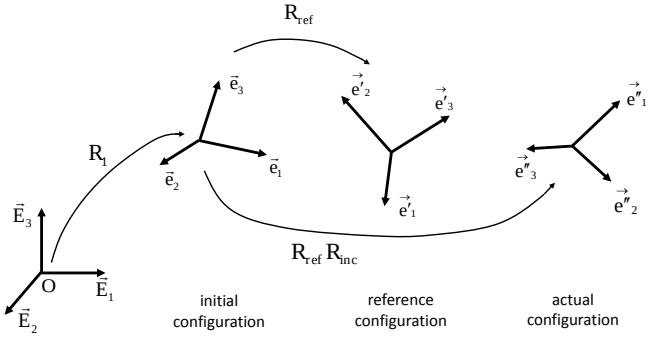

Figure 2.4: Decomposition of the global rotation matrix in 3 contributions.

The tangent operator, $\boldsymbol{T}(\boldsymbol{\Psi}_{inc})$, enables to compute the material variation of rotations ($\delta\boldsymbol{\Theta}$) from the variation of the incremental Cartesian rotation vector ($\delta\boldsymbol{\Psi}_{inc}$).

$$\delta\boldsymbol{\Theta} = \boldsymbol{T}(\boldsymbol{\Psi}_{inc}) \; \delta\boldsymbol{\Psi}_{inc} \tag{2.3}$$

with

$$\boldsymbol{T}(\boldsymbol{\Psi}_{inc}) = \frac{\sin\|\boldsymbol{\Psi}_{inc}\|}{\|\boldsymbol{\Psi}_{inc}\|}\,\boldsymbol{I} + \left(1 + \frac{\sin\|\boldsymbol{\Psi}_{inc}\|}{\|\boldsymbol{\Psi}_{inc}\|}\right)\boldsymbol{n}\boldsymbol{n}^T - \frac{1}{2}\left(\frac{\sin\frac{\|\boldsymbol{\Psi}_{inc}\|}{2}}{\frac{\|\boldsymbol{\Psi}_{inc}\|}{2}}\right)^2 \widetilde{\boldsymbol{\Psi}} \tag{2.4}$$

2.2.2 Dynamic equations of motion

The dynamics of a flexible multibody system can be expressed from the Hamilton principle. This variational principle allows to generate the equations of motion like the

d'Alembert principle which is based on the virtual work principle. It states that the trajectory of a system submitted to kinematic constraints can be found by solving a constrained minimization problem:

$$\min_{\boldsymbol{q}} \left(A = \int_{t_1}^{t_2} (\mathcal{L} + \mathcal{W}_{nc}) \, \mathrm{d}t \right) \qquad \text{subjected to} \qquad \boldsymbol{\Phi}(\boldsymbol{q}) = \mathbf{0} \tag{2.5}$$

where the Lagrangian $\mathcal{L} = \mathcal{K} - \mathcal{V}$ is the difference between the kinetic energy $\mathcal{K}(\boldsymbol{q}, \dot{\boldsymbol{q}})$ and the potential energy $\mathcal{V}(\boldsymbol{q})$, $\mathcal{W}_{nc}$ is the virtual work of non-conservative forces and $\boldsymbol{\Phi}(\boldsymbol{q})$ is a set of algebraic equations describing the holonomic bilateral kinematic constraints.

The introduction of an additional unknown, a **Lagrange multiplier** λ_i, related to each algebraic equation Φ_i enables to transform the constrained minimization problem into an unconstrained one. By expressing the stationarity condition ($\delta A^* = 0$), Eq. 2.5 can be reformulated as:

$$\delta \int_{t_1}^{t_2} \left(\mathcal{L} + \mathcal{W}_{nc} - \boldsymbol{\lambda}^T \boldsymbol{\Phi} \right) \, \mathrm{d}t = 0 \tag{2.6}$$

After integration by parts of the variation of the Lagrangian ($\delta\mathcal{L}$), the Lagrange equations are easily obtained (see [13]). The equations of motion governing the dynamics of a multibody system constrained by kinematic joints can thus be expressed in matrix form as:

$$\begin{cases} \boldsymbol{M}(\boldsymbol{q}) \, \ddot{\boldsymbol{q}} + \boldsymbol{g}(\boldsymbol{q}, \dot{\boldsymbol{q}}, t) + \boldsymbol{\Phi}_{\boldsymbol{q}}^T \boldsymbol{\lambda} = \mathbf{0} \\ \boldsymbol{\Phi}(\boldsymbol{q}, t) = \mathbf{0} \end{cases} \tag{2.7}$$

where $\boldsymbol{q}$, $\dot{\boldsymbol{q}}$ and $\ddot{\boldsymbol{q}}$ are the generalized displacements, velocities and acceleration coordinates, $\boldsymbol{M}(\boldsymbol{q})$ is the mass matrix and $\boldsymbol{g}(\boldsymbol{q}, \dot{\boldsymbol{q}}, t) = \boldsymbol{g}^{gyr}(\boldsymbol{q}, \dot{\boldsymbol{q}}) + \boldsymbol{g}^{int}(\boldsymbol{q}, \dot{\boldsymbol{q}}) - \boldsymbol{g}^{ext}(t)$ is a vector collecting all the system forces, with $\boldsymbol{g}^{gyr}$ the vector of the complementary inertia forces, $\boldsymbol{g}^{int}$ the vector of the internal forces, e.g., elastic and dissipations forces, and $\boldsymbol{g}^{ext}$ the vector of the external forces. $\boldsymbol{\Phi}_{\boldsymbol{q}}^T \boldsymbol{\lambda}$ are the constraint forces applied on the generalized coordinates. The set of Lagrange multipliers $\boldsymbol{\lambda}$ can be seen physically as the reaction forces needed to impose the algebraic constraints $\boldsymbol{\Phi} = \mathbf{0}$. The notation $\boldsymbol{\Phi}_{\boldsymbol{q}}$ is a compact form to express the constraint gradient $\partial\boldsymbol{\Phi}/\partial\boldsymbol{q}$.

The equations of motion form a set of n nonlinear differential equations with $n+m$ unknowns, supplemented with m algebraic equations associated with the kinematic joints and rigidity constraints. The nonlinearities can have of various origins: geometry, nonlinear material behaviour, nonsmooth phenomena such as contact forces, etc. Even if the multibody system only includes rigid bodies, the large rotations induce nonlinear terms in the equation of motion. Therefore, the equation system which has to be solved at each simulation time is a nonlinear DAE-system of $m + n$ equations with $n + m$ unknowns.

The form of the equation system (Eq. 2.7) is slightly modified if the **augmented Lagrangian** method is used (see Eq. 2.8). The latter constraint formulation improves

the numerical conditioning by means of a scaling factor and a penalty term. The multiplication of the constraint equations by a scaling factor k allows to obtain matrices with terms of the same order of magnitude and in this way avoid the ill-conditioning of the iteration matrix (see Eq. 2.27). The penalty term $p\boldsymbol{\Phi}^T\boldsymbol{\Phi}$ added in Eq. 2.6 facilitates the convergence of the Newton-Raphson iterative process when $\boldsymbol{\Phi} \to \mathbf{0}$. Since this term vanishes at convergence, the response of the system is independent of the choice of the penalty factor p. In a general way, the value of both numerical parameters can be adapted individually for each constraint.

$$\begin{cases} \boldsymbol{M}(\boldsymbol{q})\ \ddot{\boldsymbol{q}} + \boldsymbol{g}(\boldsymbol{q}, \dot{\boldsymbol{q}}, t) + \boldsymbol{\Phi}_{\boldsymbol{q}}^T(p\boldsymbol{\Phi} + k\boldsymbol{\lambda}) = \mathbf{0} \\ k\ \boldsymbol{\Phi}(\boldsymbol{q}, t) = \mathbf{0} \end{cases} \tag{2.8}$$

2.2.3 Numerical time integration of a DAE-system

The second-order DAE system (Eq. 2.7 or 2.8) representing the dynamics of a multibody system modelled with the nonlinear finite element method is usually composed of a large set of strongly nonlinear equations with coupled differential and algebraic equations. These equations have generally wide physical frequency content mainly due to the high frequency modes generated by the spatial discretization of the finite element mesh. Moreover, the kinematic constraints introduce infinite frequencies of mathematical origin which render automatically the system of equations stiff.

Therefore, unless some regularization method is used to transform the algebraic equations into differential ones, an **implicit time integrator** is recommended to ensure the stability of the numerical solution. Indeed, the main characteristic of implicit time integrators is that the choice of the time step size is governed essentially by accuracy considerations since the high frequencies present in the model can be filtered out by numerical damping.

With implicit integration schemes, the computation of the generalized coordinates at each time step requires the knowledge of accelerations at the current time instant and therefore confers to the algorithm its implicit nature. At each time step of the numerical simulation, the residual equation has to be solved:

$$\mathbf{res} \equiv \boldsymbol{M}\ddot{\boldsymbol{q}} + \boldsymbol{g} + \boldsymbol{\Phi}_{\boldsymbol{q}}^T(p\boldsymbol{\Phi} + k\boldsymbol{\lambda}) = \mathbf{0} \tag{2.9}$$

$$k\ \boldsymbol{\Phi} = \mathbf{0} \tag{2.10}$$

The generalized-α scheme [5, 23] is an implicit time integration algorithm able to solve second order differential equations. It is an extension of the Newmark scheme [98] which is well-suited to be very efficient for dynamic simulation of flexible multibody systems. In order to have the same number of equations as the number of unknowns ($\boldsymbol{q}$, $\dot{\boldsymbol{q}}$, $\ddot{\boldsymbol{q}}$, $\boldsymbol{\lambda}$), the equations of motion are completed by integration formulae which result

from a Taylor series expansion of the displacement and velocity fields:

$$\begin{aligned} \boldsymbol{q}_{t+h} &= \boldsymbol{q}_t + h\dot{\boldsymbol{q}}_t + h^2(0.5-\beta)\boldsymbol{a}_t + h^2\beta\boldsymbol{a}_{t+h} && (2.11)\\ \dot{\boldsymbol{q}}_{t+h} &= \dot{\boldsymbol{q}}_t + h(1-\gamma)\boldsymbol{a}_t + h\gamma\boldsymbol{a}_{t+h} && (2.12)\\ (1-\alpha_m)\boldsymbol{a}_{t+h} + \alpha_m\boldsymbol{a}_t &= (1-\alpha_f)\ddot{\boldsymbol{q}}_{t+h} + \alpha_f\ddot{\boldsymbol{q}}_t && (2.13) \end{aligned}$$

where β, γ, α_m, α_f are algorithmic parameters, h is the time step size and $\boldsymbol{a}$ is an auxiliary variable vector with can be considered as a pseudo acceleration averaging the actual acceleration $\ddot{\boldsymbol{q}}$ between time instants t and $t+h$. The integration formulas are linear and implicit with respect to the acceleration variables.

In order to solve the implicit equation system formed by Eqs. 2.9 to 2.13, an iterative **Newton-Raphson** procedure is used which consists in splitting the generalized coordinates $\boldsymbol{q}$, the velocities $\dot{\boldsymbol{q}}$ and the accelerations $\ddot{\boldsymbol{q}}$ as well as the Lagrange multipliers $\boldsymbol{\lambda}$ into an approximate solution ($\boldsymbol{q}^*$, $\dot{\boldsymbol{q}}^*$, $\ddot{\boldsymbol{q}}^*$, $\boldsymbol{\lambda}^*$) and a correction ($\Delta\boldsymbol{q}$, $\Delta\dot{\boldsymbol{q}}$, $\Delta\ddot{\boldsymbol{q}}$, $\Delta\boldsymbol{\lambda}$):

$$\begin{aligned} \boldsymbol{q} &= \boldsymbol{q}^* + \Delta\boldsymbol{q} && (2.14)\\ \dot{\boldsymbol{q}} &= \dot{\boldsymbol{q}}^* + \Delta\dot{\boldsymbol{q}} && (2.15)\\ \ddot{\boldsymbol{q}} &= \ddot{\boldsymbol{q}}^* + \Delta\ddot{\boldsymbol{q}} && (2.16)\\ \boldsymbol{\lambda} &= \boldsymbol{\lambda}^* + \Delta\boldsymbol{\lambda} && (2.17) \end{aligned}$$

The corrections are then computed owing to the **linearized form of the residual equation** around the approximate solution:

$$\begin{Bmatrix} \mathbf{res}^{lin}(\boldsymbol{q}^*+\Delta\boldsymbol{q}, \dot{\boldsymbol{q}}^*+\Delta\dot{\boldsymbol{q}}, \ddot{\boldsymbol{q}}^*+\Delta\ddot{\boldsymbol{q}}, \boldsymbol{\lambda}^*+\Delta\boldsymbol{\lambda}, t) \\ k\ \boldsymbol{\Phi}^{lin}(\boldsymbol{q}^*+\Delta\boldsymbol{q}, t) \end{Bmatrix} = \begin{Bmatrix} \mathbf{res}(\boldsymbol{q}^*, \dot{\boldsymbol{q}}^*, \ddot{\boldsymbol{q}}^*, \boldsymbol{\lambda}^*, t) \\ k\ \boldsymbol{\Phi}(\boldsymbol{q}^*, t) \end{Bmatrix} + \begin{bmatrix} \boldsymbol{M} & \mathbf{0} \\ \mathbf{0} & \mathbf{0} \end{bmatrix} \begin{Bmatrix} \Delta\ddot{\boldsymbol{q}} \\ \Delta\boldsymbol{\lambda} \end{Bmatrix} + \begin{bmatrix} \boldsymbol{C}_t & \mathbf{0} \\ \mathbf{0} & \mathbf{0} \end{bmatrix} \begin{Bmatrix} \Delta\dot{\boldsymbol{q}} \\ \Delta\boldsymbol{\lambda} \end{Bmatrix} + \begin{bmatrix} \boldsymbol{K}_t & k\boldsymbol{\Phi}_{\boldsymbol{q}}^T \\ k\boldsymbol{\Phi}_{\boldsymbol{q}} & \mathbf{0} \end{bmatrix} \begin{Bmatrix} \Delta\boldsymbol{q} \\ \Delta\boldsymbol{\lambda} \end{Bmatrix} \quad (2.18)$$

where the tangent stiffness matrix $\boldsymbol{K}_t$ and tangent damping matrix $\boldsymbol{C}_t$ are defined respectively by:

$$\boldsymbol{K}_t = \frac{\partial\ \mathbf{res}}{\partial\boldsymbol{q}} = \frac{\partial\ \boldsymbol{g}}{\partial\boldsymbol{q}} + \frac{\partial\ \left(\boldsymbol{M}\ddot{\boldsymbol{q}} + \boldsymbol{\Phi}_{\boldsymbol{q}}^T(p\boldsymbol{\Phi} + k\boldsymbol{\lambda})\right)}{\partial\boldsymbol{q}} \simeq \frac{\partial\ \boldsymbol{g}}{\partial\boldsymbol{q}} + p\ \boldsymbol{\Phi}_{\boldsymbol{q}}^T\boldsymbol{\Phi}_{\boldsymbol{q}} \quad (2.19)$$

$$\boldsymbol{C}_t = \frac{\partial\ \mathbf{res}}{\partial\dot{\boldsymbol{q}}} = \frac{\partial\ \boldsymbol{g}}{\partial\dot{\boldsymbol{q}}} \quad (2.20)$$

The Newton-Raphson iterative procedure is based on a **predictor-corrector** scheme. At each time step, a prediction of the system response (noted by a $''0''$ superscript) is computed from the integration formulas by assuming a null acceleration

$\ddot{\boldsymbol{q}}^0_{t+h} = \mathbf{0}$ as initial guess:

$$\boldsymbol{a}^0_{t+h} = \frac{1}{1-\alpha_m}\left(\alpha_f \ddot{\boldsymbol{q}}_t - \alpha_m \boldsymbol{a}_t\right) \tag{2.21}$$

$$\boldsymbol{q}^0_{t+h} = \boldsymbol{q}_t + h\dot{\boldsymbol{q}}_t + h^2(0.5-\beta)\boldsymbol{a}_t + h^2\beta \boldsymbol{a}^0_{t+h} \tag{2.22}$$

$$\dot{\boldsymbol{q}}^0_{t+h} = \dot{\boldsymbol{q}}_t + h(1-\gamma)\boldsymbol{a}_t + h\gamma \boldsymbol{a}^0_{t+h} \tag{2.23}$$

In order to verify the integration formulas (Eq. 2.11-2.13), the successive corrections of velocities and accelerations have to satisfy:

$$\Delta\ddot{\boldsymbol{q}} = \frac{1-\alpha_m}{1-\alpha_f}\frac{1}{\beta h^2}\,\Delta\boldsymbol{q} \tag{2.24}$$

$$\Delta\dot{\boldsymbol{q}} = \frac{\gamma}{\beta h}\,\Delta\boldsymbol{q} \tag{2.25}$$

Since the corrections $\Delta\dot{\boldsymbol{q}}$ and $\Delta\ddot{\boldsymbol{q}}$ can be explicitly expressed according to $\Delta\boldsymbol{q}$ using Eqs. 2.24-2.25, the number of unknowns in the linearized equation system $\{\mathbf{res}^{lin}\,;\, k\boldsymbol{\Phi}^{lin}\} = \mathbf{0}$ (see Eq. 2.18) can be easily reduced. The equation system to be solved at each iteration can thus be formulated as:

$$\boldsymbol{S}_t \begin{Bmatrix} \Delta\boldsymbol{q} \\ \Delta\boldsymbol{\lambda} \end{Bmatrix} = - \begin{Bmatrix} \mathbf{res}^* \\ k\ \boldsymbol{\Phi}^* \end{Bmatrix} \tag{2.26}$$

where the **iteration matrix** $\boldsymbol{S}_t$ is defined as:

$$\boldsymbol{S}_t = \begin{bmatrix} \boldsymbol{K}_t + \dfrac{\gamma}{\beta h}\boldsymbol{C}_t + \dfrac{1-\alpha_m}{1-\alpha_f}\dfrac{1}{\beta h^2}\boldsymbol{M} & k\boldsymbol{\Phi}^T_{\boldsymbol{q}} \\ k\boldsymbol{\Phi}_{\boldsymbol{q}} & \mathbf{0} \end{bmatrix} \tag{2.27}$$

The stiffness matrix can sometimes involve cumbersome expressions whose computation can be costly. However, only a reasonable approximation to it is needed, it is not mandatory to determine the exact full stiffness matrix. If some terms are neglected, the iterative scheme can often still converge to the actual solution. A compromise has to be found between the exact computation of the stiffness matrix and the approximation of some terms which may imply one or several additional corrections to reach convergence. A usual simplification that works generally well in the presence of mild nonlinearities consists in computing the stiffness matrix only once per time step rather than at each Newton-Raphson iteration.

The numerical parameters γ can be selected from α_m and α_f according to

$$\gamma = \frac{1}{2} + \alpha_f - \alpha_m \tag{2.28}$$

so that second-order accuracy is guaranteed.

The generalized-α scheme is a generalization of several well-known integrators often used in structural dynamics. For instance, the full generalized-α algorithm summarized

in Algorithm 1 is equivalent to the Newmark scheme if $\alpha_f = \alpha_m = 0$. The HHT (Hilbert-Hughes-Taylor) method is recovered when $\alpha_m = 0$, $\alpha_f \in [0, 1/3]$. Chung and Hulbert [23] proposed to express the numerical parameters α_m, α_f according to a third parameter which is a measure of the numerical damping:

$$\alpha_m = \frac{2\rho_\infty - 1}{\rho_\infty + 1} \tag{2.29}$$

$$\alpha_f = \frac{\rho_\infty}{\rho_\infty + 1} \tag{2.30}$$

where $\rho_\infty \in [0, 1]$ is the spectral radius at infinite frequencies. The choice $\rho_\infty = 0$ means annihilation of high frequencies whereas $\rho_\infty = 1$ corresponds to no numerical damping. The **unconditional stability** of the Chung-Hulbert scheme is ensured by Eqs. 2.29-2.30 together with the following definition of the numerical parameter β:

$$\beta = \frac{1}{4}\left(\gamma + \frac{1}{2}\right)^2 \tag{2.31}$$

The generalized-α method is an implicit **one step** integration scheme, i.e. the computation of system response at each time step is based on the values of the system variables at the current and the previous time steps only (see Eqs 2.11-2.12). Unlike the Newmark scheme, the generalized-α scheme keeps the **second order accuracy** even when numerical damping is introduced. In practice, due to the presence of kinematic constraints and spurious high frequency modes induced by the finite element discretization, a small amount of numerical damping is always needed to ensure the stability of the numerical solution.

2.3 Model reduction techniques in flexible multibody dynamics

The finite element method is a general and accurate technique to take the flexibility in multibody systems into account. Indeed, working with a FE discretization of the flexible body, complex geometries as well as nonlinear material behaviour can be considered. Besides, the FEM is based on the use of local shape functions at the element level, rather than on global ones, which allows to capture the deformation field for any configuration of the boundary conditions.

However, a large number of elastic DOFs are needed to describe the deformation field properly using a finite element model. Therefore, the size of the resulting equation system can become very large and the numerical model may lead to a high computational cost. Several decades ago, solving such huge problems, as industrial applications with millions of elements, was impossible due to the limited CPU and memory resources. Nowadays, static analysis of cumbersome models has become frequent but

Algorithm 1 Generalized-α time integration scheme

Initial values $\boldsymbol{q}_0$, $\dot{\boldsymbol{q}}_0$, $\ddot{\boldsymbol{q}}_0$
$\boldsymbol{a}_0 := \ddot{\boldsymbol{q}}_0$
for $t = 0$ to $t_f - h$ **do**
  Computation of prediction
  $\boldsymbol{a}^0_{t+h} = \frac{1}{1-\alpha_m}\left(\alpha_f \ddot{\boldsymbol{q}}_t - \alpha_m \boldsymbol{a}_t\right)$
  $\boldsymbol{q}^0_{t+h} = \boldsymbol{q}_t + h\dot{\boldsymbol{q}}_t + h^2(0.5-\beta)\boldsymbol{a}_t + h^2\beta \boldsymbol{a}^0_{t+h}$
  $\dot{\boldsymbol{q}}^0_{t+h} = \dot{\boldsymbol{q}}_t + h(1-\gamma)\boldsymbol{a}_t + h\gamma \boldsymbol{a}^0_{t+h}$
  $\ddot{\boldsymbol{q}}^0_{t+h} = \boldsymbol{0}$
  $\boldsymbol{\lambda}^0_{t+h} = \boldsymbol{0}$
  for $k = 1$ to k_{max} **do**
    Computation of residuals **res** and $\boldsymbol{\Phi}$
    if $\|\mathbf{res}\| < \mathrm{tol}_{\mathrm{res}}$ and $\|\boldsymbol{\Phi}\| < \mathrm{tol}_{\Phi}$ **then**
      break
    end if
    Computation of correction
    $$\begin{Bmatrix} \Delta \boldsymbol{q} \\ \Delta \boldsymbol{\lambda} \end{Bmatrix} = -\boldsymbol{S}_t^{-1} \begin{Bmatrix} \mathbf{res}^* \\ k\ \boldsymbol{\Phi}^* \end{Bmatrix}$$
    Incrementation
    $\boldsymbol{q}^{k+1}_{t+h} = \boldsymbol{q}^k_{t+h} + \Delta \boldsymbol{q}$
    $\dot{\boldsymbol{q}}^{k+1}_{t+h} = \dot{\boldsymbol{q}}^k_{t+h} + \frac{\gamma}{\beta h}\ \Delta \boldsymbol{q}$
    $\ddot{\boldsymbol{q}}^{k+1}_{t+h} = \ddot{\boldsymbol{q}}^k_{t+h} + \frac{1-\alpha_m}{1-\alpha_f}\frac{1}{\beta h^2}\ \Delta \boldsymbol{q}$
    $\boldsymbol{\lambda}^{k+1}_{t+h} = \boldsymbol{\lambda}^k_{t+h} + \Delta \boldsymbol{\lambda}$
  end for
  $\boldsymbol{a}_{t+h} = \boldsymbol{a}^0_{t+h} + \frac{1-\alpha_f}{1-\alpha_m}\ddot{\boldsymbol{q}}_{t+h}$
end for

transient dynamic studies have remained highly time consuming since the resulting large equation system has to be solved iteratively at each time step.

The objective of model reduction techniques is to reduce the model size while keeping an accurate representation of the flexible behaviour in the frequency range of interest. Various methods are available in the literature [10, 24, 77] and are commonly called Model Order Reduction methods (MOR). The latter methods can be classified according to different criteria: body-level or system-level reduction methods; applicability to linear or nonlinear system; modes shapes constructed by means of experimental or numerical results (FEM); free or fixed interface vibration modes,... The basic principle of each MOR method is to find a projection of the initial coordinates into a modal basis where the non-dominant modes are neglected.

In linear structural dynamics, *modal truncation* is the easiest way to define the global shape functions. It simply consists in neglecting the contribution of the high-frequency modes. Then, the modal matrix is formed by the first eigenvectors of the free structure.

Static condensation is a linear substructuring technique based on a partitioning of the set of DOFs into interface and internal DOFs. In that case, the modes represent the static response of the system, when the boundary nodes are submitted to unit displacements (see the *Guyan-Irons* method [61]). Contrary to the modal truncation, the static behaviour at the interface is exactly represented.

The *Craig-Bampton* method [24] is based on the *dynamic impedance concept* [44] and combines both aforementioned linear reduction methods: the static modes related to the boundary nodes are superimposed with a reduced set of dynamic vibration modes with clamped boundary. This substructuring technique, which opened the way to the Component Mode Synthesis (CMS), offers a convenient way to connect the superelement to the rest of the system. The new contact model developed in Chapter 6 is based on the Craig-Bampton method to construct the superelement models used as support for the proposed contact condition.

The reduction methods derived from the *dynamic admittance concept* are also based on a superimposition of static modes and vibration modes [42]. As for the modal truncation method, the vibration modes are the first eigenmodes of the free structure. However, a correction is introduced through attachment modes to get a statically correct response at the boundary nodes. The *Mac Neal* [92] and *Rubin* [116] methods enforce the assembly of the superelement with boundary displacements, whereas the *dual Craig-Bampton* method [113] uses interface forces to connect the superelement to its environment. The latter method is presented in detail in Section 7.2 and is also used to model the flexibility of bodies submitted to contact forces.

The previously mentioned MOR methods preserve the second-order nature of the initial full model. The reduction of the model size consists in condensing or neglect-

ing some DOFs. Other linear reduction techniques such as *Krylov subspaces* [51] or *balanced truncation* [81] methods deal with first order Linear Time Invariant (LTI) systems. These MOR methods originate from the domain area of system control and some of them have been extended to second-order systems. Unfortunately, they do not allow to keep boundary node coordinates in the reduced model so that the assembly of substructures within a finite element framework becomes difficult to perform.

Worth also mentioning is the Proper Orthogonal Decomposition (POD) method [71], a reduction technique based on a statistical treatment of simulation results to find the best projection on a modal basis built according to a least-square criterion.

The kinematics of flexible multibody systems subjected to large amplitude motion has a nonlinear behaviour. However, under certain circumstances (small strain assumptions), a linear elastic model can be used to account for the flexibility in a corotated or floating frame. Regardless of the MOR method adopted, the reduced model is embedded in the multibody system in the form of a *superelement*, which can be interpreted as a macro-element interconnected to the other entities of the system modelled. In addition to the time saving, the model reduction approach facilitates work sharing between different engineer teams. In this context, the portability and the size of the resulting reduced model can influence the choice of the MOR method.

The application of MOR methods is not limited to structural components. Real-time control of complex mechatronic systems requires efficient reduced models such as state-space reduction methods. Likewise, optimization algorithms extensively use reduced models, called metamodels, to avoid solving the full problem a huge number of times. This concept is the basis of the response surface theory [115].

2.4 Contact modelling

In automotive engineering and in other fields of mechanics, many transmission components include contacts between different parts. These contacts restrain the relative motion in one or several directions but they leave the motion free in the other directions. Several complex physical phenomena can appear in contact situations. For instance, if the relative velocity is high when a unilateral contact occurs, the impact produced can generate vibration waves in the entire structure. Furthermore, permanent plastic deformation can be induced (see Ref. [122]). The friction can also lead to stick-slip due to the difference between static and dynamic friction coefficients in Coulomb's law.

Accurate and efficient contact models are essential in order to get reliable drivetrain models. Gear boxes or differentials include numerous contacts which play a key role in the working principle of these mechanisms. It cannot be expected to set up a realistic dynamic model of such transmission components without a suitable and reliable mathematical formulation of contacts.

The contact models available in the literature can be classified according to their distinctive features: bilateral or unilateral, frictional or frictionless, between rigid or flexible bodies, etc. Some contact formulations are formulated in a general way and can cover several contact configurations: rigid-rigid contact [122], flexible-rigid contact [75] or flexible-flexible contact [147]. Several categories can also be identified concerning the geometrical configuration adopted during the contact detection phase: the projection method can be performed between two nodes, a node and a surface or between two element faces. The last configuration is often related to the use of mortar algorithms [53, 108] and enables a reliable computation of contact pressures and contact stresses.

The literature on contact modelling is vast since a wide range of disciplines in mechanics is spanned from the field of material mechanics where the stress distribution in the contact path is accurately computed by means of static FE simulations [130], to the dynamics of numerous collisions between small rigid granular bodies [97]. Many research works about contact modelling are dedicated to impact due to the difficulty to simulate numerically such complex and fast events depending on material and geometric properties as well as on the relative velocity level [45].

In the field of multibody system dynamics, two different approaches are often used to formulate a contact condition. Continuous contact modelling consists in assuming that the contact has a finite duration during which the displacements and velocities are supposed to vary in a continuous way. With the hypothesis of the instantaneous contact modelling, the contact duration is assumed to be zero, the positions of the contacting bodies remain continuous but their velocities undergo jumps.

The *continuous* contact formulations are often associated with penalty methods where a small penetration is allowed between the contacting bodies. This penetration is related to the compression of one or several equivalent local springs which enables to determine the magnitude of the contact force [34, 82]. Thereby, the impact is modelled at the acceleration-force level. The contact force law can be linear or nonlinear with respect to the local penetration length and a damper can be added in parallel with the penalty spring in order to introduce energy dissipation. The latter is often required in case of impacts between rigid bodies (see Section 4.2 for more details). Reference [91] gives a survey of nonlinear contact laws derived from the Hertz theory dedicated to contacts between rigid bodies having a spherical shape near the contact point. These various compliance force laws mainly differ from the definition of the damping factor which often depends on a restitution coefficient [122].

The choice of the penalty factor has a strong influence on the resulting accuracy, which is a drawback of this kind of contact model since it is sometimes not trivial to determine its value from the material and geometric data of contacting bodies. Indeed, a compromise has to be found between a too low value which involves a large and unrealistic indentation, and a too high one which induces a very stiff behaviour and raises numerical difficulties when a contact occurs. In case of a contact between

flexible bodies, the penetration is a side-effect which has no physical meaning but allows to regularize the complementary condition inherent to the contact condition. In this way, no algebraic equation is added to the set of differential equations of motion and each contact only has a contribution to the vector of internal forces. Besides the simplicity of implementation, an other advantage of continuous contact models resides in the fact that no specific transient solver is needed to manage the impact phenomena. A standard time integration scheme can be used to solve the full system. Indeed, positions and velocities of all bodies vary continuously and it is not necessary to stop the time integration at each impact time (see Ref. [80]). Moreover, these contact models naturally authorize multiple contacts.

An alternative method to formulate contacts in the special case where the bodies are flexible within the continuous framework consists in using kinematic constraints to enforce the non-penetrability between the bodies in contact. For each contact, an algebraic constraint is added to the set of equations of motion. The Lagrange multipliers method or the augmented Lagrangian method are often used to express the contact constraints (see Section 3.3.1). The latter are often expressed at the position level and represent the gap distance between the contacting bodies. The Lagrange multipliers associated with the kinematic constraints have the meaning of the magnitude of the normal contact force (eventually scaled by the scaling factor). In case of a unilateral contact condition, an activation/deactivation criterion has to be used in order to introduce or remove the constraint associated with each potential contact. The latter can be a source of discontinuities and lead to convergence complications.

In contrast to penalty methods, there is no explicit relationship between the local penetration and the normal contact force. The main advantage of the contact modelling by constraints lies in the exact contact condition enforcement that avoids unphysical penetration between the bodies in contact and keeps closer to the actual behaviour. This continuous contact formulation can only be used between flexible bodies but is not applicable for rigid contact.

Instantaneous contact formulations, also called discrete contact models, consider that unilateral contacts can occur in a infinitely short time [1, 47, 63, 149, 105]. Therefore, the simulation is divided in two periods: before and after the impact [45]. The contact constraints are often expressed at the velocity/impulse level and the Signorini's condition is modelled by means of differential inclusions or variational inequalities.

In order to account for the energy dissipation during each impact, these nonsmooth dynamic models use a coefficient of restitution. There exist several forms of the restitution coefficient according to the hypothesis adopted [122]. The Newton's model defines this coefficient as the ratio of relative velocities before and after the impact. The well-known Moreau-Jean scheme [63] is based on the kinetic coefficient of restitution proposed by Poisson. The Stronge's model [129] relies on the ratio of deformation energies during the compression and restitution phases. These three versions

of the restitution coefficient provide similar numerical results in case of basic contact configurations but significant differences can be observed for eccentric or frictional contacts [129]. For instance, Newton's or Poisson's models can lead to too high post-impact velocities.

The sudden velocity changes require the use of specific integration methods [22, 59, 83] since the classic smooth integrators are not able to deal with velocity discontinuities. Amongst all integration schemes available in the literature, two classes stand out: time-stepping schemes and event-driven schemes. Event-driven approaches require the interruption of the time integration when an impact is detected, then the contact problem is solved and a new set of initial conditions is determined to restart the integrator. Besides, the time step size has to be adjusted in order that each impact instant corresponds to a time step. Conversely, time-stepping methods discretise in time the complete multibody system dynamics including the unilateral constraints and the impact forces and the integration keeps a fixed time step size and is not interrupted.

Event-driven schemes have the advantage to provide a second or higher order of accuracy but they are not able to manage large multibody systems undergoing intermittent or multiple contacts. Time-stepping methods are more robust and enable the simulation of complex system subjected to multiple impact. However, their accuracy is limited to order one even during free flight motion. The two major time-stepping schemes are the Moreau-Jean scheme [63] and the Schatzman-Paoli scheme [103] which have lead to many divert forms. The nonsmooth contact models were initially dedicated to impacts between rigid bodies. Their extension to flexible bodies and multiple or closed contacts is not straightforward, owing notably to the very concept of the restitution coefficient [45].

The differences between continuous and instantaneous contact models can be summarized by stating that the continuous approach regularizes the nonsmoothness of the complementarity condition associated with unilateral constraints. The discontinuity produced by impact is replaced by a stiff but compliant behaviour.

Other works address the development of enhanced integration schemes to circumvent the lack of robustness and the numerical blow-up of classical integrators (e.g. generalized-α family) as for instance, the energy conserving schemes [12, 83, 126]. More recently, a research work led at the University of Liège in parallel to this PhD thesis, has resulted in the development of a non-smooth generalized-α scheme in order to model impact arising in flexible multibody systems [14, 20]. The founding principle of this new integration method consists in combining the nonsmooth Moreau-Jean scheme with the classical generalized-α scheme.

The addition of the frictional behaviour in the tangential directions is often easy for continuous contact models provided that a smooth transition is also ensured from sticking to sliding friction. Indeed, Coulomb's friction law can lead to either no feasible solution at all or to multiple solutions. In contrast, the extension of nonsmooth contact

models to friction models other than Coulomb's law is not straightforward at all (see Ref. [45]).

The influence of the lubrication is often neglected in the contact models used to simulate the dynamics of multibody models. Indeed, the numerical models achieved in multibody dynamics represent only the solid mechanical part of the system. The simulation of fluid flows is based on quite different concepts compared with those used in multibody systems. Therefore, the coupling of both effects is sometimes difficult. Besides, the fluid models are often cumbersome since numerous variables are involved to represent complex phenomena such as heat transfer, etc. However, the presence of oil between the contacting bodies can significantly influence the contact properties, for instance the friction coefficient is completely different in case of a dry or a lubricated contact.

Nevertheless, recent works bridge the gap and introduce simple lubrication models in multibody system analysis [29, 104]. For instance, the damping effect of oil film is studied in [29, 65]. As in the squeeze film model developed in Chapter 5, the Reynolds equation is often the basis to represent the global behaviour of the lubricating oil in particular within geometrical configurations such as spherical joints [35, 138], cylindrical joints [137] or gear pairs [70, 136]. The wear is also strongly dependent on the presence of lubrication (see Ref. [72]).

Due to their implementation simplicity and ability to be employed with smooth integration schemes, only continuous contact force models have been used in the various multibody systems simulated in this work (see Sections 3.3.1, 3.3.2, 4.2, 5.2.5, 6.7). These contact models are generally satisfactory to represent the interactions between bodies, so that complex multibody systems composed of rigid or flexible bodies and friction forces can be accounted for without a great effort.

2.5 Non-ideal kinematic joints

Kinematic joints are key components in multibody simulation tools. Most of the time, the joints are represented by idealized models which restrain the motion of the entire system by a set of kinematic constraints. Such formulation often considers the joints as perfect rigid elements without any default but has the advantages to be simple to implement and computationally efficient. However, physical phenomena such as clearance, misalignment, flexibility, friction, lubrication or impact can highly influence the dynamic response of the joints and have a non negligible effect on the accuracy and reliability of the full multibody model. For instance, in vehicle dynamics, the modelling of the joints between the suspension arms and the car body with bushing elements strongly influences the numerical response (see Ref. [3]). The dynamic performance of automotive transmission devices is sensitive to the imperfections of kinematic joints. Indeed, these undesirable side effects can introduce discontinuities on the transferred

torque and produce vibrations which can affect the security and comfort of the vehicle passengers.

The representation of kinematic joints taking account of their actual geometry and their material flexibility properties is with no doubt the most accurate approach. Contact conditions defined between finite element models of bodies connected by spherical joints are used in [3]. Such detailed models are able to capture a lot of disruptive factors but they are often quite complex to achieve and they highly increase the computational time.

Other models of joints are defined at an intermediate level of complexity between the two aforementioned categories [33]. These global joint representations account for some disruptive effects without increasing too much the number of degree of freedom. In [9], the influence of clearance and lubrication is studied for the hinge and spherical joints within the framework of energy preserving and decaying time integration schemes. A planar revolute joint model with clearance based on a continuous contact model is described in [32]. In that paper, the influence of clearance on the dynamic response of a planar slider-crank mechanism is compared to simulations with ideal joints. Similar continuous revolute joint models have been proposed by [111] and applied to the simulation of a double pendulum impacting a rigid plate with a study of the noise level generated by impact. The nonsmooth dynamic approach can also be used to represent kinematic joints with defects, see for example [26, 36].

2.6 Gear pair models

The literature about the dynamic modelling of gear pairs is vast since numerous mechanical transmission devices are impacted by the gear noise. The flexibility of the gear wheels, the inaccuracy of the manufacturing process, the wear or the meshing defects can lead to non-conformal contacts between the tooth flank profiles, which results in the appearance of gear noise.

Dedicated models have been developed to study the frequency response of gear pairs, see for instance Ref. [68] for a spur gear pair or Ref. [67] for a planetary gear train. Other detailed models are focused on the detailed analysis of meshing defects such as the loaded transmission error [89] or the misalignment [66]. The mechanical efficiency of gear pairs is addressed in Refs. [93, 120, 121].

In the multibody system framework, gear pairs are usually modelled as specific kinematic joints allowing to transfer force and motion between different components of a mechanism. The models proposed in Refs. [17, 28, 102] consider the gear wheels as rigid bodies and account for the tooth flexibility in a global way by using a spring along the line of pressure to determine the gear contact force. Reference [151] points out that for compliant gear bodies the flexibility of the gear web modifies significantly

the contact forces applied on teeth as well as the motion of the whole gear pair system. With rigid body models, such dynamic behaviour can not be reproduced.

The use of contact conditions between finite element models of the gear wheels allows to accurately account for the flexibility effects but it requires a very fine mesh of the whole skin [85]. Therefore, global dynamic analyses of several revolutions are highly expensive from a computational point of view and not feasible in practice.

Thus, there is a need to develop new multibody gear pair models accounting for the flexibility while keeping a reasonable model size. In this context, Refs. [133, 151] propose to prescribe contact conditions between reduced models of the gear wheels. This approach will be investigated in Chapters 6 and 7 of this dissertation thesis.

Chapter 3

FEM-MBS modelling of differentials

Contents

The topic of this PhD thesis is the modelling of driveline devices as multibody systems. In order to identify the needs for new developments in this context, an automotive transmission component, the TORSEN differential, has been modelled using the tools available in the commercial software SAMCEF/MECANO.

The proposed models of the TORSEN differentials enable to emphasize the difficulties inherent to dynamic simulation of driveline mechanisms. The resulting observations will guide the new element formulations that will be developed in the next chapters.

The present chapter is organized as follows. In order to understand the global working principle of the system under study, a technical description of TORSEN differentials is provided in section 3.1. The two main kinematic joints presented in this mechanical system being the gear pair and the contact conditions, so sections 3.2 and 3.3 describe the formulation used to model these joints.

After enumerating the various assumptions adopted in the multibody model of type B and C TORSEN differentials, numerical results are shown in a test bench configuration as well as in a vehicle operation (Section 3.4). Finally, in section 3.5

the three differentials of a four-wheel drive vehicle have been assembled with rigid driveshafts. The motion of a simple vehicle equipped with this driveline is simulated.

3.1 Working principle of TORSEN differentials

The two basic functions of any differential are to transmit the motor torque to the two output shafts and to allow a difference of rotation speed between these two outputs. In a vehicle, this mechanical device is particularly useful in turn when the outer wheels have to rotate quicker than the inner wheels to ensure good handling [52, 112].

The differentials can be used either to divide into equal parts the drive torque acting on the traction wheels of the same axle, or to divide the output torque from the gearbox between the two axles of four-wheel drive vehicles. This second application is often called the transfer box differential or central differential [57].

The main drawback of a conventional differential, also called open differential, is that the total amount of driving torque is always split between the two output shafts with the same constant ratio. This is a limitation, in particular when the driving wheels have different conditions of adherence. If the tractive torque exceeds the maximum transferable torque limited by road friction on one driving wheel, this wheel starts spinning. Although they do not reach their limit of adherence, the other driving wheels are no longer able to transfer torque because the input torque is equally split between the two output shafts.

The **limited slip differential** significantly reduces this drawback by allowing a variable distribution of the motor torque according to the available adherence of each driving wheel. For a vehicle with asymmetric road friction between the driving wheels, it is possible to transfer extra torque to the wheels having the better grip. For instance, Figure 3.1 depicts the central differential behaviour of a four-wheel drive vehicle crossing a slippery surface (snow, mud, ice, ...). In straight line, with equivalent road adherence on all wheels (Figs. 3.1(a), 3.1(d)), the motor torque is equally distributed between the two axles. If one wheel comes to the slippery area, the central differential reduces the torque provided to the front axle (Fig. 3.1(b)) or to the rear axle (Fig. 3.1(c)) and increases the torque applied on the other axle by the same amount.

The **TORSEN differentials** are limited slip differentials which are sensitive to torque imbalances between the two output shafts (TORSEN is a contraction of *torque sensing*). As soon as a difference of resisting torque applied by the ground on the wheels appears, a TORSEN differential locks up and behaves like a rigid axle, i.e., the wheels rotate at the same speed but they can be submitted to unequal torques in order to exploit the larger potential of adherence (see the vertical part of the curve in Fig. 3.2). However, the overall driving torque cannot be applied on one output shaft while no load is transferred to the second shaft of a TORSEN differential. When the

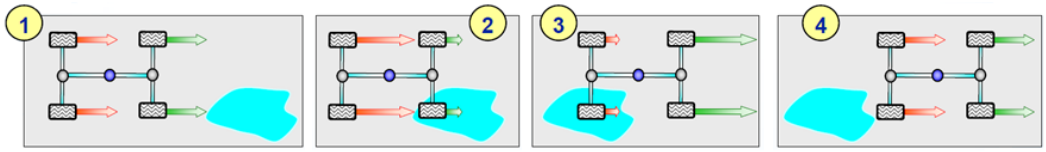

(a) Same adherence properties on each wheel (b) A front wheel on a slippery surface (c) A rear wheel on a slippery surface (d) Identical grip on each driving wheel

Figure 3.1: The TORSEN central differential transfers the torque between the two axles according to wheels adherence (courtesy of JTEKT TORSEN S.A.).

difference between the two output torques becomes too large, the differential *unlocks* and allows a difference of output rotation speeds but keeps the same constant torque ratio (horizontal parts in the Figure 3.2).

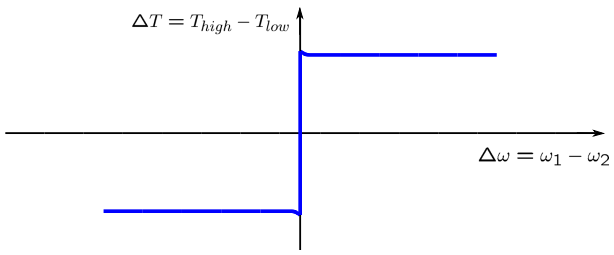

Figure 3.2: Locking effect of TORSEN differentials (when the total torque is constant).

Unlike viscous coupling (speed sensing) or electronic differentials, the TORSEN principle is an instantaneous and pro-active process which acts before wheel slip, i.e., the torque biasing is always a precondition before any difference of rotation speed between the two output shafts. The wind-up phenomenon is avoided, i.e., the differential opens before antagonistic torques appear.

TORSEN differentials are fully mechanical devices without any mechatronic components. The locking effect is only due to friction forces inside the differential. The operating principle of the TORSEN differential was invented and patented by Vernon Gleasman in 1958 [46]. The primary TORSEN differential (*type A*, see Fig. 3.3) is based on the irreversibility of worm gears. Indeed, the worm can easily drive the wheel but the wheel can hardly lead the worm because of the friction forces produced by high sliding. Later on, other configurations of gear pairs were adopted in order to reduce the size and the weight of differentials as well as to permit a wider range of torque bias ratio. The *type B* and *type C* TORSEN differentials use helical gear pairs with parallel axes complemented with several thrust washers to generate internal friction torques. The *twin-diff* differential combines a front open differential with a central type C TORSEN differential in the same unit.

In this research work, the type B and type C TORSEN differentials are studied. The type B is a front or rear axle differential whereas the type C is a central differential (see Sections 3.1.1 and 3.1.2). These components are manufactured by the JTEKT TORSEN S.A. company and equip for instance the AUDI QUATTRO.

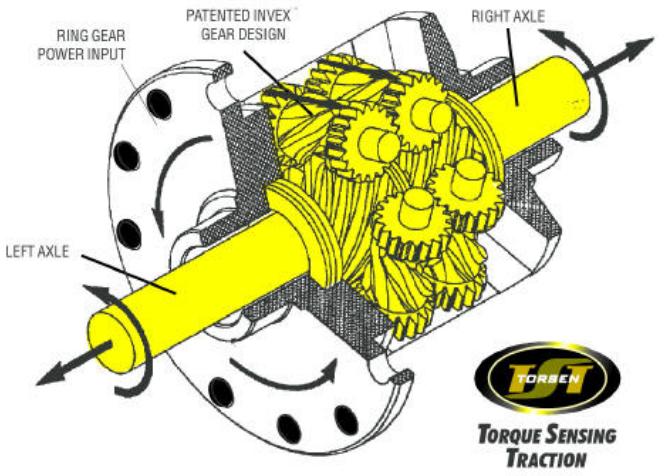

Figure 3.3: The type A TORSEN differential (courtesy of JTEKT TORSEN S.A.).

The torque transfer between driving wheels is not only an advantage in case of a variable road adherence. The handling of the vehicle can also be greatly improved in cornering. Indeed, the friction inside the differential tends to prevent the inner wheels to rotate slower than the outer wheels. Consequently, the inner wheel is submitted to a higher torque than the outer wheel, extending thus the cornering ability by reducing understeering and oversteering. Due to the weight transfer produced by the lateral acceleration, the vertical load applied on the inner wheel is reduced and the transmitted torque could exceed the available adherence of the inner wheel. In this case, the differential can lock and provide more torque to the outer wheel whereas the inner wheel slightly spins.

The variable torque distribution enhances the stability of the vehicle during braking and the operation of electronic active safety systems such as ABS[1], ESP[2], ASR[3]. Compared to a classical open differential, the installation of a TORSEN differential often needs to adjust some components like the suspensions or the anti-roll bars to ensure a proper comfort and a better driving accuracy.

Although a lot of friction occurs inside TORSEN differentials, their mean mechanical efficiency remains comparable to open differentials. In straight line motion with similar adherence on each driving wheel, the TORSEN differential is locked and there

[1]ABS: Anti-lock braking system
[2]ESP: Electronic Stability Program
[3]ASR: Acceleration Slip Regulation

is no relative motion between its parts and then there is no energy loss. In contrast, an open differential undergoes small relative sliding displacements between conical gear wheels. Difference in tyre pressures or road irregularities are sufficient to induce different resisting torques on the two differential output shafts. The friction encountered by these small slidings leads to energy losses. When a TORSEN differential is unlocked (cornering, different grip conditions), the important friction forces decrease significantly the mechanical efficiency. As a conclusion, compared with classic open differentials, the mechanical efficiency of TORSEN differentials appears to be better when there are locked but worse when there are unlocked. Thus, the global efficiency in a mix set of conditions is similar for both types of differentials.

The maximum ratio of torque imbalance permitted by a TORSEN differential is defined by the Torque Distribution Ratio (TDR) which is a constant characteristic of each differential design:

$$TDR = \frac{T_{high}}{T_{low}} \tag{3.1}$$

where T_{high} and T_{low} are the highest and lowest output torques respectively.

For instance, $TDR = 4$ means that up to 80% of the driving torque can be provided to one output shaft whereas the second output shaft receives only 20% of the torque. Let us consider that the ground under one driving wheel has a low adherence. If the wheel with the lower grip reaches its limit of adherence (e.g. 100 Nm), any additional torque provided to the differential is exclusively transferred to the wheel with the good grip condition. If the torque ratio between the two output shafts raises up to the TDR value, i.e. 400 Nm on the second wheel, any further motor torque opens the differential and result in wheel spinning.

3.1.1 Type C

The type C TORSEN differential is always used as central differential and distributes the motor torque between the front and the rear axle of a four-wheel drive vehicle. As depicted in Figures 3.4-3.5, this differential is composed of 15 parts: 7 gear wheels, 5 thrust washers and a housing in 3 parts. The basic properties of the three materials used are summarized in Table 3.1 and the geometric parameters of gear wheels are detailed in Table 3.2 .

	Cast iron GGG60	**Steel AISI 8620H**	**Steel 42CrMo4**
Young's modulus [GPa]	175	200	210
Poisson's ratio [-]	0.3	0.3	0.3
Volumic mass [kg/m^3]	7200	7800	7830
Parts	housing, case	gear wheels	thrust washers

Table 3.1: Material properties of TORSEN differential parts.

Figure 3.4: The type C TORSEN contains 15 parts: gear wheels (7), thrust washers (5), housing (3).

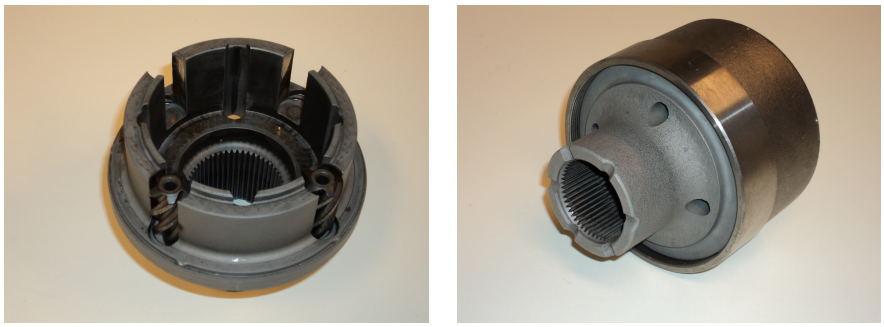

(a) interior of housing (b) assembled

Figure 3.5: Type C TORSEN differential.

	Sun Gear	**Planet Gear**	**Internal Gear**
Number of teeth Z [-]	26	5	36
Helix angle β [deg]	33	-33	33
Normal pressure angle α_{mn} [deg]	30	30	30
Normal modulus M_n [mm]	2.2	2.2	2.2
Pitch diameter [mm]	68.203	13.116	94.435
Face width [mm]	30.25	27.9	27.4

Table 3.2: Gear wheel geometric data of the type C TORSEN differential.

The various gear wheels are assembled in a compact epicyclic gear train (Fig. 3.6) which allows a non-symmetric distribution of the torque due to the different number of

teeth on the internal and sun gears. In a static situation, the differential under study tends to provide more torque (58%) to the rear axle than to the front axle and therefore favour a rear wheel drive behaviour.

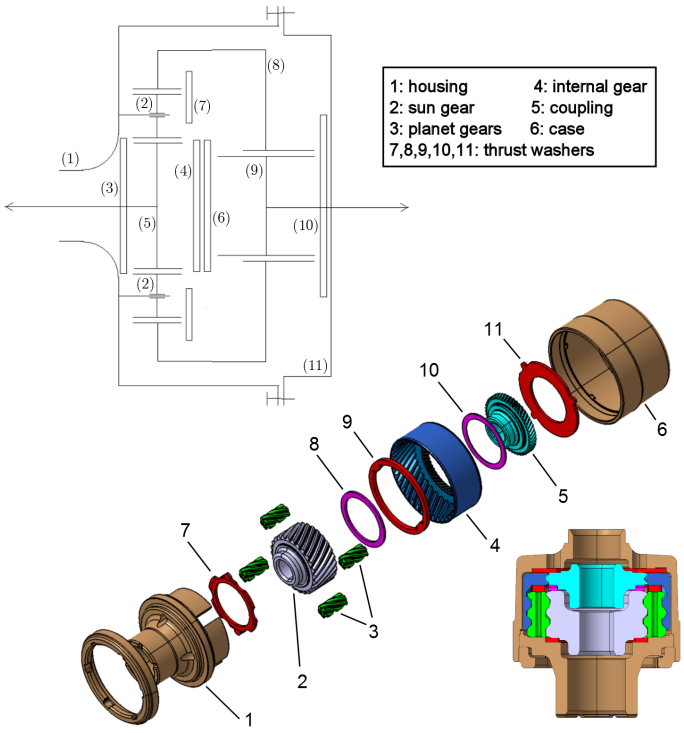

Figure 3.6: Kinematic diagram, exploded view and cut-away view of type C TORSEN differential.

The housing is connected to the case by a screw ring and can be interpreted as a planet carrier. The four planet gears do not rotate with respect to the housing when the differential is locked. The assembly of the planet gears on the planet carrier is particular in this mechanical device. Indeed, the planet gears are inserted in the housing cylindrical cavities without any physical rotational axis. The clearance between crater and planet gear diameters enables the planet gears to tilt which involves some contact between the top of gear teeth and the external surface of crater. The friction generated by these contacts tends to slow down the relative rotation and significantly contributes to the locking effect. The transient behaviour at the switching time between two working modes is also highly influenced by this specific assembly. However, this configuration allows to obtain a compact mechanism.

The motor torque coming out from the gear box is transmitted to the housing through splines with a hollow propeller shaft. The sun gear is linked to the output shaft which transmits the power to the front axle. The drive shaft towards the rear wheels is connected to the coupling.

Due to the axial force produced by the helical mesh, several gear wheels can move axially and enter in contact with the various thrust washers fixed on the case or the housing. The friction experienced by this relative sliding is at the origin of the locking effect of TORSEN differentials. The second important contribution to the limited slip behaviour is due to the friction between the planet gears and the housing holes in which they are inserted. When one axle tends to speed up, all encountered friction forces slows down the relative rotation and generate a variable torque distribution between the output shafts. The biasing on the torque only results from the differential gearing mechanical friction.

This limited slip differential has four working modes (Fig. 3.7) which depend on the direction of torque biasing and on the drive or coast situation. According to the considered mode, the gear wheels rub against one or the other thrust washers which can have different friction coefficients and contact surfaces. The friction torques change for each working mode and influence the TDR as it will be shown in section 3.4.1.

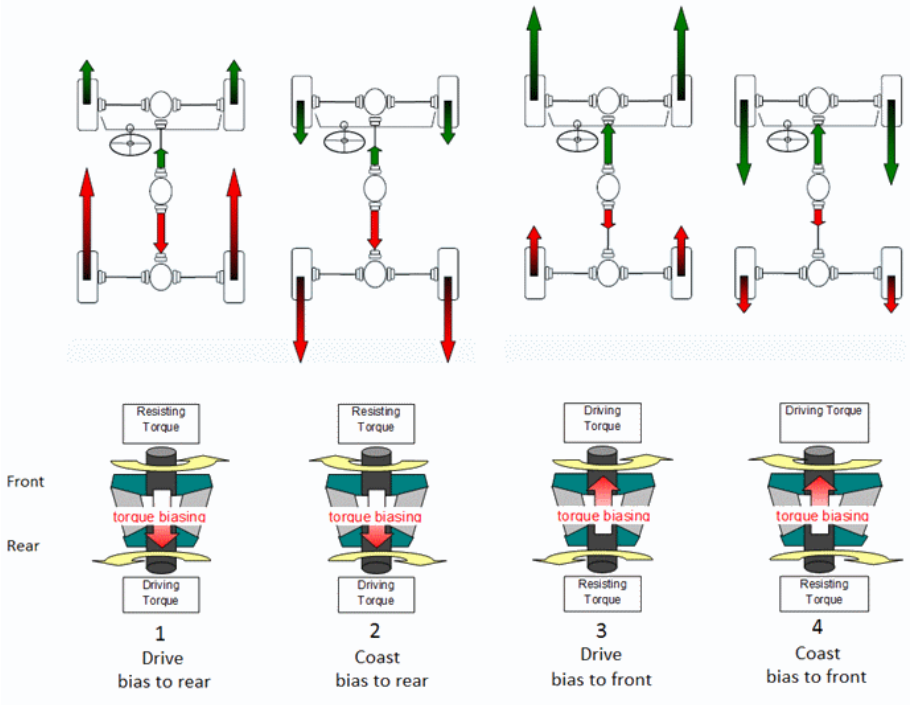

Figure 3.7: The four working modes of the type C TORSEN differential (courtesy of JTEKT TORSEN S.A.).

3.1.2 Type B

The type B TORSEN differential (Fig. 3.8) is used as front or rear differential and transfers the driving torque to the left and right wheels of a same axle. It also includes

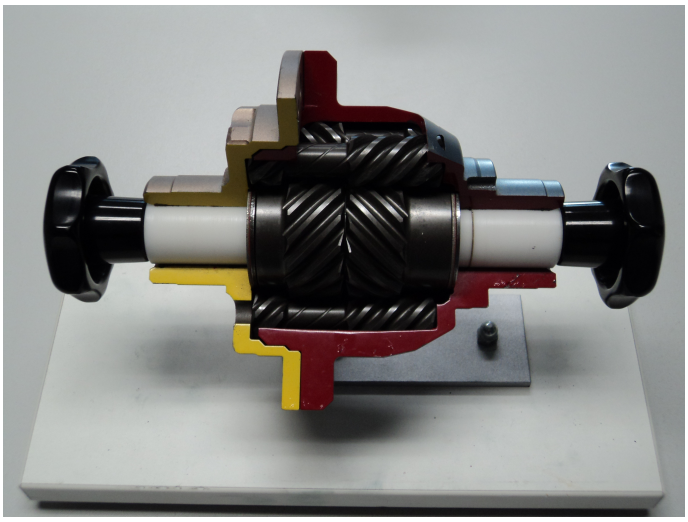

Figure 3.8: Cut-away view of a type B TORSEN differential.

thrust washers and gear pairs with helical meshing (see geometric parameters in Table 3.6). Contrarily to the type C, it is not based on an epicyclic gear train (Fig. 3.9). Indeed, the mechanism must be symmetric between the right and left half axles because in normal condition (straight line motion with the same adherence for each wheel) there is no reason to provide more torque to one lane rather than to the other.

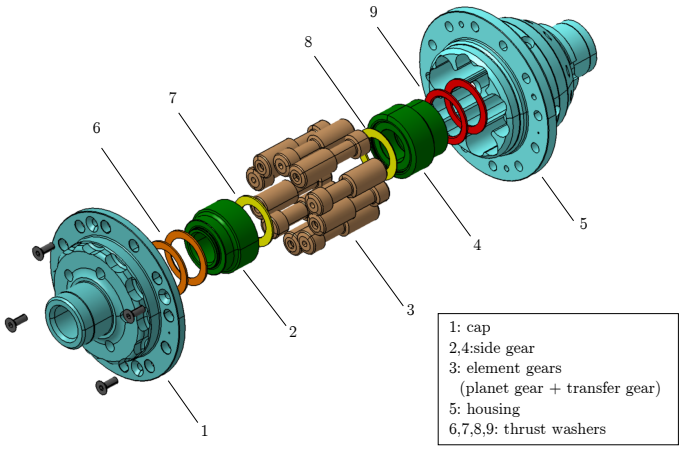

Figure 3.9: Exploded view of type B TORSEN differential.

The element gears are bodies formed of three sections: two toothed segments separated by a portion of reduced cross section without teeth. The two toothed pieces have the same number of teeth but have not the same face width; the planet gears are about three times wider than the transfer gears (see Figure 3.9). The element gears are grouped by pairs and the transfer gear of the first element gear meshes with the planet

	Side Gear	**Element Gear (planet gear)**	**Element Gear (transfer gear)**
Number of teeth Z [-]	15	5	5
Helix angle β [deg]	46 / -46	46 / -46	46 / -46
Normal pressure angle α_{mn} [deg]	30	30	30
Normal modulus M_n [mm]	2.4	2.4	2.4
Pitch diameter [mm]	51.824	17.275	17.275
Face width [mm]	20.191	33.111	10.612

Table 3.3: Gear wheel geometric data of the type B TORSEN differential.

gear of the second element gear of the pair. Besides, the planet gears are also meshing with one of the two side gears linked to the right or left wheel respectively.

The operating principle is similar to the type C central differential: the locking is created by the friction between the elements gears and housing cavities as well as between the annular lateral contact faces of the sides gears and the thrust washers. This type B TORSEN differential has also four working modes (Fig 3.10). It is possible to provide more torque to the right or to the left wheel and for each case the drive and coast situations must be considered.

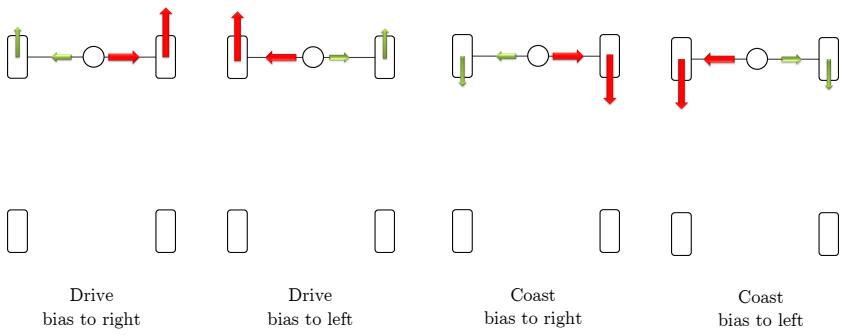

Figure 3.10: The four working modes of a type B TORSEN differential used as a front differential.

A ring gear fixed on the housing allows the input torque to be transferred to the differential with an hypoid gear mesh. The pinion is fixed on the transmission shaft coming out of the gear box in a front wheel drive vehicle or on an output shaft of central differential for a four-wheel drive vehicle. The two side gears are linked with splines to the semi-axles supplying the motor torque to the right and left wheels.

3.2 Global gear pair model

The gear pairs are the key components of automotive drivetrain components and in particular differentials. In the multibody models developed in this dissertation, each

gear pair is modelled as a joint defined between two physical nodes located at the center of each gear wheel represented by a rigid body. Nevertheless the flexibility of the gear mesh is accounted for by a nonlinear spring and damper element inserted along the pressure line (see Fig. 3.11). Several specific phenomena in gear pairs which influence significantly the dynamic response of gears are also included in the model: backlash, mesh stiffness variation, misalignment, transmission error, friction between teeth.

We summarize in this section the gear pair model developed by Cardona [16, 17] which is available for representing the meshing of gear pairs in 3D flexible multibody systems. This model is formulated in a general way so that any kind of gears often used in industrial applications can be described: spur gear, helical gear, bevel gear, ring gear, rack-and-pinion, etc. All reaction forces due to gear engagement, including tangential, axial and radial forces, are accounted for. The gear pair model is implemented in a finite element context (Section 2.2) and can be regarded as a specific kinematic joint.

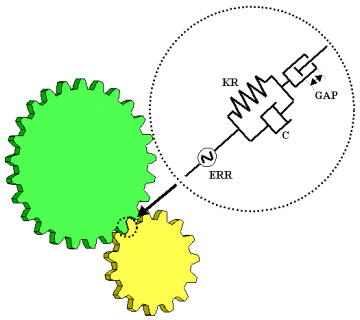

Figure 3.11: Gear pair - flexible contact law along the line of pressure [88].

The modelling of the gear wheels as flexible bodies and the introduction of contact conditions between tooth flanks would perhaps be possible through 3D finite element discretization of the solid components. However, this approach would increase dramatically the size and the complexity of the model due to the detailed FE meshes needed for such complex geometries. The simplified approach with a flexible joint between rigid wheels is sufficient to simulate the locking effects of the TORSEN differentials. The main objective of this study is to develop a global and light model of the differential in order to analyze the dynamical behaviour of the whole system. In Chapter 5, the differential model will be inserted in a complete driveline model of a vehicle including also the car body, the suspension and the tyres. Local effects such as stresses in the gear teeth which would require a 3D FE discretization, are not essential to this kind of global study.

In order to describe the flexible gear pair joint, 16 generalized coordinates are used (Fig. 3.12):

$$\boldsymbol{q}^T = \left\{ \boldsymbol{x}_A^T \quad \boldsymbol{\alpha}_A^T \quad \boldsymbol{x}_B^T \quad \boldsymbol{\alpha}_B^T \quad \psi_A \quad \psi_B \quad u_m \quad \varphi \right\} \tag{3.2}$$

where $\boldsymbol{x}_A$, $\boldsymbol{x}_B$ and $\boldsymbol{\alpha}_A$, $\boldsymbol{\alpha}_B$ are the position and rotation vectors of the wheel centers

A and B respectively, expressed in the inertial frame. The four remaining generalized coordinates $(\psi_A, \psi_B, u_m, \varphi)$ are internal scalar variables of the gear pair and they are introduced to simplify the element formulation. ψ_A and ψ_B are the rotation angles of the gear wheels in the normal direction to the wheel plane ($\boldsymbol{\mu}_1''$, $\boldsymbol{\xi}_1''$). u_m is a measure of the relative deformation and backlash in the direction normal to the tooth midplane ($\boldsymbol{\eta}_2''$). Finally, φ is a measure of the angular misalignment along the tooth vertical line ($\boldsymbol{\eta}_2''$).

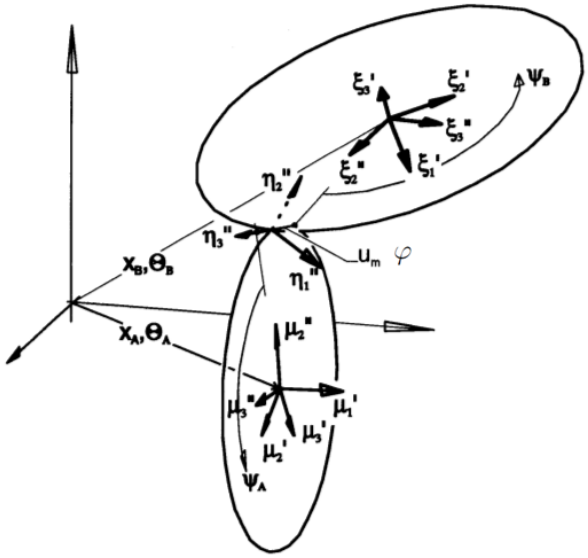

Figure 3.12: Location of generalized coordinates of the gear pair joint.

In a purely rigid gear pair, the rotation of one of the gear wheels around its rotation axis would be strictly prescribed by the rotation of the other gear wheel and vice versa. Therefore, the kinematic joint has 11 degrees of freedom in case of a three dimensional analysis. Since the flexibility of the gear meshing is taken into account in the gear pair formulation described here, the rotations of the toothed wheels remain independent and the gear pair element keeps 12 physical degrees of freedom (3 position and 3 rotation variables for each wheel). Four algebraic constraints have to be introduced to retrieve the correct number of DOFs because the model is defined by means of 16 generalized coordinates (Eq. 3.2).

In order to describe the kinematics of the joint, several local frames are defined (see Figs. 3.12-3.14). The directions of their base vectors can be considered as intermediate variables facilitating the formulation of some mathematical expressions, but they are not part of the set of generalized coordinates.

In the *initial configuration*, one local body frame is attached to each wheel center: $\{A; \boldsymbol{\mu}_1, \boldsymbol{\mu}_2, \boldsymbol{\mu}_3\}$ for the first wheel and $\{B; \boldsymbol{\xi}_1, \boldsymbol{\xi}_2, \boldsymbol{\xi}_3\}$ for the second wheel (Fig. 3.13). The base vectors $\boldsymbol{\mu}_1$ and $\boldsymbol{\xi}_1$ are aligned along the normal direction to the wheel plane.

The vectors $\boldsymbol{\mu}_2$ and $\boldsymbol{\xi}_2$ point towards the contact point C and the vectors $\boldsymbol{\mu}_3$ and $\boldsymbol{\xi}_3$ complete the right-handed reference frames. A local frame $\{C; \boldsymbol{\eta}_1, \boldsymbol{\eta}_2, \boldsymbol{\eta}_3\}$ is also defined at the contact point (see Fig. 3.14): $\boldsymbol{\eta}_1$ follows the direction of the tooth baseline; $\boldsymbol{\eta}_2$ is parallel to the tooth vertical line and is oriented in order to start at the first wheel and point towards the second one; $\boldsymbol{\eta}_3$ is perpendicular to the tooth midplane.

The user has to define only the direction of vectors $\boldsymbol{\mu}_1$ and $\boldsymbol{\xi}_1$ in the inertial frame. The vectors $\boldsymbol{\mu}_2$ and $\boldsymbol{\xi}_2$ can be computed from the knowledge of the wheel radius r_A, r_B, the cone angles γ_A, γ_B, the helix angles β_A, β_B, the misalignment angle φ, the vector $\boldsymbol{\mu}_1$ and the distance vector $\boldsymbol{x}_{AB}$ between wheel centers. Likewise, the frame $\{\boldsymbol{\eta}_1, \boldsymbol{\eta}_2, \boldsymbol{\eta}_3\}$ is fully determined from the values of angular parameters and the orientation of one of the body frames $\{A; \boldsymbol{\mu}_1, \boldsymbol{\mu}_2, \boldsymbol{\mu}_3\}$ or $\{B; \boldsymbol{\xi}_1, \boldsymbol{\xi}_2, \boldsymbol{\xi}_3\}$ (see [16] for more details).

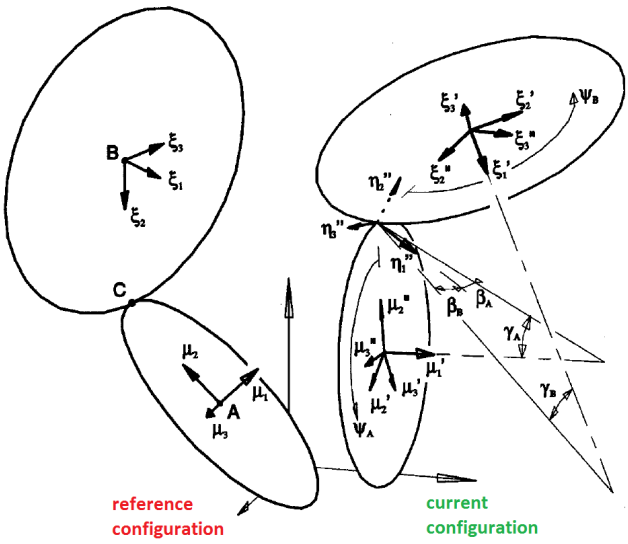

Figure 3.13: Position of various frames used to describe the joint kinematics [17].

In the *current configuration*, the orientation of the both body frames is obtained by:

$$\boldsymbol{\mu}'_i = \boldsymbol{R}_A \, \boldsymbol{\mu}_i \qquad , \qquad \boldsymbol{\xi}'_i = \boldsymbol{R}_B \, \boldsymbol{\xi}_i \qquad \text{with} \quad i = 1, 2, 3 \tag{3.3}$$

with $\boldsymbol{R}_A, \boldsymbol{R}_B$ being the rotation matrices of nodes A and B. A second set of local frames $\{A; \boldsymbol{\mu}''_1, \boldsymbol{\mu}''_2, \boldsymbol{\mu}''_3\}$ and $\{B; \boldsymbol{\xi}''_1, \boldsymbol{\xi}''_2, \boldsymbol{\xi}''_3\}$ is considered with the same orientation rules as in the initial configuration, i.e. the base vectors $\boldsymbol{\mu}''_2$ and $\boldsymbol{\xi}''_2$ are oriented to point towards the contact point. The orientation of both frames is obtained by multiplying the vectors $\boldsymbol{\mu}'_i$ or $\boldsymbol{\xi}'_i$ with the rotation matrix related to the relative angular displacement ψ of each gear wheel around its rotation axis ($\boldsymbol{\mu}_1$, $\boldsymbol{\xi}_1$):

$$\begin{bmatrix} \boldsymbol{\mu}''_1 & \boldsymbol{\mu}''_2 & \boldsymbol{\mu}''_3 \end{bmatrix} = \begin{bmatrix} \boldsymbol{\mu}'_1 & \boldsymbol{\mu}'_2 & \boldsymbol{\mu}'_3 \end{bmatrix} \boldsymbol{R}(\psi_A) \tag{3.4}$$

$$\begin{bmatrix} \boldsymbol{\xi}''_1 & \boldsymbol{\xi}''_2 & \boldsymbol{\xi}''_3 \end{bmatrix} = \begin{bmatrix} \boldsymbol{\xi}'_1 & \boldsymbol{\xi}'_2 & \boldsymbol{\xi}'_3 \end{bmatrix} \boldsymbol{R}(\psi_B) \tag{3.5}$$

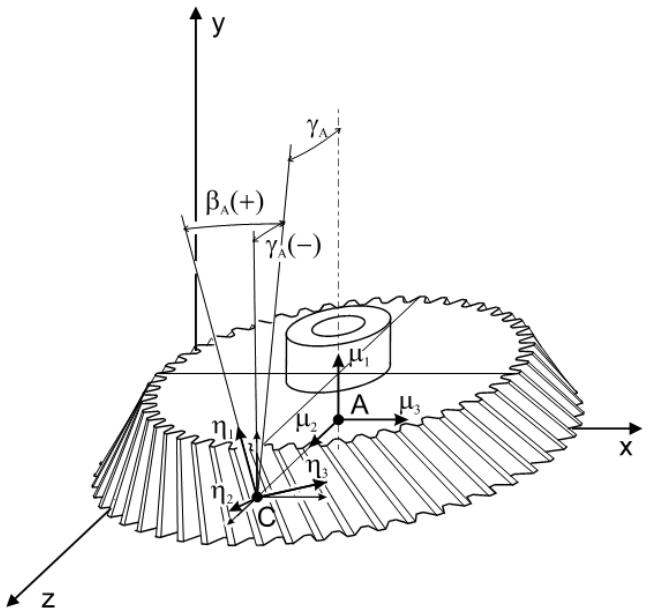

Figure 3.14: Orientation of the frame at the contact point and sign conventions for cone and helix angle [17].

The frame at the current contact point $\{C; \boldsymbol{\eta}_1'', \boldsymbol{\eta}_2'', \boldsymbol{\eta}_3''\}$ is still oriented following the tooth flank geometry as in the initial configuration. Using trigonometric expressions, it is possible to find a relation between this last frame and the frames $\{A; \boldsymbol{\mu}_1'', \boldsymbol{\mu}_2'', \boldsymbol{\mu}_3''\}$, $\{B; \boldsymbol{\xi}_1'', \boldsymbol{\xi}_2'', \boldsymbol{\xi}_3''\}$ as well as a connection matrix between these two frames (see Ref [16] for details):

$$\begin{bmatrix} \boldsymbol{\xi}_1'' & \boldsymbol{\xi}_2'' & \boldsymbol{\xi}_3'' \end{bmatrix} = \begin{bmatrix} \boldsymbol{\mu}_1'' & \boldsymbol{\mu}_2'' & \boldsymbol{\mu}_3'' \end{bmatrix} \boldsymbol{W}(\gamma_A, \gamma_B, \beta_A, \beta_B, \varphi) \tag{3.6}$$

The four algebraic equations expressing the kinematic constraints between the generalized coordinates of the gear pair element are given as:

$$\boldsymbol{\Phi}(\boldsymbol{q}) \equiv \begin{Bmatrix} (\psi_B \; Z_B - \psi_A \; Z_A) \dfrac{M_n \; \cos\alpha_n}{2} + u_m \\ \left(\boldsymbol{x}_C^A - \boldsymbol{x}_C^B\right) \cdot \boldsymbol{\eta}_3{}''^A \\ \boldsymbol{\eta}_2{}''^A \cdot \boldsymbol{\eta}_3{}''^B \\ \boldsymbol{\eta}_1{}''^A \cdot \boldsymbol{\eta}_3{}''^B - \varphi \end{Bmatrix} = \boldsymbol{0} \tag{3.7}$$

where:

- Z_A and Z_B are the numbers of teeth at each gear wheel;
- M_n is the normal module of the teeth;
- α_n is the normal pressure angle of the gear meshing;
- $\boldsymbol{x}_C^A$ and $\boldsymbol{x}_C^B$ represent the positions of the contact point computed respectively in terms of the variables of the wheels A and B;

- ${\boldsymbol{\eta}_i''}^A$ and ${\boldsymbol{\eta}_i''}^B$ are the base vectors of the local frames at the contact point computed in terms of the kinematics variables of wheels A and B respectively.

The first algebraic constraint is the kinematic relation resulting from the teeth contact and provides the relationship between the angular displacements of booth wheels. The Lagrange multiplier associated with this constraint, multiplied by a scaling factor k, can be physically interpreted as the normal contact force between gear teeth.

The remaining constraints enable to impose the magnitude of the relative angular displacements ψ_A and ψ_B and the misalignment angle φ. The second equation of constraint expresses the hoop contact (oriented along $\boldsymbol{\eta}_3''$) between gear teeth and allows to accounts for the hoop and axial components of the contact force. The third algebraic equation expresses that the local frame $\{\boldsymbol{\eta}_1'', \boldsymbol{\eta}_2'', \boldsymbol{\eta}_3''\}$ is unique whatever the gear wheel used to compute its base vectors. Finally, the fourth constraint enables to determine the value of the angular misalignment around $\boldsymbol{\eta}_2''$.

The radial component of the contact force needs to be added explicitly since the second kinematic constraint (Eq. 3.7) provides only the tangential and axial contact forces. This force is non-conservative due to its non-holonomic nature, and is formulated as:

$$\boldsymbol{f}_r = -|k\lambda_1| \sin\alpha_n \; {\boldsymbol{\eta}_2}'' \tag{3.8}$$

This radial force is applied on both wheels at the contact point C and always tends to separate the gear wheels (see Fig. 3.15), $\boldsymbol{f}_r^A = \boldsymbol{f}_r = -\boldsymbol{f}_r^B$. In contrast to the axial and tangential gear meshing forces, its orientation does not change with the sign of the transmitted torque.

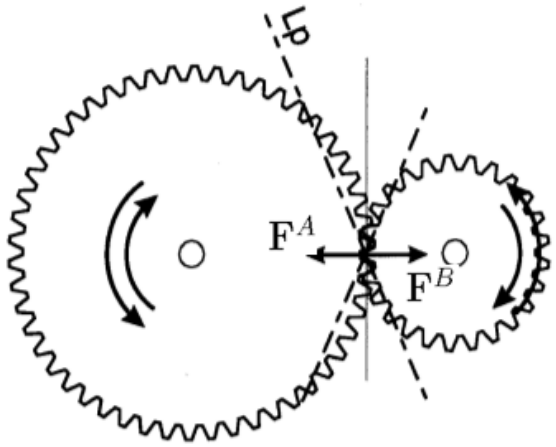

Figure 3.15: The radial component of the gear meshing force always tends to separate the gear wheels whatever the rotation direction [17].

The deformation of gear teeth as well as the meshing defaults (misalignment, load transmission error, backlash) are modelled by an elastic potential defined as:

$$\delta \mathcal{V}_m = \delta u_m \; F + \delta \varphi \; T \tag{3.9}$$

where the force F and the torque T are computed by assuming a cubic pressure distribution on the tooth width following Niemann's approach [99]. According to the value of the misalignment angle φ, the contact along the tooth width can be considered as partial or total and F, T are therefore defined by different expressions. In these formulations, the backlash distance in the normal direction to the tooth and the displacement due to errors with respect to the theoretical gear profile are added to the tooth deformation magnitude u_m. The mesh stiffness can be automatically computed from the gear geometrical parameters and can have a non constant value to represent the time variations of the number of teeth simultaneously in contact.

It is also possible to model the friction force between the two wheels, which is not a negligible force if the mutual sliding speed along teeth in contact is non-zero. The effects of the variation of the center distance length can be considered too but they will be not detailed here for the sake of conciseness, and the expressions of the constraint gradients will neither be given.

Compared with other gear pair models available in the literature, for example [28, 69], the advantage of Cardona's formulation lies in its generality. Indeed, besides allowing to model the various gear pair configurations (rack-pinion, bevel gear, helix gear...), the gear pair model can also be used to model gear trains. Several gear pair joints have simply to be assembled in the same mechanism model. The connection with the rest of the system is straightforward as the nodes at wheel centers are generalized coordinates. For instance, these nodes can be attached to the transmission shafts modelled themselves as flexible beam elements and one can perform the dynamic analysis of a complex mechanical system composed of numerous rigid and flexible bodies and including gear pair joints. The forces produced by gear meshing are also transferred to the supports of the gear wheels through these nodes. Although the gear pair model remains relatively light, disruptive phenomena (friction, backlash,...) influencing significantly the dynamical behaviour can be globally represented.

3.3 Unilateral contact condition

In this section, two different methods are presented to formulate a node to surface contact element inside a multibody model based on the finite element approach. The first formulation uses kinematic constraints to express the contact condition whereas the second one is based on a penalty method.

3.3.1 Formulation based on kinematic constraints

In the context of an implicit scheme, the contact constraints are solved at the same time as the other nonlinearities and no distinction is done between the degrees of freedom linked by contact and the other ones (see Ref. [64] for more details). Following the approach developed by Alart and Curnier in [2], an Augmented Lagrangian approach enables to express the complementarity condition and to define the kinematic constraints related to each contact condition. The resulting system of equations is solved simultaneously for the displacements and for the Lagrange multipliers. Bilateral but also unilateral contacts can be represented: the kinematic constraints are deactivated when the two bodies are separated by a gap.

This formulation is suitable for an implicit nonlinear analysis and allows to model contacts between a flexible part and a rigid surface (*flexible/rigid* contact) as well as between two flexible bodies (*flexible/flexible* contact). In both cases, contact elements are created automatically between each slave node located on the candidate contact face of the first support and a master surface of the second support. This master face is a finite element face in case of a double flexible contact or the single rigid face in case of rigid/flexible contact. The contact method described in the sequel of this section needs to be repeated for each candidate pair of slave node and master face.

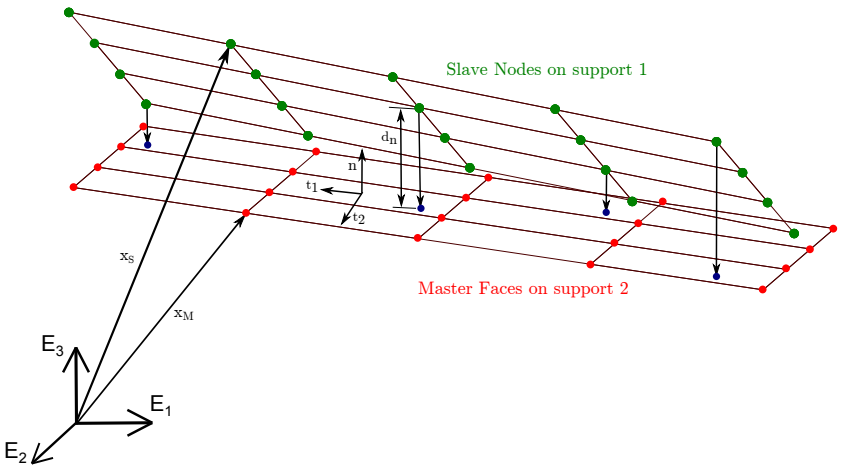

Figure 3.16: Contact condition - projection of a slave node on the master surface.

The contact algorithm can be decomposed in two steps. The *first step* is purely geometric and consists in projecting each slave node on the master surface(s) (see Fig. 3.16). The determination of the projection point is direct in case of first degree triangular master faces but requires Newton iterations for quadrangular element faces. If the projection point is outside the master face, it is obvious that this couple slave node - master face is not in effective contact and the associated kinematic constraints can be deactivated or omitted.

The distance d_n from the slave node to the master face along the normal direction is computed from:

$$d_n = \boldsymbol{n}^T(\boldsymbol{x}_S - \boldsymbol{x}_{M^*}) \tag{3.10}$$

where $\boldsymbol{n}$ is the unit normal vector to the considered master face, $\boldsymbol{x}_S$ is the absolute position of the slave node and $\boldsymbol{x}_{M^*}$ is the absolute position of a point located on the master surface. For a rigid master face, this point is the master node attached to the rigid surface while it is the projection point of the slave node or one vertex defining the master element face in case of a flexible master face.

Moreover, if the friction is modelled, the displacement increments (Δu_1,Δu_2) in the tangent directions during the current time step are also computed:

$$\Delta u_1 = \boldsymbol{t}_1^T(\boldsymbol{x}_S - \boldsymbol{x}_{M^*}) \tag{3.11}$$

$$\Delta u_2 = \boldsymbol{t}_2^T(\boldsymbol{x}_S - \boldsymbol{x}_{M^*}) \tag{3.12}$$

where $\boldsymbol{t}_1, \boldsymbol{t}_2$ are two orthogonal unit vectors in the tangential plane at the contact point ($\boldsymbol{t} = \boldsymbol{v}_t/v_t = \alpha_1\boldsymbol{t}_1 + \alpha_2\boldsymbol{t}_2$, $\boldsymbol{v}_t$ being the tangential velocity vector and $\boldsymbol{t}$ the unit tangential vector).

The projection method will be not described at this stage but a similar method is presented in detail in Chapter 6 where the contact formulation between superelements is developed.

The virtual variations δd_n, $\delta\Delta u_1$, $\delta\Delta u_2$ can be expressed as functions of the infinitesimal variations of generalized coordinates $\boldsymbol{q}$:

$$\delta d_n = \boldsymbol{n}^T\boldsymbol{B}\ \delta\boldsymbol{q} \tag{3.13}$$

$$\delta\Delta u_1 = \boldsymbol{t}_1^T\ \boldsymbol{B}\ \delta\boldsymbol{q} \tag{3.14}$$

$$\delta\Delta u_2 = \boldsymbol{t}_2^T\ \boldsymbol{B}\ \delta\boldsymbol{q} \tag{3.15}$$

where $\boldsymbol{B}$ is a $3 \times n$ matrix defined by $\boldsymbol{B} = \partial(\boldsymbol{x}_S - \boldsymbol{x}_{M^*})/\partial\boldsymbol{q}$. The vector of generalized coordinates of each individual contact element includes the absolute position of the slave node and the absolute positions of the nodes defining the master face (flexible-flexible contact) or the absolute position and rotation variables of the master node linked to the rigid surface (flexible-rigid contact).

The *second step* of the contact algorithm sets the contact conditions whose expression depends on the current status of the contact. For unilateral contact, the case of an *active* or an *inactive* contact can be distinguished in the normal direction. The friction coefficient and the normal force enable to determine if *stick* or *slip* behaviour in the tangential directions has to be considered.

Contact in the normal direction

In order to assess the contact status, the contact criterion defined in Eq. 3.16 is used. This scalar value is a simple addition of the normal distance d_n and the Lagrange

multiplier λ_n weighted by the penalty and scaling positive factors p and k respectively.

$$\sigma_n = pd_n + k\lambda_n \tag{3.16}$$

The complementarity condition is illustrated by the bold red line in Fig. 3.17 and represents the set of possible solutions at convergence of the DAE-system: either the normal distance d_n is null or the Lagrange multiplier λ_n vanishes. During the iterations of the Newton-Raphson procedure, the system is not at the equilibrium and the contact criterion σ_n allows to choose if the contact condition related to an *active* or an *inactive* contact has to be used. The linear equation $\sigma_n = 0$ divides the space in two zones (see dotted line in Fig. 3.17). If σ_n is positive, the algebraic constraint is deactivated and the assessed couple (slave node - master face) is not considered in contact. In contrast, when σ_n has a negative value, the system is considered in contact and the contact constraint is active. At equilibrium, the contact constraint enforces the normal distance d_n to be equal to zero and can therefore be expressed as:

$$\phi \equiv d_n = \boldsymbol{n}^T(\boldsymbol{x}_S - \boldsymbol{x}_{M^*}) = 0 \tag{3.17}$$

The constraint forces are simply obtained by formulating the virtual work of the algebraic constraint:

$$\begin{aligned} \delta\mathcal{W} &= \delta d_n(pd_n + k\lambda_n) + \delta\lambda_n \; kd_n \\ &= \left\{\delta\boldsymbol{q}^T \quad \delta\lambda_n\right\} \begin{Bmatrix} \boldsymbol{B}^T\boldsymbol{n} \; (pd_n + k\lambda_n) \\ kd_n \end{Bmatrix} \end{aligned} \tag{3.18}$$

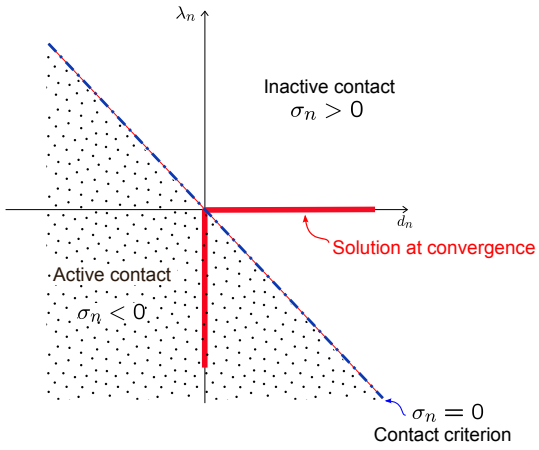

Figure 3.17: Contact criterion and solution.

The Lagrange multiplier λ_n scaled by the factor k can be interpreted as the contact force. This parameter is often chosen equal to some stiffness measure of the structural elements in order to have the same order of magnitude in the various terms of the iteration matrix. The convergence property of this approach to formulate the contact

condition depends on the slope $(-p/k)$ of the line $\sigma_n = 0$. The scaling factor k being often constant, the choice of the penalty parameter p influences the convergence speed but the solution at convergence will not depend on this penalty parameter.

Friction in tangential directions

In the tangential plane, an activation test σ_t is also needed to evaluate if the bodies are sticking or sliding at the contact point. Two additional Lagrange multipliers $\lambda_{t_1}, \lambda_{t_2}$ are introduced to manage the frictional behaviour. The friction criterion is defined by analogy with the contact criterion (Eq. 3.16):

$$\sigma_t = \sqrt{\sigma_{t_1}^2 + \sigma_{t_2}^2} \tag{3.19}$$

with

$$\sigma_{t_i} = p\Delta u_i + k\lambda_{t_i} \qquad i = 1, 2 \tag{3.20}$$

Sticking

The two contacting bodies are sticked if the magnitude of the friction force is smaller than the normal force multiplied by the friction coefficient. This situation occurs when the following condition between the normal and tangential criteria is satisfied:

$$\sigma_t - \mu|\sigma_n| \leq 0 \tag{3.21}$$

In order to avoid relative motion between the slave node and the master face, two constraints are introduced (Eq. 3.22).

$$\phi \equiv \begin{Bmatrix} \Delta u_1 \\ \Delta u_2 \end{Bmatrix} = \mathbf{0} \tag{3.22}$$

The virtual work principle enables to compute the associated constraint forces:

$$\begin{aligned} \delta\mathcal{W} = {} & \delta\Delta u_1(p\Delta u_1 + k\lambda_{t_1}) + \delta\Delta u_2(p\Delta u_2 + k\lambda_{t_2}) \\ & + \delta\lambda_{t_1} k\Delta u_1 + \delta\lambda_{t_2} k\Delta u_2 \end{aligned} \tag{3.23}$$

The friction coefficient is assumed constant, no distinction being made between the static and kinetic friction coefficients.

Sliding

If the sticking condition (Eq. 3.21) is not fulfilled, a sliding behaviour is considered. Therefore, the relative tangential displacements do no longer cancel and both kinematic

constraints have to be desactivated. The friction forces are equal to the friction coefficient μ multiplied by the normal contact force $f_n = k\ \lambda_n$ and a distribution coefficient $\chi_i = \sigma_{t_i}/\sigma_t$ between the two tangential directions $\boldsymbol{t}_1, \boldsymbol{t}_2$.

In order to ensure the continuity of Lagrange multipliers at the switching time between sticking and sliding periods, their values are prescribed in sliding situation. The resulting algebraic equations do not constrain the generalized coordinates. The full set of element forces can be summarized as:

$$\delta\mathcal{W} = \begin{Bmatrix} \delta\Delta u_1 & \delta\Delta u_2 & \delta\lambda_{t_1} & \delta\lambda_{t_2} \end{Bmatrix} \begin{Bmatrix} \mu|f_n|\chi_1 \\ \mu|f_n|\chi_2 \\ (\mu|\sigma_n|\chi_1 - k\lambda_{t_1})k/p \\ (\mu|\sigma_n|\chi_2 - k\lambda_{t_2})k/p \end{Bmatrix} \tag{3.24}$$

With this formulation, the friction Lagrange multipliers represent forces parallel to the variation of sliding displacements (Δu_1, Δu_2).

Inactive contact

When the contact is not active, i.e., $\sigma_n > 0$, there is no contact and no friction forces applied on the nodes. So, it is not needed to impose any kinematic constraint. The Lagrange multipliers having the physical meaning of forces, they have to be set to zero. This can be achieved by defining the constraint equations as $\boldsymbol{\Phi} \equiv \boldsymbol{\lambda} = \boldsymbol{0}$ and the virtual work takes then the form:

$$\delta\mathcal{W} = \delta\boldsymbol{\lambda}^T\ (-k\boldsymbol{\lambda}) \tag{3.25}$$

with $\boldsymbol{\lambda}^T = \begin{Bmatrix} \lambda_n & \lambda_{t_1} & \lambda_{t_2} \end{Bmatrix}$.

The evidence of this last virtual work expression can be found in Reference [2] where a unique Lagrangian is defined for all contact status. With this approach, the uniqueness of the solution can be proven and one avoids the discontinuities of the Lagrange multipliers when the constraints are activated.

The iteration matrix of each contact status is not given in this document but it can be found in [64]. In case of the sliding friction, the iteration matrix is not symmetric so that it is recommended to use a non-symmetric solver.

3.3.2 Formulation based on a penalty method

An alternative method to formulate the contact condition consists in replacing the augmented Lagrangian method by a pure penalty method. In contrast to the Lagrangian approach where no penetration is allowed, the penalty approach enables a small penetration between the two bodies, that slightly relaxes the discontinuity. The penalty function can be linear or nonlinear and can be seen physically as a finite stiffness that

is active in compression but not in traction. To have a smoother response, it can also be useful to account for damping in the contact model.

The projection method of the slave nodes on the master faces is unchanged compared with the Lagrangian approach but the contact detection criterion is not the same. Indeed, with a penalty method, the contact is considered as active when the normal distance d_n (Eq. 3.10) is negative. In case of a linear contact law, the magnitude of the contact force can be computed by:

$$f_n = k_p \, |d_n| \; + c \, \dot{d}_n \qquad \text{if} \quad d_n < 0 \tag{3.26}$$

where k_p is the contact stiffness and c is the damping coefficient.

The friction force amplitude is simply given the multiplication of the normal contact f_n by the friction coefficient μ:

$$f_{fr} = -\mu_r \; f_n \tag{3.27}$$

A regularization is often used to avoid the discontinuity when the sign of the relative sliding velocity shifts or at the transition between sticking and sliding contacts (see Fig. 3.18). The regularized friction coefficient μ_r can be defined in different ways with appropriate functions such as the simple quadratic function used in this study:

$$\mu_r(\dot{\xi}) = \begin{cases} \mu_{dyn} \left(2 - \dfrac{|\dot{\xi}|}{\epsilon_v} \right) \dfrac{\dot{\xi}}{\epsilon_v} & |\dot{\xi}| < \epsilon_v \\ \mu_{dyn} \dfrac{\dot{\xi}}{|\dot{\xi}|} & |\dot{\xi}| \geq \epsilon_v \end{cases} \tag{3.28}$$

$\dot{\xi}$ being the relative sliding velocity, μ_{dyn} the dynamic friction coefficient and ϵ_v the regularization tolerance which corresponds to the relative velocity at which the friction coefficient reaches its constant value.

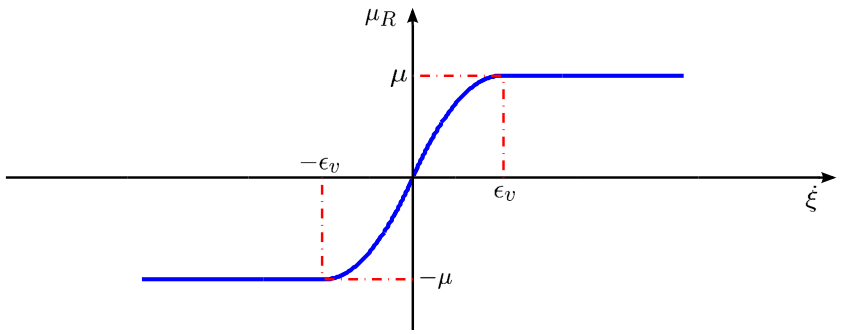

Figure 3.18: Regularization of friction coefficient with two quadratic functions.

The internal forces at the element level ($\boldsymbol{g}^{int} = \boldsymbol{B}^T \left(f_n \ \boldsymbol{n} + f_{fr} \ \boldsymbol{t} \right)$) are obtained by expressing the virtual work principle of contact forces

$$\begin{aligned} \delta \mathcal{W} &= \delta d_n \ f_n + \delta \Delta u \ f_{fr} && (3.29) \\ &= \delta \boldsymbol{q}^T \ \boldsymbol{B}^T \ \boldsymbol{n} \ f_n + \delta \boldsymbol{q}^T \ \boldsymbol{B}^T \ \boldsymbol{t} \ f_{fr} && (3.30) \end{aligned}$$

with the tangential unit vector defined as

$$\boldsymbol{t} = \frac{\boldsymbol{v}_t}{v_t} = \frac{\dot{\boldsymbol{x}}_S - \dot{\boldsymbol{x}}_{M^*}}{\| \dot{\boldsymbol{x}}_S - \dot{\boldsymbol{x}}_{M^*} \|} \tag{3.31}$$

3.3.3 Penalty method versus algebraic constraint at position level to model impact

Impact phenomena occur when the relative normal velocity of the colliding bodies is high at the contact establishment. The modelling of nonsmooth unilateral contact conditions by means of kinematic constraints formulated only at position level leads to inconsistencies (see for instance Ref. [20]). Indeed, simulations of multibody systems including this kind of contact model can fail to converge due to numerical difficulties. In order to illustrate this non consistent behaviour, let us considered a very simple system composed of a cube distant of a gap d_n from a rigid plane (see Fig. 3.19). It is at rest at the initial time and is submitted to a constant force $F = 100$ N during the whole simulation. Only a displacement along the vertical direction is allowed and the rotations are blocked. The cube is made of steel and is meshed using linear hexahedral volume finite elements. Since the plane is rigid, the rigid-flexible version of the unilateral contact condition described in section 3.3.1 is used to model the system. The presented simulation is performed with a fixed time step equals to 10^{-4} s and the Hilbert-Hughes-Taylor scheme (Section 2.2.3) is used with $\alpha_f = 1/3$.

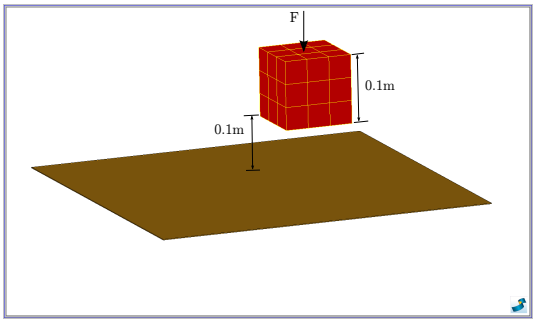

Figure 3.19: Benchmark: impact of a flexible cube on a rigid plane.

Figure 3.20 shows the vertical position of one node of the cube contact face. The dynamic response provided by the numerical model is obviously not physical. Indeed, the rebounds after impact have unreliable amplitude and frequency. The cube seems to

gain energy after some impacts and loses energy after others. This erratic phenomenon is highly dependent on the impact instant between two computed time steps. The numerical response is also strongly influenced by the amount of numerical damping introduced by the integration scheme since it is the sole source of energy dissipation in the model.

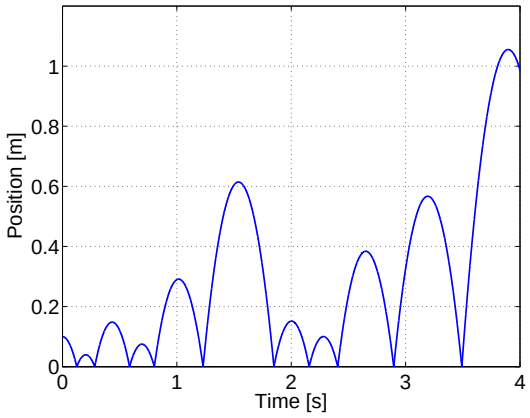

Figure 3.20: Position of one contact node of the cube when the contact model is based on a kinematic constraint at position level.

The literature mentions alternative contact models and solution methods able to represent impact. Formulating the contact constraints at velocity level and not at position level is beneficial for the consistency of the algorithm. The replacement of the continuous integrator by a non smooth scheme (e.g., the Moreau-Jean method [63]) or a energy preserving scheme is often recommended to deal with impact simulation. The modelling of the contact condition by a pure penalty method offers a simple and easy way to implement contact formulation, which can still be used with a smooth solver, such as the Newmark, the HHT or the generalized-α method.

The simple cube-plane benchmark has also been simulated by using the penalty-based contact model detailed in section 3.3.2. The solver parameters remain unchanged and the penalty factor has been fixed to 1E.10 $\mathrm{N/m^3}$ whereas no damping contribution is considered ($c = 0$ in Eq. 3.26). Now, the model reproduces the expected behaviour (see Fig. 3.21). The decrease of bounce amplitudes is due to the non negligible numerical damping.

The large frequency content of the impact response can disturb the automatic time step strategy which tends to reduce the time step size to very small values. With a smooth integrator and a contact modelling with position-level constraints, the convergence is often easier with large time steps because, in this case, the impulse due to an impact is averaged on a larger time period between two time steps. The friction is not accounted for in the test model but the switching between stick and slip situations can also lead to strong discontinuities especially in case of high speed systems.

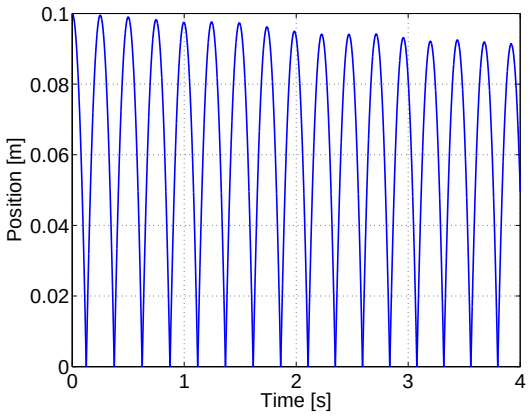

Figure 3.21: Position of one contact node of the cube computed using a penalty based contact model.

The contact model based on a kinematic constraint does not provide any adjustable parameter while the contact stiffness and the damping coefficient of the penalty method can be chosen in order to ensure the convergence. Although the penalty approach is much more robust, the stability and the accuracy of the numerical response can nevertheless not be guaranteed. Unstable response can sometimes also be observed when using a continuous contact model (see Section 4.2.2).

3.4 MBS simulation of TORSEN differentials

This section presents a comprehensive preliminary modelling of types B and C TORSEN differentials. The objective here is to develop a robust modelling approach allowing to simulate the four working modes and the locking effect of TORSEN differentials. Therefore, several assumptions which appear reasonable for the analysis of the global operation of differentials have been introduced. The multibody simulations are carried out using the software SAMCEF FIELD and its module MECANO devoted to implicit nonlinear analysis.

In order to validate and check the accuracy of the mathematical model, the numerical results have been compared with measurements on an experimental test bench provided by the JTEKT TORSEN company (see Fig. 3.22). To this purpose, the test bench configuration has been reproduced virtually. Contrarily to the operation in a vehicle, the housing does not rotate during the test (Fig. 3.23). It is nevertheless possible to observe the four working modes since the locking effect of TORSEN differentials is due to relative motion and to the forces between the output shafts and the housing.

As pointed out in the previous section, the contact formulation based on a Lagrangian approach is not well adapted in case of impact phenomena. Therefore, the

Figure 3.22: Test bench for TORSEN differentials.

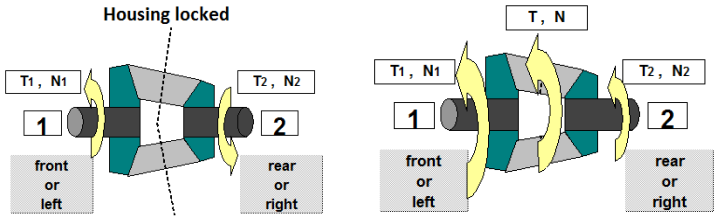

(a) test bench (b) vehicle

Figure 3.23: Schematic representation of differential working configuration (courtesy of JTEKT TORSEN S.A.).

penalty based contact formulation (Section 3.3.2) has been used in order to model the contacts between the thrust washers and the rim faces of the gear wheels included in the TORSEN differentials. When the switching between two operation modes is very fast, the impact is high and the addition of a damping contribution in the contact law might be needed to enable the convergence of the integration scheme.

Dynamic analyses have been performed using the Chung-Hulbert generalized-α integration scheme [23] because it permits to introduce a large numerical damping without reducing significantly the response accuracy. A spectral radius equals to 0.01 is reached when $\alpha_m = -0.97$ and $\alpha_f = 0.01$. A high level of numerical damping thus enables to annihilate the high frequency content produced by the impact events. Due

to the presence of gear elements and contact conditions with friction, the iteration matrix is not symmetric and therefore a non-symmetric resolution algorithm has been adopted. This option is computationally more expensive but permits better convergence in complex situations with high Coulomb friction.

3.4.1 Type C TORSEN: central differential

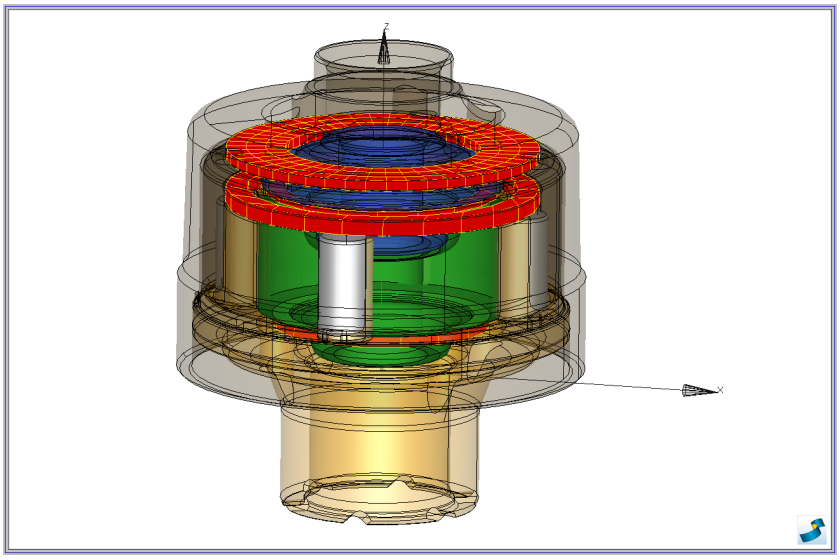

Figure 3.24: SAMCEF model of type C TORSEN differential.

The type C TORSEN differential contains 15 bodies which are all included in the multibody model (see Fig. 3.24). The material behaviour as well as the joints between the various bodies are subjected to the following modelling assumptions:

- Only the thrust washers are modelled as flexible bodies, the gear wheels and the three parts of the housing being assumed rigid. The thrust washers are meshed with nonlinear volume finite elements obtained by extrusion of a 2-D grid, what is well suited for the selected contact formulation.

- The geometry of the thrust washers is simplified, the latter being modelled as perfect rings: the locking bolts ensuring the positioning of the various thrust washers inside the housing or case are neglected.

- The planet gears are connected to the differential housing by means of hinge joints. The real link between these two parts is quite complex since the planet gears are inserted in housing cylindrical cavities without physical rotation axis. The tooth tips are in contact with the cavity external surface and the friction contributes to the limited slip behaviour of the differential. Hence, the friction is accounted

for in the hinges used to model these joints. The small axial displacement and the tilting of planet gears allowed by clearance can not be represented by the hinges but both kinds of motion are second order effects to the operation of the differential.

- Several contact zones of minor importance on the global operation are not considered. Since some washers have completely different friction coefficients on their two opposite faces, only the contact condition with the lower friction coefficient is modelled while the washer is considered to be fixed on the body in contact with the high friction face of the washer (in Fig. 3.6 washer #8 is fixed on the sun gear and washer #10 is fixed on the coupling). The contacts between the lateral faces of the planet gears and the housing or thrust washer #9 are not modelled since the axial displacement of the planet gears is prevented by the hinge joints with the housing.

- The thrust washers $\#7, 9, 11$ are clamped on the housing or case in the model whereas a small axial displacement can potentially appear in reality.

- A screw joint is used to represent the connection between the internal gear and the coupling. The internal bevel gear pair with the same number of teeth on the pinion and the ring gear having the same rotation axis, they cannot be modelled by the gear pair formulation (Section 3.2). Therefore, this particular assembly is approximated by a screw joint.

- The housing and the case are considered as rigidly connected: the screw is neglected since in normal operation, there is no relative motion between both parts.

The epicyclic gear train of type C TORSEN is modelled by 8 independent gear pair elements as described in section 3.2. The values of the main parameters are given in Table 3.6. As described in [152], a detailed FE study can provide an accurate value for the mesh stiffness parameter of each gear pair element. Here, approximated values are computed according to the ISO 6336 standard (method B) [62]. In this case, the computed mesh stiffness and mesh damping depend on material properties and geometrical characteristics (addendum, number of teeth, helical and pressure angles...) of gear wheels and teeth. Since the gear wheels are connected to the housing through hinge joints, their rotation axes remain parallel and it is not needed to account for the misalignment in the gear pair model. Likewise, the effects of load transmission error have not been included in the system.

The model also includes 5 flexible/rigid unilateral contact conditions using a penalty method (Section 3.3.2). The contact stiffness has been chosen in order to relax the discontinuity at the impact instant and enable the numerical convergence. A sufficiently high value has been adopted in order to avoid large penetration depth between contacting bodies compared with the body strains.

	Sun Gear / Planet Gear	**Planet Gear / Internal Gear**
Center distance d [mm]	40.660	40.660
Normal pressure angle α_n [deg]	30	30
Backlash b [mm]	0.06	0.06
Mesh stiffness [N/m]	5.58E8	4.20E8
Mesh damping [kg/s]	847	733
Friction coefficient between teeth μ [-]	0.1	0.1
Total contact ratio ϵ_γ [-]	3.007	2.923

Table 3.4: Data of gear meshing between a planet gear and the sun gear or the internal gear of the type C TORSEN differential.

The friction coefficient of all contact conditions have been chosen based on experimental data provided by the manufacturer JTEKT TORSEN. In most cases, the friction coefficient is 0.1 which is a common value for friction between two lubricated steel surfaces. As in Fig. 3.18, a regularization of the friction coefficient has been needed to avoid a large discontinuity when the sign of the relative rotation between the gear wheel and the thrust washer changes at the switching time between operation modes.

Finally, the total number of generalized coordinates of the whole model amounts to 8209. This huge number is mainly due to the 596 nodes of the FE modelling of thrust washers and the distance sensors of the contact elements.

Test bench configuration

In the test bench configuration, the housing and the case are locked in translation and rotation. In order to reproduce the various operation modes of the differential, a torque is applied to one of the output shafts whereas the rotation speed of the second one is prescribed, which is equivalent to apply a resisting torque. This torque is measured and used to compute the TDR defined by Eq. 3.1. This index represents the torque distribution due to the locking effects and is simply computed with the applied torque value divided by the resistant torque measured value.

The sun gear and the coupling being linked to the front and rear axles respectively, the two operation modes with torque biasing to the front axle are reproduced when a torque is applied on the sun gear while the coupling rotation speed is limited. The two operation modes with torque biasing to the rear axle can be activated by exchanging the boundary conditions of both shafts. According to the direction of the applied torque, it is a drive or a coast mode. Within the inertial frame used to construct the model, a positive torque gives rise to a drive mode and a negative torque, to a coast mode.

In Figure 3.25(a), the numerical simulation of the two operation modes with torque biasing to the rear axle is represented. A torque of 125 Nm is applied on the coupling and the rotation speed of the sun gear is controlled in order to keep a difference of

20 rpm between output shafts. The choice of 125 Nm and 20 rpm is only due to the capacity of the experimental test bench used for the measurement. Indeed, the TDR is constant for each locking mode whatever be the amplitudes of the applied torque and the relative rotation between output shafts (cf. Fig. 3.2). The time evolution of the applied torque and the prescribed rotation speed has been determined to observe both operation modes with biasing to rear axle in a same simulation and in order to have a smooth transition between the two modes. The parts of interest to compute the TDR are the steady state parts: $0.4\,\mathrm{s} - 1\,\mathrm{s}$ and $2.2\,\mathrm{s} - 2.8\,\mathrm{s}$.

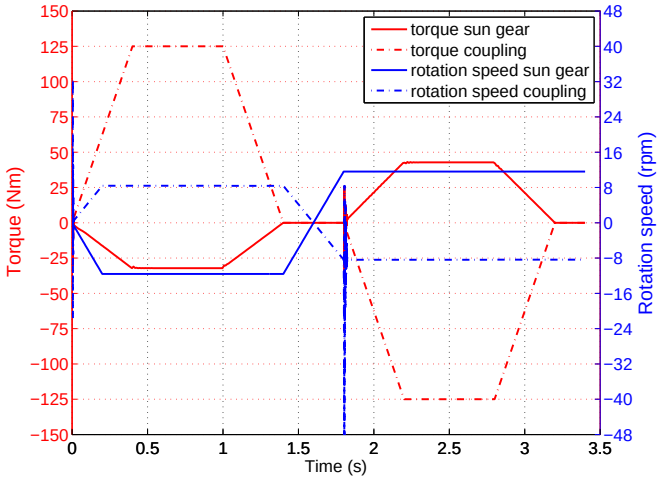

(a) drive to rear and coast to rear modes

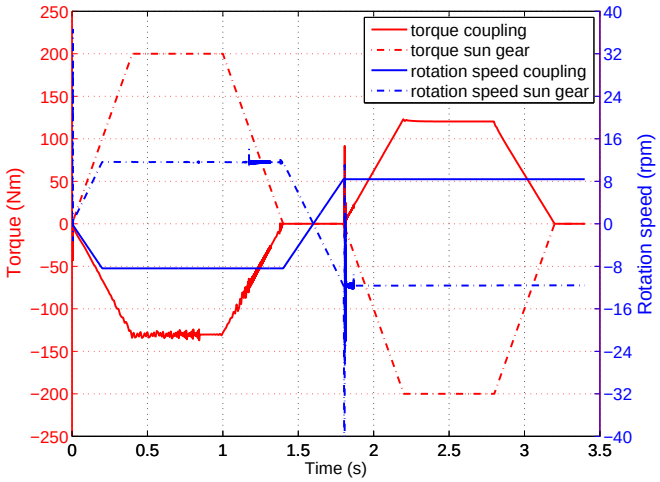

(b) drive to front and coast to front modes

Figure 3.25: Simulation of type C on test bench.

Figure 3.25(a) depicts the simulation of the operation modes with torque biasing

to the front axle. Here, a 200 Nm torque is applied to the sun gear and the rotation speed of the coupling is regulated. For each locking mode, Table 3.5 shows the good agreement between the experimental TDR values and the results provided by the numerical simulation. The error is lower than 5% for the four modes.

TDR	**Mode 1** Drive bias to rear	**Mode 2** Coast bias to rear	**Mode 3** Drive bias to front	**Mode 4** Coast bias to front
Experimental	4.02	2.82	1.57	1.62
Simulation	3.89	2.92	1.53	1.66
Error (%)	3.23	3.55	2.55	2.47

Table 3.5: Comparison of torque distribution ratios for the four operation modes (type C TORSEN).

As mentioned in the list of modelling assumptions, the complex joint between the planet gear and the housing has been modelled as a simple hinge. The friction forces occurring between the tooth heads and the holes in the housing are represented by a friction torque along the axis of the hinge. Owing to the significant difference between a hinge model and the actual joint, the friction coefficient in the hinge joint is not equal to the true friction coefficient which would be difficult to assess. In order to determine the value of this friction coefficient, a parametric study has been performed with several friction coefficients. Then, the least squares criterion is used to find the best friction coefficient, i.e. the value for which the sum of squared differences between experimental and simulated TDR for the four operation modes is minimum. Figure 3.26 shows that a value of the friction coefficient of 0.185 leads to the model with the closest TDR values compared to the experimental data (see Tab. 3.5). This parameter identification has been achieved using the BOSS QUATTRO software [86]. The friction coefficient of the hinge joints is the only parameter that can be fitted in order to match the TDR values. The values of the other parameters are imposed by the physics of the problem. The accordance of numerical TDRs with respect to the experimental data shows the accuracy of the MBS model of the TORSEN differential while only one parameter has been adjusted.

Oscillations can be observed on the torque curve of the coupling in Figure 3.25(b). Investigations have been carried out and have led to the conclusion that these oscillations have a purely numerical origin. They result mainly from the time step selection strategy which induces acceleration and force discontinuities at the time step size changes. Morevover, these oscillations are highly sensitive to the solver parameters and to the contact stiffnesses.

This simulation also allows to compute the contact pressure, friction stress, dissipated power or the sliding velocity. Figure 3.27 illustrates the contact pressures for all the contact elements introduced in the model for the drive to rear mode.

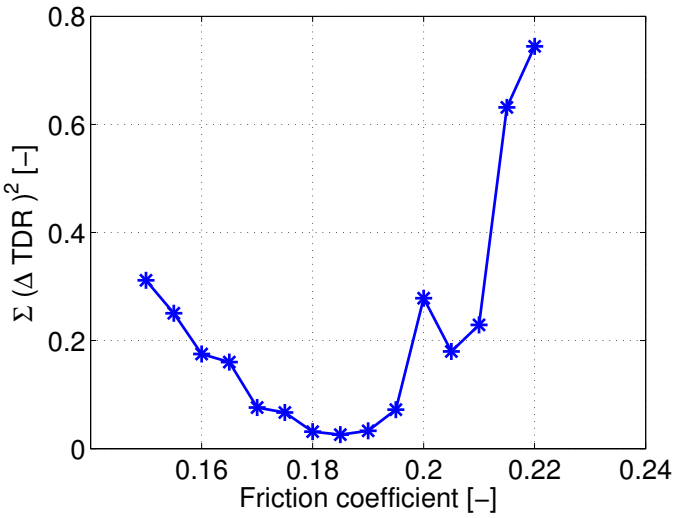

Figure 3.26: Parametric study: influence of the friction coefficient in hinge joints on the sum of squared differences between experimental and computed TDRs for the four operation modes.

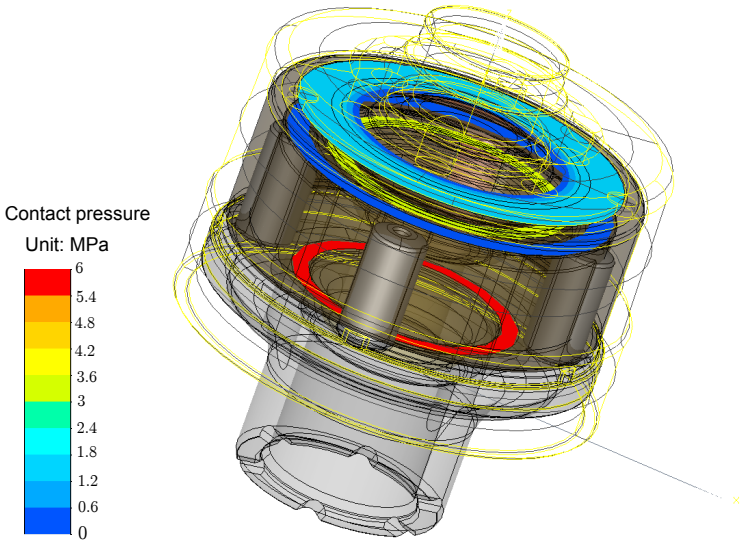

Figure 3.27: Contact pressure on thrust washers for drive to rear mode (test bench configuration at time $t = 0.6$ s).

Vehicle configuration

In the vehicle configuration, the housing is driven in rotation by the output torque of the gear box. In order to mimic the vehicle behaviour, the following load cases are applied on the differential: a torque is applied to the housing and the rotation speeds

of both output shafts are prescribed. The rotation speed difference is arbitrary because it does not affect the TDR (see Fig. 3.2). According to the orientation of the inertial frame used, the rotation speeds have negative values when the vehicle moves forward. The motor torque is positive for coast modes and negative for drive modes.

In order to observe the four locking modes during the same simulation, the time evolution depicted in Fig. 3.28 has been used for the three loadings. An intermediate level is introduced during the increase and the decrease stages of the motor torque to assess the robustness of the numerical model. Contrarily to the situation on the test bench, the two output shafts rotate in the same direction. The housing rotation speed assigned is set by the ratio of teeth numbers of the sun gear and the internal gear.

In drive modes, more torque is sent to the slower axle whereas it is the opposite for the coast modes. The difference in the number of teeth on the sun gear and the internal gear induces an uneven distribution of the motor torque between both output shafts. This torque difference between the sun gear and the coupling is increased by the torque biasing due to friction inside the differential. Therefore, the torque ratio is higher than the teeth ratio for the four operation modes. For each mode, the TDR value computed with this simulation is similar to the value obtained from the test bench simulation.

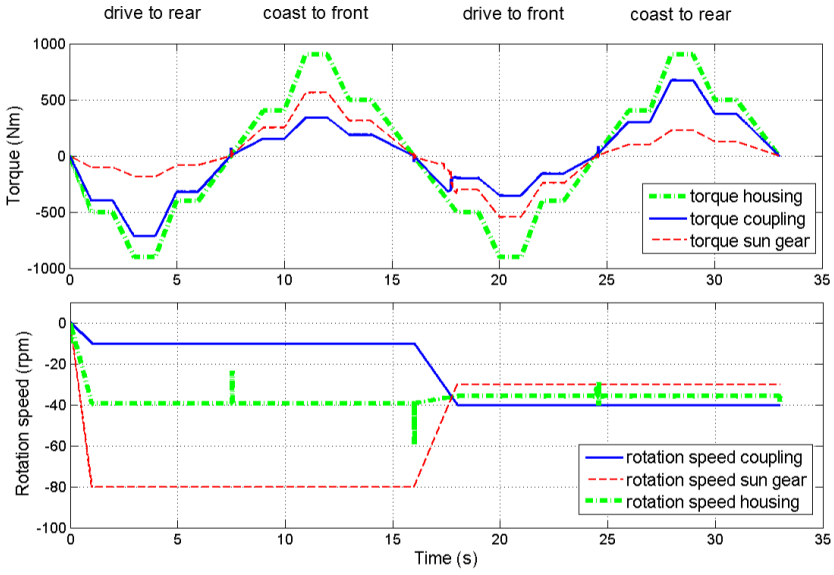

Figure 3.28: Time evolution of torque and rotation speed of housing and output shafts of type C TORSEN on vehicle configuration.

As soon as the sign of the torque applied to the housing changes, the sun gear, the coupling and the internal gear move axially very quickly (see Figure 3.29). That leads to impacts onto the thrust washers. The axial displacements of the sun gear and the coupling are always in the same direction while the internal gear moves in the opposite direction. The sun gear and the coupling are then in contact for all the

operation modes. This contact has a very low friction coefficient that allows reducing the stick-slip phenomenon.

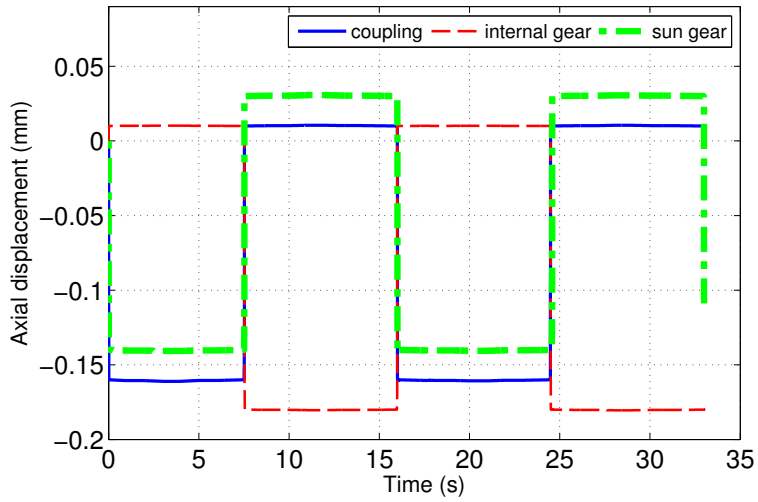

Figure 3.29: Axial displacements of gear wheels (vehicle configuration).

The spikes observable in several time responses (e.g. Figs. 3.25, 3.28, 3.36) are due to the transient behaviour at the impact time. The discontinuity created can affect the convergence of the time integrator. The time step control algorithm often decreases significantly the time step size near the impact time in order to ensure the convergence. If the contact and the solver parameters such as the stiffness or the numerical damping are not chosen adequately, the integration scheme might not override the discontinuity.

Figure 3.30 illustrates the contact pressure of all contact elements introduced in the model when the differential is in the *drive to rear mode*. The time evolution of contact pressures is depicted in Fig. 3.31 during the whole simulation. It can be observed that at each time and for each operation mode, three contact elements are active and two are inactive. The contact between the thrust washers #8 and #10 (cf. Fig. 3.6) is the only contact element that are always active. The *drive modes* ($[0; 7]$ s and $[16; 24]$ s) activate the contacts between the sun gear and the washer #7 and between the internal gear and the washer #11. On the other hand, the contacts between the coupling and the washer #11 and between the internal gear and washer #9 are active during the *coast modes* ($[8; 15]$ s and $[25; 32]$ s). The friction is taken into account in the five contacts. Fig. 3.32 shows the spatial distribution of the power dissipated by friction at $t = 28.5$ s.

The stresses in the thrust washers can be also provided by the numerical model. For instance, Figure 3.33 shows the stress distribution at $t = 11.6$ s. The maximum stress at this time step is 23 MPa and is located on the inner radius of the thrust washers #11. This value is much lower than the yield strength of the steel material used. The same observation can be done for the three other modes. The maximum torque supplied to the housing of the type C TORSEN differential in normal conditions

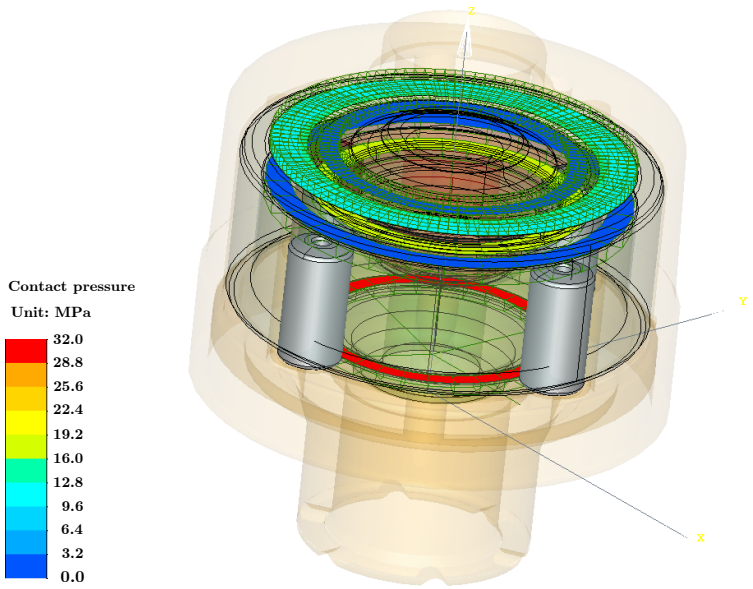

Figure 3.30: Contact pressure on thrust washers ($t = 3.5$ s : *Drive to rear mode*).

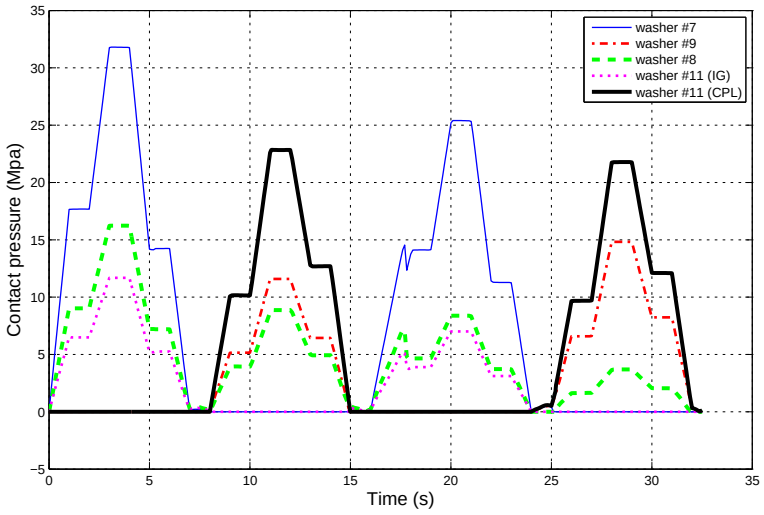

Figure 3.31: Time evolution of the contact pressure in thrust washers.

of a commercial vehicle is often close to 1100 Nm, i.e. slightly higher than the 900 Nm applied in the presented simulation. However, it is obvious that the maximum stress will remain also much lower than the ultimate strength. Nevertheless, the various parts of the differential can be submitted to high stresses at impact times, which is the sizing criterion.

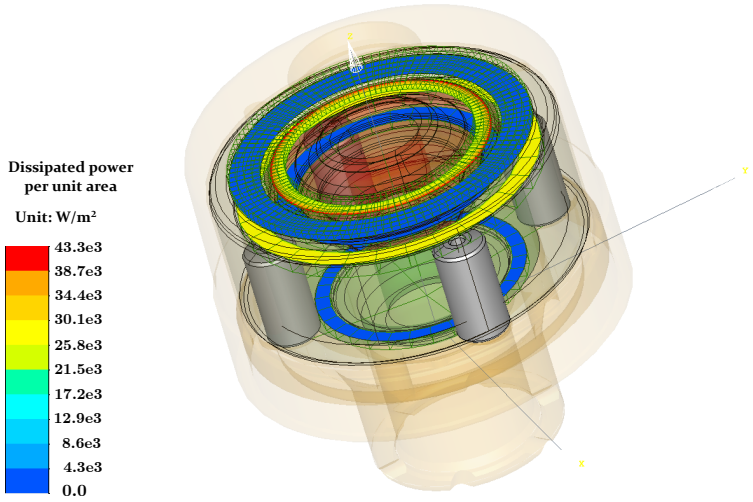

Figure 3.32: Power dissipated by friction between gear wheels and thrust washers ($t =$ 28.2 s: *Coast to rear mode*).

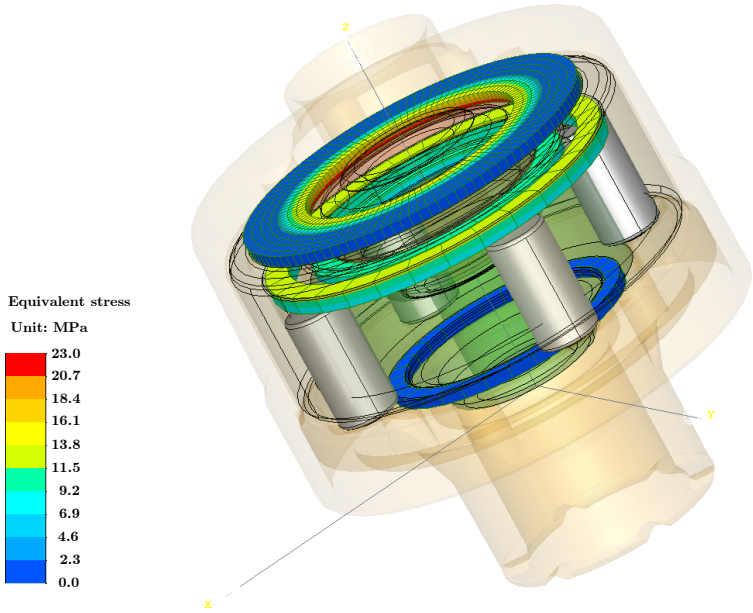

Figure 3.33: Stress in the thrust washers ($t = 11.6$ s : *Coast to front mode*).

3.4.2 Type B TORSEN: front or rear differential

In order to assess if the modelling approach elaborated for the type C TORSEN can also be applied to another system, the type B TORSEN differential has been modelled following a similar procedure. Moreover, this model (Fig. 3.34) will be used to test the formulations developed in the next chapters.

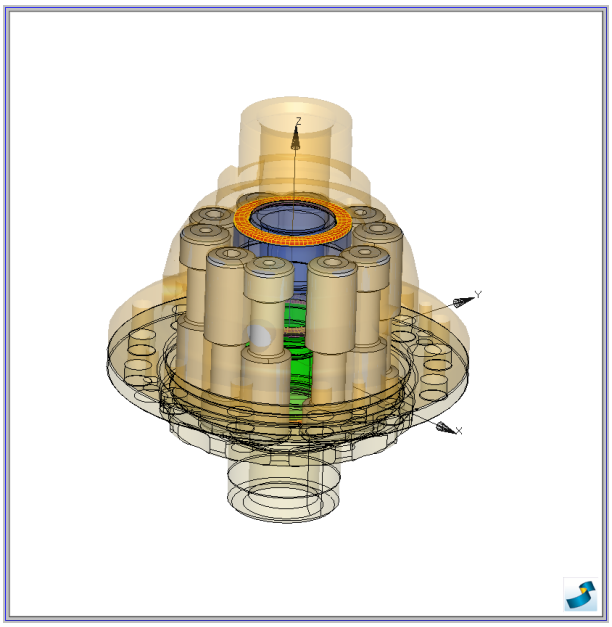

Figure 3.34: SAMCEF model of type B TORSEN differential.

Except for the screws, all the parts have been modelled with a set of assumptions similar to those of the type C model:

- The thrust washers are modelled by a finite element mesh composed of volume elements. The element gears, the housing and the gap are rigid bodies.
- As for the type C TORSEN differential, the joint between each element gear and the housing is represented by a hinge. This is the major simplification adopted in the model compared to the physical device.
- The contacts with insignificant influence on the locking operation have not been accounted for in the model. For the three pairs of thrust washers (Fig. 3.9), only the contact between the two washers is modelled since its friction coefficient is much lower than on the opposite face of the thrust washer. The connection between the element gears and the housing is modelled as an ideal hinge joint, so that their axial displacement is not represented. Therefore, the frictional contact between the lateral faces of element gears and the housing or the cap are neglected.

The multibody model includes 20 gear pair elements whose geometric parameters are summarized in Table 3.6. Three contact elements using a penalty formulation are also introduced. In order to identify the value of the friction coefficient in the hinge joints, a parametric study has been performed. A value of 0.15 is retained for the friction coefficient because it leads to the lowest sum of squared differences between experimental and computed TDR for the four operation modes (see Fig. 3.35).

	Planet Gear / Side Gear	**Transfer Gear / Planet Gear**
Center distance d [mm]	34.549	17.275
Normal pressure angle α_n [deg]	30	30
Backlash b [mm]	0.08	0.09
Mesh stiffness [N/m]	3.96E8	2.12E8
Mesh damping [kg/s]	703	515
Friction coefficient between teeth μ [-]	0.1	0.1
Friction regularization tolerance ϵ_v [-]	0.1	0.1
Total contact ratio ϵ_γ [-]	2.433	1.505

Table 3.6: Data of gear meshing between an element gear and a side gear or between two element gears of type B TORSEN differential.

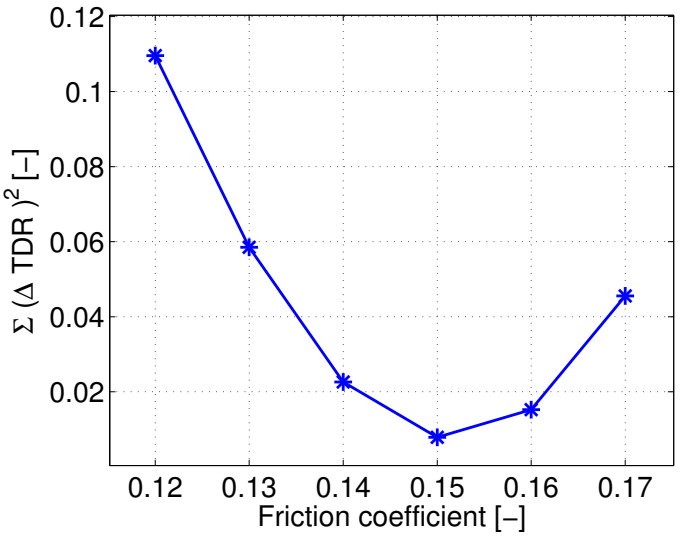

Figure 3.35: A value of 0.15 for the friction coefficient in hinge joints leads to the lowest sum of squared differences between experimental and computed TDR for the four operation modes.

Test bench configuration

In order to validate the model, the tests on the experimental test bench have been reproduced using the simulation tool. The procedure is similar to the one explained for the type C TORSEN. The housing is fixed and a torque is applied on one of the output shafts whereas the rotation speed of the second shaft is imposed.

Figure 3.36 depicts the torques and rotation speeds of the side gears attached to both semi-axles. The TDR computed on the basis of the simulation results is in good agreement with the experimental values as shown in Table 3.7 for the four operation modes. Let us note that the computation of the error factor suffers from a small lack

of accuracy because the experimental data have been given with a relative accuracy of only 6% (0.1/1.6). The geometrical configuration of the type B TORSEN being symmetric from the point of view of the output shafts, the TDR for the operation modes with torque biasing to the left and to the right are similar. The friction coefficients have similar values for all contacts with thrust washers, which explains the very small difference between the TDR for drive and coast modes.

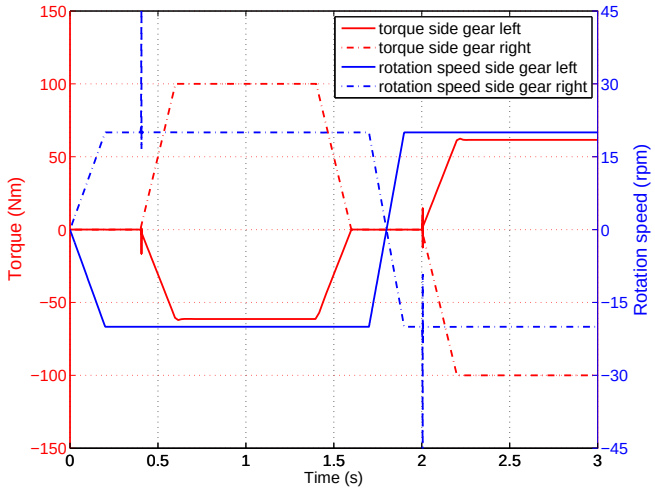

(a) torque biasing to the right wheel

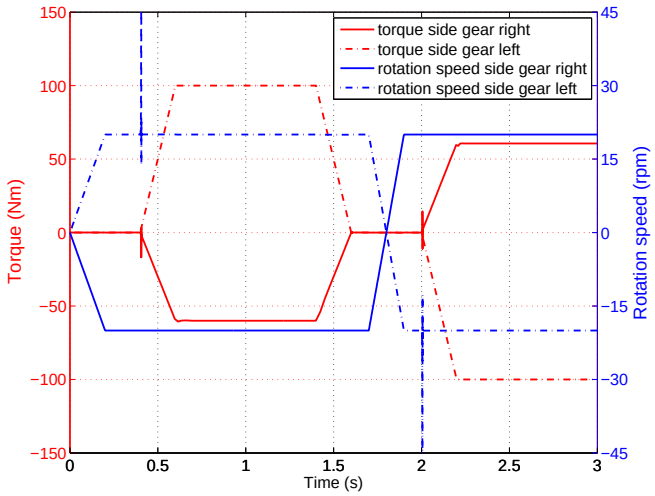

(b) torque biasing to the left wheel

Figure 3.36: Simulation of type B on test bench.

TDR	**Mode 1** Drive bias to right	**Mode 2** Coast bias to right	**Mode 3** Drive bias to left	**Mode 4** Coast bias to left
Experimental	1.6	1.7	1.6	1.7
Simulation	1.58	1.66	1.61	1.64
Error (%)	3.20	2.35	0.62	3.53

Table 3.7: Comparison of torque distribution ratios for the four working modes (type B TORSEN).

Vehicle configuration

The configuration on vehicle has also been simulated too. A torque is applied on the housing and the side gear rotation speeds are prescribed (see Fig. 3.37). Although very seldom effective in reality, the four locking modes can be observed in backward motion of the vehicle. In practice, the backward motion is often used for experimental tests on a small test track. Indeed, an acceleration of the vehicle in backward motion activates a coast mode of the differential which enables to quickly observe the behaviour of the differential. The vehicle starts from rest and has to travel only a few meters. The TDR values for these modes are of course the same as for the vehicle forward motion. In the second part of the simulation (34 s - 67 s), the direction of prescribed rotation speed of side gears has been changed which enables to reproduce the differential behaviour in backward motion. The time evolutions of the resisting torque on both side gears are symmetric with respect to the middle of the simulation ($t = 34$ s). This proves that the model is able to represent also the locking effects in backward motion with accurate prediction of the TDR.

3.5 TORSEN differentials included in a simplified vehicle drivetrain

As final application of this chapter, a global four-wheel drive vehicle equipped with three TORSEN differentials has been modelled (Figure 3.38).

The objective of this model is to observe the distribution of the engine torque between the four wheels. In this context, a very simplified vehicle model is considered. The car body is modelled by a lumped mass and the suspension mechanisms are ignored. The differentials are attached to the vehicle frame with hinge joints. In order to connect the central differential (type C) with the front and rear differentials (type B), conical gear pairs are introduced in the model. The drive shafts linked to the inputs and the outputs of the differentials are represented by rigid bodies. Simple wheel models are also considered in this simulation.

As depicted on Fig. 3.39, a driving torque of 100 Nm is applied to the housing of the

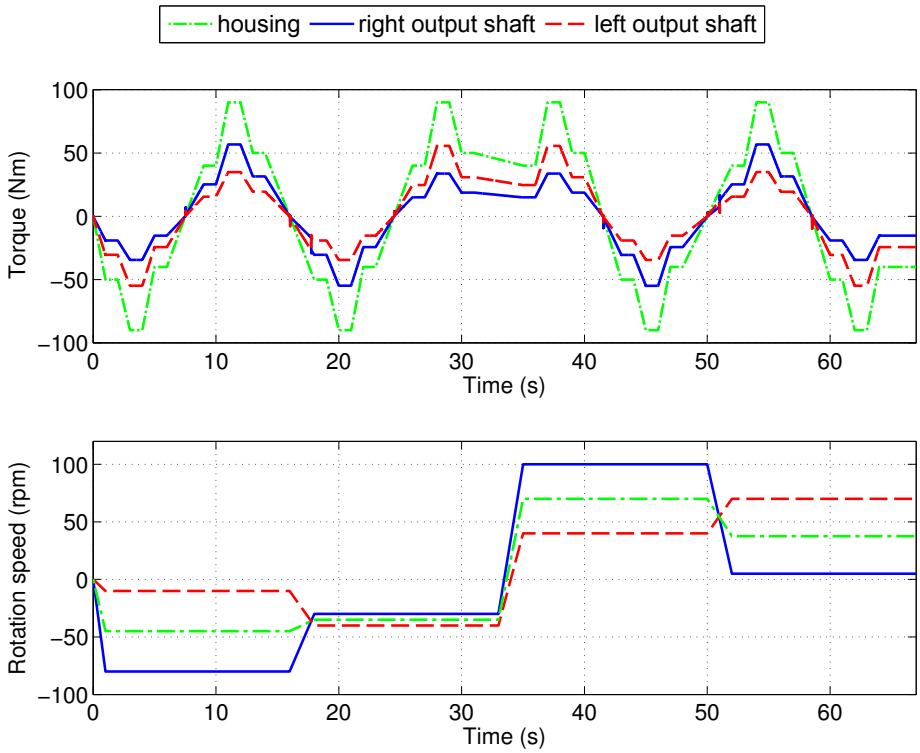

Figure 3.37: Time evolution of torque and rotation speed of housing and output shafts of type B TORSEN on vehicle configuration.

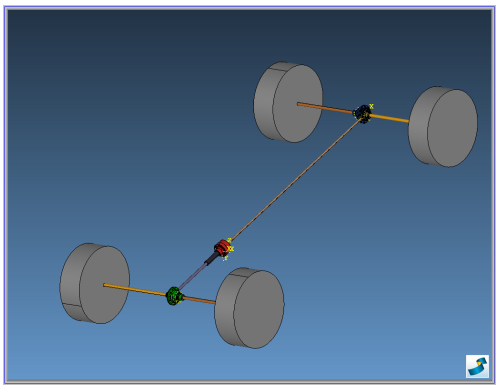

Figure 3.38: Four-wheel drive simplified vehicle model with three differentials.

central differential. Friction coefficients are prescribed with a different value for each wheel-ground contact. For this simple application, quite different friction coefficients have been arbitrarily assigned to illustrate the torque biasing resulting from limited slip behaviour. For the sake of simplicity, the drive ratios have been chosen equal to one for the conical gear pairs which mesh the housing of the front and rear differentials with the pinion fixed on the drive shafts of the central differential. Friction coefficients

in all contact conditions have been modified compared to the previous models with the consequence that the TDR values are modified with respect to Tables 3.5 and 3.7.

The torque provided to each wheel is different and the distribution of the motor torque is consistent with the ground-wheel friction coefficient. The wheel with the higher road friction gets more torque than the other ones which is the advantage of TORSEN differentials. With open differentials without slip limitation the torque on each wheel would be limited by the lowest friction potential (front left wheel) and any extra motor torque would contribute to wheel spin up.

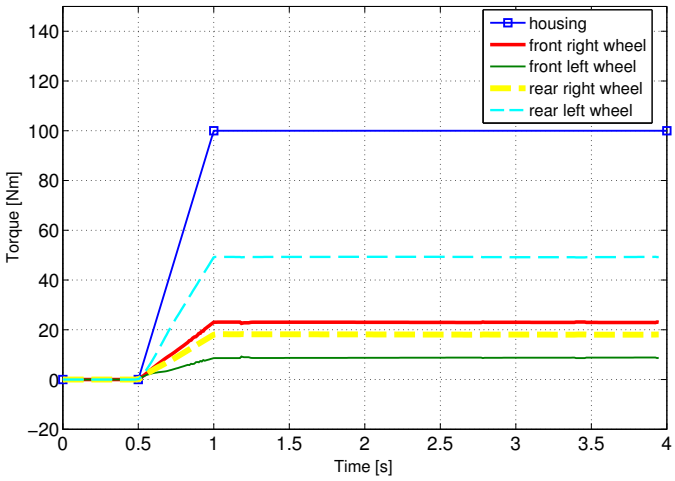

Figure 3.39: Torque distribution on each wheel for a four-wheel drive vehicle equipped with three TORSEN differentials.

3.6 Concluding remarks

The multibody models developed in this chapter can be useful tools in the design process of TORSEN differentials. Indeed, the results provided can reduce the number of physical experiments. For instance, thanks to the numerical model, the radius of the thrust washers or the friction coefficient can be modified to reach a desired locking ratio for each operation mode. The washer thickness can also be modified by means of the stress analysis.

Although the models have shown a good agreement with some experimental data, some drawbacks have been highlighted. The major difficulties encountered are due to contact element modelling. The formulation using algebraic constraints at position level has a poor robustness in the presence of discontinuities generated by impacts. The model based on a penalty method permits the convergence if one uses sufficiently small time steps. Nevertheless, the contact element remains highly sensitive to the value of the contact stiffness and other parameters such as the numerical damping. Moreover,

the aforementioned contact formulation requires that at least one of the contacting bodies is flexible. However, for some applications, it might not be essential to account for the flexibility of the bodies in contact. In the differential model, the rigid-flexible contact element would unnecessarily complicate the model and would increase its size, especially if the mesh is composed of volume finite elements as in global models of industrial mechanisms. The computational time would be highly increased, making the simulation expensive. This has motivated for the development in Chapter 4 of a contact element between two rigid bodies better adapted to simulation of impact.

Some of the modelling assumptions introduced in the TORSEN differential models will be removed thanks to the new formulations presented in the next chapters. A simple joint element will be presented in Section 4.5 to model the interactions between the planet gears and the housing. The flexibility of the gear body will be taken into account by the superelement formulation developed in Chapter 6.

The damping assumption introduced in the contact element to facilitate the convergence at impact time is described by a linear function with respect to penetration velocity. However, this damping can also have a physical meaning. Indeed, in real operation the lubrication oil film between the contacting surfaces tends to slow down the bodies before the contact and then plays the role of a damper. A model of squeeze film is given in section 5.1 to describe the nonlinear damping behaviour according to oil properties and washer geometry.

Finally, the simulation of the simple four-wheel drive vehicle has demonstrated that the integrated simulation of the differential with the vehicle dynamics is possible but lacks robustness with the model currently used. The substitution by the new elements mentioned hereabove will improve the capabilities to model global applications including a large number of bodies (see section 5.5).

Chapter 4

Modelling of contact between rigid bodies

Contents

In this chapter, the continuous impact modelling approach is investigated to model unilateral contact conditions between rigid bodies in dynamic simulations of multibody systems. In addition to the normal contact forces, the contact formulation also accounts for friction forces.

Firstly, the continuous impact theory is described in section 4.2. After validation test models (Sections 4.2.2), the relevance of the developed contact elements has been assessed with the modelling of contacts inside the type C TORSEN differentials (see Sections 4.4.1, 4.5.3). Indeed, the former models of this drivetrain component presented in Chapter 3 have underlined the need to express contact conditions between rigid bodies. The proposed rigid contact models being formulated with a sufficient level of generality, they can also be applied to other transmission devices. The formulation developed for the contact between the thrust washers and the gear wheels is valid for any contact between rigid circular rings which remain parallel. Likewise, the joint between the planet gears and the differential housing can be considered as a non-ideal cylindrical joint with clearance.

4.1 Introduction

When modelling industrial applications including numerous parts as global multibody systems, accounting for flexibility of all bodies is not conceivable for a computational point of view. Numerous bodies are generally assumed to have a rigid behaviour in order to reduce the complexity and the size of the MBS models and simulations.

The rigid body assumption makes sense when the deformations are sufficiently small to assume that their influence is negligible on the overall system motion. Since most bodies from mechanical transmission systems are massive and made of stiff material (e.g. metals), they can be modelled as rigid bodies with limited loss of accuracy on the numerical response.

The modelling of contact between rigid bodies is not trivial, especially in presence of **impacts**. Indeed, the actual physical components are never completely rigid even when they are very stiff. Therefore, the shock produced at the impact point initiates a wave propagation inside the bodies so that the different zones of each contacting body are not simultaneously submitted to the same stress and strain level. A part of the initial kinetic energy is converted into strain energy to propagate the vibration. At the end of the impact period, this elastic energy is converted into kinetic energy of the separating bodies. Owing to material damping, the strain waves are attenuated, which can be macro-mechanically interpreted as a loss of kinetic energy induced by each impact. If the impact duration is long compared to the fundamental period of the impacting bodies, the stress wave effects are negligible since they can experience numerous reflexions inside the bodies during the contact phase. The impact can even be treated with a quasi-static impact theory such as the well-known elastic Hertz's theory. In case of high velocity impact, the deformations can sometimes not be fully recovered after the impact and lead to permanent plastic deformations which increase the kinetic energy loss. Other physical phenomena (e.g. acoustic propagation, thermal dissipation, visco-elasticity) can also contribute to the loss of kinetic energy.

In compliant contact force models as well as in nonsmooth ones, these different sources of kinetic energy loss are globally represented by a **restitution coefficient** e ($0 \leq e \leq 1$). An impact with $e = 1$ means no energy loss (complete elastic contact), whereas $e = 0$ corresponds to a total loss of energy (plastic contact). This restitution coefficient depends on the shape and material properties of the impacting bodies and other parameters such as temperature or friction. Most contact models assume that the restitution coefficient does not depend on the relative approach velocity [37, 45] even if it is not fully true.

The restitution coefficient cannot be computed within the multibody system simulation. It has to be roughly estimated from experience, measured by experiment or determined by numerical simulation on a fast time scale [122].

There exist several definitions of the restitution coefficient. In the kinematic version e_N (Eq. 4.1), also referred as Newton's law, the restitution coefficient is defined as the ratio of the relative velocity between the two bodies in the normal direction before and after impact ($\dot{\ell}_e, \dot{\ell}_s$, the indexes e and s meaning contact end and start respectively).

Poisson's model is based on a kinetic relationship (Eq. 4.2). The coefficient of restitution e_P is the ratio of the normal impulses ΔP_c, ΔP_r of the contact force f during the compression and restitution phases (the time intervals $[t_s, t_c]$ and $[t_c, t_e]$ correspond to the compression and restitution durations).

Finally, the energetic restitution coefficient e_E proposed by Stronge [129] is based on a comparison of the deformation energies between the compression and restitution phases $\mathcal{V}_c$, $\mathcal{V}_r$.

$$e_N = -\frac{\dot{\ell}_e}{\dot{\ell}_s} \tag{4.1}$$

$$e_P = \frac{\Delta P_r}{\Delta P_c} = \frac{\int_{t_c}^{t_e} f \,\mathrm{d}t}{\int_{t_s}^{t_c} f \,\mathrm{d}t} \tag{4.2}$$

$$e_E^2 = -\frac{\mathcal{V}_r}{\mathcal{V}_c} = -\frac{\int_{t_c}^{t_e} f \;\dot{\ell}\,\mathrm{d}t}{\int_{t_s}^{t_c} f \;\dot{\ell}\,\mathrm{d}t} = -\frac{\int_{\ell_c}^{\ell_e} f \,\mathrm{d}t}{\int_{\ell_s}^{\ell_c} f \,\mathrm{d}t} \tag{4.3}$$

These three forms of the restitution coefficient are equivalent unless the configuration is eccentric and the direction of the slip varies during the impact or if the bodies are rough. Some differences can also appear in case of frictional contact or if several impacts occur simultaneously (see [129] for more details).

As an outcome of the brief review of contact models presented in Section 2.4, a continuous impact modelling approach has been chosen for the contact models presented in the sequel of this chapter. This choice has been made because it allows using a smooth solver of the generalized-α family and because friction forces are easily taken into account.

4.2 Continuous impact modelling

The compliant contact models are based on a continuous relationship between the contact force and the local indentation between the two contacting bodies during the overall contact period. The associated penetration length ℓ can be interpreted as a global measure of the local deformation of the contacting surfaces for both bodies. Then, it is assumed that the bodies in contact have a global rigid behaviour but have soft surfaces undergoing non negligible deformations in the contact zone.

In this way, the penetration inherent to the contact models based on a penalty

approach gets a physical meaning and is not introduced for purely numerical reasons. Provided that the penetration remains small, the hypothesis is coherent with the physical nature of the problem.

The magnitude of the contact force is directly related to the local penetration multiplied by a penalty factor, also called the contact stiffness. Such compliant model enables to relax the discontinuities induced by impact. As for all impact models, the goal of the contact force law is to predict the post impact velocity from the system state before the impact. The loss of kinetic energy at each impact is accounted for by means of a restitution coefficient.

The continuous contact models take a different form if it is an elastic or a plastic impact. Elastic impact corresponds to impact at low velocity, i.e. the relative velocity v before impact being negligible compared with the propagation speed of deformation waves across the solids ($v < 10^{-5}\sqrt{E/\rho}$, where E is the Young's modulus and ρ is the mass density of the contacting body having the higher propagation speed, see Ref. [80]). The energy dissipation can be simply represented by adding an internal damping contribution. The initial kinetic energy is mainly dissipated through heating.

Conversely, plastic impact is often associated with high velocity impact and leads to a permanent indentation at the contact location. The main source of energy loss being now the local plasticity near the impact point, it can no longer be represented by a simple material damping contribution. The contact period has to be decomposed into a compression and a restitution phase, a different continuous contact force law being used for each phase.

In both cases (elastic or plastic impact), the Hertz theory is often the basic law for direct and central impacts between rigid bodies having locally a contact surface which can be described by a quadratic function. In the sequel of this section, a brief review of the main elastic contact laws is presented. Owing to the load cases given in the various MBS simulations performed in this thesis, it can be reasonably assumed that no permanent deformations are induced by impact. Besides, the transmission components are usually designed to avoid plastic deformation. Therefore, the plastic contact force models will be not described here, see Refs. [33, 50, 80, 91] for more details.

4.2.1 Elastic contact laws

The **Hertz** theory is often the foundation for contact situations encountered in engineering applications. The Hertz law represents the contact force magnitude f as a nonlinear function of the normal penetration ℓ with a contact stiffness coefficient k_p:

$$f = k_p \, \ell^n \tag{4.4}$$

the exponent n being often equal to 1.5 for metallic bodies having an elliptic contact surface. This contact model is valid for static analysis of frictionless contact between

bodies undergoing small strains thus remaining in the elastic domain. Moreover, the contact area has to be small with respect to the body dimension (e.g. a spherical shape around the contact point).

The contact stiffness parameter k_p depends on the material properties and the shape of the surfaces in contact. For two spheres in contact, the contact stiffness is given by:

$$k_p = \frac{4}{3(\sigma_1 + \sigma_2)} \sqrt{\frac{R_1 R_2}{R_1 + R_2}} \tag{4.5}$$

where R_1 and R_2 are the radii of the two spheres. The material parameters σ_i are computed from the Young's modulus E_i and the Poisson's ratio ν_i of the body materials:

$$\sigma_i = \frac{1 - \nu_i^2}{E_i} \tag{4.6}$$

The Hertz law is limited to contact between isotropic elastic bodies and does not account for any kinetic energy loss. Therefore, it cannot be considered strictly speaking as an impact model.

The **Kelvin-Voigt** model can be used in order to include the energy dissipation during the contact process

$$f = k_p \, \ell + c \, \dot{\ell} \tag{4.7}$$

This model simply consists of a linear spring to represent the elastic force and a linear damper to model the energy loss. The damping parameter c is often called hysteresis coefficient; $\dot{\ell}$ is the relative normal contact velocity. The parameters k_p and c have to be chosen in order to get realistic values for the impact duration, the local penetration and the kinetic energy loss.

The contact force law 4.7 has two major drawbacks. The first one is the linearity of the contact force with respect to the local indentation. Therefore, the physical nonlinear nature of the deformation and the energy transfer related to each impact is not correctly represented. The second drawback results from the discontinuity at the contact establishment and at the end of the contact due to the damping term. Indeed, contrarily to the penetration length, the penetration velocity is not negligible at the beginning or at the end of the contact period. The damping contribution introduces thus abrupt changes of the contact force at the transition between active and inactive states of unilateral contacts.

Hunt and Crossley proposed to combined somehow both previous contact force laws (see Eq. 4.8 and Ref. [60]). They extend the nonlinear Hertz's law to account for the kinetic energy loss. Moreover, in order to avoid a jump at the beginning of the impact and tension force at the end, the classical viscous damping term $c \, \dot{\ell}$ has been multiplied by ℓ^n. Thus, the internal damping contribution depends on the penetration velocity but also on the penetration length

$$f = k_p \, \ell^n + c \, \ell^n \, \dot{\ell} \tag{4.8}$$

One way to set the damping parameter consists in expressing this coefficient as a function of the restitution coefficient e. Hunt and Crossley proposed the following expression:

$$c = \frac{3(1-e)}{2}\frac{k_p}{\dot{\ell}_s} \tag{4.9}$$

where $\dot{\ell}_s$ is the initial relative normal velocity between impacting bodies. The considered restitution coefficient corresponds to the kinematic version described in Eq. 4.1, i.e. the post-impact velocity is the opposite of the pre-impact velocity scaled by the restitution coefficient. This dependency of the damping coefficient with respect to the restitution coefficient allows controlling the amount of energy dissipated by each impact.

As depicted in Fig. 4.1, the force law 4.8 yields a **hysteresis loop**. The enclosed area represents the kinetic energy loss during impact. It can be noted that this force-penetration curve verify $\ell_s = \ell_e = 0$ so that there is no residual indentation after the contact.

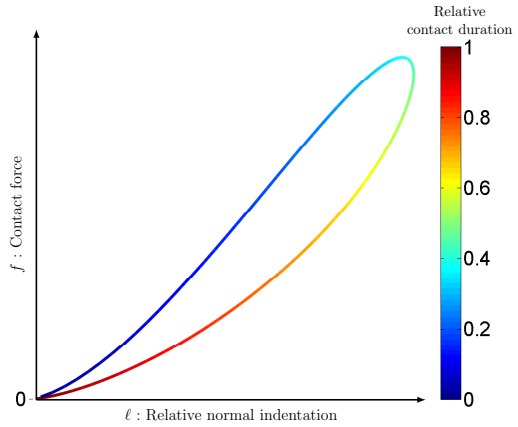

Figure 4.1: The area encircled by the hysteresis loop represents the kinetic energy loss due to the force law of the continuous impact model.

Many authors have developed variants of the Hunt and Crossley impact law. They only differ in the definition of the damping coefficient.

The continuous contact force model proposed by **Lankarani and Nikravesh** [79] is based on the following expression of the damping coefficient:

$$c = \frac{3\left(1-e^2\right)}{4}\frac{k_p}{\dot{\ell}_s} \tag{4.10}$$

which has been evaluated from the physics of the problem by equating the kinetic energy loss in the system to the work done by the contact force. Since the kinetic energy loss is expressed in terms of the squared relative velocity, the expression of the hysteresis damping factor includes a term in e^2.

As the Hunt and Crossley impact law, the Lankarani-Nikravesh law provides a good estimate of the dissipated energy only for large values of the restitution coefficients ($e > 0.8$), see Fig. 4.2. Then, these definitions of the damping term are valid provided that the loss of kinetic energy is small compared to the maximum elastic energy stored at the instant of greatest penetration. This is due to the fact that the indentation velocity has been approximated by the same expression during the whole contact period whereas two different expressions should be employed for the compression and restitution phases. This is the reason why the kinematic restitution coefficient given as model input (pre-restitution coefficient in Fig. 4.2) is overestimated in the numerical response (see post-restitution coefficient which is computed from the ratio of the relative normal velocity before and after the first impact).

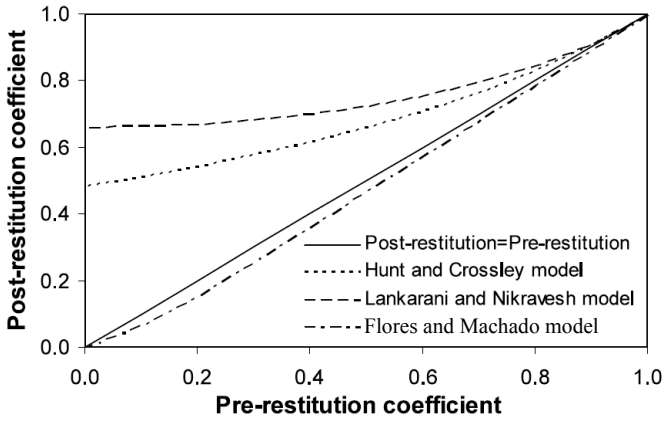

Figure 4.2: Relation between the post and pre-restitution coefficient [37].

In order to circumvent this drawback, **Flores and Machado** have developed a contact law suited for low to medium values of the restitution coefficient as occuring with soft materials [37]. The damping coefficient of this contact law (Eq. 4.8) takes the form:

$$c = \frac{8\,(1-e)}{5\;e}\,\frac{k_p}{\dot{\ell}_s} \tag{4.11}$$

Expression 4.11 has the advantage that it can be used whatever be the amount of energy dissipation. Let us note that if $e = 0$, i.e. the impact is purely plastic, the damping coefficient takes an infinite value. By comparison, the Lankarani-Nikravesh model (Eq. 4.10) does not verify this feature.

Others continuous impact laws based on the same expression (Eq. 4.8) are also available in the literature. Worth mentioning are the works of Gonthier [50], Goldsmith [48] and Khulief [73]. Each model has its own peculiarities. Some of them have been extended to model the friction forces.

4.2.2 Bouncing ball

In order to assess the continuous impact modelling method, the well-known problem of the bouncing ball has been used as benchmark. This very simple one DOF system is composed of a rigid ball of radius R submitted to a gravity field g and dropped at rest from an initial height h_0[1] (see Fig. 4.3). The ball rebounds against a rigid plane ground with a restitution coefficient e.

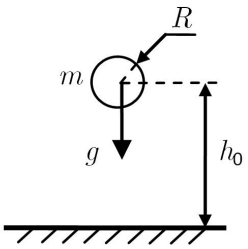

Figure 4.3: Bouncing ball ($R = 0.2$ m, $e = 0.8$, $m = 1$ kg, $h_0 = 1.001$ m).

An exact closed-form solution exists if nonsmooth effects are accounted for (see for instance Ref. [20]). At each time, the vertical position and the velocity of the ball are given by Eqs. 4.12-4.13 where n denotes the n^{th} impact. The impact instants t_n and the velocity before the first impact v_1^- are given by Eq. 4.14 and Eq. 4.15 respectively.

This analytical solution will be compared with the dynamic response provided by various numerical simulations using a continuous impact model and discussed in the sequel of this section. Nevertheless, we have to keep in mind that the analytical solution and the numerical response of the ball are not based on the same modelling assumption. Indeed, the nonsmooth behaviour of the analytical solution enables to represent the impulse and velocity jump at each impact whereas the continuous impact solution assumes a smooth transition at impact instants. Moreover, the impact duration is considered as infinitesimal in the nonsmooth solution while each impact has a finite duration when using a continuous contact model. Therefore, the closed form solution (Eqs. 4.12-4.15) can not be strictly considered as the reference solution for the bouncing ball problem solved with a continuous contact model.

[1] If $h_0 = 1$ m, the first impact is synchronized with a time step. Then, to avoid this peculiar situation, the ball is dropped 1 mm higher [20].

$$q(t) = \begin{cases} h_0 - \frac{1}{2}gt^2 & t \in [0, t_1) \\ R - \frac{1}{2}g(t-t_n)^2 - e^n v_1^-(t-t_n) & t \in [t_n, t_{n+1}) \\ R & t \in \left[\frac{1+e}{1-e}\ t_1, +\infty\right) \end{cases} \tag{4.12}$$

$$v(t) = \begin{cases} -gt & t \in [0, t_1) \\ -g(t-t_n) - e^n v_1^- & t \in [t_n, t_{n+1}) \\ 0 & t \in \left[\frac{1+e}{1-e}\ t_1, +\infty\right) \end{cases} \tag{4.13}$$

$$t_n = \sqrt{\frac{2(h_0-R)}{g}}\left(2e\frac{1-e^{n-1}}{1-e}+1\right) \tag{4.14}$$

$$v_1^- = -\sqrt{2g(h_0-R)} \tag{4.15}$$

With the physical data (dimensions, material) and initial conditions adopted, it can be assumed that no plastic deformation occur, so that an elastic contact law can be used. Only impact laws derived from the Hunt and Crossley model (Eq. 4.8) have been tested. Therefore, the unilateral impact-contact force between the ball and the ground is formulated as:

$$f(\ell, \dot{\ell}) = \begin{cases} k_p\ \ell^n + c\ \ell^n\ \dot{\ell} & \text{if} \quad \ell > 0 \\ 0 & \text{if} \quad \ell < 0 \end{cases} \tag{4.16}$$

with the exponent n is equal to 1.5 for circular and elliptic contact areas (see Hertz theory). The case when the penetration length ℓ has a negative value means that the contact is not effective and consequently no contact force is applied on the ball. For such a simple system, the penetration length and the penetration velocity are easily determined: $\ell = -(q - R)$ and $\dot{\ell} = -\dot{q}$.

According to Ref. [79], the contact stiffness for a contact between a locally spherical surface and a plane can be approximated by Eq. 4.5 where it is assumed that the radius of the plane is infinite ($R_{ground} = \infty$), which gives $k_p = \frac{4}{3(\sigma_1+\sigma_2)}\sqrt{R_{ball}}$. With the parameters adopted and if the ball and the plane are made of steel, $k_p = 6.88\text{E}.10$ N/m.

Figures 4.4-4.8 illustrate the sensitivity of the dynamic response of the ball when one of the following parameters varies: the time step size h, the contact stiffness k_p, the restitution coefficient e, the contact law, the spectral ratio of the time integrator (α-parameter of the generalized-α scheme).

Owing to the fact that the indentation velocity is defined by the same expression during the compression and the restitution phases, the ratio of the relative normal velocity before and after an impact is not equivalent to the restitution coefficient given as parameter of the contact law (see Ref. [79] and Fig. 4.2). That allows to explain the significant differences observed in Figure 4.4 between the Lankarani-Nikravesh contact

model and the analytic nonsmooth solution when $e = 0.8$ in both models. For the first impact, the plot of the contact force magnitude versus the indentation distance shows that the maximum indentation increases with the restitution coefficient. Conversely, the contact duration and the energy dissipation represented by the area of the hysteresis loop are larger when the coefficient of restitution is small.

A detailed parametric study has shown that a restitution coefficient $e = 0.709$ leads to the closest response to the nonsmooth solution with $e = 0.8$. Therefore, this value of the restitution coefficient will be used in the simulations presented hereafter based on the Lankrani-Nikravesh contact law.

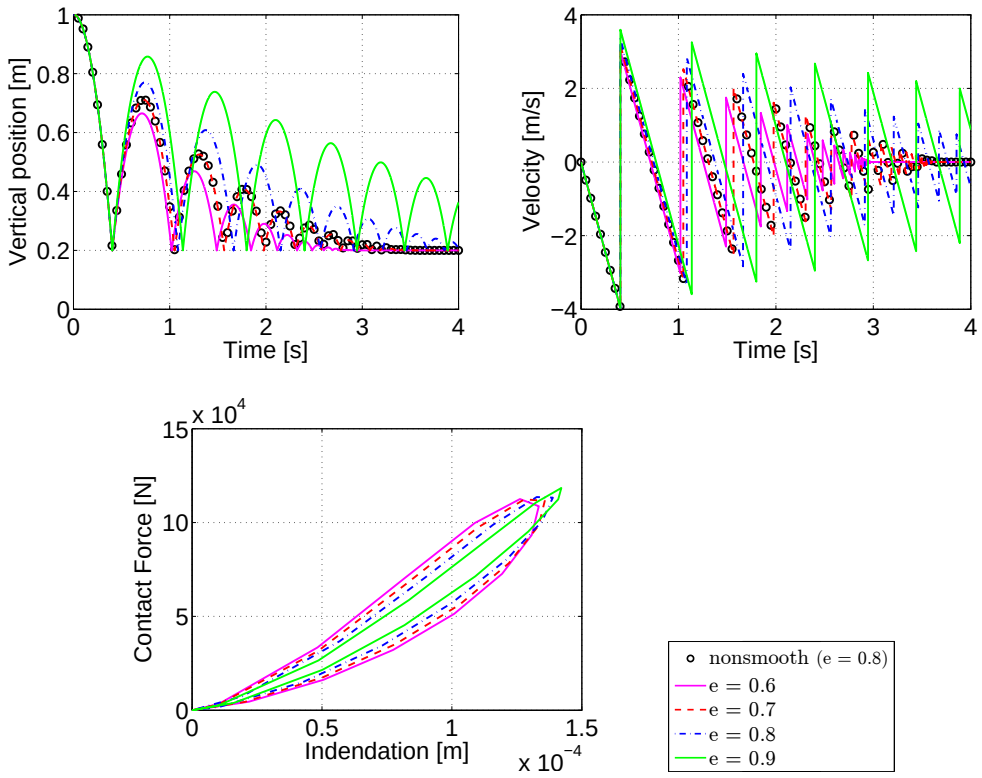

Figure 4.4: Sensitivity of the Lankarani-Nikravesh impact law to the restitution coefficient ($k = 6.88$E.10 N/m, $h =$ 1E.-5 s, $\alpha = 0.1$).

The influence of the time step size on the dynamic response of the ball is depicted in Figure 4.5. With the parameters used for this simulation (h_0, m, e, k_p, α), a time step size of 1E.-5 s or smaller is needed to have a response in agreement with the nonsmooth solution. Indeed, a larger time step size leads to huge discrepancy (e.g. $h =$ 1E.-4 s) or even fully unrealistic response since the ball gains energy after impact (see the curve for $h =$ 1E.-3 s in Fig. 4.5(d)). Such results are due to the insufficient number of time steps during the impact duration. It is also observed that the hysteresis loops degenerate in such situations (Fig. 4.5(c)). From this benchmark, it can be deduced as

practical rule that at least ten time steps over the impact duration are needed to have a correct representation of the energy dissipation.

The use of time steps as small as required for the bouncing ball system with the parameters used in Fig. 4.5, would be strongly penalizing for complex systems including numerous DOFs and several impact-contact conditions. In order to avoid using too small time steps while keeping a reliable response, the contact parameters have to be adjusted. For instance, the contact stiffness can be fixed to a lower value than the physical value based on the Hertz theory (see Eq. 4.5). An alternative method to circumvent this drawback consists in using an automatic time step strategy: small time steps are used around impacts and the time step size is increased in free flight motions.

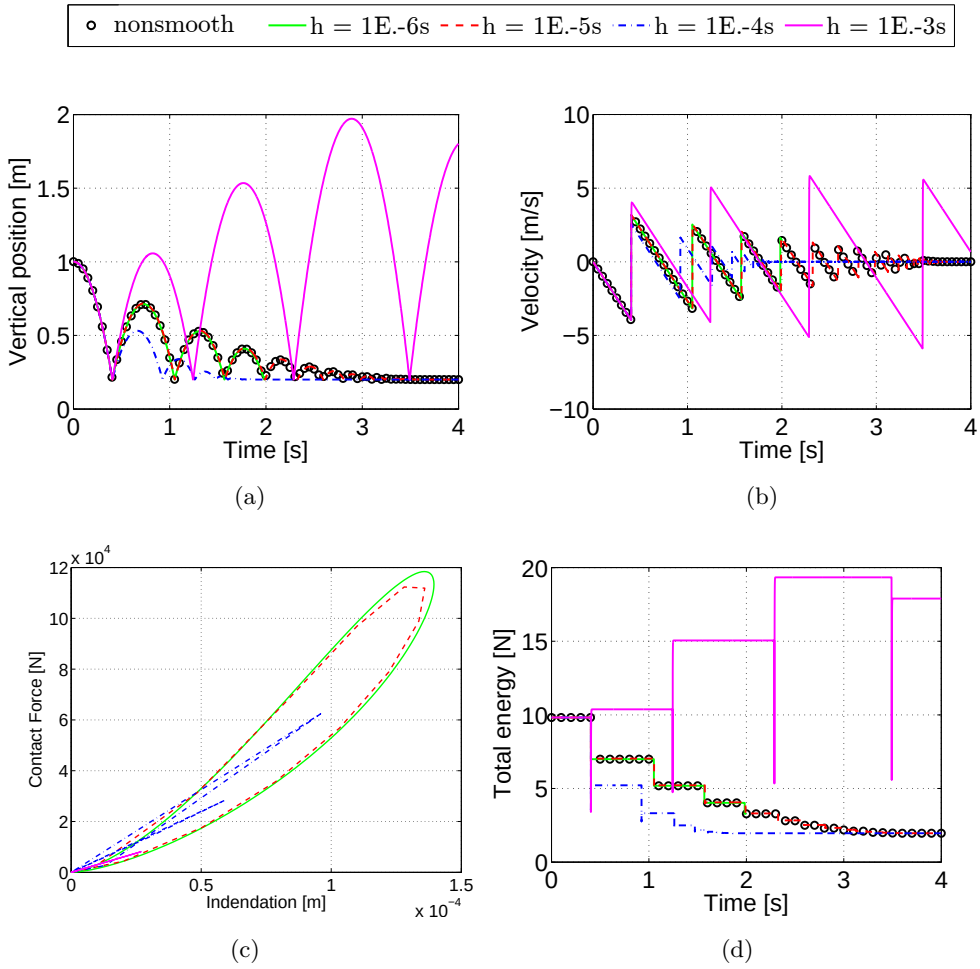

Figure 4.5: Sensitivity of the Lankarani-Nikravesh impact law to the time step size ($k = 6.88\text{E}.10$ N/m, $e = 0.709$, $\alpha = 0.1$).

Figures 4.5(a)-4.5(b) show that with a time step equal 1E.-4 s, the numerical simulation exhibits a large difference with the analytical solution. The other parameters

being constant, the bouncing ball response is assessed with various values of the contact stiffness in Fig. 4.6. This parametric study has for objective to observe the convergence of the system response to the exact solution when the contact stiffness increases.

As expected, the local penetration of the ball in the ground increases when the contact stiffness is reduced. In this way, the discontinuity at impact instant is relaxed. Nevertheless, a too low contact stiffness can also lead to unrealistic responses of the system since the non-penetration condition inherent to rigid contact is no longer respected. On the other hand, a large contact stiffness reduces the penetration but can produce erratic rebound amplitudes unless very small time steps are used. Therefore, for a given time step size, an optimum exists in the choice of the contact stiffness.

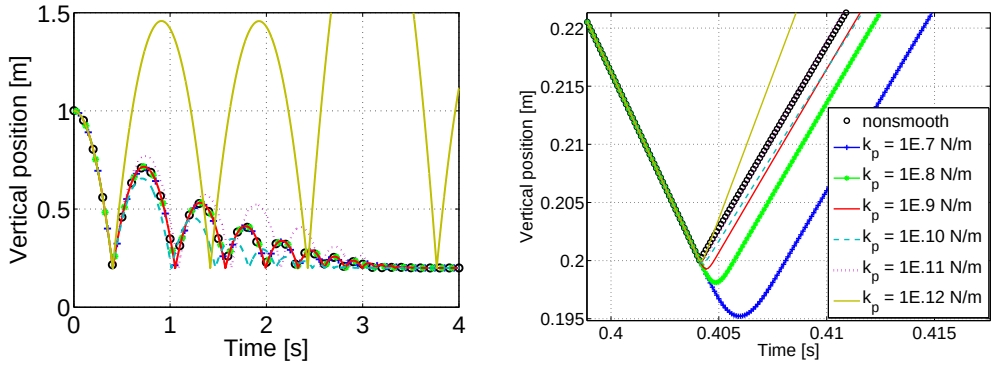

(a) (b) zoom around the first impact

Figure 4.6: Influence of the contact stiffness on the Lankarani-Nikravesh impact law ($e = 0.709$, $h =$ 1E.-4 s, $\alpha = 0.1$).

Contrarily to a nonsmooth contact formulation, the continuous impact model approach yields a finite contact duration for each impact. In order to show this effect, the behaviour around the first impact of the bouncing ball benchmark has been studied in detail. The simulation presented in Fig. 4.7 starts with a ball height $h_0 = 0.21$ m and an initial velocity $v_0 = -4$ m/s. The smaller contact stiffness ($k =$ 1E.7 N/m) used in Fig. 4.6 has been chosen so as to have a sufficient number of time steps during the indentation period and consequently a physically correct dynamic response for all considered time step sizes. The other simulation parameters are mentioned in the figure caption.

Figure 4.7(b) shows that the contact duration tends to converge to a constant contact duration ($\approx$ 1.8E.-3 s) as the time step size decreases.

The convergence analysis on the interval $[0; 0.1$ s$]$ is given in Figures 4.7(e)-4.7(f), where the relative error being based on the L^1 norm. The latter is defined for constant

time steps as:

$$\|e\|_1 = \frac{\sum_{i=0}^{N} |f_i - r_i|}{\sum_{i=0}^{N} |r_i|} \tag{4.17}$$

where N is the number of time steps used to compute the relative error, r_i is the reference solution and f_i is the numerical solution. In the present case, the reference solution is taken as the numerical solution with the smallest time step tested (h = 1E.-7 s). As expected, a second order convergence is observed.

The contact laws derived from the Hunt and Crossley model have the same nonlinear dependance to the local indentation ℓ (Eq. 4.16) but they differ by the definition of the damping coefficient. The positions of the ball are compared in Figure 4.8 when the Lankarani-Nikravesh (Eq. 4.10) and the Flores-Machado (Eq. 4.11) contact laws are used. For both values of the restitution coefficient adopted, the Lankarani-Nikravesh model overestimates the energy dissipation whereas the Flores-Machado underestimates the energy dissipation. Contrarily to the Lankarani-Nikravesh model, the Flores-Machado model provides good agreement with the exact solution for small restitution coefficients. These observations are in accordance with Figure 4.2.

When the number of time steps during the indentation periods is reduced or if the contact stiffness is increased, the spectral radius α of the numerical integration scheme may have a strong influence on the dynamic response. Figure 4.9 illustrates this situation: $\alpha = 0.1$ means that the high frequencies are nearly annihilated by the numerical damping while $\alpha = 0.9$ corresponds to only a few damping of high frequencies. Therefore, the simulation with $\alpha = 0.1$ leads to a dynamic response converging to a closed contact at the end of the simulation but with an energy dissipation at each impact higher that the nonsmooth exact solution. In contrast, a response with erratic magnitudes of rebounds is obtained when $\alpha = 0.9$.

As demonstrated in this section, the parameters of a continuous impact model cannot be varied independently. For instance, a high contact stiffness, requires using small time steps.

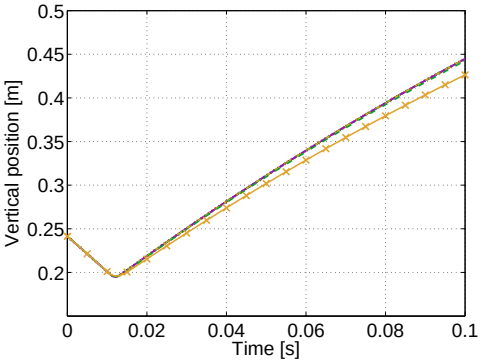

(a)

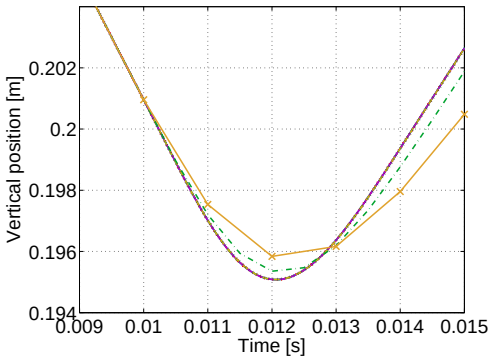

(b) zoom on contact duration

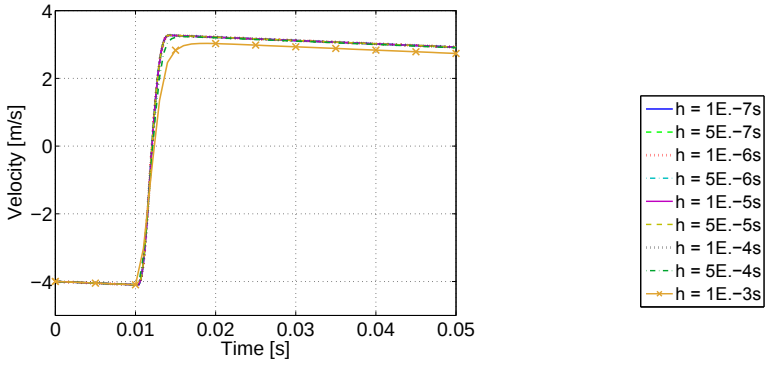

(c)

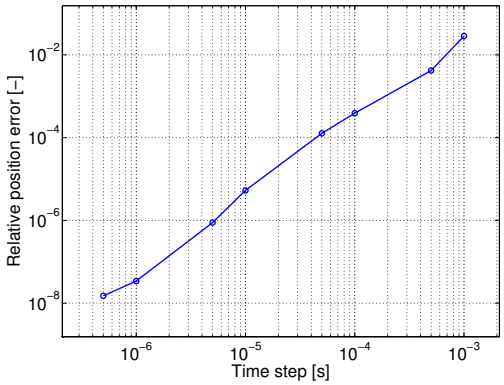

(e)

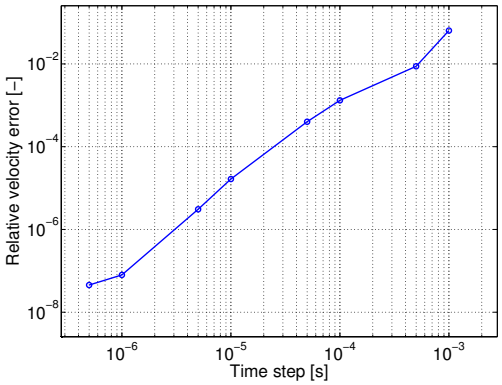

(f)

Figure 4.7: Convergence analysis of the Lankarani-Nikravesh impact law ($e = 0.709$, $k_p = 1\text{E}.7$ N/m, $\alpha = 0.1$).

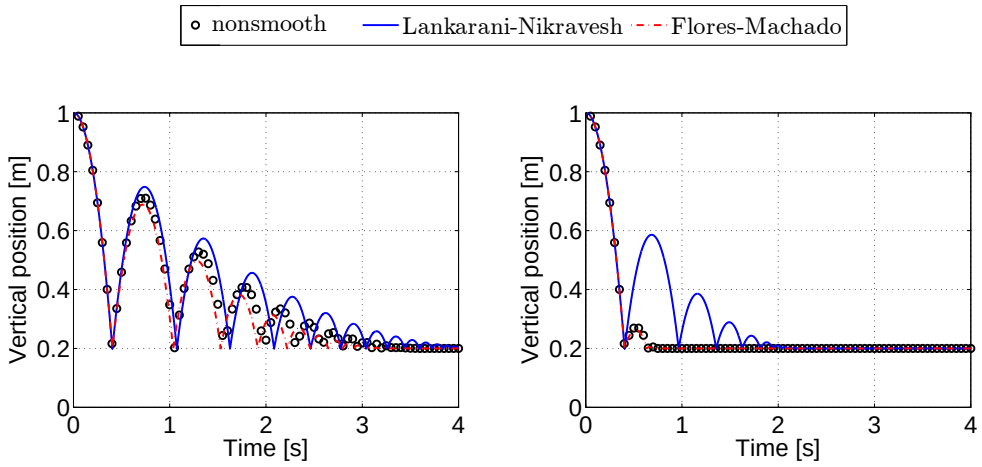

(a) $e = 0.8$ (b) $e = 0.3$

Figure 4.8: Dynamic response of the bouncing ball with different expressions of the damping coefficient included in the contact law (k = 1E.9 N/m, h = 1E.-4 s, $\alpha = 0.1$).

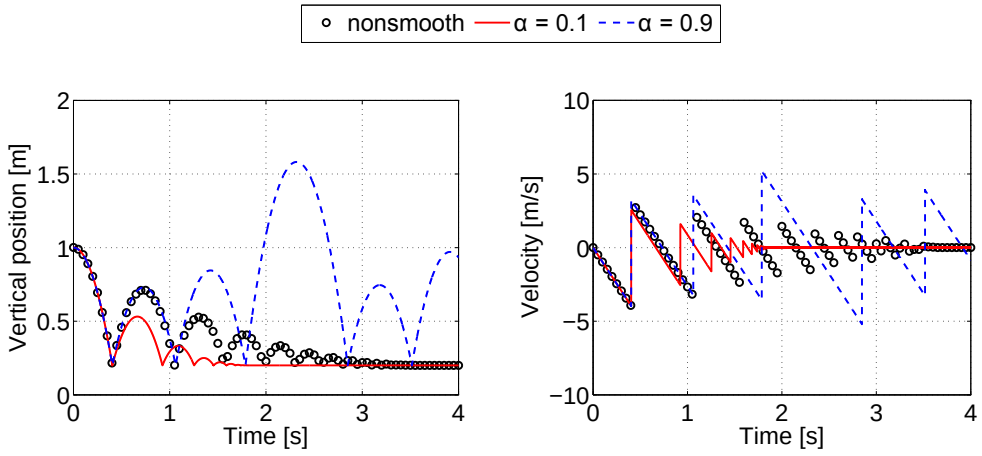

Figure 4.9: Influence of the spectral radius of the generalized-α integration scheme on the Flores-Machado impact law (k = 6.88E.10 N/m, h = 1E.-4 s, $e = 0.8$).

4.3 Kinematics of the contact between two rigid bodies

This section describes the formulation of an element capable to model the normal contact forces and the friction forces between two rigid planar rings. This contact element allows to simulate unilateral contacts when the contacting bodies are subjected to large displacements and rotations in 3D analysis. The formulation follows the guidelines of the finite element framework (Section 2.2) and has been implemented as a *user element* in the multibody software SAMCEF/MECANO [88].

As for most contact models between rigid bodies, the proposed contact element is defined between two nodes fixed on the two rigid bodies potentially in contact. These nodes A and B are not necessarily located at the center of gravity of the two bodies (see Fig. 4.10) and are the origins of two local frames (namely $\{A; \boldsymbol{e}''_{A_1}, \boldsymbol{e}''_{A_2}, \boldsymbol{e}''_{A_3}\}$ and $\{B; \boldsymbol{e}''_{B_1}, \boldsymbol{e}''_{B_2}, \boldsymbol{e}''_{B_3}\}$) following body motion.

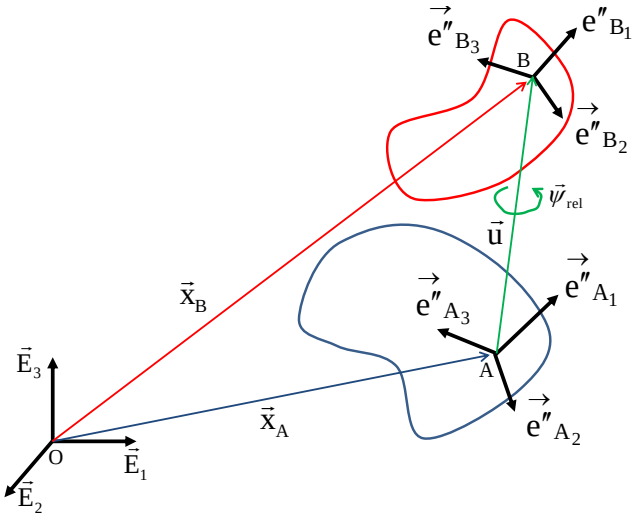

Figure 4.10: Kinematics conventions for the contact between two rigid bodies.

At the initial configuration, these body frames denoted by the vectors $\boldsymbol{e}_{A_i}$ and $\boldsymbol{e}_{B_i}$ in Fig. 4.11 are chosen parallel for simplicity. The rotation matrix $\boldsymbol{R}_1$ gives the initial orientation of both material frames with respect to the absolute inertial frame $\{O; \boldsymbol{E}_1, \boldsymbol{E}_2, \boldsymbol{E}_3\}$:

$$\boldsymbol{e}_{A_i} = \boldsymbol{R}_1 \, \mathbf{E}_i \tag{4.18}$$

$$\boldsymbol{e}_{B_i} = \boldsymbol{R}_1 \, \mathbf{E}_i \tag{4.19}$$

The rotation operators $\boldsymbol{R}_A$,$\boldsymbol{R}_B$ enable to compute the rotation from initial to current configuration (Eqs. 4.20-4.21).

$$\boldsymbol{e}''_{A_i} = \boldsymbol{R}_A \, \boldsymbol{e}_{A_i} = \boldsymbol{R}_A \, \boldsymbol{R}_1 \, \boldsymbol{E}_i \tag{4.20}$$

$$\boldsymbol{e}''_{B_i} = \boldsymbol{R}_B \, \boldsymbol{e}_{B_i} = \boldsymbol{R}_B \, \boldsymbol{R}_1 \, \boldsymbol{E}_i \tag{4.21}$$

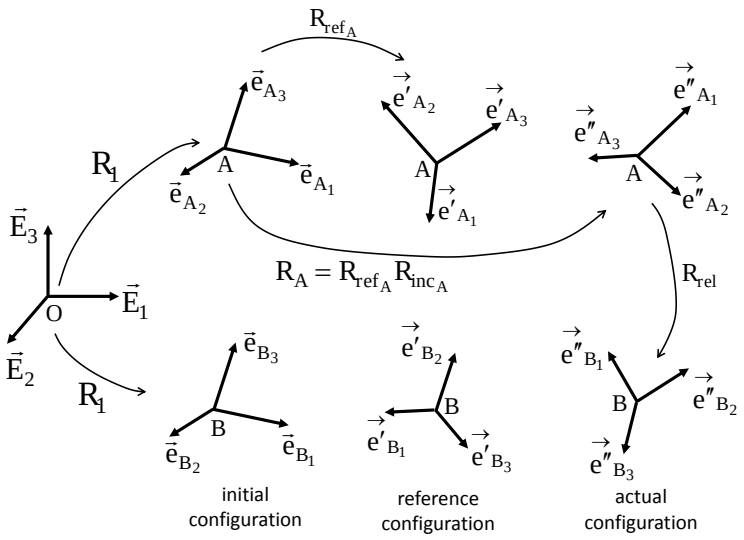

Figure 4.11: Schematic representation of rotation matrices linking the local frames attached to nodes A and B of the colliding bodies.

The magnitude and the direction of the contact and friction forces depend on the instantaneous relative position and orientation of both material frames at each time. Therefore, the force vectors will be first computed according to the relative position and rotation vectors expressed in the frame attached to node A. Afterwards, these force vectors will be transferred in the inertial frame (Section 4.3.1).

The relative position vector $\boldsymbol{u}$ of node B with respect to node A in the frame $\{A; \boldsymbol{e}''_{A_1}, \boldsymbol{e}''_{A_2}, \boldsymbol{e}''_{A_3}\}$ can be easily computed from the fundamental equation describing the rigid body kinematics [13]:

$$\boldsymbol{u} = \boldsymbol{R}_1^T \boldsymbol{R}_A^T (\boldsymbol{x}_B - \boldsymbol{x}_A) \tag{4.22}$$

The vectors $\boldsymbol{e}''_{B_i}$ are defined in the inertial frame but can also be expressed in the frame $\{A; \boldsymbol{e}''_{A_1}, \boldsymbol{e}''_{A_2}, \boldsymbol{e}''_{A_3}\}$:

$$\boldsymbol{e}''_{B_i\ /A} = (\boldsymbol{R}_A \boldsymbol{R}_1)^T \ \ \boldsymbol{e}''_{B_i} = \boldsymbol{R}_1^T \boldsymbol{R}_A^T \boldsymbol{R}_B \boldsymbol{R}_1 \ \mathbf{E}_i = \boldsymbol{R}_{rel} \ \mathbf{E}_i \tag{4.23}$$

where $\boldsymbol{R}_{rel}$ is the relative rotation matrix.

4.3.1 Nodal forces at the element level

Since the contact model is defined between the nodes A and B, the generalized coordinates vector $\boldsymbol{q}$ of the contact element is simply composed of the absolute nodal DOFs

in translation and rotation of these two nodes:

$$\boldsymbol{q} = \begin{Bmatrix} \boldsymbol{x}_A \\ \boldsymbol{\Psi}_{A\ inc} \\ \boldsymbol{x}_B \\ \boldsymbol{\Psi}_{B\ inc} \end{Bmatrix} \tag{4.24}$$

The contribution vector $\boldsymbol{g}_{int}^{con}$ of the contact element to the internal forces of the multibody system is obtained by identification between the two expressions of the virtual work stated in Equation 4.25. The vectors $\boldsymbol{f}_t$ and $\boldsymbol{f}_r$ represent the contact forces and torques expressed in the frame attached to node A.

$$\delta W = \delta \boldsymbol{q}^T\ \boldsymbol{g}_{int}^{con}\ (\boldsymbol{q}, \dot{\boldsymbol{q}}) = \delta \boldsymbol{u}^T\ \boldsymbol{f}_t + \delta \boldsymbol{\Theta}_{rel}^T\ \boldsymbol{f}_r \tag{4.25}$$

The variation vectors $\delta\boldsymbol{u}$, $\delta\boldsymbol{\Theta}_{rel}$ of the relative displacement and material relative rotation are computed by deriving the expressions 4.22 and 4.23:

$$\delta \boldsymbol{u} = \widetilde{\boldsymbol{u}} \boldsymbol{R}_1^T \boldsymbol{T}(\boldsymbol{\Psi}_{A\ inc})\ \delta \boldsymbol{\Psi}_{A\ inc} + \boldsymbol{R}_1^T \boldsymbol{R}_A^T\ (\delta \boldsymbol{x}_B - \delta \boldsymbol{x}_A) \tag{4.26}$$

$$\delta \boldsymbol{\Theta}_{rel} = \boldsymbol{R}_1^T \boldsymbol{T}(\boldsymbol{\Psi}_{B\ inc})\ \delta \boldsymbol{\Psi}_{B\ inc} - \boldsymbol{R}_1^T \boldsymbol{R}_B^T \boldsymbol{R}_A \boldsymbol{T}(\boldsymbol{\Psi}_{A\ inc})\ \delta \boldsymbol{\Psi}_{A\ inc} \tag{4.27}$$

In summary, we have

$$\begin{Bmatrix} \delta \boldsymbol{u} \\ \delta \boldsymbol{\Theta}_{rel} \end{Bmatrix} = \boldsymbol{B}\ \delta \boldsymbol{q} \tag{4.28}$$

where the matrix $\boldsymbol{B}$ is defined by:

$$\boldsymbol{B} = \begin{bmatrix} -(\boldsymbol{R}_A \boldsymbol{R}_1)^T & \widetilde{\boldsymbol{u}} \boldsymbol{R}_1^T \boldsymbol{T}(\boldsymbol{\Psi}_{A\ inc}) & (\boldsymbol{R}_A \boldsymbol{R}_1)^T & \boldsymbol{0} \\ \boldsymbol{0} & -\boldsymbol{R}_1^T \boldsymbol{R}_B^T \boldsymbol{R}_A \boldsymbol{T}(\boldsymbol{\Psi}_{A\ inc}) & \boldsymbol{0} & \boldsymbol{R}_1^T \boldsymbol{T}(\boldsymbol{\Psi}_{B\ inc}) \end{bmatrix} \tag{4.29}$$

Now, the internal force vector due to contact can be formulated as:

$$\boldsymbol{g}_{int}^{con}(\boldsymbol{q}, \dot{\boldsymbol{q}}) = \boldsymbol{B}^T\ \begin{Bmatrix} \boldsymbol{f}_t \\ \boldsymbol{f}_r \end{Bmatrix} \tag{4.30}$$

The contribution to the iteration matrix is detailed in Appendix A.1 and the final expression of the tangent stiffness and damping matrices are given in Eqs 4.31-4.32:

$$\boldsymbol{K}_t^{con} = \boldsymbol{B}^T \begin{bmatrix} \frac{\partial \boldsymbol{f}_t(\boldsymbol{u}, \dot{\boldsymbol{u}})}{\partial \boldsymbol{u}} & \boldsymbol{0} \\ \boldsymbol{0} & \frac{\partial \boldsymbol{f}_r(\boldsymbol{\Psi}_{rel}, \dot{\boldsymbol{\Psi}}_{rel})}{\partial \boldsymbol{\Psi}_{rel}} \end{bmatrix} \boldsymbol{B} + \begin{bmatrix} \boldsymbol{0} & \boldsymbol{R}_A \boldsymbol{R}_1 \widetilde{f}_t \boldsymbol{R}_1^T \boldsymbol{T}(\boldsymbol{\Psi}_{A\ inc}) & \boldsymbol{0} & \boldsymbol{0} \\ \boldsymbol{0} & \frac{1}{2}\widetilde{\left(\boldsymbol{R}_1 \widetilde{\boldsymbol{u}} \boldsymbol{f}_t\right)} + \boldsymbol{R}_1 \widetilde{f}_t \widetilde{\boldsymbol{u}} \boldsymbol{R}_1^T & \boldsymbol{0} & \boldsymbol{0} \\ \boldsymbol{0} & -\boldsymbol{R}_A \boldsymbol{R}_1 \widetilde{f}_t \boldsymbol{R}_1^T \boldsymbol{T}(\boldsymbol{\Psi}_{A\ inc}) & \boldsymbol{0} & \boldsymbol{0} \\ \boldsymbol{0} & \boldsymbol{0} & \boldsymbol{0} & \boldsymbol{0} \end{bmatrix} \tag{4.31}$$

$$\boldsymbol{C}_t^{con} = \boldsymbol{B}^T \begin{bmatrix} \frac{\partial \boldsymbol{f}_t(\boldsymbol{u}, \dot{\boldsymbol{u}})}{\partial \dot{\boldsymbol{u}}} & \boldsymbol{0} \\ \boldsymbol{0} & \frac{\partial \boldsymbol{f}_r(\boldsymbol{\Psi}_{rel}, \dot{\boldsymbol{\Psi}}_{rel})}{\partial \dot{\boldsymbol{\Psi}}_{rel}} \end{bmatrix} \boldsymbol{B} \tag{4.32}$$

4.4 Contact between two planar rings

The kinematic relations (Eqs. 4.18-4.23) and the nodal forces computed hereabove are valid for any contact between two rigid bodies. However, in order to simplify the problem, only the geometric configuration in which **two planar rings** remain parallel and in which their relative motion is composed of a translation and a rotation in the sole normal direction, has been tested in numerical simulations.

The kinematics of the contact in this situation is depicted in Figure 4.12. The nodes A and B are located on the revolution axis of the rigid rings at a normal distance D_A or D_B from the contact surface. The first vector of local frames is the normal direction of the contact force.

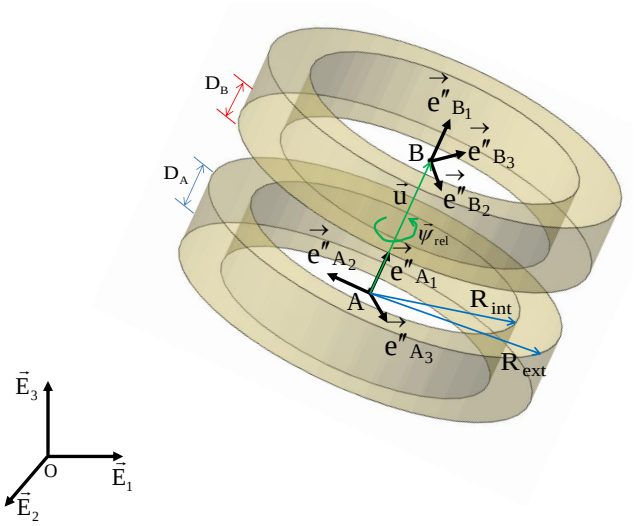

Figure 4.12: Kinematics of the contact between two planar rings.

With these geometric assumptions, the contact forces and torques $\boldsymbol{f}_t$, $\boldsymbol{f}_r$ are reduced to the following expressions:

$$\boldsymbol{f}_t = \begin{Bmatrix} -f \\ 0 \\ 0 \end{Bmatrix} \quad , \quad \boldsymbol{f}_r = \begin{Bmatrix} T_{fr} \\ 0 \\ 0 \end{Bmatrix} \tag{4.33}$$

where f is the magnitude of the normal contact force and T_{fr} is the magnitude of the friction torque.

The value of the **normal contact force** f can be computed by means of one of the continuous contact laws presented in Section 4.2.1. However, due to the peculiarity of the geometric configuration in case of contact between two planar rings, it is advised to use a **linear** contact law with respect to the penetration length ($n = 1$ in Eq. 4.8). Indeed, as described in Refs. [79, 139], the contact between two locally planar surfaces

is a linear phenomenon provided that the local irregularities due to, for instance, the manufacturing properties of the contact surfaces are neglected. Since the local contact area is not small neither elliptic, the Hertz theory is not applicable here.

In the general case of a constant pressure p applied on a rectangular contact area of surface S, the contact stiffness is given by:

$$k_p = \frac{\sqrt{S}}{\chi\left(\frac{1-\nu_A^2}{E_A} + \frac{1-\nu_B^2}{E_B}\right)} \tag{4.34}$$

where E_i and ν_i are the Young's modulus and the Poisson's ratio of the body material; χ is an empirical parameter depending on the side ratio of the rectangle [139].

The penetration length ℓ is easily determined thanks to the simple geometric configuration:

$$\ell = -(\boldsymbol{x}_{AB}^T\, \boldsymbol{n} - D_A - D_B) \tag{4.35}$$

$$= -(\boldsymbol{u}(1) - D_A - D_B) \tag{4.36}$$

where the D_i are the distances from the reference nodes A, B to the contact surfaces in the normal direction $\boldsymbol{n}$ (see Fig. 4.12). The penetration velocity is equivalent to the opposite of the first component of the relative velocity vector: $\dot{\ell} = -\dot{\boldsymbol{u}}(1)$, see Eq. A.4 for the detailed expression of $\dot{\boldsymbol{u}}$.

The magnitude of the friction force in the tangent plane simply consists in multiplying the normal contact force f by a regularized friction coefficient μ_R (see Eq. 3.28 for the expression). The **friction torque** T_{fr} produced by the contact between the two rigid rings is defined by:

$$T_{fr} = \int_S \mu_R\; p\; r\; \mathrm{d}S = 2\pi\; \mu_R\; \frac{f}{S}\; \frac{R_{ext}^3 - R_{int}^3}{3} \tag{4.37}$$

4.4.1 Application to the contact between gear wheels and thrust washers of TORSEN differentials

In order to test the proposed element formulation dedicated to the modelling of contact between two planar rings, the type C TORSEN differential is considered as an application test case. Indeed, the contacts between the thrust washers and the lateral annular face of the gear wheels can be regarded as contacts between two planar rings.

The first node of the contact element (see node A in Fig. 4.12) corresponds to the center of mass of the thrust washer and the second node (node B) is the rotation center or the center of mass of the gear wheel. The distance D_A is equal to the half the thickness of the thrust washer and D_B is the distance from the reference node B to the face of the gear wheel web which enters into contact.

As pointed out in Chapter 3, at the switching time between two working modes of the TORSEN differential, the gear wheels move quickly in the axial direction, that leads to an impact phenomenon when they enter in contact with the thrust washers. Therefore, the contact element should be able to manage such type of situation.

According to the material and geometric data of the differential parts as well as their relative velocity when they are impacting in normal working conditions, the impacts are purely elastic, i.e., no plastic deformation occurs. Moreover, the coefficient of restitution can be assumed to be relatively high so that the Lankarani-Nikravesh contact law can be used (see Fig. 4.2).

In a first step, in order to have a simple MBS test model, only a reduced part of the differential has been modelled. As depicted in Figure 4.13, this model includes four rigid bodies: two thrust washers, the sun gear and one planet gear. The only motion allowed for the planet gear is a rotation around its rotation axis while the sun gear can move in the axial direction before entering in contact with the lower or the upper thrust washer which are both clamped.

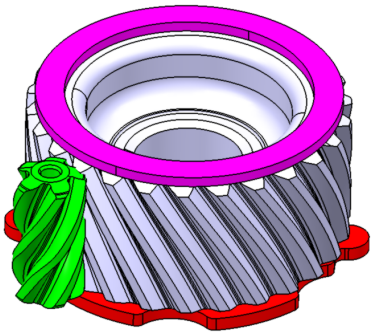

Figure 4.13: Benchmark: unilateral contacts between the sun gear and two thrust washers of the type C TORSEN differential.

A torque is applied on the planet gear whereas the rotation speed of the sun gear is prescribed (their time evolution is depicted in Figure. 4.14). Due to the helical meshing, the sun gear undergoes an axial displacement as soon as the sign of the torque applied on the planet gear changes (see Fig. 4.15(a)). The zoom around the second axial displacement represented in Fig. 4.15(b) shows some rebounds of the sun gear against the thrust washer before reaching a closed contact configuration. The magnitude and the frequency of these rebounds depends on the value of the contact stiffness ($k_p = 10^{10}$ N/m) and the restitution coefficient ($e = 0.8$).

Figure 4.16 illustrates the hysteresis loops observed when plotting the contact force versus the penetration length. The area defined by theses loops is a measure of the energy dissipation introduced by each impact and is directly related to the value of the restitution coefficient. It can be noticed that the median of each loop follows a linear

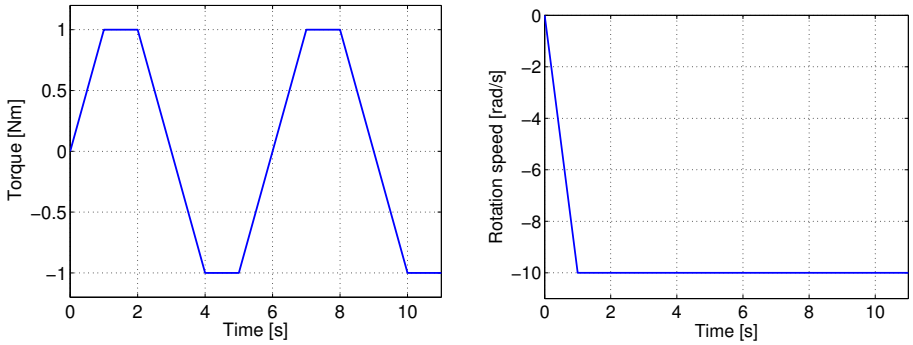

(a) planet gear (b) sun gear

Figure 4.14: Load case for the benchmark model.

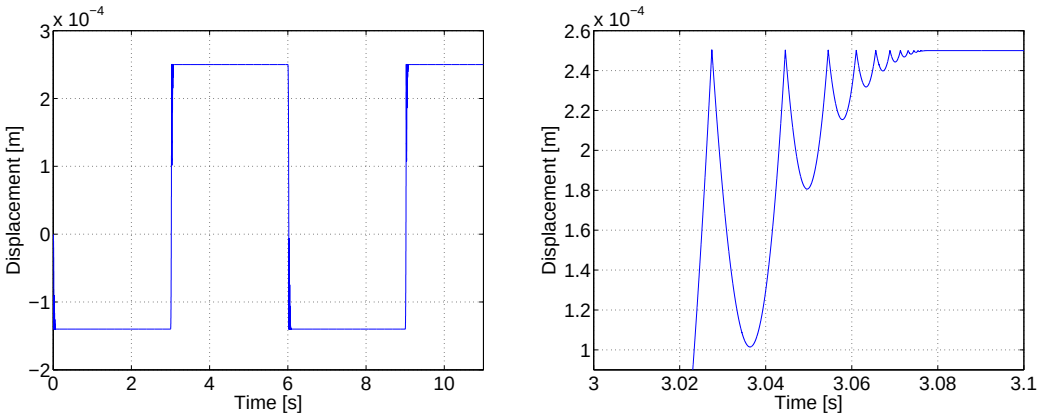

(a) (b) zoom

Figure 4.15: Axial displacement of the sun gear.

law instead of a nonlinear law as depicted in Figs. 4.1, 4.4, 4.5(c) and 4.25. This is a consequence of the replacement of the nonlinear nature of Hertz's contact by a linear contact force model in case of contact between two planar surfaces (the exponent n is fixed to 1 in Eq. 4.8).

In order to have a correct modelling of the the kinetic energy loss, the hysteresis loops have to be represented by a sufficient number of time steps. An automatic time step selection strategy is able to reduce the time step size at impact instants while keeping a reasonable time step size during closed contact periods (see Fig. 4.17).

In a second stage, the full TORSEN differential has been modelled. The loading and boundary conditions are the same as described in Section 3.4.1 when the differential is in the vehicle configuration. Let us remind that a torque is applied on the differential housing while the rotation speed of the output shafts (sun gear and coupling) are

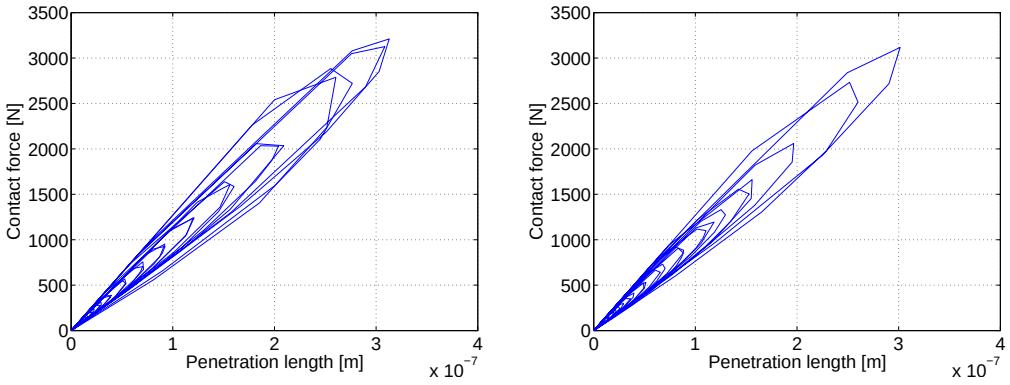

(a) contact with the above thrust washer (b) contact with the under thrust washer

Figure 4.16: Hysteresis loop representing the kinetic energy loss at each impact between the gear wheel and the thrust washers.

prescribed. The only modification addresses the replacement of the five rigid/flexible contact conditions (see Section 3.3) by the new contact element between rigid bodies.

The time evolution of the torque on the sun gear and the coupling are depicted in Fig. 4.18. These torques can be interpreted as the reaction torques on the differential output shafts linked to the sun gear and the coupling because their rotation speed is prescribed. At each time step, the sum of the two output torques is equal to the input torque applied on the differential housing. The gap between the two output torques is different according to the active working mode of the differential. This asymmetric torque splitting is representative of the locking rate of TORSEN differentials.

The Torque Distribution Ratios (see Eq. 3.1) computed from these torque curves are similar to the values obtained with the rigid/flexible contact element used in chapter 3 (see Fig. 3.28 and Table 3.5) and are therefore also in good agreement with the experimental data.

Compared with the rigid/flexible contact condition described in section 3.3, the main advantage of the proposed rigid/rigid contact element is the reduction of the computational time. For the simulation of the full type C TORSEN differential presented hereabove and in Section 3.4.1, the CPU time is reduced by a factor of 50. This is mainly due to the drastic decrease of the number of degrees of freedom: from 27867 DOFs with the “coarse” FE models of thrust washers (see Fig. 3.30) to 851 DOFs with the rigid thrust washers models. The projection method of the rigid/flexible contact element is also highly time consuming and is avoided with the rigid contact model.

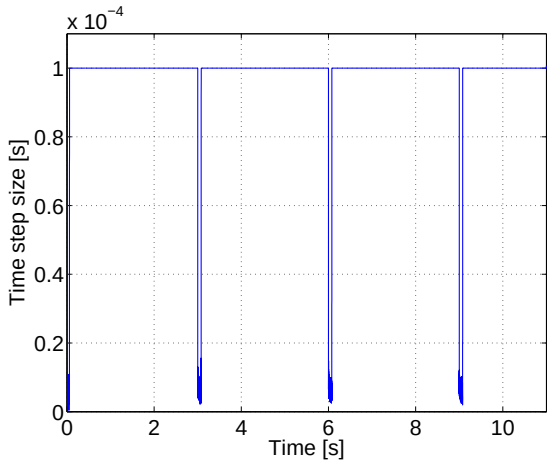

Figure 4.17: The automatic time step algorithm reduces the size of time steps around impact instants.

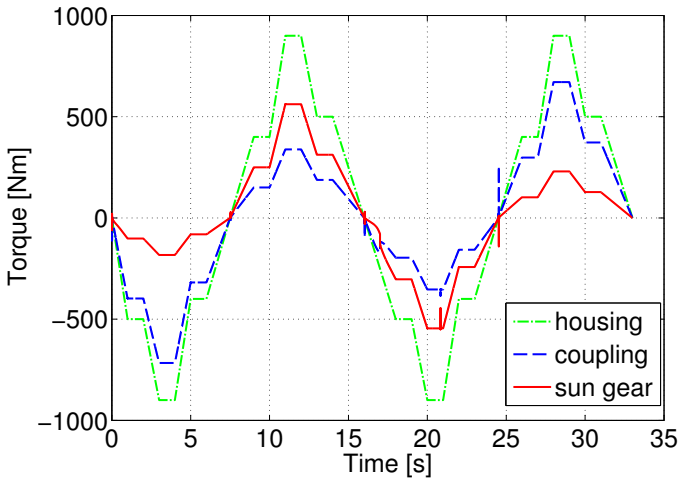

Figure 4.18: Reaction torque on the sun gear and the coupling.

4.5 Cylindrical joint with clearance and friction

As discussed in the state of the art chapter (Section 2.5), there is a need to develop global models of kinematic joints able to simulate the operation defects.

The formulation of a cylindrical joint where the clearance, the misalignment and the friction forces are accounted for is presented in this section. The continuous impact modelling approach is used to determined the magnitude of the contact force between the pin and the internal cylinder, both being represented as rigid bodies. As for the contact element between plane rings (Section 4.3), the new joint has been formulated in the FE context and implemented as a *user element* in SAMCEF/MECANO.

According to the kind of mechanism under study, the contact between the pin and the external surface of the hollow cylinder can occur at one point, at two points or along a line. In this work, in order to simplify the joint formulation, it is assumed that the contact only takes place at the top or at the bottom of the pin. The proposed contact element models the interactions between the cylindrical face of the hollow cylinder and one extremity of the pin. Therefore, the joint needs to be used twice for each pin, one time for each extremity.

The direction of the contact and friction forces depends on the geometry of the pin and the inner cylinder near the contact point and can be hardly determined in case of intricate configurations: sharped edge or small fillet radius on the pin external surface for example. This study does not aim to analyse the detailed phenomena at the contact point but simply to get a global representation of the dynamic behaviour. Therefore, in order to have a simple formulation for this 3D contact element, the top and the bottom of the cylinder are both considered as having a spherical shape (see Fig. 4.19). This assumption seems reasonable in practical situations where the clearance is small and the relative inclination of the pin is limited since the contact point would then remain close to the intersection circle between the sphere and the cylinder. Thus, it would be close to the physical contact point even if the geometry of the cylinder edge is not accurately represented.

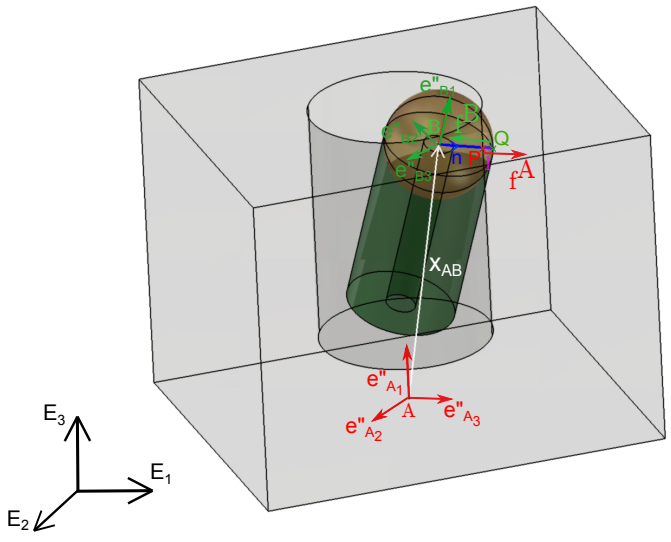

Figure 4.19: Position of reference and contact points as well as orientation of reference vectors used to compute the normal contact force.

The new joint is defined by one physical node attached on each of the two rigid bodies subject to contact. Node A is located on the axis of the hollow cylinder and node B is fixed at the center of the top or bottom circular face of the pin which is also the center of the contact sphere.

A material local frame attached to each body is used in the joint model. The local frames $\{\boldsymbol{e}''_{A_1}, \boldsymbol{e}''_{A_2}, \boldsymbol{e}''_{A_3}\}$ and $\{\boldsymbol{e}''_{B_1}, \boldsymbol{e}''_{B_2}, \boldsymbol{e}''_{B_3}\}$ have their origin at node A of the hollow cylinder and at node B of the pin respectively. The first triad vectors $\boldsymbol{e}''_{A_1}$ and $\boldsymbol{e}''_{B_1}$ are aligned with the axis of the cylinders. The second triad vectors $\boldsymbol{e}''_{A_2}, \boldsymbol{e}''_{B_2}$ are arbitrary oriented in the plane perpendicular to $\boldsymbol{e}''_{A_1}$ and $\boldsymbol{e}''_{B_1}$. The third unit vectors $\boldsymbol{e}''_{A_3}$, $\boldsymbol{e}''_{B_3}$ complete the right-handed reference frame.

The vectors $\boldsymbol{e}_{A_i}$, $\boldsymbol{e}_{B_i}$ represent the orientations of both material frames at the initial configuration. For the sake of simplicity the pin and the hollow cylinder have their axes parallel at the initial time. Therefore, the initial rotation matrix $\boldsymbol{R}_1$ is identical for both bodies.

The points P and Q in Figure 4.19 are the approximated contact points respectively on the rigid bodies A and B due to the geometrical assumptions introduced previously. As it will be shown in section 4.5.1, the position vectors $\boldsymbol{x}_P, \boldsymbol{x}_Q$ of these contact points can be easily computed according to the position vectors $\boldsymbol{x}_A, \boldsymbol{x}_B$ of the nodes A and B, the rotation matrices $\boldsymbol{R}_A, \boldsymbol{R}_1$ and the radii r_A, r_B of the contact surfaces near the contact points. The formulation of the normal contact forces and friction forces is described in Sections 4.5.1 and 4.5.2 as well as their contributions to the motion equations of the multibody system.

In order to determine the contact stiffness, the most accurate approach involves a fully flexible finite element model of the bodies in contact with their actual geometric configuration. The contact stiffness can be obtained by applying a load on one body and using a flexible-flexible contact condition. However, such detailed models can be difficult to elaborate and CPU time expensive. In case of global multibody models, it is preferable to use analytical formulations to compute the contact stiffness. For a sphere in contact with an internal cylinder, approximate expressions are available in the literature. Reference [109] provides a good approximation for the contact stiffness k_p (see Eqs. (4.38-4.41)).

$$k_p = \frac{2\ \pi}{3(\sigma_1 + \sigma_2)} \left(\frac{-\frac{1}{e}\frac{\mathrm{d}E}{\mathrm{d}e}}{A} \right)^{\frac{1}{2}} K^{-\frac{3}{2}} \tag{4.38}$$

The material parameters σ_i are computed from the Young's modulus E_i and the Poisson's ratio ν_i of the bodies materials:

$$\sigma_i = \frac{1 - \nu_i^2}{E_i} \qquad \text{with} \quad i = 1, 2 \tag{4.39}$$

The parameter A is given by the following expression:

$$A = \frac{1}{D_1} - \frac{1}{D_2} \tag{4.40}$$

where D_1 and D_2 are the diameter of the sphere and the cylinder respectively. The empirical parameters $-\frac{1}{e}\frac{\mathrm{d}E}{\mathrm{d}e}$ and K are available in lookup tables [109] and are determined

according to the ratio $\frac{A}{B}$, defined by:

$$\frac{A}{B} = \frac{\frac{1}{D_1} - \frac{1}{D_2}}{\frac{1}{D_1}} \tag{4.41}$$

4.5.1 Normal contact force

The continuous contact force models described in section 4.2 do not involve any kinematic constraint. Therefore the contribution of this force element to the motion equations (Eq. 2.7) of the multibody system consists only of the internal forces, $\boldsymbol{g}^{int}(\boldsymbol{q}, \dot{\boldsymbol{q}})$. The virtual work principle is used in order to formulate the internal force vector of this contact element:

$$\delta \mathcal{W}_n = \delta \boldsymbol{x}_P^T \ \boldsymbol{f}^A + \delta \boldsymbol{x}_Q^T \ \boldsymbol{f}^B \tag{4.42}$$

where $\boldsymbol{x}_P$, $\boldsymbol{x}_Q$ are the position vectors expressed in the absolute frame of the contact point P on the body A and of the contact point Q on the body B (see Figure4.19); $\boldsymbol{f}^A$,$\boldsymbol{f}^B$ are the contact forces applied on bodies A and B respectively.

In order to express the virtual displacements $\delta \boldsymbol{x}_P$ and $\delta \boldsymbol{x}_Q$, the points P and Q are considered as rigidly fixed on the bodies A and B:

$$\delta \boldsymbol{x}_P = \delta \boldsymbol{x}_A + \delta \boldsymbol{\theta}_A \times \boldsymbol{x}_{AP} \tag{4.43}$$

$$\delta \boldsymbol{x}_Q = \delta \boldsymbol{x}_B + \delta \boldsymbol{\theta}_B \times \boldsymbol{x}_{BQ} \tag{4.44}$$

The relation between the variation of the spatial angular vector ($\delta \boldsymbol{\theta}$) and the material angular variation vector ($\delta \boldsymbol{\Theta}$) is provided by the initial rotation matrix ($\boldsymbol{R}_1$) and the rotation operators ($\boldsymbol{R}_A$,$\boldsymbol{R}_B$):

$$\delta \boldsymbol{\theta}_A = \boldsymbol{R}_1 \boldsymbol{R}_A \ \delta \boldsymbol{\Theta}_A \tag{4.45}$$

$$\delta \boldsymbol{\theta}_B = \boldsymbol{R}_1 \boldsymbol{R}_B \ \delta \boldsymbol{\Theta}_B \tag{4.46}$$

The virtual displacement of P and Q can be now reformulated as:

$$\delta \boldsymbol{x}_P = \delta \boldsymbol{x}_A - \widetilde{\boldsymbol{x}}_{AP} \boldsymbol{R}_1 \boldsymbol{R}_A \ \delta \boldsymbol{\Theta}_A \tag{4.47}$$

$$\delta \boldsymbol{x}_Q = \delta \boldsymbol{x}_B - \widetilde{\boldsymbol{x}}_{BQ} \boldsymbol{R}_1 \boldsymbol{R}_B \ \delta \boldsymbol{\Theta}_B \tag{4.48}$$

The unit vector $\boldsymbol{n}$ normal to the collision surface between the sphere and the hollow cylinder and aligned with the vector $\boldsymbol{x}_{PQ}$ of maximal indentation ℓ can be defined as:

$$\boldsymbol{n} = \frac{\left(\boldsymbol{I} - \boldsymbol{e}''_{A_1} \boldsymbol{e}''^{\,T}_{A_1}\right) \boldsymbol{x}_{AB}}{\left\| \left(\boldsymbol{I} - \boldsymbol{e}''_{A_1} \boldsymbol{e}''^{\,T}_{A_1}\right) \boldsymbol{x}_{AB} \right\|} \tag{4.49}$$

where $\boldsymbol{e}''_{A_1}$ is the first axis of the material local frame attached to the node A which represents the cylinder axis (see Eq. 4.20).

The vector $\boldsymbol{x}_{AP}$ and $\boldsymbol{x}_{BQ}$ can be expressed according to the normal vector $\boldsymbol{n}$ and the distance vector $\boldsymbol{x}_{AB}$:

$$\begin{aligned} \boldsymbol{x}_{BQ} &= r_B\ \boldsymbol{n} && (4.50)\\ \boldsymbol{x}_{AP} &= \boldsymbol{x}_{AB} + \boldsymbol{x}_{BQ} + \boldsymbol{x}_{QP} && (4.51)\\ &= \boldsymbol{x}_{AB} + (r_B - \ell)\ \boldsymbol{n} && (4.52) \end{aligned}$$

with r_B the radius of the sphere attached at the top of the pin.

The contact forces $\boldsymbol{f}_A$ and $\boldsymbol{f}_B$ are aligned with the normal direction $\boldsymbol{n}$ and their magnitude f is given by the contact law (Eq. 4.16). The formulation proposed in [37] has been chosen for the definition of the damping parameter c (see Eq. 4.11).

$$\boldsymbol{f} = \boldsymbol{f}^B = -\boldsymbol{f}^A = f\ \boldsymbol{n} \tag{4.53}$$

f depends on the relative normal indentation ℓ and indentation velocity $\dot{\ell}$, which are computed according to the following expressions:

$$\begin{aligned} \ell &= \boldsymbol{x}_{PQ}^T\ \boldsymbol{n} = \boldsymbol{x}_{AB}^T\ \boldsymbol{n} + r_B - r_A && (4.54)\\ \dot{\ell} &= \dot{\boldsymbol{x}}_{PQ}^T\ \boldsymbol{n} + \boldsymbol{x}_{PQ}^T\ \dot{\boldsymbol{n}} && (4.55) \end{aligned}$$

where the second term of $\dot{\ell}$ is always null because $\boldsymbol{x}_{PQ}$ is parallel to $\boldsymbol{n}$ whereas $\dot{\boldsymbol{n}}$ is perpendicular to $\boldsymbol{n}$. The vector $\dot{\boldsymbol{x}}_{PQ}$ can be obtained as the difference of the velocity vectors of P and Q:

$$\begin{aligned} \dot{\boldsymbol{x}}_P &= \dot{\boldsymbol{x}}_A + \boldsymbol{\omega}_A \times \boldsymbol{x}_{AP} && (4.56)\\ \dot{\boldsymbol{x}}_Q &= \dot{\boldsymbol{x}}_B + \boldsymbol{\omega}_B \times \boldsymbol{x}_{BQ} && (4.57) \end{aligned}$$

The spatial angular velocity vectors $\boldsymbol{\omega}$ are related to their material expressions $\boldsymbol{\Omega}$ by:

$$\begin{aligned} \boldsymbol{\omega}_A &= \boldsymbol{R}_1\boldsymbol{R}_A\ \boldsymbol{\Omega}_A && (4.58)\\ \boldsymbol{\omega}_B &= \boldsymbol{R}_1\boldsymbol{R}_B\ \boldsymbol{\Omega}_B && (4.59) \end{aligned}$$

Finally, the virtual work expression (Eq. 4.42) can be reformulated as:

$$\delta\mathcal{W}_n = \left(\delta\boldsymbol{x}_{AB}^T + \delta\boldsymbol{\Theta}_B^T\boldsymbol{R}_B^T\boldsymbol{R}_1^T\ \widetilde{\boldsymbol{x}}_{BQ} - \delta\boldsymbol{\Theta}_A^T\boldsymbol{R}_A^T\boldsymbol{R}_1^T\ \widetilde{\boldsymbol{x}}_{AP}\right)\boldsymbol{f} \tag{4.60}$$

The internal force vector $\boldsymbol{g}_n^{int}$ (Eq. 4.63) of the normal contact force can be easily obtained by identification of the last expression with the classical virtual work expression for a force element:

$$\delta\mathcal{W} = \delta\boldsymbol{q}^T\ \boldsymbol{g}^{int}\left(\boldsymbol{q}, \dot{\boldsymbol{q}}\right) \tag{4.61}$$

$\boldsymbol{q}$ being the vector of generalized coordinates involved in the force element. For the contact model developed here, the vector $\boldsymbol{q}$ includes the absolute nodal degrees of freedom in translation and rotation of the nodes A and B.

$$\boldsymbol{q} = \left\{ \begin{array}{c} \boldsymbol{x}_A \\ \boldsymbol{\Psi}_{A\ inc} \\ \boldsymbol{x}_B \\ \boldsymbol{\Psi}_{B\ inc} \end{array} \right\} \tag{4.62}$$

$$\boldsymbol{g}_n^{int}(\boldsymbol{q},\dot{\boldsymbol{q}}) = f \left\{ \begin{array}{c} -\boldsymbol{n} \\ -\boldsymbol{T}^T(\boldsymbol{\Psi}_{A\ inc})\boldsymbol{R}_A^T\boldsymbol{R}_1^T\widetilde{\boldsymbol{x}}_{AB}\ \boldsymbol{n} \\ \boldsymbol{n} \\ \boldsymbol{0} \end{array} \right\} \tag{4.63}$$

4.5.2 Friction force and torque

The friction forces $\boldsymbol{f}_{fr}^A$ and $\boldsymbol{f}_{fr}^B$ produced by the contact between the bodies A and B are considered as applied on the geometric point M, located at the middle between the points P and Q (Fig. 4.20).

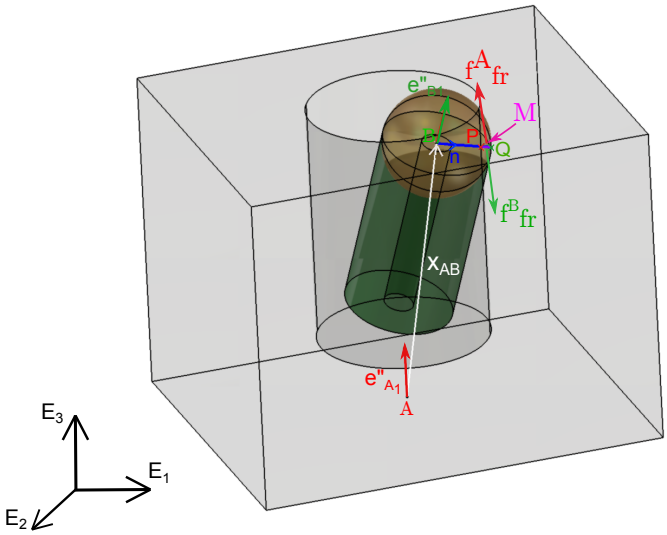

Figure 4.20: Position of the reference and contact points as well as orientation of the reference vectors used to compute the friction force and torque.

The virtual work of the friction forces can be expressed as:

$$\delta\mathcal{W}_{fr} = \delta\boldsymbol{x}_M^{A\,T}\ \boldsymbol{f}_{fr}^A + \delta\boldsymbol{x}_M^{B\,T}\ \boldsymbol{f}_{fr}^B \tag{4.64}$$

where $\delta\boldsymbol{x}_M^A$ is the virtual displacement of the material point located at M and attached to the body A; $\delta\boldsymbol{x}_M^B$ is the virtual displacement of the material point located at M and attached to the body B. By analogy with Eqs. (4.47-4.48), the expression of these virtual displacements can be easily obtained:

$$\delta\boldsymbol{x}_M^A = \delta\boldsymbol{x}_A - \widetilde{\boldsymbol{x}}_{AM}\boldsymbol{R}_1\boldsymbol{R}_A\delta\boldsymbol{\Theta}_A \tag{4.65}$$

$$\delta\boldsymbol{x}_M^B = \delta\boldsymbol{x}_B - \widetilde{\boldsymbol{x}}_{BM}\boldsymbol{R}_1\boldsymbol{R}_B\delta\boldsymbol{\Theta}_B \tag{4.66}$$

The vectors $\boldsymbol{x}_{AM}$ and $\boldsymbol{x}_{BM}$ between the nodes A and B and the application point M

of the friction force can be formulated in terms of $\boldsymbol{x}_{AB}$, $\boldsymbol{n}$, r_B and ℓ

$$\boldsymbol{x}_{AM} = \boldsymbol{x}_{AP} + \frac{\ell}{2}\boldsymbol{n} = \boldsymbol{x}_{AB} + \left(r_B - \frac{\ell}{2}\right)\boldsymbol{n} \tag{4.67}$$

$$\boldsymbol{x}_{BM} = \boldsymbol{x}_{BQ} - \frac{\ell}{2}\boldsymbol{n} = \left(r_B - \frac{\ell}{2}\right)\boldsymbol{n} \tag{4.68}$$

The friction forces are aligned with the tangential vector $\boldsymbol{t}$ but they have opposite directions ($\boldsymbol{f}_{fr} = \boldsymbol{f}^B_{fr} = -\boldsymbol{f}^A_{fr}$) and are defined by:

$$\boldsymbol{f}_{fr} = -\mu_r(v_t)\ f\ \boldsymbol{t} \tag{4.69}$$

where f is the magnitude of the normal contact force (see Eq. 4.16), $\boldsymbol{t}$ is the unit tangential vector described hereafter in Eq. (4.71) and μ_r is the regularized friction coefficient which allows to avoid the large discontinuity when the sign of the relative sliding velocity shifts. Several formulations can be found in the literature for the regularization function and some of them require physical parameters which are quite difficult to determine by numerical simulation or experiment. In this work, a simple quadratic function of v_t, the norm of the tangential velocity vector, is used

$$\mu_r(v_t) = \begin{cases} \mu_{dyn}\left(2\ \dfrac{v_t}{\epsilon_v} - \left(\dfrac{v_t}{\epsilon_v}\right)^2\right) & v_t < \epsilon_v \\ \mu_{dyn} & v_t \geq \epsilon_v \end{cases} \tag{4.70}$$

As depicted in Fig. 4.21, the regularization tolerance ϵ_v corresponds to the magnitude of the tangential velocity where the regularized friction coefficient μ_r reaches the constant dynamic friction coefficient μ_{dyn}. When $\epsilon_v \approx 0$, the regularized friction coefficient tends to the Coulomb model. Therefore, the sticking phenomena are only represented in an approximate way with this continuous definition of the friction coefficient when assuming $\epsilon_v \neq 0$ to avoid discontinuities.

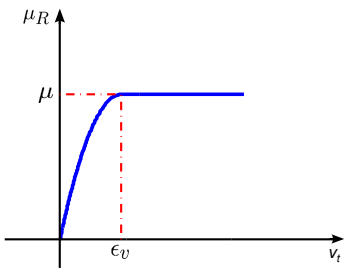

Figure 4.21: Evolution of the regularized friction coefficient according to the tangential velocity.

The unit tangential vector $\boldsymbol{t}$ can be expressed by:

$$\boldsymbol{t} = \frac{\boldsymbol{v}_t}{v_t} \tag{4.71}$$

where $\boldsymbol{v}_t$ is the tangential velocity vector at the point M where the friction forces are applied:

$$\boldsymbol{v}_t = \left(\boldsymbol{I} - \boldsymbol{n}\boldsymbol{n}^T\right)\left(\dot{\boldsymbol{x}}_M^B - \dot{\boldsymbol{x}}_M^A\right) \tag{4.72}$$

$\dot{\boldsymbol{x}}_M^A$ and $\dot{\boldsymbol{x}}_M^B$ are the velocity vectors when the point M is attached to the bodies A and B respectively.

$$\dot{\boldsymbol{x}}_M^A = \dot{\boldsymbol{x}}_A + \boldsymbol{\omega}_A \times \boldsymbol{x}_{AM} \tag{4.73}$$
$$\dot{\boldsymbol{x}}_M^B = \dot{\boldsymbol{x}}_B + \boldsymbol{\omega}_B \times \boldsymbol{x}_{BM} \tag{4.74}$$

The virtual work expression of the friction forces can be reformulated as:

$$\delta\mathcal{W}_{fr} = \left(\delta\boldsymbol{x}_{AB}^T + \delta\boldsymbol{\Theta}_B^T\boldsymbol{R}_B^T\boldsymbol{R}_1^T\ \widetilde{\boldsymbol{x}}_{BM} - \delta\boldsymbol{\Theta}_A^T\boldsymbol{R}_A^T\boldsymbol{R}_1^T\ \widetilde{\boldsymbol{x}}_{AM}\right)\boldsymbol{f}_{fr} \tag{4.75}$$

The identification with the equation (4.61) is straightforward and allows to obtain the vector of internal forces $\boldsymbol{g}_{fr}^{int}$:

$$\boldsymbol{g}_{fr}^{int}(\boldsymbol{q},\dot{\boldsymbol{q}}) = \left\{\begin{array}{c} -\boldsymbol{f}_{fr} \\ -\boldsymbol{T}^T(\boldsymbol{\Psi}_{A\ inc})\boldsymbol{R}_A^T\boldsymbol{R}_1^T\widetilde{\boldsymbol{x}}_{AM}\ \boldsymbol{f}_{fr} \\ \boldsymbol{f}_{fr} \\ \boldsymbol{T}^T(\boldsymbol{\Psi}_{B\ inc})\boldsymbol{R}_B^T\boldsymbol{R}_1^T\widetilde{\boldsymbol{x}}_{BM}\ \boldsymbol{f}_{fr} \end{array}\right\} \tag{4.76}$$

The tangent stiffness and damping matrices have also been computed analytically and are given in Appendix A.2.

4.5.3 Application to the contact between the planet gears and the housing of TORSEN differentials

In this section, the proposed non-ideal cylindrical joint model is used to model the connection between the planet gears and the housing of the type C TORSEN differential. In the former differential model presented in section 3.4.1, this link was represented by a standard idealized hinge joint. This assumption can be now removed thanks to the new cylindrical joint model accounting for the clearance and the friction.

The assembly of the planet gears on the planet carrier is particular in the TORSEN differentials. Indeed, the planet gears are inserted in cylindrical cavities without any physical rotation axis (see Fig. 4.22). The clearance between the crater and the planet gear enables the tilting of the latter, until contact occurs between the top of gear teeth and the crater cylindrical surface. The displacement and the inclination of the planet gears modify the gear mesh properties: the center distance, the pressure angle, the orientation of the wheel axis. The transient behaviour at the switching time between two working modes is also highly influenced by this peculiar assembly.

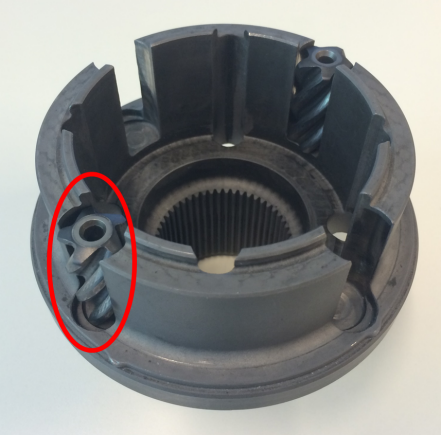

Figure 4.22: The planet gears are inserted inside cavities of the differential housing; there is no physical rotation axis.

Nevertheless, the interactions between the planet gears and the housing play a key role in the differential response since it is through this joint that the driving torque applied on the housing is transferred to the two output driveshafts connected to the sun gear and to the coupling respectively. Moreover, the friction generated in this joint contributes significantly to the locking effect of the differential. From a global point of view, the joint between each planet gear and the housing can be represented by a cylindrical joint where the clearance and the friction are taken into account.

In order to study in a simple way the behaviour of the new cylindrical joint in the configuration of the TORSEN differential, only a reduced part of the differential has been modelled in a first step. As depicted in Figure 4.23, this model includes the sun gear, a single planet gear, the housing and one thrust washer. The housing and the thrust washer are clamped to the ground. The sun gear is linked to the housing with a hinge joint and is submitted to a torque linearly increasing from 0 Nm at $t = 0$ s to 10 Nm at $t = 0.02$ s and staying constant during the period $t = [0.02\text{ s}; 0.04\text{ s}]$ before decreasing following a linear function until -20 Nm in $t = 0.06$ s. Finally, this value is maintained until the end of the simulation in $t = 0.2$ s. The planet gear is meshing with the sun gear and its displacement in the $x - y$ plane is constrained by the new joint developed in this work.

The described element formulation is used twice for each planet gear. The node B (see Figs. 4.19, 4.20) is attached successively to the top and the bottom face center of the planet gear whereas the same node A can be used for both elements and simply has to be located along the axis of the housing crater.

The displacements in the $x-y$ plane of the top and the bottom face centers of the planet gear inside the housing hole are depicted in Fig. 4.24. At the initial time, the planet gear is located at the center of the housing cavity and their axes are parallel.

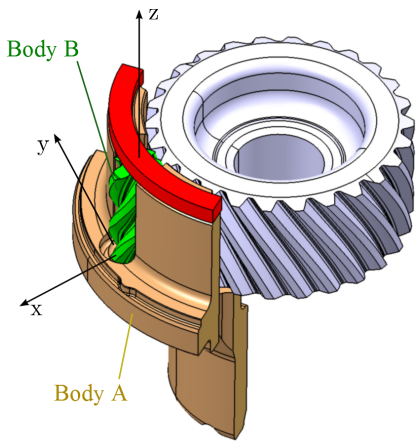

Figure 4.23: Test model for the new cylindric joint in the geometrical configuration of the TORSEN differential.

As soon as a torque is applied on the sun gear, the meshing force tends to increase the center distance of the gear pair and the planet gear is deported against the circular face of the housing cavity. After the first impact, the planet gear undergoes several rebounds and afterwards tends to keep a constant global orientation until the torque applied on the sun gear changes of sign. At this time, the planet gear quickly moves to negative values of y-axis and also tends to maintain a fixed position after the transient period. Due to the helical shape of gear teeth, the planet gear tilts during the transient phases, which explains the small differences of trajectory observed in Fig. 4.24(a) compared with Fig. 4.24(b). When the planet gear position is stabilised, the rotation axis is almost parallel to the fixed axis of the sun gear.

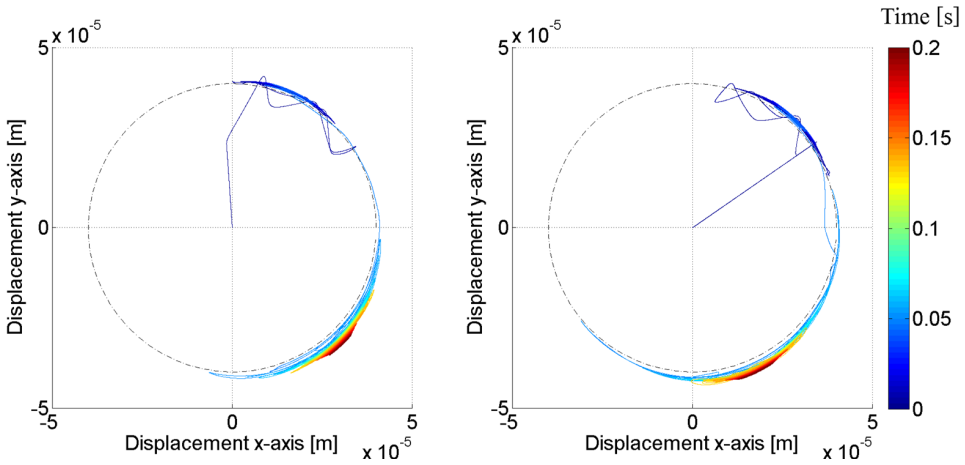

(a) bottom face center (b) top face center

Figure 4.24: Trajectory of the face center relative to the center of the housing cavity.

Figure 4.25 illustrates the kinetic energy dissipation during the first impacts. Indeed, the area covered by each hysteresis loop represents the amount of energy dissipated owing to the damping term used in the contact force law (Eq. 4.16). The areas of these hysteresis loops highly depend on the choice of the restitution coefficient and the contact stiffness. In this example, this coefficient has been fixed to 0.8, a frequently used value for contacts between two metallic bodies. The contact stiffness is determined according to Eq. 4.38 and amounts to $k_p = 5.77\ 10^{10}$ N/m.

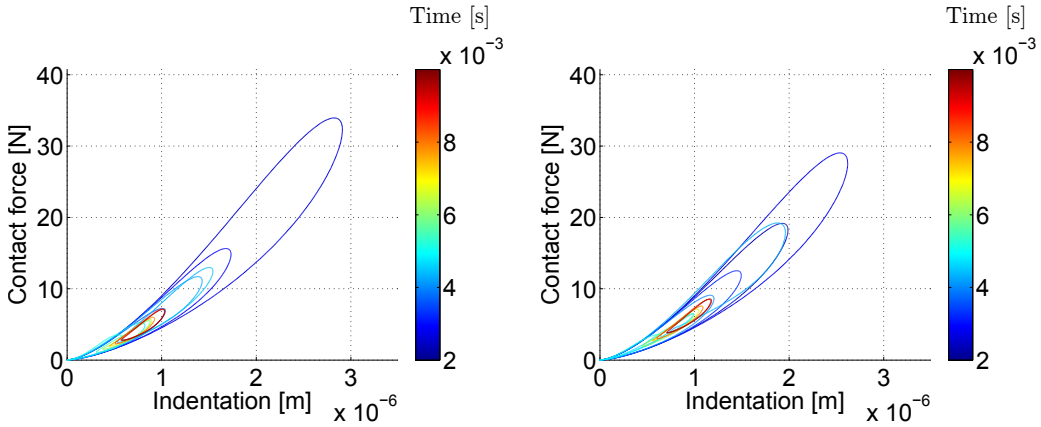

(a) planet gear bottom (b) planet gear top

Figure 4.25: Hysteresis loops of the contact force illustrating the energy dissipation for the first impacts.

Since the benchmark model has shown the ability of the new cylindrical joint formulation to model the interaction between the planet gears and the housing, the full type C TORSEN differential has been modelled. For this simulation the same configuration as in experimental settings on a test rig has been reproduced (see Section 3.4.1). Let us recall that for these experimental tests, a torque is progressively applied on one output shaft (Fig. 4.26(a)) whereas the rotation speed is prescribed on the second output shaft (Fig. 4.26(b)) and the housing is clamped on the test bench.

Figure 4.27(a) depicts the resistant torque which allows to limit the angular velocity of the sun gear while a torque is applied on the coupling. The limited slip behaviour of the differential for both operation modes with torque biaising to the rear axle can be observed on this figure. Indeed, the resistant torque is much smaller than the input torque multiplied by the tooth number ratio between the sun gear and the coupling. This difference is due to the friction inside the differential. The friction between the planet gears and the housing is one of the major contributions to the total friction torque. As described in section 3.1, the torque distribution differs for each locking mode and can be computed from this torque curve.

A detailed view at the beginning of the simulation is given in Fig. 4.28 and enables to analyze the transient motion at switching between operation modes of the differential.

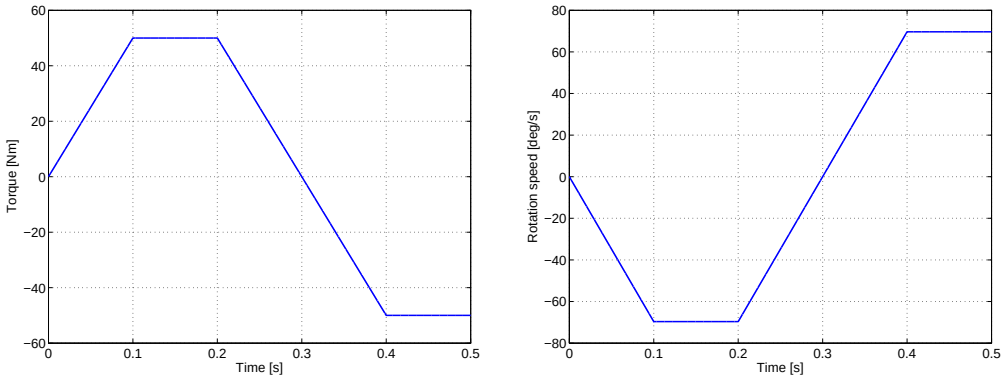

(a) output shaft #1 (b) output shaft #2

Figure 4.26: Load cases for the type C TOSREN differential in the test bench configuration.

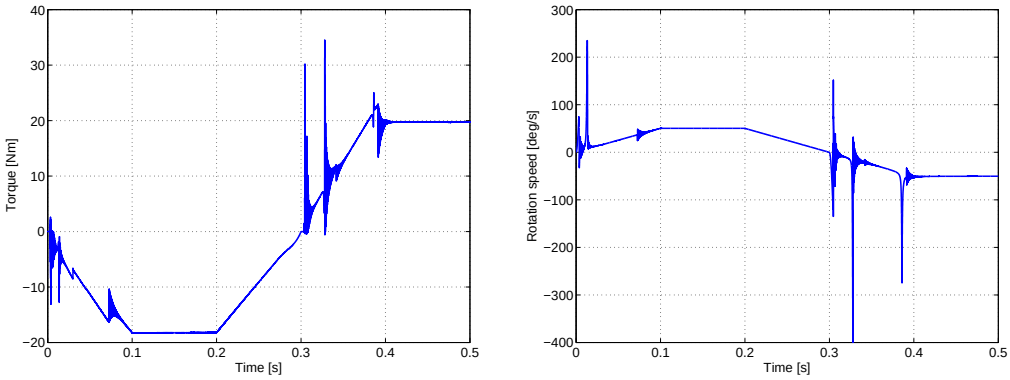

(a) sun gear (b) coupling

Figure 4.27: Operation modes of the type C TORSEN with torque biaising to the rear axle.

In the initial configuration ($t = 0$ s), the different bodies are not in contact and then no friction occurs which explains the null value of the resistant torque during the first time steps ($t < 3\ 10^{-3}$ s). The first spikes on the torque curve are caused by the shocks when the planet gears collide with the housing. The oscillations are quickly damped thanks to the energy dissipation introduced by the restitution coefficient.

The discontinuities observed during the second part of the simulation ($t > 0.025$ s) are due to the contact establishment between the gear wheels and the thrust washers. The contact between the sun gear and the thrust washer #7 is at the origin of the jump at $t = 0.03$ s. The friction inherent to the contact between the internal gear and the thrust washer #11 modifies the friction torques in the differential as soon as this unilateral contact is active and explains the step on the curve at $t = 0.07$ s.

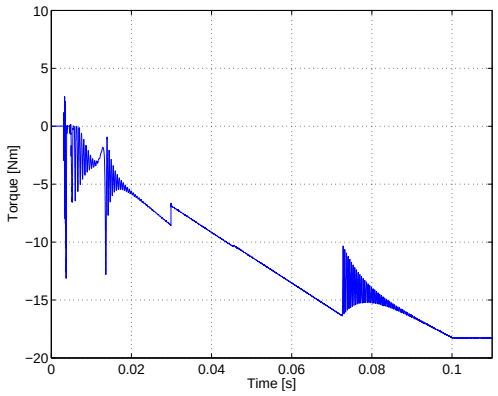

Figure 4.28: The spikes on the output torque are due to the transient behaviour when bodies enter in contact at an operation mode switching.

The displacements of the top and bottom face centers of the four planet gears in the plane perpendicular to the axis of housing cavities is depicted in figure 4.29. As for the benchmark model, in the initial configuration, the planet gears are located at the middle of the housing cavities and their respective symmetry axes are coinciding. It is the reason why all the trajectories of displacements start from the origin in the $x - y$ plane. For each operation mode, the motion to reach the steady-state position of the planet gears corresponds to a displacement in the tangential direction given by the sign of the input torque. During the transient phase before reaching this position, the planet gears tilt and undergo several rebounds due to impact against the housing cavities.

The differential model including the non-ideal cylindric joints can capture the local effects which influence the dynamics of the whole transmission device, especially during the transient periods at the switching time between two working modes. The modelling of the other drivetrain components could be considered to study the propagation of the vibrations generated by the contact between the planet gears and the housing and assess its effect on the driveline dynamic behaviour.

Nevertheless, the main drawback of the proposed joint model lies in the need to use very small time steps to ensure the numerical convergence. For the simulation presented in this section, the time step size had to be decreased up to $2\ 10^{-6}$ s during the almost entire simulation. The automatic time step algorithm can rarely increase the time step size.

Therefore, the computational time is very high so that it cannot be afforded to account for these local effects between the planet gears and the housing in case of global MBS models where the differential is embedded in a full vehicle model submitted to manoeuvres (see Section 5.5). For example, the CPU time amounts to 4 hours for 0.5 s of simulation (see Fig. 4.26) although the model size is still reasonable since the number

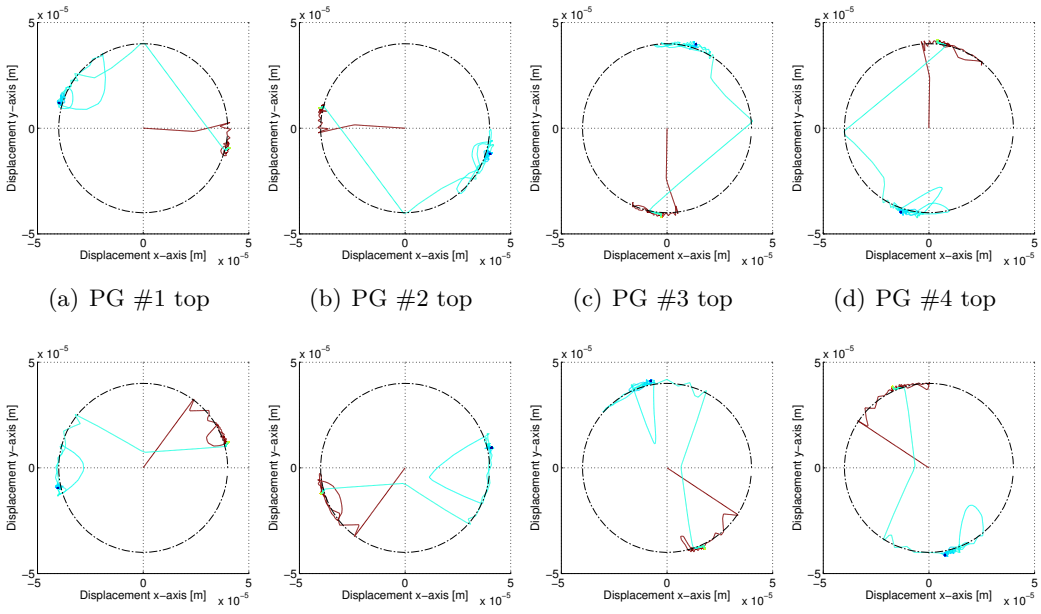

(a) PG #1 top (b) PG #2 top (c) PG #3 top (d) PG #4 top

(e) PG #1 bottom (f) PG #2 bottom (g) PG #3 bottom (h) PG #4 bottom

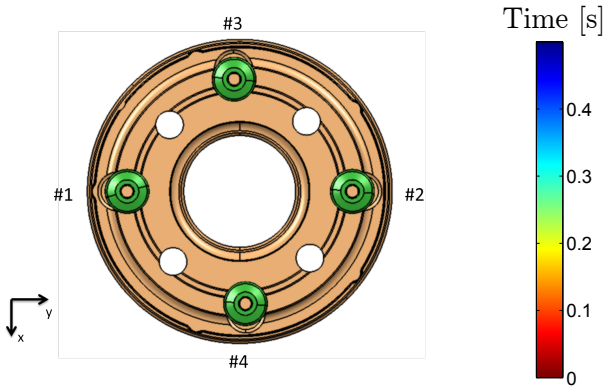

(i) ID number of the four planet gears and reference axis

Figure 4.29: Trajectory in the $x - y$ plane of the four planet gears of the type C TORSEN differential.

of DOFs is 776. In comparison, the same MBS modelled with classic hinge joints to represent the connection between the planet gear and the housing allows to reduce the CPU time by a factor of 300.

Owing to its computational cost, the proposed cylindrical joint model based on a contact modelling will be not employed in the global differential models presented in the following of this dissertation (Sections 5.4, 5.5). Besides, the global operation of the TORSEN differential is still accurately represented with standard hinge joints (see the good correlation of TDR values in Table 3.5).

Finally, let us mention that a parametric study should be performed in order to determine the value of the friction coefficient which allows the best fitting of the TDR with the experimental data of the four working modes. The procedure should be the same as the one described in Section 3.4.1 (see Figs. 3.26) but will be not reproduced here since the cylindrical joint with clearance and friction will be not used in the sequel. The results presented hereabove have been obtained with a friction coefficient equal to 0.1, which is the same value used to model the contacts with the thrust washers.

4.6 Concluding remarks

In this chapter, it has been shown that the continuous impact modelling method is suitable to model rigid/rigid contact conditions in global models of automotive transmission components. The contact stiffness and the restitution coefficient are the only two parameters of this contact model. The formulation leads to a simple implementation and is robust in presence of impact. The dynamic responses considered here are characterized by a very short duration, a huge force and acceleration magnitude, a rapid energy dissipation leading to a highly nonlinear behaviour.

The simulation of the bouncing ball benchmark has been performed in order to assess the sensitivity of the dynamic response according to the values of the restitution coefficient, the contact stiffness, the time step size and the spectral radius of the integrator. From this detailed analysis, we conclude that a sufficient number of time steps (> 10) are needed during the indentation phase to ensure a correct prediction of the energy dissipation. The convergence to a fixed contact duration has been verified when decreasing the time step size. It can also be observed that owing to the assumptions adopted in main continuous contact laws, the restitution coefficient given as parameter of the contact force expression is not exactly corroborated in the numerical response especially for low values of the restitution coefficients. The elastic contact law proposed by Flores and Machado [37] only slightly underestimates the restitution coefficient for the whole range ($0 < e < 1$). It is the reason why the latter law is used in the various models presented in this chapter.

A kinematic description for the contact between two rigid bodies, each one represented by a unique finite element node, has been developed for two specific geometric configurations. The first one addresses the contact between two planar rings and is used to model the contact between the thrust washers and the lateral faces of gear wheels included in the type C TORSEN differential. The numerical results prove the ability of the contact formulation to simulate impacts and allow to divide by 50 the computational time compared to the model based on a rigid/flexible contact formulation presented in Chapter 3.

The second kinematic formulation is dedicated to the contact between the pin and the hollow cylinder of a cylindrical joint. This general approach enables to account

for the clearance, the tilting and the friction forces in a natural way. The assembly of planet gears on the TORSEN differential housing has been represented using this joint model in order to replace the idealized hinge joints used in the former differential model. The transient displacements of planet gears inside their housing holes can be observed at switching between operating modes. Nevertheless, the proposed joint formulation requires small time steps to ensure the numerical convergence. Therefore, the consideration of these local effects can not be achieved for global vehicle models with reasonable computer effort.

Besides the modelling of TORSEN differentials, the contact formulations proposed in this chapter could be easily extended to model the contact between plates in clutches or between synchronization devices in gear boxes.

Chapter 5

Contact modelling with squeeze film

Contents

The presence of lubricant inside drivetrain components influences the contact properties in a non negligible way. The dynamic response of unilateral contacts is modified in both normal and tangential directions.

This chapter presents a simple squeeze film model allowing to model the damping effect due to the lubricating film when two rigid bodies are approaching. The proposed model has a very compact formulation (Section 5.2) thanks to a set of geometrical assumptions. The relevance of the model is demonstrated with the modelling of the lubricated contacts between the gear wheels and the thrust washers of TORSEN differentials. In a first step, a detailled study of the type C TORSEN differential is presented in Section 5.4. Then, the dynamics of three global vehicle models are simulated together with the differential model including the developed combined squeeze film contact model (Section 5.5).

5.1 Introduction

In order to have a proper operation of many transmission devices, a lubrication is often required. The oil film enables to evacuate fragments of materials and the heat generated by friction. Wear is greatly reduced when mechanisms are adequaly lubricated. Therefore, the contact properties are significantly influenced by the presence of the lubricant. For instance, the film of lubricating oil between mechanical parts plays the role of a damper and tends to slow down the contacting bodies before the contact establishment. Therefore, the impact phenomenon is reduced since the relative velocity is lower at the impact time.

The rigid/flexible unilateral contact element described in section 3.3 and used to model the TORSEN differentials (see Section 3.4) is based on a linear damping contribution in its contact law (Eq. 3.26) to manage the discontinuities induced by the impact. The damping coefficient is a constant parameter whatever be the magnitude of the impact.

The rigid/rigid contact force formulation proposed by Hunt and Crossley (Eq. 4.8) and its derived contact laws introduce a damping term depending on the indentation velocity but also on the penetration length in a nonlinear way. The damping coefficient is function of the contact stiffness, the relative impact velocity and a coefficient of restitution. Consequently, the damping coefficient is different for each impact. However, as discussed in Section 4.2, the choice of the restitution coefficient is not trivial, specially when the contact is lubricated.

This section shows that a model of oil film between contacting bodies leads to a physical definition of the damping behaviour before the effective contact between bodies. A simple squeeze film model is proposed and has been implemented in the *user element* framework of SAMCEF/MECANO. Our objective is to model at a macroscopic level the damping due to the squeeze film between two axisymmetric surfaces under several assumptions, but not to represent detailed and localized tribology effects.

5.2 Squeeze film formulation

The squeeze film model presented here is based on the Poiseuille flow assumption [145] and has been particularized to two simple geometric configurations: the squeeze film between discs and the squeeze film between the planar faces of two superimposed rings. Therefore, several **assumptions** are made:

- the fluid is Newtonian and incompressible;

- the fluid is isothermal in steady state;

- the surfaces are plane and parallel with an axisymmetric geometry (2 discs or 2 rings);
- the film thickness h_{sf} is much smaller than the external radius of the plate walls;
- the flow is laminar and parallel to the plates; there is no sliding on walls;
- the pressure is constant in the normal direction to the walls.

This system can be considered as a quasi-steady problem since the squeeze film is considered at equilibrium for any value of the film thickness.

In order to formulate the squeeze film model, we start from the **Navier-Stokes** equation which represents the **conservation of momentum** in incompressible flow of Newtonian fluids:

$$\rho\left(\frac{\partial \boldsymbol{v}}{\partial t} + (\boldsymbol{v} \cdot \boldsymbol{\nabla})\, \boldsymbol{v}\right) = -\boldsymbol{\nabla} p + \mu_{vis}\boldsymbol{\nabla}^2\boldsymbol{v} + \rho\, \boldsymbol{f}_d \tag{5.1}$$

with:

ρ the mass density;

$\boldsymbol{v}$ the velocity vector of fluid flow;

t the time;

$\boldsymbol{\nabla}$ the nabla operator;

p the fluid pressure;

μ_{vis} the dynamic viscosity;

$\boldsymbol{f}_d$ the vector of forces per volume unit acting on the fluid.

Since the system is axisymmetric, the model will be expressed using cylindrical coordinates. The radial component of the Navier-Stokes equation 5.1 takes the form:

$$\begin{aligned}\rho\,&\left(\frac{\partial v_r}{\partial t} + v_r\frac{\partial v_r}{\partial r} + \frac{v_\phi}{r}\frac{\partial v_r}{\partial \phi} + v_z\frac{\partial v_r}{\partial z} - \frac{v_\phi^2}{r}\right)\\ &= -\frac{\partial p}{\partial r} + \mu_{vis}\left[\frac{1}{r}\frac{\partial}{\partial r}\left(r\frac{\partial v_r}{\partial r}\right) + \frac{1}{r^2}\frac{\partial^2 v_r}{\partial \phi^2} + \frac{\partial^2 v_r}{\partial z^2} - \frac{v_r}{r^2} - \frac{2}{r^2}\frac{\partial v_\phi}{\partial \phi}\right] + \rho g_r\end{aligned} \tag{5.2}$$

This last expression can be reduced to Eq. 5.3 owing to the simplification hypothesis introduced and if $\frac{v_r}{r^2}$ is considered negligible compared with $\frac{\partial^2 v_r}{\partial z^2}$.

$$\frac{\partial p}{\partial r} = \mu_{vis}\frac{\partial^2 v_r}{\partial z^2} \tag{5.3}$$

The second principle at the basis of the squeeze film model is the conservation of mass expressed by the **continuity equation**:

$$\boldsymbol{\nabla} \cdot \boldsymbol{v} = 0 \tag{5.4}$$

In cylindrical coordinates, the continuity equation is formulated as:

$$\frac{1}{r}\frac{\partial}{\partial r}(r\ v_r) + \frac{\partial v_z}{\partial z} = 0 \tag{5.5}$$

5.2.1 Squeeze film between discs

The simplified Navier-Stokes equation 5.3 and the continuity equation 5.5 will be combined and integrated with the boundary conditions in agreement with the geometric configuration where the walls of the lubricating film are perfect discs (see Fig. 5.1).

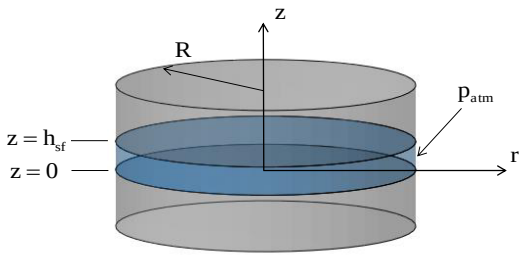

Figure 5.1: Squeeze film between two metallic plates.

After double time integration in the axial direction (z-axis), Equation 5.3 of the conservation of momentum becomes:

$$\frac{\partial p}{\partial r}\frac{z^2}{2} = \mu_{vis}\ v_r + C_1\ z + C_2 \tag{5.6}$$

The constants of integration C_1 and C_2 are computed by means of the boundary conditions representing the no sliding condition at the walls, i.e. $v_r = 0$ in $z = 0$ or $z = h_{sf}$:

$$C_1 = \frac{\partial p}{\partial r}\ \frac{h_{sf}}{2} \tag{5.7}$$

$$C_2 = 0 \tag{5.8}$$

The velocity at a given radial position r has a parabolic profile in the longitudinal direction z and has a sign opposite to the pressure gradient $\delta p/\delta r$:

$$v_r = -\frac{1}{2\mu_{vis}}\frac{\partial p}{\partial r}\left(h_{sf}\ z - z^2\right) \tag{5.9}$$

The continuity equation is integrated over the volume filled by the fluid. To this end, after having replaced the velocity profile by its expression 5.9, the integration of Equation 5.5 is achieved in the longitudinal direction between $z = 0$ and $z = h_{sf}$

$$- \frac{\partial}{\partial r}\left(r\frac{1}{2\mu_{vis}}\frac{\partial p}{\partial r}\right)\ \frac{h_{sf}^3}{6} + r\dot{h}_{sf} = 0 \tag{5.10}$$

Then, this last expression is integrated in the radial direction:

$$- r\frac{1}{2\mu_{vis}}\frac{\partial p}{\partial r}\frac{h_{sf}^3}{6} + \frac{r^2}{2}\dot{h}_{sf} + C_3 = 0 \tag{5.11}$$

where the integration constant $C_3 = 0$ if we considered the boundary condition in $r = 0$. Now, the pressure gradient can be expressed as:

$$\frac{\partial p}{\partial r} = 6\mu_{vis}\frac{\dot{h}_{sf}}{h_{sf}^3}\ r \tag{5.12}$$

Performing integration along the radial direction enables to compute the pressure at a given radial distance r from the revolution axis

$$p(r) = p_{atm}\ + 6\mu_{vis}\frac{\dot{h}_{sf}}{h_{sf}^3}\left(\frac{r^2}{2} - \frac{R^2}{2}\right) \tag{5.13}$$

where the boundary condition at the external radius of the disc ($r = R$) considered that the fluid pressure is equal to the atmospheric pressure, $p(R) = p_{atm}$.

The global force applied on each disc is obtained after integration of the pressure over the disc area:

$$f_{di} = \int_0^R 6\mu_{vis}\frac{\dot{h}_{sf}}{h_{sf}^3}\ \left(\frac{r^2}{2} - \frac{R^2}{2}\right)\ 2\pi r\ \mathrm{d}r = -\frac{3}{2}\pi\mu_{vis}R^4\ \frac{\dot{h}_{sf}}{h_{sf}^3} \tag{5.14}$$

5.2.2 Squeeze film between rings

If the walls of the squeeze film have a planar ring geometry rather than a disc shape, a similar mathematical development has to be carried out to find the force applied on the walls. The first part from Eq. 5.6 to Eq. 5.11 is still valid, the change starts with the definition of the integration constant C_3 since the boundary conditions has be modified from $r = 0$ to $r = R_{int}$:

$$C_3 = R_{int}\frac{1}{2\mu_{vis}}\ \frac{\partial p}{\partial r}\bigg|_{r=R_{int}}\ \frac{h_{sf}^3}{6} - \frac{R_{int}^2}{2}\ \dot{h}_{sf} \tag{5.15}$$

Therefore, the pressure gradient is restated as:

$$\frac{\partial p}{\partial r} = \frac{1}{r}\left[6\mu_{vis}\frac{\dot{h}_{sf}}{h_{sf}^3}\left(r^2 - R_{int}^2\right) + R_{int}\ \frac{\partial p}{\partial r}\bigg|_{r=R_{int}}\right] \tag{5.16}$$

In order to compute the pressure in function of the radius r, the pressure gradient is integrated, what gives:

$$p(r) = 6\mu_{vis}\frac{\dot{h}_{sf}}{h_{sf}^3}\left(\frac{r^2}{2} - R_{int}^2 \ln r\right) + R_{int}\left.\frac{\partial p}{\partial r}\right|_{r=R_{int}} \ln r + C_4 \tag{5.17}$$

The constant C_4 is determined according to the boundary condition in $r = R_{int}$ where it is assumed that $p(R_{int}) = p_{atm}$:

$$C_4 = p_{atm} - 6\mu_{vis}\frac{\dot{h}_{sf}}{h_{sf}^3}\left(\frac{R_{int}^2}{2} - R_{int}^2 \ln R_{int}\right) - R_{int}\left.\frac{\partial p}{\partial r}\right|_{r=R_{int}} \ln R_{int} \tag{5.18}$$

In order to compute the total force applied on the rings, the pressure gradient in $r = R_{int}$ has first to be determined. That is easily achieved thanks to Equation 5.17 where it is also assumed that $p(R_{ext}) = p_{atm}$:

$$\left.\frac{\partial p}{\partial r}\right|_{r=R_{int}} = 6\mu_{vis}\frac{\dot{h}_{sf}}{h_{sf}^3}\left(R_{int} - \frac{R_{ext}^2 - R_{int}^2}{2R_{int}\ln\frac{R_{ext}}{R_{int}}}\right) \tag{5.19}$$

Finally, the global force applied by the squeeze film on the two rings results from the integration of the fluid pressure over the ring area S:

$$\begin{aligned} f_{ri} &= \iint_S p(r) - p_{atm}\ \mathrm{d}S \qquad (5.20)\\ &= \int_{R_{int}}^{R_{ext}} 6\mu_{vis}\frac{\dot{h}_{sf}}{h_{sf}^3}\left(\frac{r^2}{2} - R_{int}^2\ln r\right) + R_{int}\left.\frac{\partial p}{\partial r}\right|_{r=R_{int}} \ln r + C_4 - p_{atm}\ 2\pi r\ \mathrm{d}r \end{aligned}$$

In summary, the force applied on the two plates can be reduced to the following expression:

$$f_{sf}(h_{sf}, \dot{h}_{sf}) = -A^*\ \frac{\dot{h}_{sf}}{h_{sf}^3} \tag{5.21}$$

with:

$$A^* = \begin{cases} \frac{3}{2}\pi\mu_{vis}R^4 & \text{for the squeeze film between two discs} \\ \\ \frac{3}{2}\pi\mu_{vis}R_{ri}^4 & \text{for the squeeze film between two rings} \end{cases} \tag{5.22}$$

The constant R_{ri} is introduced to have analogous expressions for the two types of plates and can be interpreted as the equivalent radius of the ring to produce the same effect as a plate with a disc shape.

$$R_{ri} = \left(\left(R_{int}^2 - R_{ext}^2\right)\left(\frac{R_{ext}^2 - R_{int}^2}{\ln\frac{R_{ext}}{R_{int}}} - 2R_{ext}^2\right) - \left(R_{ext}^2 - R_{int}^2\right)^2\right)^{\frac{1}{4}} \tag{5.23}$$

Expression 5.21 enables to conclude that the developed squeeze film model represents the behaviour of a nonlinear damper ($f_{sf} = 0$ when $\dot{h}_{sf} = 0$). Nevertheless, this model presents a tangent stiffness when $\dot{h}_{sf} \neq 0$.

5.2.3 Test example

In this section, the time response of the squeeze film model will be determined if a constant force F is applied on the plates by the mechanical parts connected to them and tends to put closer the two plates.

From Equation 5.21, it can be easily deduced that:

$$\frac{F}{A^*}\,\mathrm{d}t \;=\; -\frac{1}{h_{sf}^3}\,\mathrm{d}h_{sf} \tag{5.24}$$

After a time integration, we get:

$$\frac{F}{A^*}\,t = \frac{1}{2h_{sf}^2} - \frac{1}{2h_0^2} \tag{5.25}$$

where h_0 is the film thickness at the initial time $t = 0$ s.

Finally, the film thickness at each time instant t can then be expressed by Eq. 5.26 where it can be noticed that the film thickness evolves inversely proportional to the square root of time.

$$h_{sf}(t) = \frac{h_0}{\sqrt{1 + \frac{2h_0^2 F}{A^*}\,t}} \tag{5.26}$$

5.2.4 Resisting viscous torque

The viscosity of the lubricating oil tends also to act against the relative rotation between the two plates. This viscous resistance is introduced in the model by means of a torque along the z-axis:

$$T_{vis} = \int_S \frac{\mu_{vis}\;\omega\;r^2}{h_{sf}}\,\mathrm{d}S = 2\pi\;\frac{\mu_{vis}\;\omega}{h_{sf}}\;\frac{R_{ext}^4 - R_{int}^4}{4} \tag{5.27}$$

where ω is the relative rotation velocity in the longitudinal direction.

5.2.5 Influence of the wall asperities

As demonstrated in Eq. 5.26, the squeeze film tends to reach a null thickness $h_{sf} \approx 0$ if a constant force is applied during a sufficient time period. However, if at a given instant the mechanical system in which the plates are included tries to separate the two plates, the squeeze film model acts as an adhesive and prevents the split motion. If the film thickness is very small, the predicted sticking effect is too large and is not physically realistic. Indeed, in reality the roughness on the plate surface is such that the lubricating film thickness can never decrease below a limit value because contacts appear between plates asperities (see Fig. 5.2).

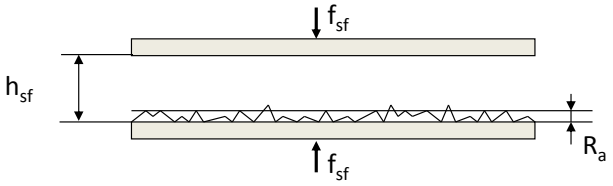

Figure 5.2: The rugosity of the plates limits the thickness to a minimal value.

Therefore, when the film thickness becomes lower than the arithmetic roughness R_a, the contact force between the rigid walls is added to the squeeze film model. This very simple contact model simply consists in a linear penalty method, where k_p is the global contact stiffness of the two plates.

$$f_{sf+con}(h_{sf}, \dot{h}_{sf}) = \begin{cases} -A^* \ \frac{\dot{h}_{sf}}{h_{sf}^3} & \text{if} \quad h_{sf} > R_a \\ \\ -A^* \ \frac{\dot{h}_{sf}}{h_{sf}^3} + k_p \ (h_{sf} - R_a) & \text{if} \quad h_{sf} < R_a \end{cases} \tag{5.28}$$

Moreover, the additional contact force allows to avoid the ill conditioning of the squeeze film model, when h_{sf} and $\dot{h}_{sf}$ are simultaneously close to zero.

The `friction` involved by the contact between the two plates is taken into account in the model through a friction torque in the longitudinal direction z:

$$T_{fr} = \begin{cases} 0 & \text{if} \quad h_{sf} > R_a \\ \\ \displaystyle\int_S \mu_R \ \frac{k_p(h_{sf} - R_a)}{S} \ r \ \mathrm{d}S = 2\pi \ \mu_R \ \frac{k_p(h_{sf} - R_a)}{S} \ \frac{R_{ext}^3 - R_{int}^3}{3} & \text{if} \quad h_{sf} < R_a \end{cases} \tag{5.29}$$

with μ_R the regularized friction coefficient (see Eq. 4.70) and $R_{int} = 0$ in case of contact between two perfects discs.

The total torque applied on the two plates by both viscous and friction contributions can be summarized as:

$$T_{fr+vis}(h_{sf}, \omega) = \begin{cases} T_{vis} & \text{if} \quad h_{sf} > R_a \\ \\ T_{vis} + 2\pi \ \mu_R \ \frac{k_p(h_{sf} - R_a)}{S} \ \frac{R_{ext}^3 - R_{int}^3}{3} & \text{if} \quad h_{sf} < R_a \end{cases} \tag{5.30}$$

5.3 Implementation in a FE context

In order to include the proposed squeeze film model within a dynamic multibody system formulated with finite element coordinates, the same kinematic description developed

for the rigid contact model in section 4.3.1 can be used (see Fig. 4.12). The element is defined with twelve generalized coordinates representing the DOFs in translation and rotation of the two nodes between which is squeeze film is formulated (Eq. 4.24).

In the local frame attached to node A, the forces (Eq. 4.30) applied between the two plates are expressed as:

$$\boldsymbol{f}_t = \begin{Bmatrix} f_{sf} + f_{con} \\ 0 \\ 0 \end{Bmatrix} \quad , \quad \boldsymbol{f}_r = \begin{Bmatrix} T_{vis} + T_{fr} \\ 0 \\ 0 \end{Bmatrix} \tag{5.31}$$

5.4 Application to the contact between gear wheels and thrust washers of TORSEN differentials

The TORSEN differentials are usually located inside the casing of the gear box. The holes drilled in the housing and the case of the differential (see Figs. 5.3) enable the flow of the lubricating oil through the differential.

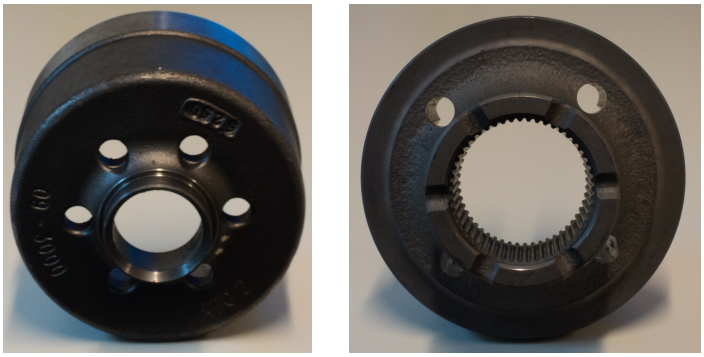

(a) case (b) housing

Figure 5.3: Bores in the housing and the case of the differential for the flow of the lubricating oil.

The gap between the gear wheels and the thrust washers are then filled by the lubricant that influences significantly the properties and the dynamic response of the various contacts. For instance, the relative velocity when the two bodies enter in contact is highly reduced since the film of lubricant acts as a damper, hence the impacts are moderated or even avoided. Likewise, the value of 0.1 used for the friction coefficient (see Table 3.6) between these two parts is a common value for a lubricated contact between metallic bodies made of basic steel.

The geometric configuration of the space between the lateral face of the gear wheels and the thrust washers as well as the properties of the lubricating oil satisfy the assumptions introduced in the proposed squeeze film model detailed in Section 5.2. Indeed,

the contacting surfaces are plane rings which remain parallel during the operation of the differential. The gap between the two bodies is very narrow (≈ 0.1 mm) and then much smaller than the radius of film walls. The supports of the squeeze film are only loaded in the normal direction to the walls: the gear wheel is either approaching or separating from the thrust washer according to the active operation mode. Consequently, the squeeze film hypothesis is valid.

The model construction of the type C TORSEN differential is similar to what has been described in section 3.4.1, except that the axial locking of the planet gears and of the thrust washer #9 are replaced by a contact condition based on the squeeze film model. Indeed, the squeeze film formulation (Eq. 5.28) enables to smooth the discontinuities induced by unilateral contacts and then the number of contact conditions included in the MBS model can be enlarged without degrading the convergence properties.

Due to the fact that the new cylindrical joint with clearance and friction developed in Section 4.5 necessitates a very small time step size, this joint is not used here. Moreover, the objective of the model presented in this section is not to study the local behaviour of the planet gears but rather to have a reliable, computationally efficient and robust representation of the differential with the aim to include this transmission device in a full vehicle model (Section 5.5).

The four planet gears are now connected to the housing by a combination of a hinge and a prismatic joint. Like the sun gear, the coupling and the internal gear, the planet gears move quickly in the axial direction as soon as the differential switches of working mode. These axial displacements are limited by contacts against either the housing or the thrust washer #9 (see Fig. 3.6). The contacts have the same geometric configuration as the previous ones, hence they are also modelled by the squeeze film model combined with the penalty method (Eq. 5.28).

The complete type C TORSEN differential model includes 14 unilateral contact conditions based on the squeeze film model whose parameters are given in Table 5.1. Eight gear pair elements (Section 3.2) are needed to represented the epicyclic gear train. In addition to the six idealized hinge joints, there are also one screw joint and seven prismatic joints. The seventh prismatic joint constrains the displacement of the thrust washer #9 with respect to the housing. The total number of generalized coordinates amounts to 878 which is close to the DOF number of the model presented in Section 4.4.1 but much smaller than the former model detailed in Section 3.4.1 with FEM representation of the thrust washers.

The behaviour of the differential in a vehicle is reproduced by applying a torque on the housing while the rotation speeds of the two differential outputs (sun gear and coupling) are prescribed (see Fig. 5.9 for the time evolution given to these three quantities). With this set of load cases, the drive to rear mode is active at the beginning of the simulation, the coast to front and drive to front modes are observed during the

Dynamic viscosity μ_{vis} [Pl]	0.0741
Friction coefficient μ [-]	0.1 / 0.03
Friction regularization tolerance ϵ_v [m/s]	0.01
Contact stiffness k_p [N/m]	10^{14}
Arithmetic roughness R_a [m]	$1.6\ 10^{-6}$ / $0.5\ 10^{-6}$

Table 5.1: Parameters of the contact model based on the squeeze film used in the type C TORSEN differential.

periods $t = [4; 8]$ s and $t = [8; 12]$ s respectively and the coast to rear mode at the end of the simulation.

Figure 5.4 shows the displacements in the axial direction of the gear wheels and the thrust washer #9 inside the differential. Each working mode corresponds to a different configuration of this set of bodies. The sun gear and the coupling are always pressed together whereas the internal gear moves in the opposite direction. The four planet gears go down and enter in contact with the housing for the two first modes. As soon as the third mode (drive to front) is activated, the planet gears go up and enter in contact with the thrust washer #9. After a short time, the axial force applied by the planet gear enable to lift up this thrust washer until its displacements are stopped by a contact with the inner face of the internal gear. During the last mode (coast to rear), the internal gear is submitted to a negative axial force which produces a downward motion so that the thrust washer #9 and the planet gears are pushed until the contact establishment of the thrust washer with the housing. Therefore, the thrust washers #9 is simultaneously in contact with the internal gear and the planet gears for two of the four working modes of the differential.

The damping effect of the squeeze film model can be observed on the displacement curves (Fig. 5.4(b)): the gear wheels are slowed down before the establishment of contact against the thrust washers. In this way, the impacts between these rigid bodies are avoided or at least greatly reduced. The sticking effect which acts against the separation of the contacting bodies is also visible and explains why some gear wheels move sometimes with a small delay at the switching time between two working modes. The little step on the displacement of the planet gears when the drive to front mode is activated at $t = 8$ s is also due to this sticking phenomenon.

The contribution of the squeeze film force and the penalty based contact force in the magnitude of the total axial force (Eq. 5.28) are compared in figure 5.5. The squeeze film produces a significant force during the transient phases between two working modes but this force vanishes when the bodies are in closed contact situation (Fig. 5.5(a)). This is due to the fact that the squeeze film force is directly proportional to the velocity of the film thickness (see Eq. 5.21). The latter is null when the lubricating film has reached a steady-state thickness slightly lower than the arithmetic roughness.

The forces induced by the contact between the rigid bodies present an opposite

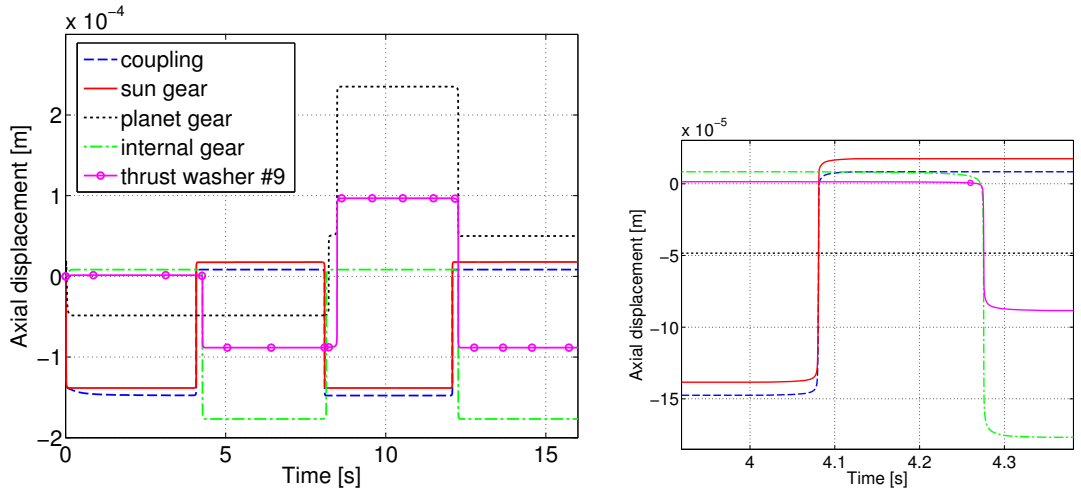

(a) (b) zoom

Figure 5.4: Axial displacement of bodies inside the differential.

time evolution (see Fig. 5.5(b)), i.e. these forces are null when the squeeze film is sufficiently thick to separate the two bodies but support most of the axial load when the contact is established. Since the input torque applied on the housing is a function linear by parts (fig. 5.9(a)), the contact forces continue to increase once the contact is closed and decrease when the torque is released.

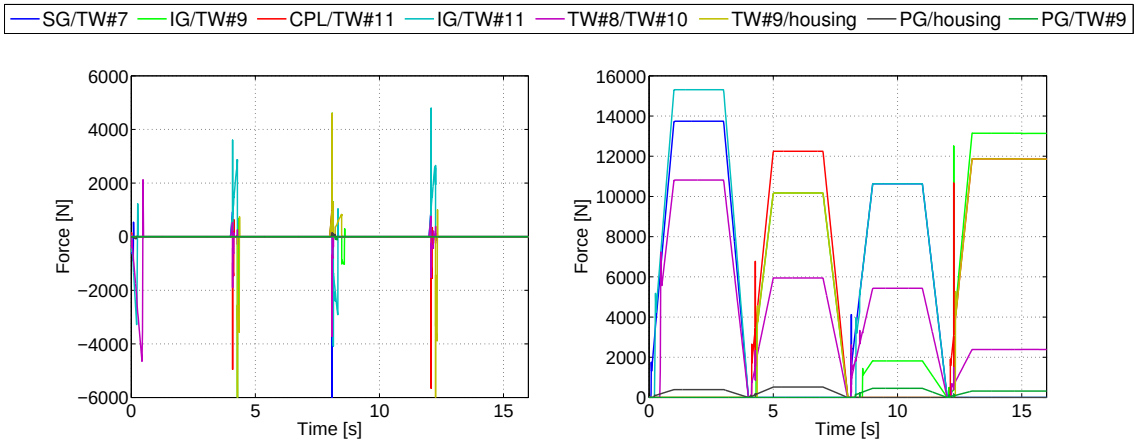

(a) squeeze film forces (b) contact forces

Figure 5.5: Force in the axial direction due to the squeeze film and the contact between bodies.

Figure 5.6 shows the viscous torque (Eq. 5.27) and the friction torque (Eq. 5.30) for each element combining the squeeze film and the contact model. In the normal operation of a vehicle, the difference of rotation speed between the two axles is not

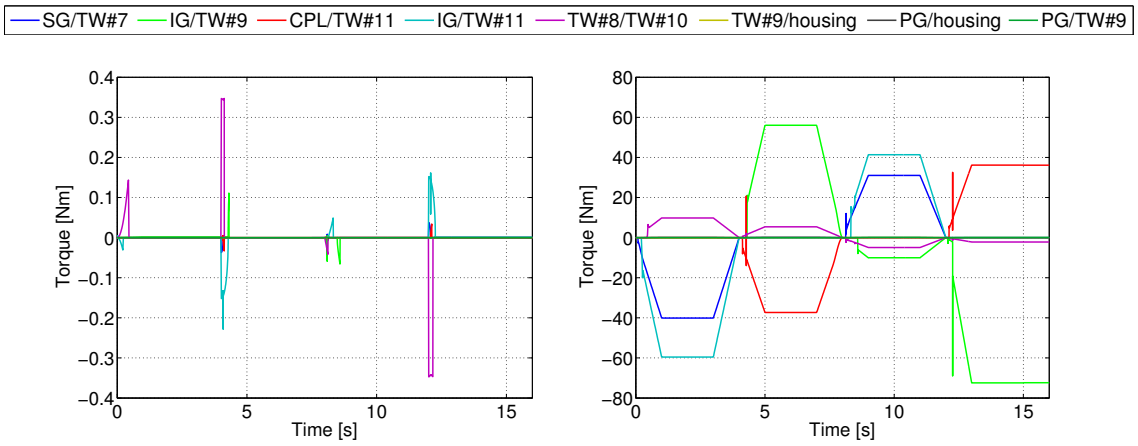

(a) viscous torques

(b) friction torques

Figure 5.6: Dissipative torques for contacts inside the TORSEN differential.

tremendous so that the magnitude of the viscous torques is insignificant compared with the friction torques. Due to the lower axial force transmitted by the contacts on the top and bottom faces of the planet gears (see Fig. 5.5(b)) and the smaller radius of their contact area, the related friction torques are much lower than the friction torques of the other contacts with the thrust washers. Nevertheless, the axial motions of the planet gears enable to account for the contact between the thrust washer #9 and the internal gear in the drive to front mode (third mode). The friction torque involved by this contact is sizeable and modifies the torque distribution in the differential. This phenomenon could not be represented using the previous differential model with locking of the planet gears (see Section 3.4.1).

In order to model the correct amount of friction, the regularization tolerance (ϵ_v in Eq. 4.70) has to be chosen in such a way that the regularized friction coefficient reaches the constant dynamic friction coefficient when the torques are measured to compute the TDRs. The smooth transition to avoid the discontinuity of the friction coefficient has to be crossed as fast as possible. The fullfillment of this condition is verified in Fig. 5.7 where it can be observed that the dynamic friction coefficient is quickly reached for all contact conditions.

Since additional friction forces have been added in the system due to the planet gear displacements, the friction coefficient in the hinge joints has to be checked and readjusted if necessary. From a parametric study, the friction coefficient leading to the best agreement between the numerical and experimental TDR values is determined equal to 0.17 (see Fig. 5.8). All the results given in this section have been obtained by using this value of the friction coefficient. The small difference with the value obtained in Chapter 3 (0.185) proves the minor but not negligible influence of the contacts on the lateral faces of planet gears.

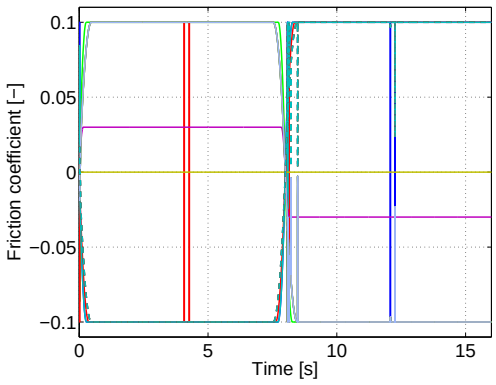

Figure 5.7: Evolution of the regularized friction coefficients.

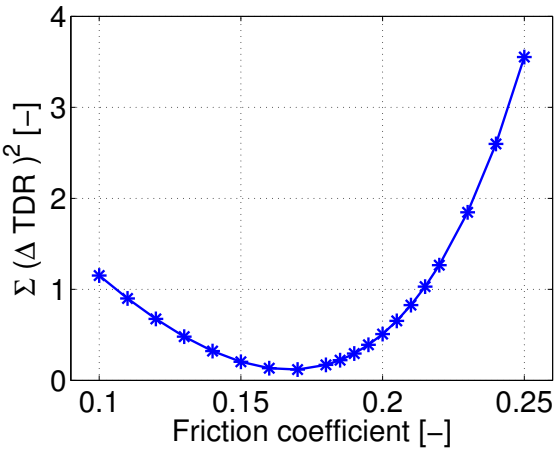

Figure 5.8: Parametric study: influence of the friction coefficient in hinge joints on the sum of squared differences between experimental and computed TDRs for the four working modes (type C TORSEN differential with squeeze film contact model).

The resisting torques allowing to impose the rotation speed of the sun gear and the coupling are depicted in figure 5.9(a). The gap between these two curves is a measure of the locking rate of TORSEN differentials for each working mode. The TDRs computed from these torque curves are given in Table 5.2. Similarly to the differential model using the rigid/flexible contact model (Section 3.4.1), the numerical TDR values agree with the experimental data; for each mode the relative error is lower than 5%. However, the model including the squeeze film contacts is more robust and can be simulated using larger time step which reduce the CPU time by a factor of 100 for the proposed simulation.

The developed squeeze film contact model can also replace the rigid/flexible contact conditions used in the type B TORSEN differential model described in section 3.4.2. For the sake of conciseness, the numerical results are not presented here for a system

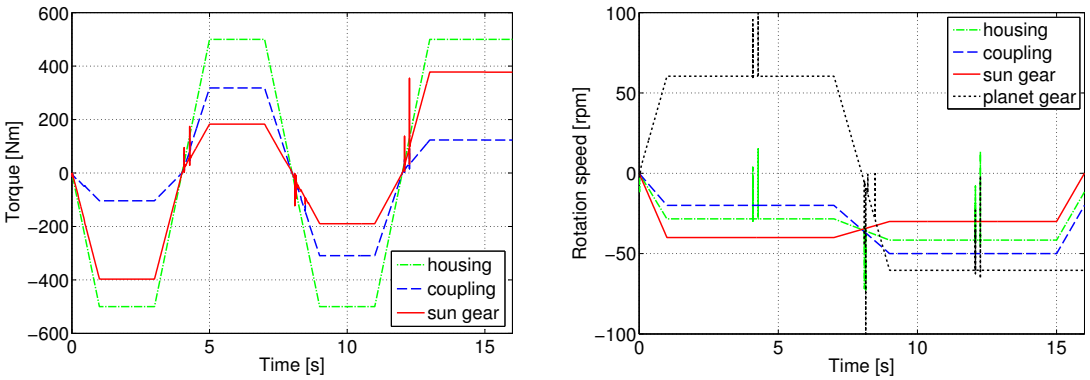

(a) torque

(b) angular velocity

Figure 5.9: Torque and angular velocity of the various gear wheels.

including only the TORSEN differential. Nevertheless, the model will be used in the next section where the interactions between the differential and the vehicle dynamics are studied.

Similarly to the central differential (type C), the axial displacements of the element gears are now authorized whereas they were locked in the former type B TORSEN differential model presented in Section 3.4.2. Since additional friction torques are introduced by the contacts between the element gears and the housing or the case, the friction coefficient inside hinge joints has also been fitted again. This friction coefficient is now 0.14 instead of 0.15 and allows us to obtain the TDR values given in Table 5.3. Similar errors as the rigid/flexible contact model are observed but the CPU cost of the squeeze film model is much smaller.

TDR	**Mode 1** Drive bias to rear	**Mode 2** Coast bias to rear	**Mode 3** Drive bias to front	**Mode 4** Coast bias to front
experimental	4.02	2.82	1.57	1.62
rigid/flexible contact	3.89	2.92	1.53	1.66
error (%)	3.23	3.55	2.55	2.47
squeeze film model	3.95	2.95	1.49	1.6
error (%)	1.74	4.61	5.10	1.23

Table 5.2: Comparison of torque distribution ratios for the four working modes of the type C TORSEN when the squeeze film model is used.

TDR	**Mode 1** Drive bias to right	**Mode 2** Coast bias to right	**Mode 3** Drive bias to left	**Mode 4** Coast bias to left
experimental	1.6	1.7	1.6	1.7
rigid/flexible contact	1.58	1.66	1.61	1.64
error (%)	3.20	2.35	0.62	3.53
squeeze film model	1.62	1.67	1.64	1.67
error (%)	1.25	1.76	2.50	1.76

Table 5.3: Comparison of torque distribution ratios for the four working modes of the type B TORSEN when the squeeze film model is used.

5.5 Integrated simulation of differentials with the vehicle dynamics

The TORSEN differentials strongly interact with the others transmission components (e.g. the gear box) and the others vehicle subsystems such as the suspension mechanisms. Therefore, in order to get a desired vehicle handling behaviour, the differential design has to be adapted according to the feature of the vehicle (suspensions, car frame, etc). As well, the use of a TORSEN differential sometimes requires some modifications in other vehicle devices, for instance the size of the anti-roll bar.

Therefore, there is a need to develop integrated simulations of differentials together with the vehicle dynamics. These virtual prototypes are useful during the design phase of any component and allow to reduce the number of physical tests.

In this section, the TORSEN differentials have been included in three vehicle models of increasing complexity. In order to ensure robustness and computational efficiency for these global models, the planar contacts inside the differentials have been modelled by the squeeze film formulation.

5.5.1 Simple four-wheel drive vehicle

The model of the four-wheel drive vehicle briefly introduced in section 3.5 was too computationally expensive and not sufficiently robust to simulate vehicle manoeuvres during long periods. About 28 hours were needed for the simulation of the 4 s represented in Fig. 3.39. This was mainly due to the large number of DOFs involved by the FE models of the thrust washers and to the cost of the rigid/flexible contact conditions using a projection method of slave nodes on the master face (see Section 3.3).

Thanks to the proposed squeeze film contact model, these drawbacks are circumvented and the drivetrain model including three TORSEN differentials is efficiently simulated together with rigid driveshafts and wheel models (Pacejka's magic formula, see Ref. [88]).

In this simplified vehicle model, the three differentials are connected through hinge joints to the car body which is modelled as a lumped mass. The suspensions and the steeering mechanism are not represented (see Fig. 3.38). The output shafts of the central differential (type C TORSEN) are linked to the housing of the front or rear differential (type B TORSEN) with a conical gear pair; by simplicity the axle ratio has been chosen equal to 4 for both axles.

The whole MBS model contains 64 rigid bodies, 34 hinge joints, 31 prismatic joints, 1 srew joint, 4 wheel models, 50 gear pair elements and 60 unilateral contact conditions. The total number of DOFs amounts to 4637. The full system is submitted to the gravity field and a 1 m/s initial velocity is given to the vehicle which is moving forward in straight line motion. The vehicle is driven by a torque applied on the housing of the central differential. The time evolution of this torque is simply made by a piecewise quadratic function with two parts as depicted in Fig. 5.10(a).

In order to study the torque transfers induced by the limited slip behaviour of the three TORSEN differentials, quite different grip conditions have been chosen for each wheel of the vehicle, even if it is not very realistic. The rear right wheel has a good adherence whose parameters are given by the Pacejka's wheel model. The ground in contact with the other wheels has a lower adherence whose properties are given by scaling the grip potential of the rear right wheel with a factor equals to 0.5 for the rear left wheel, 0.4 for the front right wheel and 0.1 for the front left wheel.

The torque distribution between the four driving wheels is illustrated in Fig. 5.10. Since a driving torque is applied on the central differential and the rear wheels have a better adherence than the front wheels, the drive to rear mode of the type C TORSEN differential is activated. Therefore, the rear wheels receive more torque than the front wheels. It can be verified that the torque ratio between the front axle and the rear axle matches the TDR value of the drive to rear mode given in Table 5.2.

Likewise, both front and rear differentials provide more torque to the right wheels because the right lane has a better adherence. The torque ratios are also in accordance with the TDR of the drive to right mode (see Tab. 5.3).

Figure 5.11 depicts the angular velocities of the planet gears and the four wheels. The three differentials are nearly locked since all the wheels almost rotate at the same speed and the planet gears have only a small angular velocity. Let us remark that the purely closed configuration of TORSEN differentials correspond to no relative sliding inside differential. Nevertheless, a small sliding is still observed in the proposed numerical model because of the regularization of the friction coefficients.

The model can also represent the open configuration. To this end, the same system has been simulated with a higher driving torque: the maximal value of the torque amounts to 500 Nm instead of 300 Nm (see Fig. 5.12(a)). The torque curves keep similar time evolution as illustrated in Fig. 5.12(b).

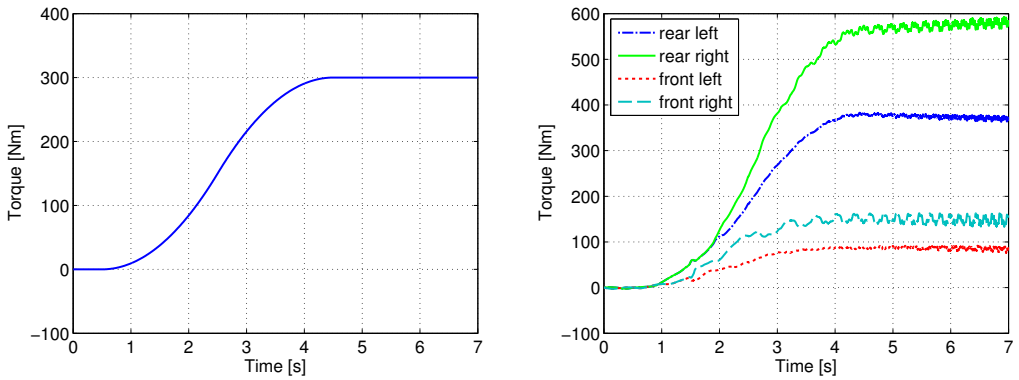

(a) torque applied on the housing of the central differential

(b) torque provided on the four driving wheels

Figure 5.10: Distribution of the driving torque between the four driving wheels having a different friction coefficient (maximum torque = 300 N/m).

In contrast, the graphics with the rotation speeds are significantly different (Fig. 5.13 compared with Fig. 5.11). Indeed, the potential of adherence is exceeded for the front left wheel and results in the spinning of this wheel. The other wheels have almost the same speed whereas the housing of the front differential rotates at a mean velocity between the right and the left front wheels. The planet gears of the central and the front differential turn much quicker than in the previous simulation which is representative of the fully open status of the two differentials.

5.5.2 AUDI A6 RWD with a detailed suspension system

In order to perform reliable simulations of the dynamics of cars during manoeuvres, the suspensions and the steering system have to be modelled. As proof-of-concept, the AUDI A6 model presented here (Fig. 5.14) includes four independent multi-link suspensions articulated to the car body which is simply represented by a rigid body. The steering mechanism is composed of a rack and pinion system connected to the knuckles by means of spherical joints and universal joints.

The full MBS model is formulated with 3268 DOFs, 56 rigid bodies and numerous kinematic joints (constant velocity joints, universal joints, hinge joints, prismatic joints, spherical joints).

Lane change manoeuvre

The well-known elk test is a standardized lane change manoeuvre (Fig. 5.15) often used to assess the drivability of a vehicle. An initial velocity (10 m/s) is given to the

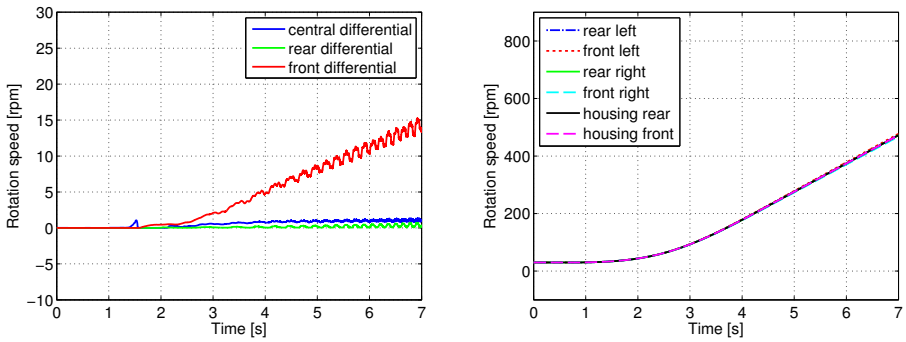

(a) planet gears

(b) output shafts and differential housings

Figure 5.11: Rotation speed of the planet gears and the output shafts of the three TORSEN differentials (maximum torque = 300 N/m).

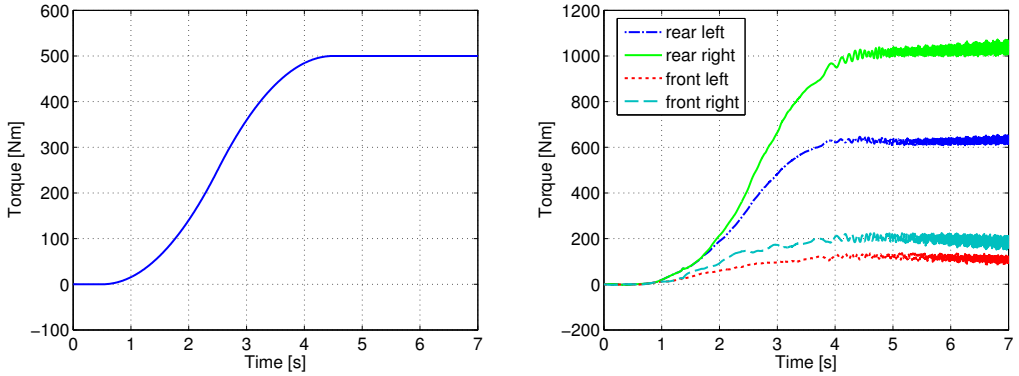

(a) torque applied on the housing of the central differential

(b) torque provided on the four driving wheels

Figure 5.12: Distribution of the driving torque between the four driving wheels having a different friction coefficient (maximum torque = 500 N/m).

vehicle and no torque is provided by the engine or the brakes, the car is coasting. This qualification test is defined by the command given to the steering mechanism. In the present model, it simply consists in prescribing the displacement of the steering rack following the function depicted in Fig. 5.16. This is an open-loop command without any correction of the driver. This latter should have been modelled by a simple controller such as a PID in order to track a given vehicle trajectory (see Ref. [95]).

When the rack of the steering system moves, the inner wheel is slowed down while the outer wheel is speeded up by the same relative velocity with respect to the differential housing (Fig. 5.17). From the point of view of the differential, this situation is equivalent to brake the inner wheel and provide a torque to the other wheel. Since

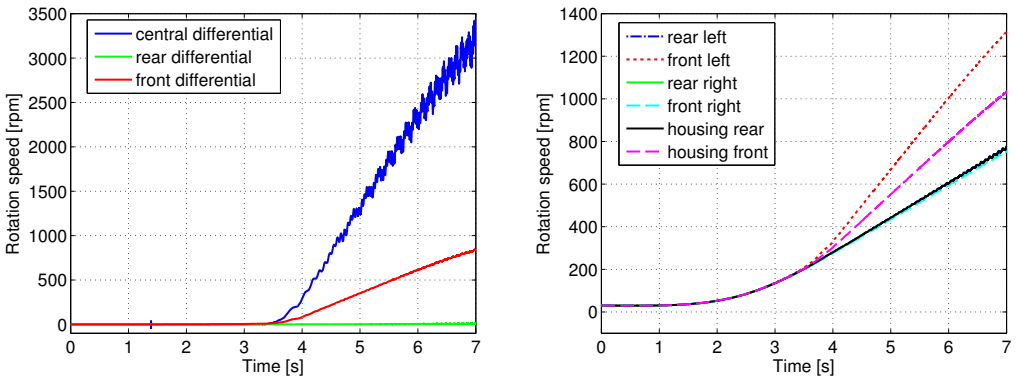

(a) planet gears (b) output shaft and differential housings

Figure 5.13: Rotation speed of the planet gears and the output shafts of the three TORSEN differentials (maximum torque = 500 N/m).

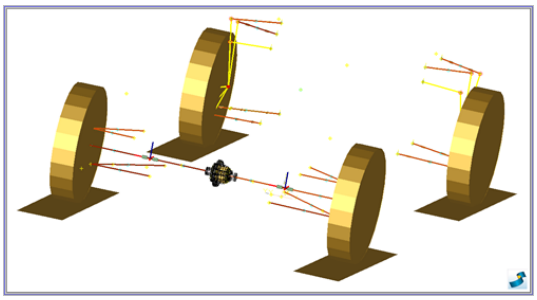

Figure 5.14: AUDI A6 vehicle model including the suspension system.

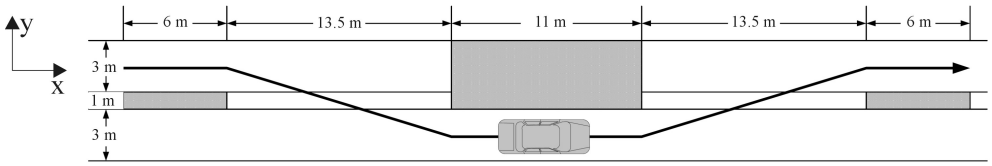

Figure 5.15: Elk test: standard lane change manoeuvre.

no torque is applied by the engine in this test, the sum of the torques provided by the differential on both wheels has to be null. This is the reason why the torques have the same magnitude but an opposite sign in Fig. 5.18(a).

In order to assess the torque transfer characteristic of TORSEN differentials, the same model has been simulated without considering the friction forces inside the differential. As depicted in Fig. 5.18(b), the torque transfer is insignificant in this case and is equivalent to the behaviour of an open differential. Finally, let us note that the load case used to simulate the elk test is not common since no torque is applied by the

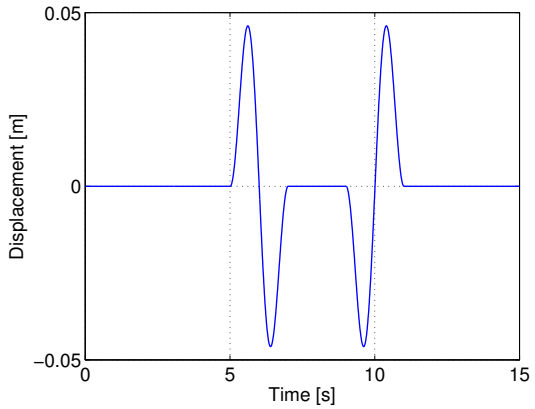

Figure 5.16: Displacement prescribed on the rack steering during the elk test manoeuvre.

motor.

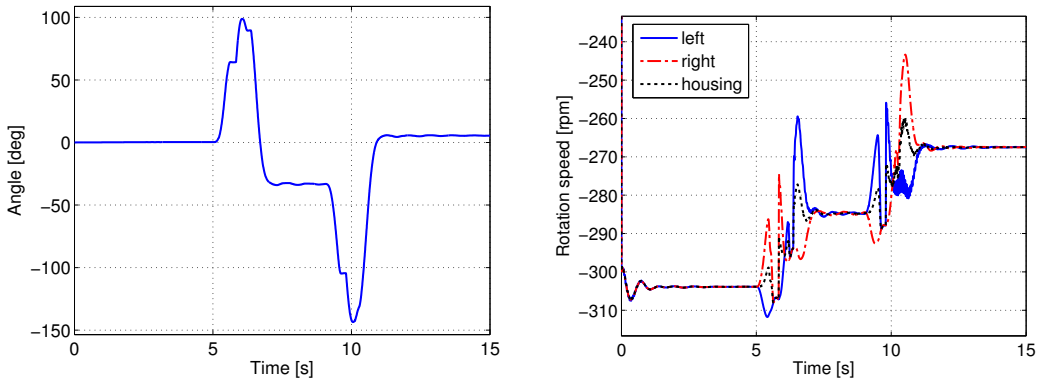

(a) planet gears

(b) housing and output shafts

Figure 5.17: Elk test: rotation of the planet gears, the housing and the output shafts of the rear differential.

Slippery ground

In this section, the AUDI A6 model including the rear TORSEN differential is simulated when the vehicle is moving forward in straight line thanks to a driving torque applied on the differential housing. In order to represent the behaviour of the vehicle on a slippery patch successively below the left wheel and right wheel, the friction parameters of the wheel model are multiplied by a factor comprised between 0 and 1 when the vehicle has covered a given distance (see Fig. 5.19).

The maximum driving torque is 200 Nm and is progressively applied following a

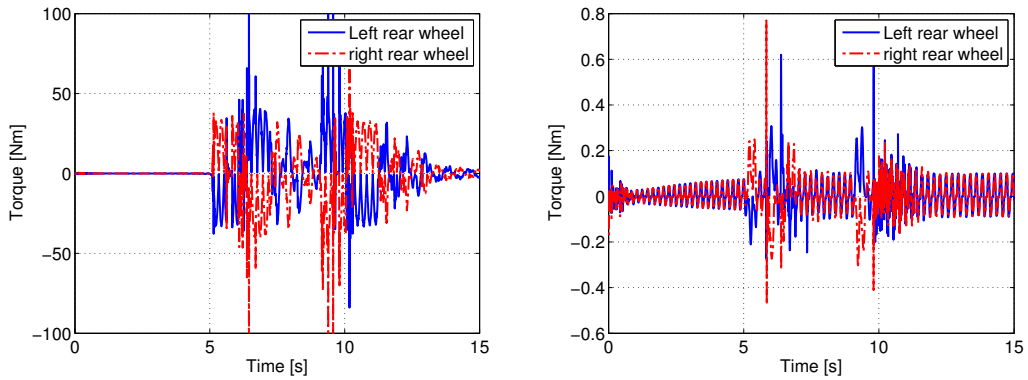

(a) with friction (b) without friction

Figure 5.18: Comparison of the torque on differential output shafts between a TORSEN and an open differential.

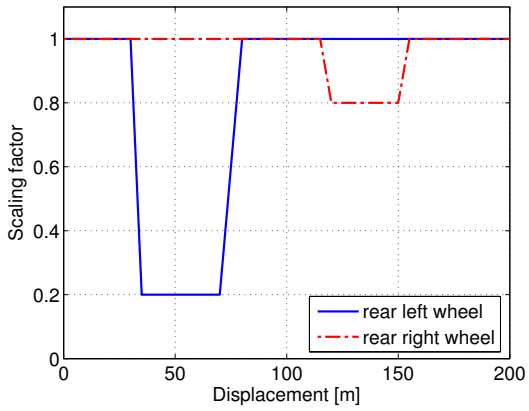

Figure 5.19: In order to represent slippery ground surface, the friction coefficient computed by the Pacejka's wheel model is scaled.

ramp function in the interval $[0; 2]$ s. The torque transfers between the two differential output shafts can be observed in Fig. 5.20(b). The torque ratio for the first slippery surface matches the TDR value (Tab. 5.3) because the left wheel has almost no adherence in this situation. The adherence of the second slippery surface being better, the differential provides more torque to the rear left wheel but the torque ratio does not reach the TDR since the difference of adherence is not sufficient. The asymmetric distribution of the torque enables the vehicle to continue to move forward in the presence of a slippery ground on one wheel which would not be possible with a conventional differential.

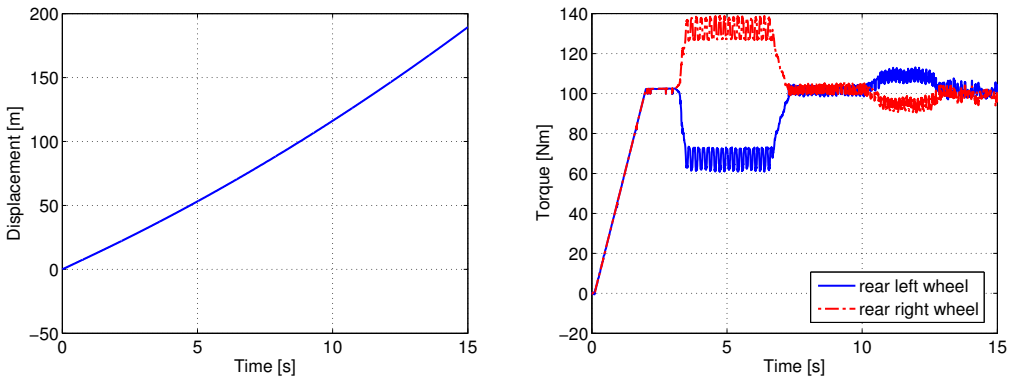

(a) displacement of the center of mass of the vehicle along the longitudinal direction

(b) torque on rear wheels

Figure 5.20: When the vehicle moves forward on a slippery surface, the TORSEN differential provides more torque to the wheel having a better adherence.

5.5.3 IMPERIA prototype with flexible chassis frame

With the aim of having a more accurate car model, the various vehicle components can be extended to capture other physical effects (e.g. structural flexibility) or other subsystems can be included in the model (e.g. gear box, clutch, chassis, joints with bushings and clearance). In addition to the suspension system, the rear TORSEN differential and the steering system, the vehicle model presented in this section also contains a flexible body frame represented by means of beam elements. The car modelled is the IMPERIA prototype which is a vehicle driven by a hybrid engine (see Fig. 5.21).

The flexibility could also be taken into account for other components such as the suspensions wishbones, the differential case or the driveshafts. But the current model is sufficient to demonstrate the ability of the proposed integrated simulation approach to simulate efficiently the dynamics of a global vehicle with a transmission component. The model depicted in Fig. 5.22 already contains about 12000 DOFs.

In the simulation presented in this section, the load case has been chosen in order to activate the four working modes of the type B TORSEN differential. During the first five seconds of the simulation, the IMPERIA vehicle is running in straight line at a 10 m/s constant velocity. This phase allows the vanishing of transient effects of numerical origin at the beginning of the simulation. Afterwards, a driving torque is applied on the differential housing until $t = 12$ s where the torque is applied in the other direction in order to produce the same effect as the brakes (Fig. 5.23(b)). During both acceleration and deceleration phases, a cornering sequence to the right and to the left is prescribed to the vehicle by moving the steering rack (see Fig. 5.23(a)).

The axial displacements of all the gear wheels included in the differential are

depicted in Fig. 5.24. It can verified that the side gears are pushing in opposite direction, against the cap and the housing respectively, when the drive modes are active. For the coast modes, the axial position of the two side gears is synchronized since they are in contact. Moreover, a contact also occurs with the upper or the lower thrust washer according to the direction of the torque transfer between the driving wheels (bias to the right or bias to the left). On the other hand, the axial position of the element gears is only influenced by the direction of torque transfer and not by the drive or the coast situation.

The friction torques involved by the contacts inside the differential lead to an unequal distribution of the torque between the right and the left wheels when the vehicle turns (Fig. 5.25). In driving conditions, the inner wheel receives more torque whereas it is the opposite in coast condition.

Since the flexibility of the car body is modelled, the magnitude of stresses and strains can be analysed thanks to this kind of numerical model. At $t = 8$ s, Figure 5.26 shows that the stresses in the car body are maximum near the attachments points of the four suspension systems. A more detailed study should be performed in order to assess the effects of the chassis deformations on the dynamics of the vehicle, but this kind of analysis is out of the scope of this thesis.

5.6 Concluding remarks

A unilateral contact model considering the squeeze film of the lubricant in the narrow gap between two rigid bodies in intermittent contact has been developed in this chapter. The expression of the normal force produced by the squeeze film has a compact form thanks to a set of geometric and physical hypotheses. When the thickness of the oil film is lower than the arithmetic roughness, the contact occurs between the two metallic bodies and is modelled by a penalty method. In addition to the contact forces in the normal direction, the friction torques in the tangential plane are also included in the

Figure 5.21: IMPERIA CAR (http://www.imperia-auto.be/).

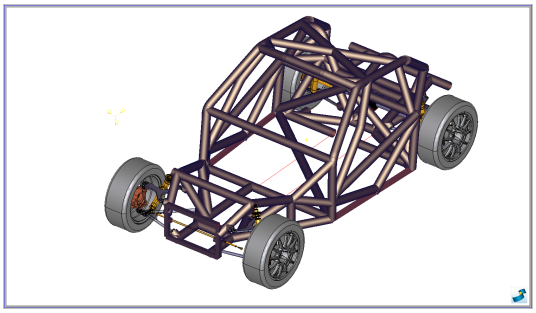

Figure 5.22: Multibody model of the Imperia including the type B TORSEN differential as rear differential.

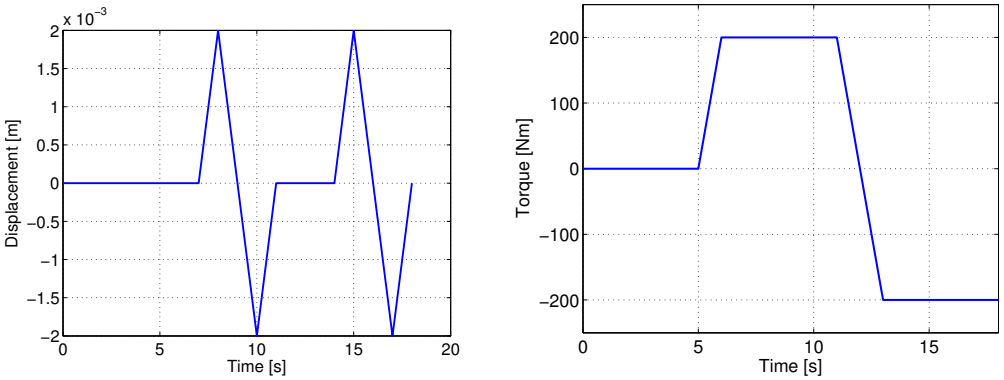

(a) displacement prescribed to the steering rack

(b) torque on differential housing

Figure 5.23: Load case imposed to the vehicle for the simulation of the four working modes of the differential during the same simulation.

proposed model.

The TORSEN differentials have been used as an application to assess the squeeze film model. The presence of the squeeze film model allows to reduce the discontinuities when the gear wheels enter in contact with the thrust washers at each transition between two working modes. The relative velocity is decreased by the damping force introduced by the squeeze film model which is proportional to the velocity of the film thickness and inversely proportional to the cube of the film thickness.

The modelling of the squeeze film allows us to better describe the physical behaviour of the differential and also leads to an increased robustness and a reduced computational time since larger time steps can be used. Moreover, the axial locking of the planet gears can be removed which involves additional contact conditions in the model. Similarly to the models using the rigid/flexible contact model presented in Chapter 3, the comparison of the TDR values for the four working modes has shown a

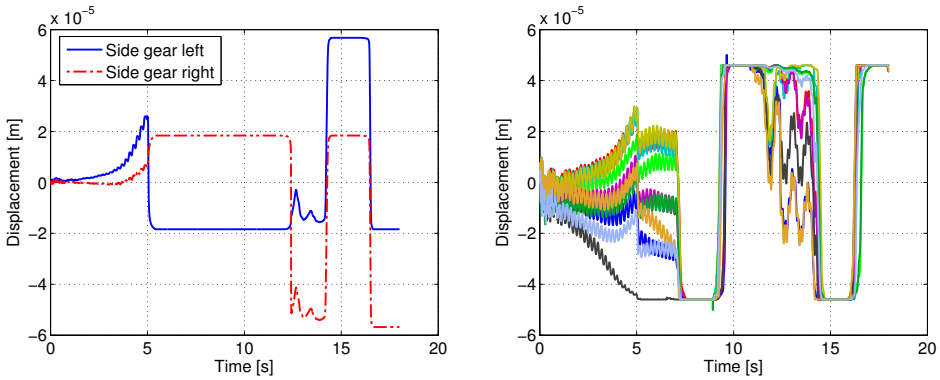

(a) Side gear attached to the output shafts (b) Element gears

Figure 5.24: Axial displacement of the two side gears and the element gears inside the type B TORSEN differential.

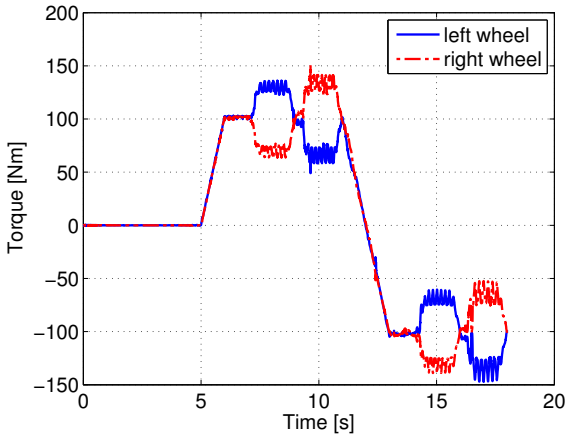

Figure 5.25: Torque provided by the differential to the left and right rear wheel.

good correlation with the experimental data.

Finally, the TORSEN differential models have been included in several vehicle models in order to simulate the interactions with the vehicle dynamics. These global models have shown the feasibility to integrate transmission components in full vehicle models.

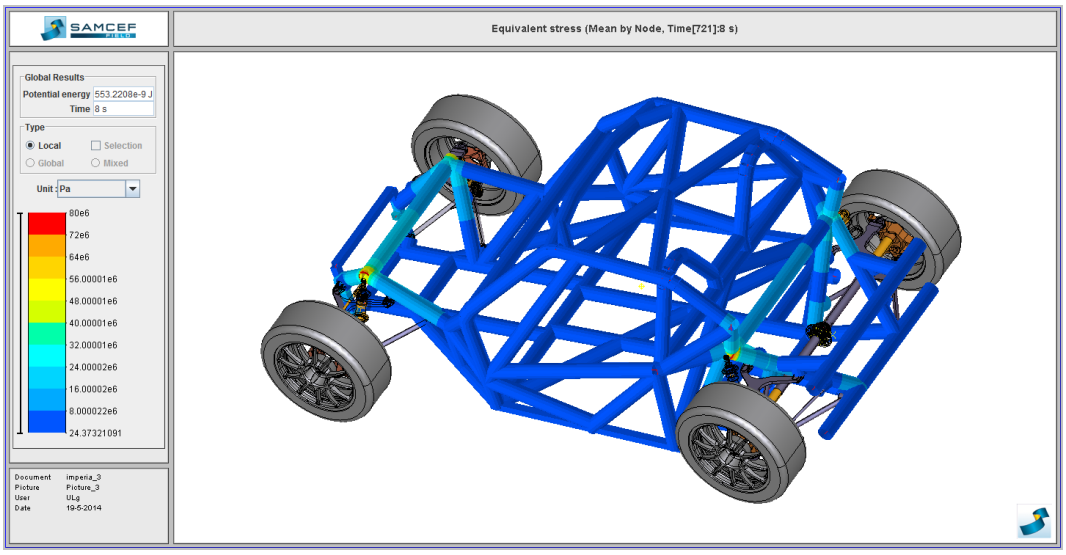

Figure 5.26: Stress distribution in the body frame of the IMPERIA vehicle modelled with FE beam elements.

Chapter 6

Modelling of contact between superelements

Contents

The contact model described in Chapter 3 requires that at least one of the two contacting bodies is represented by a finite element model. In order to have a contact formulation more suited to represent impact phenomena and less CPU time consuming, global contact models defined between rigid bodies have been proposed in Chapter 4. These models have been developed for specific geometries, namely planar rings and cylinders. Now, the rigidity assumption will be withdrawn and more general geometries will be considered. For that purpose, a contact element between superelements is presented in the present chapter. The superelement approach allows to account for the flexible behaviour while keeping a reduced model size. The main application of this new contact formulation is the modelling of gear pairs. Therefore, contrarily to

the gear pair model used until now, the flexible effects inside gear components can be represented.

The outline of the chapter is the following. Firstly, the principles of the Craig-Bampton are reminded in Sections 6.2-6.3. The superelement formulation (Section 6.4) as well as the corotational frame definition (Section 6.5) used in this study are briefly presented. Then, the various steps of the contact detection algorithm will be looked over in Section 6.6. The contact law and the expression of the contact forces are described next (Sections 6.7-6.8). Finally, the relevance of the approach for the dynamic analysis of transmission devices is demonstrated through simulation results based on simplified examples first (Sections 6.9- 6.10), and then on a gear pair model (Section 6.11).

6.1 Introduction

The contact models defined between rigid bodies are appropriate to represent the interactions between bodies in large and complex mechanical systems. Their formulation is often compact and does not require large computer resources while keeping the number of bodies small. However, due to the rigidity assumption, it is not possible to study the wave propagation caused by hard contact or impact, so that the dynamic responses may not lead to realistic predictions. Reference [151] points out that for compliant gear bodies the flexibility effects modify significantly the teeth contact forces and alter the motion of the whole gear pair system. With rigid body models, this kind of dynamic behaviour can not be captured.

An accurate way to account for flexibility effects in contact situations is to rely on finite element models of bodies since this approach accounts for a description of deformation and vibration phenomena (see Ref. [19]). Nevertheless, if the number of bodies and the number of contact conditions become large, the numerical simulation may become computationally ineffective since requiring large computational time and huge memory requirements. For example, in order to model the contact between gear pairs, a rather fine mesh of the whole skin of the rotating wheels would be required, which would be highly penalizing for a global dynamic analysis [85].

In order to simulate quickly and properly the contacts included in multibody models of industrial applications where the flexibility effects are not negligible, a contact model at an intermediate detail level between both aforementioned approaches is therefore needed.

Model reduction techniques of finite element models enables to significantly reduce the size of the structural component models while representing the flexibility effects with good accuracy. For example, the superelement formulation based on the Craig-Bampton technique [44] relies on a partitioning of the nodal coordinates into interface DOFs which need to be kept in the superelement and internal DOFs which can be

condensed in order to reduce the size of the problem. However, as such, this approach is impractical for contact problems since the coordinates of all the nodes in the potential contact zone should appear in the interface set and cannot be condensed. The size of the resulting superelement would thus be prohibitive.

This chapter proposes an alternative superelement formulation in which a large part of the nodes in the potential contact zone can be condensed. This means that the number of generalized coordinates of the reduced model can be much smaller than the number of nodal coordinates of the skin. Then, the formulation of the contact forces relies on a reconstruction of the skin geometry based on the generalized coordinates of the superelement. The active contact zone is determined by a contact detection algorithm which considers the condensed nodes as virtual nodes. At last, the contact forces computed in the 3D space are reformulated and directly applied upon the superelement generalized coordinates. The implementation is carried out within the framework of absolute nodal coordinates that are well suited with the corotational formulation of a superelement as described in Ref. [18].

6.2 Linear reduction of a finite element model

The nonlinear finite element method for flexible multibody systems as presented in section 2.2 requires using a nonlinear definition of the strain tensor even for small elastic deformations. Furthermore, the number of nodal coordinates can become large if 3D meshes are used, and consequently the model size can also become large.

However, the dynamics of an MBS is often characterized by large rotations but only small elastic displacements. Therefore, in that case the only nonlinearities result from geometric effects linked to large rotation of the bodies. In a local frame (that can be either a floating [124] or a corotational one [42]) that follows the gross motion of the flexible body, a simple linear elastic model can be used to compute the elastic forces if the assumption of small strains remains valid. Afterwards, the body model can be reduced by using one of the various model reduction methods which have been introduced in Section 2.3.

The basic principle of a reduction technique for decreasing the size of an eigenvalue problem

$$\boldsymbol{K}\boldsymbol{d} = \omega^2 \boldsymbol{M}\boldsymbol{d} \tag{6.1}$$

consists in finding a linear expansion of the elastic displacement field ($\boldsymbol{d}$) in a basis of deformation modes ($\overline{\boldsymbol{\Psi}}$) of the body (Eq.6.2).

$$\boldsymbol{d} \cong \overline{\boldsymbol{\Psi}}\ \boldsymbol{\eta} \tag{6.2}$$

Matrix $\overline{\boldsymbol{\Psi}}$ is of dimension $n \times m$, with n being the size of the displacement field $\boldsymbol{d}$ of the initial model, m ($m < n$) the length of the reduced variable vector $\boldsymbol{\eta}$ which can

be of various nature according to the substructuring technique used. The columns of this matrix contain the global shape functions of the reduced model.

The accuracy of the reduced model depends on the ability of the subspace spanned by the deformation modes $\overline{\boldsymbol{\Psi}}$ to describe the actual node displacements of the initial finite element model. The various reduction techniques only differ from each other by the definition of the reduction matrix $\overline{\boldsymbol{\Psi}}$.

The reduced stiffness $\overline{\boldsymbol{K}}$ and mass $\overline{\boldsymbol{M}}$ matrices can be easily obtained from the variational principle of the reduced problem (see Ref. [44])

$$\overline{\boldsymbol{K}} = \overline{\boldsymbol{\Psi}}^T \boldsymbol{K} \overline{\boldsymbol{\Psi}} \tag{6.3}$$

$$\overline{\boldsymbol{M}} = \overline{\boldsymbol{\Psi}}^T \boldsymbol{M} \overline{\boldsymbol{\Psi}} \tag{6.4}$$

The term **superelement** is generally given to the set of reduced matrices ($\overline{\boldsymbol{K}}$, $\overline{\boldsymbol{M}}$, $\overline{\boldsymbol{\Psi}}$). The main advantage of the superelement approach to model flexible multibody bodies lies in its ability to represent geometrically complex components connected to the rest of the system while keeping a relatively simple global dynamic model based on a limited number of coordinates.

6.3 Craig-Bampton method

The Craig-Bampton method is a reduction technique based on the mechanical impedance or component-mode synthesis (CMS) concepts. With this approach, the dynamic behaviour of a superelement is described as the superposition of:

- static modes attached to boundary nodes;
- vibration modes describing internal deformation.

The displacement field $\boldsymbol{d}$ of the initial model is split up into two parts: a set of n_B boundary degrees of freedom $\boldsymbol{d}_B$ on one the hand and a set of n_I internal degrees of freedom $\boldsymbol{d}_I$ on the other hand (see Fig.6.1).

If it is assumed that no external force is applied on the internal degrees of freedom, the static equilibrium of a mechanical component can be written as:

$$\begin{bmatrix} \boldsymbol{K}_{BB} & \boldsymbol{K}_{BI} \\ \boldsymbol{K}_{IB} & \boldsymbol{K}_{II} \end{bmatrix} \begin{Bmatrix} \boldsymbol{d}_B \\ \boldsymbol{d}_I \end{Bmatrix} = \begin{Bmatrix} \boldsymbol{g}_B \\ \boldsymbol{0}_{n_I \times 1} \end{Bmatrix} \tag{6.5}$$

where $\boldsymbol{K}_{ij}$ are the different blocks of the stiffness matrix and $\boldsymbol{g}_B$ is the vector of interface forces between the superelement and its connected neighbouring parts. The internal degrees of freedom can be eliminated by static condensation (see second equation of Eq. 6.5):

$$\boldsymbol{d}_I = -\boldsymbol{K}_{II}^{-1} \boldsymbol{K}_{IB} \, \boldsymbol{d}_B \tag{6.6}$$

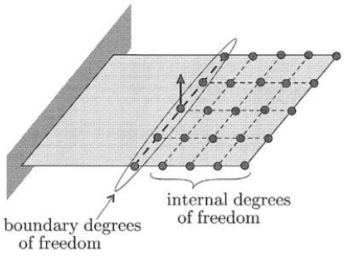

Figure 6.1: The nodes of the initial finite element model are partitioned into boundary nodes and internal nodes [42].

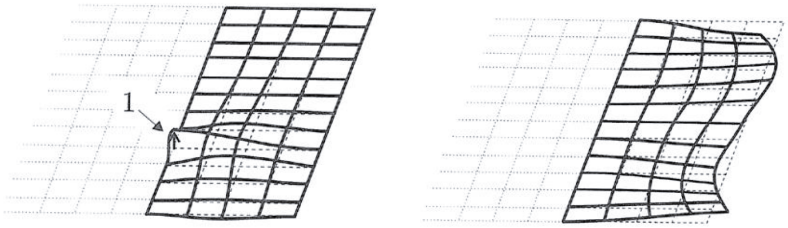

(a) static mode (b) vibration mode

Figure 6.2: Deformations due to solicitations of superelement modes [42].

The **static modes** $\boldsymbol{\Psi}_B$ can be interpreted as constrained modes representing the static deformations of the structure if a unit displacement is successively prescribed to each boundary degree of freedom (Fig. 6.2(a)):

$$\begin{bmatrix} \boldsymbol{K}_{BB} & \boldsymbol{K}_{BI} \\ \boldsymbol{K}_{IB} & \boldsymbol{K}_{II} \end{bmatrix} \begin{bmatrix} \boldsymbol{I}_{n_B \times n_B} \\ \boldsymbol{\Psi}_B \end{bmatrix} = \begin{Bmatrix} \boldsymbol{G}_B \\ \boldsymbol{0}_{n_I \times n_B} \end{Bmatrix} \tag{6.7}$$

with

$$\boldsymbol{\Psi}_B = -\boldsymbol{K}_{II}^{-1} \boldsymbol{K}_{IB} \tag{6.8}$$

and $\boldsymbol{G}_B$ is a matrix containing the reaction forces at boundary nodes for the n_B static modes.

The reduction subspace formed with the static modes is then enriched by independent vibration modes obtained when the boundary nodes are clamped (Fig. 6.2(b)). The **internal vibration modes** $\boldsymbol{\Psi}_I$ can be computed by solving the internal eigenvalue problem:

$$\left(\boldsymbol{K}_{II} - \omega^2 \boldsymbol{M}_{II}\right) \boldsymbol{\Psi}_I = \boldsymbol{0}_{n_I \times n_I} \tag{6.9}$$

In order to significantly reduce the size of the initial model, only a limited number ($\overline{n_I} < n_I$) of eigenmodes are included in the modal basis. This truncation of the modal expansion means that the higher frequencies are neglected, which is relevant since it

can be shown from the mechanical impedance concept that the effect of lower frequency terms is dominating [42]. The internal vibration modes retained are chosen according to the magnitude of the reactions $(\boldsymbol{K}_{IB} - \omega_i^2 \boldsymbol{M}_{IB})\boldsymbol{\Psi}_{I_i}$ produced by the eigenmode $\boldsymbol{\Psi}_{I_i}$ on the retained nodes. All the boundary static modes have to be kept to ensure the compatibility of the displacements at the interfaces.

Finally, the displacement of any node of the initial finite element model can be expressed as a linear combination of both static and dynamic modes

$$\begin{Bmatrix} \boldsymbol{d}_B \\ \boldsymbol{d}_I \end{Bmatrix} \cong \begin{bmatrix} \boldsymbol{I} \\ \boldsymbol{\Psi}_B \end{bmatrix} \boldsymbol{d}_B + \begin{bmatrix} \boldsymbol{0} \\ \overline{\boldsymbol{\Psi}}_I \end{bmatrix} \boldsymbol{\eta}_I \tag{6.10}$$

where $\overline{\boldsymbol{\Psi}}_I$ is the subset of selected internal dynamic modes and $\boldsymbol{\eta}_I$ is the $(\overline{n_I} \times 1)$ vector of internal variables representing the modal intensity of each vibration mode retained.

The full reduction matrix $\overline{\boldsymbol{\Psi}}$ of dimension $n \times (n_B + \overline{n_I})$ (see Eq. 6.2) is simply constructed by the concatenation of the two mode matrices:

$$\overline{\boldsymbol{\Psi}} = \begin{bmatrix} \boldsymbol{I} & \boldsymbol{0} \\ \boldsymbol{\Psi}_B & \overline{\boldsymbol{\Psi}}_I \end{bmatrix} \tag{6.11}$$

The reduced stiffness and mass matrices are obtained from Eqs. 6.3-6.4 and have the following structure if the eigenmodes are orthogonal in the metrics of the mass matrix:

$$\overline{\boldsymbol{K}} = \begin{bmatrix} \overline{\boldsymbol{K}}_{BB} & \boldsymbol{0} \\ \boldsymbol{0} & \boldsymbol{\mu}\, \boldsymbol{\omega}_I^2 \end{bmatrix}, \qquad \overline{\boldsymbol{M}} = \begin{bmatrix} \overline{\boldsymbol{M}}_{BB} & \overline{\boldsymbol{M}}_{BI} \\ \overline{\boldsymbol{M}}_{IB} & \boldsymbol{\mu} \end{bmatrix} \tag{6.12}$$

where $\boldsymbol{\omega}_I = \mathrm{diag}(\omega_1 \ldots \omega_i \ldots \omega_{\overline{n_I}})$ collects the eigenfrequencies $\omega_i = 2\pi f_i$ of the subsystem, and $\boldsymbol{\mu} = \mathrm{diag}(\mu_1 \ldots \mu_i \ldots \mu_{\overline{n_I}})$ is a diagonal matrix containing the modal masses $\mu_i = \overline{\boldsymbol{\Psi}}_{I_i}^T \boldsymbol{M}_{II} \overline{\boldsymbol{\Psi}}_{I_i}$. Like the finite element stiffness matrix $\boldsymbol{K}$, the reduced stiffness matrix $\overline{\boldsymbol{K}}$ is also singular due to the existence of rigid body modes.

6.4 Superelement formulation

In dynamic multibody systems submitted to large displacements but undergoing small strains, the linear elasticity hypothesis required by the Craig-Bampton reduction method is only admissible inside a moving frame following the gross motion of a substructure modelled as superelement. Indeed, in an inertial frame, geometric nonlinearities are present for large amplitude motion even for a rigid body motion. The reduced stiffness and mass matrices ($\overline{\boldsymbol{K}}$,$\overline{\boldsymbol{M}}$) of a superelement remain constant in this local frame but, if the system is expressed in an absolute inertial frame, the superelement matrices are no longer constant and depend on the generalized coordinates.

The **corotational frame** approach allows a simplified nonlinear formulation of a superelement which is based on the superposition of a global motion represented by the

corotational frame position with small linear elastic deformations. This method uses the absolute nodal coordinates and is therefore fully compatible with the finite element approach described in Section 2.2. For instance, multibody models of complex systems can include corotational superelements connected by means of the boundary nodes to nonlinear finite elements (e.g., beams) or rigid bodies. The modelling of flexible bodies with one or the other approach depends on the level of accuracy needed and the CPU time requested.

6.4.1 Kinematic description

As depicted in Fig. 6.3, the position $\boldsymbol{x}_P$ and the rotation matrix $\boldsymbol{R}_P$ of each point P of a superelement can be written as:

$$\boldsymbol{x}_P = \boldsymbol{x}_0 + \boldsymbol{R}_0(\boldsymbol{X}_P + \boldsymbol{u}_P) \tag{6.13}$$

$$\boldsymbol{R}_P = \boldsymbol{R}_0\ \boldsymbol{R}(\boldsymbol{\gamma}_P) \tag{6.14}$$

where $\boldsymbol{x}_0$ is the absolute position of the corotational frame $\{O; \boldsymbol{e}_1, \boldsymbol{e}_2, \boldsymbol{e}_3\}$, $\boldsymbol{R}_0$ is the rotation matrix of the corotational frame about the inertial frame, $\boldsymbol{X}_P$ is the undeformed position of P in the corotational frame, $\boldsymbol{u}_P$ is its small elastic displacement, $\boldsymbol{\gamma}_P$ is a set of variables representing the small relative rotation with respect to the corotational frame and $\boldsymbol{R}(\boldsymbol{\gamma}_P)$ is the rotation matrix associated with the three independent rotation variables $\boldsymbol{\gamma}_P$.

The local displacements and relative rotations of any point P can be directly obtained by the linear reduction relationship provided by the Craig-Bampton technique:

$$\begin{Bmatrix} \boldsymbol{u}_P \\ \boldsymbol{\gamma}_P \end{Bmatrix} \cong \overline{\boldsymbol{\Psi}}_P\ \boldsymbol{\eta} \tag{6.15}$$

with $\overline{\boldsymbol{\Psi}}_P$ are the rows of the mode matrix $\overline{\boldsymbol{\Psi}}$ related to the the point P. The latter can be easily deduced from Eq. 6.2. The vector of local coordinates $\boldsymbol{\eta}$ of the superelement expressed in the corotational frame is defined by:

$$\boldsymbol{\eta} = \begin{Bmatrix} \boldsymbol{u}_B \\ \boldsymbol{\gamma}_B \\ \boldsymbol{\eta}_I \end{Bmatrix} \tag{6.16}$$

where $\boldsymbol{u}_B$, $\boldsymbol{\gamma}_B$ are the local displacement amplitudes in translation and rotation of the interface nodes and $\boldsymbol{\eta}_I$ is the vector of internal mode intensities.

The corotational formulation of the superelement presented in this section is inspired from Ref. [18]. However, unlike in this reference, the position and orientation of the corotational frame is represented by an independent, massless node of coordinates

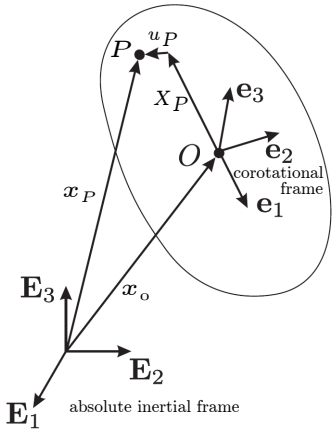

Figure 6.3: Kinematics of a superelement.

($\boldsymbol{x}_0$,$\boldsymbol{\alpha}_0$) explicitly added to the set of generalized coordinates $\boldsymbol{q}$ of the superelement:

$$\boldsymbol{q} = \begin{Bmatrix} \boldsymbol{x}_0 \\ \boldsymbol{\alpha}_0 \\ \boldsymbol{x}_B \\ \boldsymbol{\alpha}_B \\ \boldsymbol{\eta}_I \end{Bmatrix} \tag{6.17}$$

where $\boldsymbol{x}_B$ and $\boldsymbol{\alpha}_B$ are the absolute nodal positions and nodal rotation parameters of the boundary nodes; $\boldsymbol{\eta}_I$ are the modal amplitudes of the internal modes. This approach introduces 6 additional unknowns ($\boldsymbol{x}_0$, $\boldsymbol{\alpha}_0$) in the set of generalized coordinates of the system and therefore increases the number of the equations of motion. But this allows to simplify some expressions, especially in the contact formulation and in the definition of the corotational frame as it will be shown in the next sections. Moreover, matching the corotational frame to an additional node offers a convenient way to prescribe the overall motion of the superelement.

The local displacement $\boldsymbol{u}_B$ and the local rotation $\boldsymbol{\gamma}_B$ in the corotational frame can be computed from the absolute positions $\boldsymbol{x}_B$ and orientation variables $\boldsymbol{\alpha}_B$ of the boundary nodes by inverting Eqs. 6.13-6.14

$$\boldsymbol{u}_{B_i} = \boldsymbol{R}_0^T(\boldsymbol{x}_{B_i} - \boldsymbol{x}_0) - \boldsymbol{X}_{B_i} \tag{6.18}$$

$$\boldsymbol{R}(\boldsymbol{\gamma}_{B_i}) = \boldsymbol{R}_0^T \boldsymbol{R}_{B_i} \tag{6.19}$$

Remarks

- The rotation variables are represented within the framework of the Lie group theory [15, 128] whereas a parametrization of spherical motion is used in Ref. [18] as briefly summarized in section 2.2.1. This choice has been made to circumvent

the drawbacks of the rotation parametrization and to benefit from parts of a MATLAB code based on Lie groups and developed at the University of Liège to simulate multibody systems (see [128]). From the point of view of the superelement and the contact condition formulation, only a few things change between these two different representations of spherical motion. The formulations presented hereafter could be easily particularized if a rotation parametrization with a Cartesian rotation vector was used.

- One can notice that $\{\boldsymbol{x}_B^T\ \boldsymbol{\alpha}_B^T\}^T$ is a condensed notation since all boundary nodes have not necessarily 6 DOFs. Indeed, according to the type of finite elements (beam, shell, volume, etc) in the initial mesh before linear reduction, the boundary nodes can have only translational or only rotational degrees of freedom. For each boundary node, the three corresponding DOFs are removed from the set $\{\boldsymbol{x}_B^T\ \boldsymbol{\alpha}_B^T\}^T$ if not present in the initial FE model.

6.4.2 Elastic and inertia forces

In order to generate the equations of motion and thus compute the elastic and inertia forces, the **Hamilton principle** summarized in section 2.2.2 is used. The stationarity condition $\delta A = 0$ of a conservative system is expressed as:

$$\delta A = \delta \int_{t_1}^{t_2} \mathcal{L}\ \mathrm{d}t = 0 \tag{6.20}$$

where the Lagrangian $\mathcal{L}$ is defiend by $\mathcal{L} = \mathcal{K} - \mathcal{V}$, with $\mathcal{K}$ is the kinetic energy and $\mathcal{V}$ is the potential energy of a superelement.

The **potential energy** $\mathcal{V}$ can be seen as the internal deformation energy of the superelement. In the corotational frame, $\mathcal{V}$ and its variation $\delta\mathcal{V}$ have the following expressions:

$$\mathcal{V} = \frac{1}{2}\boldsymbol{\eta}^T\ \overline{\boldsymbol{K}}\boldsymbol{\eta} \qquad , \qquad \delta\mathcal{V} = \delta\boldsymbol{\eta}^T\ \overline{\boldsymbol{K}}\boldsymbol{\eta} \tag{6.21}$$

The various terms of the variation of the local coordinates vector $\delta\boldsymbol{\eta}$ are defined by:

$$\delta\boldsymbol{u}_{B_i} = \boldsymbol{R}_0^T(\delta\boldsymbol{x}_{B_i} - \delta\boldsymbol{x}_0) + \widetilde{\boldsymbol{R}_0^T(\boldsymbol{x}_{B_i} - \boldsymbol{x}_0)}\ \delta\boldsymbol{\Theta}_0 \tag{6.22}$$

$$\delta\boldsymbol{\gamma}_{B_i} \cong \mathrm{vect}\left(\delta\boldsymbol{R}(\boldsymbol{\gamma}_{B_i})\right) = [\boldsymbol{B}_1\ \boldsymbol{B}_2]\begin{Bmatrix}\delta\boldsymbol{\Theta}_{B_i}\\ \delta\boldsymbol{\Theta}_0\end{Bmatrix} \tag{6.23}$$

with:

$$\boldsymbol{B}_1 = \frac{1}{2}\begin{bmatrix} R_{22}+R_{33} & -R_{21} & -R_{31} \\ -R_{12} & R_{11}+R_{33} & -R_{32} \\ -R_{13} & -R_{23} & R_{11}+R_{22} \end{bmatrix} \tag{6.24}$$

$$\boldsymbol{B}_2 = \frac{1}{2}\begin{bmatrix} -(R_{22}+R_{33}) & R_{12} & R_{13} \\ R_{21} & -(R_{11}+R_{33}) & R_{23} \\ R_{31} & R_{32} & -(R_{11}+R_{22}) \end{bmatrix} \tag{6.25}$$

The expression 6.23 is valid if the assumption of small rotations can be adopted, i.e. $\boldsymbol{R}(\delta\boldsymbol{\gamma}_{B_i}) \cong \boldsymbol{I} + \delta\widetilde{\boldsymbol{\gamma}}_{B_i}$. The operator vect represents the vectorial map.

From Equations 6.22 and 6.23, a kinematic tangential relationship between $\delta\boldsymbol{\eta}$ and $\delta\boldsymbol{q}$ can be easily obtained:

$$\delta\boldsymbol{\eta} = \boldsymbol{P}(\boldsymbol{q})\ \delta\boldsymbol{q} \tag{6.26}$$

with

$$\delta\boldsymbol{\eta} = \begin{Bmatrix} \delta\boldsymbol{u}_B \\ \delta\boldsymbol{\gamma}_B \\ \delta\boldsymbol{\eta}_I \end{Bmatrix}, \quad \boldsymbol{P}(\boldsymbol{q}) = \begin{bmatrix} -\boldsymbol{R}_0^T & \overbrace{\boldsymbol{R}_0^T(\boldsymbol{x}_{B_i}-\boldsymbol{x}_0)} & \boldsymbol{R}_0^T & \boldsymbol{0} & \boldsymbol{0} \\ \boldsymbol{0} & \boldsymbol{B}_2 & \boldsymbol{0} & \boldsymbol{B}_1 & \boldsymbol{0} \\ \boldsymbol{0} & \boldsymbol{0} & \boldsymbol{0} & \boldsymbol{0} & \boldsymbol{I} \end{bmatrix}, \quad \delta\boldsymbol{q} = \begin{Bmatrix} \delta\boldsymbol{x}_0 \\ \delta\boldsymbol{\Theta}_0 \\ \delta\boldsymbol{x}_B \\ \delta\boldsymbol{\Theta}_B \\ \delta\boldsymbol{\eta}_I \end{Bmatrix} \tag{6.27}$$

Following the approach described in [42], the **kinetic energy** $\mathcal{K}$ evaluated in the corotational frame is expressed by Eq. 6.28 even though this expression is not fully consistent.

$$\mathcal{K} = \frac{1}{2}\boldsymbol{\tau}^T\overline{\boldsymbol{M}}\boldsymbol{\tau} \tag{6.28}$$

The vector $\boldsymbol{\tau}$ represents the velocities in the corotational frame and is defined by:

$$\boldsymbol{\tau} = \begin{Bmatrix} \boldsymbol{R}_0^T\dot{\boldsymbol{x}}_B \\ \boldsymbol{\Omega}_B \\ \dot{\boldsymbol{\eta}}_I \end{Bmatrix} \tag{6.29}$$

where the term $\boldsymbol{R}_0^T\dot{\boldsymbol{x}}_B$ can be interpreted as the absolute translational velocities of the boundary nodes expressed in the corotational frame. $\boldsymbol{\Omega}_B$ is the angular velocities of the boundary nodes expressed in the material frame and corresponds also, in first approximation, to the angular velocity vector in the corotational frame. Finally, $\dot{\boldsymbol{\eta}}_I$ is the time derivative of the vibration mode intensities.

Equation 6.30 represents the linear relation of the frame transformation between the velocity vector in the corotational frame ($\boldsymbol{\tau}$) and in the absolute inertia frame (vector $\boldsymbol{v}$ defined in Eq. 6.31).

$$\boldsymbol{\tau} = \boldsymbol{V}_1\ \boldsymbol{v} \qquad \text{with} \qquad \boldsymbol{V}_1(\boldsymbol{q}) = \begin{bmatrix} \boldsymbol{0} & \boldsymbol{0} & \boldsymbol{R}_0^T & \boldsymbol{0} & \boldsymbol{0} \\ \boldsymbol{0} & \boldsymbol{0} & \boldsymbol{0} & \boldsymbol{I} & \boldsymbol{0} \\ \boldsymbol{0} & \boldsymbol{0} & \boldsymbol{0} & \boldsymbol{0} & \boldsymbol{I} \end{bmatrix} \tag{6.30}$$

$$\boldsymbol{v} = \begin{Bmatrix} \dot{\boldsymbol{x}}_0 \\ \boldsymbol{\Omega}_0 \\ \dot{\boldsymbol{x}}_B \\ \boldsymbol{\Omega}_B \\ \dot{\boldsymbol{\eta}}_I \end{Bmatrix} \tag{6.31}$$

The variation of the kinetic energy can be simply expressed as:

$$\delta\mathcal{K} = \delta\boldsymbol{\tau}^T \overline{\boldsymbol{M}}\boldsymbol{\tau} \tag{6.32}$$

with

$$\delta\boldsymbol{\tau} = \begin{Bmatrix} \delta(\boldsymbol{R}_0^T\dot{\boldsymbol{x}}_B) \\ \delta\boldsymbol{\Omega}_B \\ \delta\dot{\boldsymbol{\eta}}_I \end{Bmatrix} \tag{6.33}$$

The first two terms of $\delta\boldsymbol{\tau}$ are computed by:

$$\delta(\boldsymbol{R}_0^T\dot{\boldsymbol{x}}_B) = \boldsymbol{R}_0^T\,\delta\dot{\boldsymbol{x}}_B + \widetilde{\boldsymbol{R}_0^T\dot{\boldsymbol{x}}_B}\,\delta\boldsymbol{\Theta}_0 \tag{6.34}$$

$$\delta\boldsymbol{\Omega}_B = \widetilde{\boldsymbol{\Omega}}_B\,\delta\boldsymbol{\Theta}_B + \delta\dot{\boldsymbol{\Theta}}_B \tag{6.35}$$

Finally, $\delta\boldsymbol{\tau}$ can be reformulated as:

$$\delta\boldsymbol{\tau} = \boldsymbol{V}_1\,\delta\dot{\boldsymbol{q}} + \boldsymbol{V}_2\,\delta\boldsymbol{q} \tag{6.36}$$

where $\boldsymbol{V}_1$ is already defined in Eq. 6.30 and $\boldsymbol{V}_2$ has the following expression:

$$\boldsymbol{V}_2 = \begin{bmatrix} \boldsymbol{0} & \widetilde{\boldsymbol{R}_0^T\dot{\boldsymbol{x}}_B} & \boldsymbol{0} & \boldsymbol{0} & \boldsymbol{0} \\ \boldsymbol{0} & \boldsymbol{0} & \boldsymbol{0} & \widetilde{\boldsymbol{\Omega}}_B & \boldsymbol{0} \\ \boldsymbol{0} & \boldsymbol{0} & \boldsymbol{0} & \boldsymbol{0} & \boldsymbol{0} \end{bmatrix} \tag{6.37}$$

The Hamilton principle (Eq. 6.20) can now be explicitly restated according to the potential and kinetic energies detailed hereabove:

$$\delta A = \int_{t_1}^{t_2} \delta\mathcal{L}\;\mathrm{d}t = \int_{t_1}^{t_2} \delta\dot{\boldsymbol{q}}^T\boldsymbol{V}_1^T\overline{\boldsymbol{M}}\boldsymbol{\tau} + \delta\boldsymbol{q}^T\boldsymbol{V}_2^T\overline{\boldsymbol{M}}\boldsymbol{\tau} - \delta\boldsymbol{q}^T\boldsymbol{P}^T\overline{\boldsymbol{K}}\boldsymbol{\eta}\;\mathrm{d}t \tag{6.38}$$

If the first term of Eq. 6.38 is integrated by parts, this equation becomes:

$$\int_{t_1}^{t_2} \delta\mathcal{L}\;\mathrm{d}t = \left[\delta\boldsymbol{q}^T\boldsymbol{V}_1^T\overline{\boldsymbol{M}}\boldsymbol{\tau}\right]_{t_1}^{t_2} - \int_{t_1}^{t_2} \delta\boldsymbol{q}^T\left[\left(\dot{\boldsymbol{V}}_1^T\overline{\boldsymbol{M}}\boldsymbol{\tau} + \boldsymbol{V}_1^T\overline{\boldsymbol{M}}\dot{\boldsymbol{\tau}}\right) - \boldsymbol{V}_2^T\overline{\boldsymbol{M}}\boldsymbol{\tau} + \boldsymbol{P}^T\overline{\boldsymbol{K}}\boldsymbol{\eta}\right]\mathrm{d}t \tag{6.39}$$

Because of the independence and arbitrary nature of the variations $\delta\boldsymbol{q}$, the combined expression of the elastic, the inertia and the gyroscopic forces can be easily deduced:

$$\boldsymbol{g}(\boldsymbol{q},\boldsymbol{v},\dot{\boldsymbol{v}}) = \left(\dot{\boldsymbol{V}}_1^T\overline{\boldsymbol{M}}\boldsymbol{\tau} + \boldsymbol{V}_1^T\overline{\boldsymbol{M}}\dot{\boldsymbol{\tau}}\right) - \boldsymbol{V}_2^T\overline{\boldsymbol{M}}\boldsymbol{\tau} + \boldsymbol{P}^T\overline{\boldsymbol{K}}\boldsymbol{\eta} \tag{6.40}$$

The time derivative of the vector $\boldsymbol{\tau}$ and of the matrix $\boldsymbol{V}_1$ are expressed by Eqs. 6.41 and 6.42 respectively.

$$\dot{\boldsymbol{\tau}} = \left\{ \begin{array}{c} \boldsymbol{R}_0^T \ddot{\boldsymbol{x}}_B - \widetilde{\boldsymbol{\Omega}}_0 \boldsymbol{R}_0^T \dot{\boldsymbol{x}}_B \\ \dot{\boldsymbol{\Omega}}_B \\ \ddot{\boldsymbol{\eta}}_I \end{array} \right\} = \boldsymbol{V}_1 \ \dot{\boldsymbol{v}} + \boldsymbol{V}_3 \ \boldsymbol{\Omega}_0 \qquad \text{with} \qquad \boldsymbol{V}_3 = \begin{bmatrix} \widetilde{\boldsymbol{R}_0^T \dot{\boldsymbol{x}}_B} \\ \boldsymbol{0} \\ \boldsymbol{0} \end{bmatrix} \tag{6.41}$$

$$\dot{\boldsymbol{V}}_1 = -\boldsymbol{V}_4 \boldsymbol{V}_1 \qquad \text{with} \qquad \boldsymbol{V}_4 = \begin{bmatrix} \widetilde{\boldsymbol{\Omega}}_0 & \boldsymbol{0} & \boldsymbol{0} \\ \boldsymbol{0} & \boldsymbol{0} & \boldsymbol{0} \\ \boldsymbol{0} & \boldsymbol{0} & \boldsymbol{0} \end{bmatrix} \tag{6.42}$$

After replacing Eqs. 6.41-6.42 into the force vector $\boldsymbol{g}$ (Eq. 6.40), the various contributions can be easily identified: $\boldsymbol{g}^{el}$ is the vector of elastic forces in the superelement, $\boldsymbol{g}^{iner}$ is the vector of inertia forces, and $\boldsymbol{g}^{gyr}$ is the vector of gyroscopic forces.

$$\boldsymbol{g}^{el}(\boldsymbol{q}) = \boldsymbol{P}^T \overline{\boldsymbol{K}} \boldsymbol{\eta} \tag{6.43}$$

$$\boldsymbol{g}^{iner}(\boldsymbol{q}, \dot{\boldsymbol{v}}) = \boldsymbol{V}_1^T \ \overline{\boldsymbol{M}} \boldsymbol{V}_1 \ \dot{\boldsymbol{v}} \tag{6.44}$$

$$\boldsymbol{g}^{gyr}(\boldsymbol{q}, \boldsymbol{v}) = \left(\boldsymbol{V}_1^T \boldsymbol{V}_4 - \boldsymbol{V}_2^T \right) \overline{\boldsymbol{M}} \boldsymbol{V}_1 \ \boldsymbol{v} + \boldsymbol{V}_1^T \overline{\boldsymbol{M}} \boldsymbol{V}_3 \ \boldsymbol{\Omega}_0 \tag{6.45}$$

Contribution to the iteration matrix

In order to compute the tangent stiffness matrix of the superelement, the dependency with respect to $\boldsymbol{q}$ of inertia and gyroscopic forces can often be ignored in first approximation so that only the spatial derivative of elastic forces has to be accounted for. If the derivative of the connection matrix $\boldsymbol{P}$ is neglected, the tangent stiffness matrix such that the directional derivative satisfies $D\boldsymbol{g}^{el}(\boldsymbol{q}) \cdot \delta\boldsymbol{q} = \boldsymbol{K}_t^{se} \ \delta\boldsymbol{q}$ takes the form:

$$\boldsymbol{K}_t^{se} = \frac{\partial \boldsymbol{g}^{el}}{\partial \boldsymbol{q}} \simeq \boldsymbol{P}^T \overline{\boldsymbol{K}} \boldsymbol{P} \tag{6.46}$$

The tangent mass matrix of the superelement is obtained by differentiation of the inertia forces with respect to the generalized accelerations $\dot{\boldsymbol{v}}$:

$$\boldsymbol{M}^{se} = \frac{\partial \boldsymbol{g}^{iner}}{\partial \dot{\boldsymbol{v}}} = \boldsymbol{V}_1^T \ \overline{\boldsymbol{M}} \boldsymbol{V}_1 \tag{6.47}$$

Finally, in some specific cases, it could be useful to include the contribution of gyroscopic forces into the iteration matrix to improve the convergence rate. The tangent damping matrix is computed by differentiating the gyroscopic forces with respect to the velocity vector in the absolute frame ($\boldsymbol{v}$):

$$\boldsymbol{C}_t^{se} = \frac{\partial \boldsymbol{g}^{gyr}}{\partial \boldsymbol{v}} = \left(\boldsymbol{V}_1^T \boldsymbol{V}_4 - \boldsymbol{V}_2^T \right) \overline{\boldsymbol{M}} \boldsymbol{V}_1 + \boldsymbol{V}_1^T \left(\overline{\boldsymbol{M}} \boldsymbol{C}_1 + \boldsymbol{C}_2 \right) + \boldsymbol{C}_3 \tag{6.48}$$

where the matrices $\boldsymbol{C}_1$, $\boldsymbol{C}_2$ and $\boldsymbol{C}_3$ and given by:

$$\boldsymbol{C}_1 = \begin{bmatrix} \boldsymbol{0} & \boldsymbol{V}_3 & \begin{bmatrix} -\widetilde{\boldsymbol{\Omega}}_0 \boldsymbol{R}_0^T \\ \boldsymbol{0} \\ \boldsymbol{0} \end{bmatrix} & \boldsymbol{0} & \boldsymbol{0} \end{bmatrix} \quad , \quad \boldsymbol{C}_2 = \begin{bmatrix} \boldsymbol{0} & -\widetilde{(\overline{\boldsymbol{M}}\boldsymbol{V}_1\boldsymbol{v})_{\boldsymbol{x}_B}} & \boldsymbol{0} & \boldsymbol{0} & \boldsymbol{0} \\ \boldsymbol{0} & \boldsymbol{0} & \boldsymbol{0} & \boldsymbol{0} & \boldsymbol{0} \\ \boldsymbol{0} & \boldsymbol{0} & \boldsymbol{0} & \boldsymbol{0} & \boldsymbol{0} \end{bmatrix}$$

$$\boldsymbol{C}_3 = \begin{bmatrix} \boldsymbol{0} & \boldsymbol{0} & \boldsymbol{0} & \boldsymbol{0} & \boldsymbol{0} \\ \boldsymbol{0} & \boldsymbol{0} & -\widetilde{(\overline{\boldsymbol{M}}\boldsymbol{V}_1\boldsymbol{v})_{\boldsymbol{x}_B}}\boldsymbol{R}_0^T & \boldsymbol{0} & \boldsymbol{0} \\ \boldsymbol{0} & \boldsymbol{0} & \boldsymbol{0} & \boldsymbol{0} & \boldsymbol{0} \\ \boldsymbol{0} & \boldsymbol{0} & \boldsymbol{0} & -\widetilde{(\overline{\boldsymbol{M}}\boldsymbol{V}_1\boldsymbol{v})_{\alpha_B}} & \boldsymbol{0} \\ \boldsymbol{0} & \boldsymbol{0} & \boldsymbol{0} & \boldsymbol{0} & \boldsymbol{0} \end{bmatrix} \tag{6.49}$$

The notations $(\overline{\boldsymbol{M}}\boldsymbol{V}_1\boldsymbol{v})_{\boldsymbol{x}_B}$ and $(\overline{\boldsymbol{M}}\boldsymbol{V}_1\boldsymbol{v})_{\alpha_B}$ mean that some components of the vector $\overline{\boldsymbol{M}}\boldsymbol{V}_1\boldsymbol{v}$ are extracted. The indexes $\boldsymbol{x}_B$ and $\boldsymbol{\gamma}_B$ correspond respectively to the components in translation or in rotation at the boundary nodes.

6.5 Corotational frame definition

A corotational frame is attached to each body modelled by a superelement and follows its gross motion. This local frame is defined by the position vector $\boldsymbol{x}_0$ of the frame origin and the rotation matrix $\boldsymbol{R}_0$ that depends on the rotation variables $\boldsymbol{\alpha}_0$ and gives the orientation of the local frame about the inertial frame. Several formulations are available to determine the corotational frame. The simplest way would be to associate the reference frame with one of the boundary nodes. However, with this method the mechanical response of the superelement can be sensitive to the chosen boundary node. In Ref. [42] another definition is presented where the position and orientation of the local frame are obtained by a weighted mean of positions and orientations of the boundary nodes. The drawback of such definition results from complex couplings between global and local variables, and thus involves the manipulation of large matrices where the sparsity is not preserved.

The corotational frame definition described in this section requires that the frame variables $\boldsymbol{x}_0$, $\boldsymbol{\alpha}_0$ are explicitly added to the vector $\boldsymbol{q}$ of generalized coordinates of the superelement (Eq. 6.17). A set of 6 holonomic kinematic constraints is needed to link these local frame variables to the boundary node coordinates. Therefore, in addition to $\boldsymbol{x}_0$ and $\boldsymbol{\alpha}_0$, six other unknowns, the Lagrange multipliers associated with the constraints, are added for each superelement. The resulting reference frame is equivalent to a Buckens frame [142].

The boundary node displacements ($\boldsymbol{u}_B$,$\boldsymbol{\gamma}_B$) in the corotational frame are defined relatively to $\boldsymbol{x}_0$ and $\boldsymbol{\alpha}_0$ (see Eqs. 6.18-6.19). Therefore, small variations of the generalized coordinates ($\boldsymbol{x}_0$,$\boldsymbol{\alpha}_0$) are equivalent to add a small rigid body motion to the relative displacements and rotations of the boundary nodes. The aim of the new constraints

(Eq. 6.50) is to minimize the virtual work of the boundary node inertia forces in a rigid body displacement. In other words, the rigid body motion defined in the corotational frame ($\boldsymbol{U}_{rig}$) and the relative displacements and rotations ($\boldsymbol{\eta}_B^T = \{\boldsymbol{u}_B^T \ \boldsymbol{\gamma}_B^T\}$) must be M-orthogonal.

$$\boldsymbol{\Phi}(\boldsymbol{q}) \equiv \boldsymbol{U}_{rig}^T \ \overline{\boldsymbol{M}}_{BB} \ \boldsymbol{\eta}_B(\boldsymbol{q}) = \boldsymbol{0} \tag{6.50}$$

The matrix of the 6 rigid body modes in the corotational frame is written as:

$$\boldsymbol{U}_{rig} = \begin{bmatrix} \boldsymbol{U}_{rig,1} \\ \vdots \\ \boldsymbol{U}_{rig,i} \\ \vdots \\ \boldsymbol{U}_{rig,n_{Bnode}} \end{bmatrix} \tag{6.51}$$

where each matrix $\boldsymbol{U}_{rig,i}$ is related to the i^{th} boundary node:

$$\boldsymbol{U}_{rig,i} = \begin{bmatrix} \boldsymbol{I}_{3\times3} & -\widetilde{\boldsymbol{X}}_{B_i} \\ \boldsymbol{0}_{3\times3} & \boldsymbol{I}_{3\times3} \end{bmatrix} \tag{6.52}$$

$\boldsymbol{X}_{B_i}$ being the undeformed position of the boundary node B_i in the corotational frame. The first three columns of $\boldsymbol{U}_{rig}$ represent the rigid body modes in translation and the last three columns are the rigid body modes in rotation.

The corotational frame coordinates ($\boldsymbol{x}_0$,$\boldsymbol{\alpha}_0$) do not appear explicitly in the constraint formulation (Eq. 6.50), but the dependence with respect to them is included in the definition of the local displacement vector ($\boldsymbol{\eta}_B$) according to Eqs. 6.18-6.19. The matrices ($\boldsymbol{U}_{rig}$, $\overline{\boldsymbol{M}}_{BB}$) involved in the kinematic constraints are invariant.

Contrarily to both corotational frame formulations previously mentioned, the superelement frame can be defined even if the boundary nodes have no rotational degrees of freedom, which is often the case if the initial finite element model is meshed with volume finite elements. At equilibrium, the values given to $\boldsymbol{x}_0$ and $\boldsymbol{R}_0$ can be interpreted as the position and orientation of the center of gravity of the body.

The constraints (Eq. 6.50) are enforced by using the Lagrange multiplier method. The virtual work of the kinematic constraints 6.50 is expressed as:

$$\delta\mathcal{W} = \delta\boldsymbol{q}^T \boldsymbol{\Phi}_{\boldsymbol{q}}^T \ \boldsymbol{\lambda} + \delta\boldsymbol{\lambda}^T \ \boldsymbol{\Phi} \tag{6.53}$$

where $\boldsymbol{\Phi}_{\boldsymbol{q}}$ is defined by:

$$\boldsymbol{\Phi}_{\boldsymbol{q}} = \boldsymbol{U}_{rig} \overline{\boldsymbol{M}}_{BB} \boldsymbol{P}_B \tag{6.54}$$

The matrix $\boldsymbol{P}_B$ is the submatrix of $\boldsymbol{P}$ (Eq. 6.27) obtained by wiping out the last column.

Equation 6.53 can be now restated as:

$$\delta\mathcal{W} = \left\{\delta\boldsymbol{q}^T \ \delta\boldsymbol{\lambda}^T\right\} \begin{Bmatrix} \boldsymbol{P}_B^T \overline{\boldsymbol{M}}_{BB}^T \boldsymbol{U}_{rig}^T \ \boldsymbol{\lambda} \\ \boldsymbol{\Phi} \end{Bmatrix} \tag{6.55}$$

The constraint forces induced by the corotational frame formulation adopted can be easily identified in this last expression:

$$\boldsymbol{g}^{coro}(\boldsymbol{q},\boldsymbol{\lambda}) = \boldsymbol{P}_B^T \overline{\boldsymbol{M}}_{BB}^T \boldsymbol{U}_{rig}^T \, \boldsymbol{\lambda} \tag{6.56}$$

They apply on the boundary degrees of freedom and on the corotational frame coordinates, but not on the internal modal variables $\boldsymbol{\eta}_I$ since the last column of $\boldsymbol{P_B}$ is full of zeros.

The virtual work needs to be further differentiated in order to obtain the iteration matrix associated with these 6 kinematic constraints:

$$\delta \mathrm{d}\mathcal{W} = \left\{ \delta \boldsymbol{q}^T \;\; \delta \boldsymbol{\lambda}^T \right\} \begin{bmatrix} \mathbf{0} & k\,\boldsymbol{\Phi}_{\boldsymbol{q}}^T \\ k\,\boldsymbol{\Phi}_{\boldsymbol{q}} & \mathbf{0} \end{bmatrix} \begin{Bmatrix} \mathrm{d}\boldsymbol{q} \\ \mathrm{d}\boldsymbol{\lambda} \end{Bmatrix} \tag{6.57}$$

The contribution to the iteration matrix is then expressed as:

$$\boldsymbol{K}_t^{coro} = \begin{bmatrix} \mathbf{0} & k\,\boldsymbol{\Phi}_{\boldsymbol{q}}^T \\ k\,\boldsymbol{\Phi}_{\boldsymbol{q}} & \mathbf{0} \end{bmatrix} \tag{6.58}$$

6.6 Contact detection algorithm

In order to determine the presence or absence of contact for each candidate contact area over the superelement skin, a contact detection algorithm based on a standard node-to-face projection method is used. The goal of this search procedure is to find which node of the slave body is in contact with which element face of the master body (see Fig. 6.4).

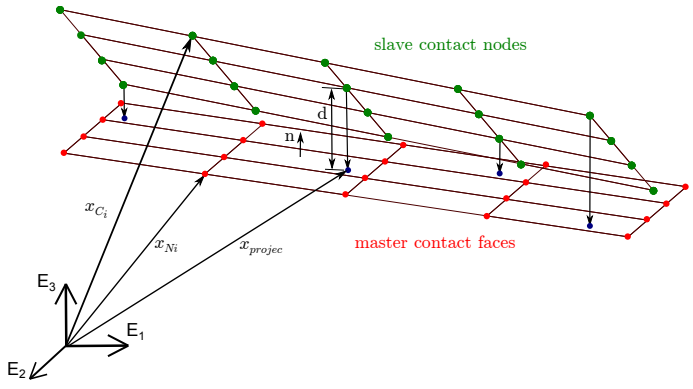

Figure 6.4: Projection of slave nodes on master faces.

In case of a large number of potential contact nodes, the size of the superelement matrices could not be drastically reduced compared with initial finite element model if all the contact nodes are retained as boundary nodes. The solution adopted to keep

a compact superelement model consists in considering the candidate contact nodes as virtual nodes. This approach allows retaining only a few boundary nodes and not all the candidate contact nodes.

The contact detection algorithm presented here is suitable for a master triangular surface and can be summarized by the following steps (see Fig. 6.9):

1. Computation of the absolute positions $\boldsymbol{x}_{C_i}$, $\boldsymbol{x}_{N_i}$ of the candidate contact nodes on the slave and master bodies respectively.

   The absolute position of virtual nodes is computed from the corotational frame coordinates ($\boldsymbol{x}_0$,$\boldsymbol{R}_0$) and the modal amplitudes ($\boldsymbol{\eta}$), see Equations (6.59-6.60) which are obtained by combining Equations (6.13) and (6.15).

   $$\boldsymbol{x}_{C_i} = \boldsymbol{x}_0^s + \boldsymbol{R}_0^s(\boldsymbol{X}_{C_i} + \overline{\boldsymbol{\Psi}}_{C_i}\boldsymbol{\eta}^s) \tag{6.59}$$
   $$\boldsymbol{x}_{N_i} = \boldsymbol{x}_0^m + \boldsymbol{R}_0^m(\boldsymbol{X}_{N_i} + \overline{\boldsymbol{\Psi}}_{N_i}\boldsymbol{\eta}^m) \tag{6.60}$$

   The exponents s and m permit to distinguish the variables relative to the slave and master bodies. The accuracy of the computed contact node positions depends on the detail level provided by the 3 rows of the reduction basis ($\overline{\boldsymbol{\Psi}}$) relative to the contact node C_i or N_i.

   The candidate contact nodes are a fixed set of nodes located on the skin of the non-reduced model. These nodes are selected by the model analyst during the model construction and their absolute positions are computed at each Newton-Raphson iteration of the time integration scheme (see Section 2.2.3).

   Let us note that if some candidate contact nodes are retained as superelement boundary nodes, their position vectors are readily available in the vector $\boldsymbol{q}$ of generalized coordinates and do not have to be computed.

2. Determination of the normal direction for each master contact face.

   The normal direction of a triangular face can be easily obtained by:

   $$\boldsymbol{n} = \frac{\boldsymbol{x}_{N12} \times \boldsymbol{x}_{N13}}{\|\boldsymbol{x}_{N12} \times \boldsymbol{x}_{N13}\|} = \frac{\widetilde{\boldsymbol{x}}_{N12}\ \boldsymbol{x}_{N13}}{\|\widetilde{\boldsymbol{x}}_{N12}\ \boldsymbol{x}_{N13}\|} \tag{6.61}$$

   with $\boldsymbol{x}_{Nij} = \boldsymbol{x}_{Nj} - \boldsymbol{x}_{Ni}$ (see Fig. 6.5). The master nodes are numbered in order that $\boldsymbol{n}$ points towards the outside of the body faces.

   The topology of the potential contact zone has to be saved from the initial finite element model in order to determine the contact nodes that are the vertices of each master surface.

3. Computation of the normal distance between a slave node and the plane of a master surface.

   The basic equation of a plane is:

   $$n_x\ x + n_y\ y + n_z\ z + a = 0 \tag{6.62}$$

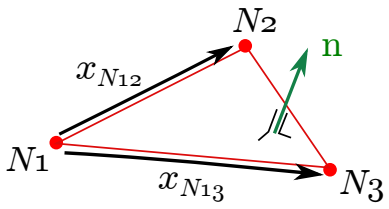

Figure 6.5: Definition of the normal vector to a master contact face.

where n_x, n_y, n_z are the three components of the normal direction to this plane (Eq. 6.61).

The independent term a can be simply determined if the coordinates of one point of the plane is known. For instance, if the first vertex of the master face is considered, a is defined by:

$$a = -(n_x\ x_{N1} + n_y\ y_{N1} + n_z\ z_{N1}) \tag{6.63}$$

The normal distance d between a slave node and a master surface can be then simply computed by:

$$d = n_x\ x_C + n_y\ y_C + n_z\ z_C + a \tag{6.64}$$

If d is positive, there is a gap between the slave node and the master surface and consequently this pair (slave node - master surface) is not in active contact. In this case, the next steps of the contact detection algorithm have not to be carried out.

4. Computation of the absolute coordinates of the projection of the slave node onto the master face plane.

   The position vector $\boldsymbol{x}_{projec}$ of a slave node projected onto the plane of a master surface is given by:

$$\begin{Bmatrix} x_{projec} \\ y_{projec} \\ z_{projec} \end{Bmatrix} = \begin{Bmatrix} (n_y^2 + n_z^2)\ x_C - n_x n_y\ y_C - n_x n_z\ z_C - a\ n_x \\ -n_x n_y\ x_C + (n_x^2 + n_z^2)\ y_C - n_y n_z\ z_C - a\ n_y \\ -n_x n_z\ x_C - n_y n_z\ y_C + (n_x^2 + n_y^2)\ z_C - a\ n_z \end{Bmatrix} \tag{6.65}$$

5. Determination of the relative position of the projection point inside the surface element.

   In the previous step, the slave node has been projected onto the plane containing the triangular-shaped master surface. Then, one has to determine whether the projection point is inside or outside the surface element. To this end, the barycentric coordinates can be used.

The position coordinates (x_{projec} , y_{projec} , z_{projec}) of the projected point can be expressed using a set of three barycentric coordinates (β_1,β_2,β_3):

$$x_{projec} = \beta_1\ x_{N1} + \beta_2\ x_{N2} + \beta_3\ x_{N3} \tag{6.66}$$

$$y_{projec} = \beta_1\ y_{N1} + \beta_2\ y_{N2} + \beta_3\ y_{N3} \tag{6.67}$$

$$z_{projec} = \beta_1\ z_{N1} + \beta_2\ z_{N2} + \beta_3\ z_{N3} \tag{6.68}$$

where $N1$,$N2$,$N3$ are the three vertices of the master face.

The space transformation from the absolute inertial frame to the barycentric coordinate space can be expressed as:

$$\begin{Bmatrix} \beta_1 \\ \beta_2 \\ \beta_3 \end{Bmatrix} = \begin{bmatrix} x_{N1} & x_{N2} & x_{N3} \\ y_{N1} & y_{N2} & y_{N3} \\ z_{N1} & z_{N2} & z_{N3} \end{bmatrix}^{-1} \begin{Bmatrix} x_{projec} \\ y_{projec} \\ z_{projec} \end{Bmatrix} \tag{6.69}$$

The projected point is inside the triangular area defined by the nodes N_i if $\beta_i > 0$ and $\beta_1 + \beta_2 + \beta_3 = 1$.

In order to avoid solving the system of equations (6.69), which is time consuming if the operation is repeated a lot of times, this step is only achieved if the node projected lies in the neighbourhood of the contact element. For instance, if the projection point is not located inside a 3D box surrounding the master surface element (see Fig. 6.6), it is not necessary to compute the barycentric coordinates since the slave node considered is not likely to be in contact with the master face tested.

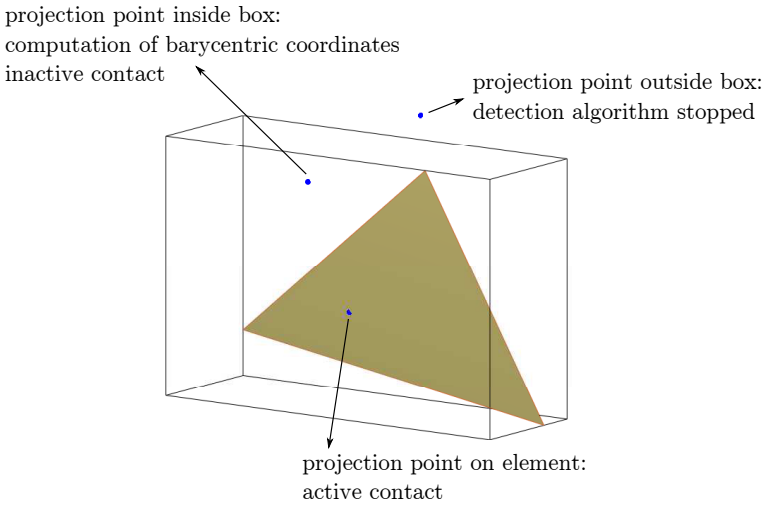

Figure 6.6: The contact detection algorithm can be stopped if the projection of the slave node in not in the vicinity of the master surface.

If the last condition is satisfied, the slave node and the master face tested by the contact detection algorithm are considered to be in active contact. This slave-master pair in effective contact has then to be saved and will be used in the formulation of the contact force vector as described in section 6.8.

Like for all node-to-surface projection approaches, it is recommended that the mesh of the slave body in the contact zone should be finer than the mesh of the master body. It prevents unreliable effective contact zones and numerical problems which can affect the robustness of the numerical simulation.

In particular geometric configurations such as the contact between two cylinders (see Fig. 6.7), spurious contacts can be erroneously detected. If all nodes of the cylindrical face are candidate contact nodes, the projection points of several slave nodes are inside the master surface element and the associated normal distances are negative. To circumvent this problem the (slave node)-(master surface) pair for which the norm of the normal distance d is higher than a threshold value $-|d_{max}|$ is eliminated from the set of active contacts. This constant parameter d_{max} is chosen according to the characteristic dimensions of the system and the maximum penetration length allowed between the bodies in contact.

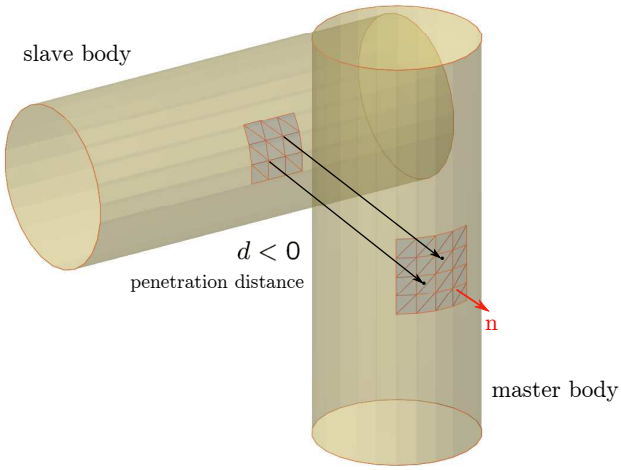

Figure 6.7: False contact detections.

If the penetration length is small, a given slave node is usually in contact at most with one master face. However, in particular situations such as depicted in Fig. 6.8, a slave node can be detected in contact with two or more master faces. Furthermore, due to accuracy errors, the same situation occurs when the projection point of the slave node is on or very close to an edge between two master faces.

The contact detection procedure detailed hereabove is simple but could be im-

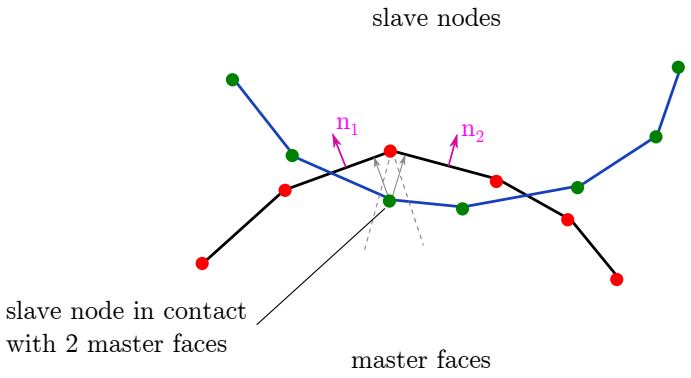

Figure 6.8: A slave node detected in contact with two master faces.

proved at nearly all stages from the point of view of the computational efficiency. For instance, in order to avoid the projection of each slave node on each master face, the implementation of a tree data structure such as an octree could greatly reduce the number of mathematical operations due to the projection method. Moreover, with the proposed algorithm the potential contact surfaces have to be triangular-shaped. Despite its limitations, this simple method will allow us to implement and assess the contact force formulation between superelements, which is the main original contribution of this chapter.

A similar contact detection procedure is described in Ref. [151] for quadrangular faces on the master body but this method involves nonlinear relations and therefore needs an iterative procedure to detect the active contact nodes. In our algorithm, each quadrangular face is split into two triangles.

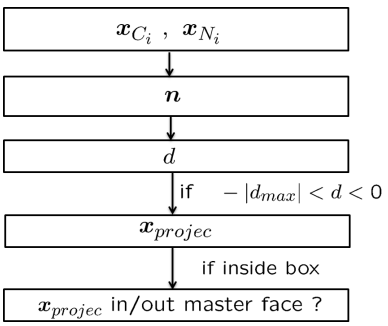

Figure 6.9: Flow chart of the contact detection algorithm.

6.7 Contact law

In Chapter 3, it has been shown that continuous contact models can be solved using a smooth integration scheme of the generalized-α family. Imposing non-penetration constraints would require the use of a nonsmooth time integration scheme, which is beyond the scope of the present thesis. Therefore, a penalty method is chosen as contact law for the developed contact formulation between two superelements.

In a general context such as the contact between spherical-shaped bodies, the local deformation is a *nonlinear* phenomenon in the contact zone. However, the compliance of the contacting bodies is accounted for by the *linear* elastic model embedded in the reduced matrices of each superelement. The nonlinearity can be represented in two different ways using whether a linear or a nonlinear contact law.

If the spatial discretization in the contact zone is sufficiently refined, a *linear* penalty function can be used since the contact nonlinearity is properly accounted for by the geometric variation of the active contact area with the magnitude of the approaching load applied on contacting bodies. The contact stiffness has to be high enough so that the local penetration is negligible with respect to the body strains. A superelement model should be able to model accurately the deformation of the contact area.

On the other hand, when the mesh in the potential contact zone is coarse or the superelement does not provide a detailed description of the deformations on the contact surface, a *nonlinear* contact law has to be used. Indeed, in this situation the contact phenomenon can be decomposed in two parts: local nonlinear effects at the contact points and a global linear elastic behaviour in the rest of the body. The penetration allowed by the penalty method can be seen as a measure of the local deformation near the contact point whereas the global flexibility is accounted for by the linear superelement.

In both cases, the contact law is expressed by Eq. 6.70 where ℓ represents the penetration length, k_p is the contact stiffness and c the damping coefficient. S_c^* is the mean area around the slave node in contact. As in the continuous impact model presented in Section 4.2, a damping contribution is added to introduce the energy dissipation involved by hard impact. The linear contact law is simply recovered by setting $n = 1$.

$$f(\ell,\dot{\ell}) = \begin{cases} S_c^* \left(k_p \, \ell^n + c \, \ell^n \, \dot{\ell} \right) & \text{if} \quad \ell > 0 \quad \text{active contact} \\ 0 & \text{if} \quad \ell < 0 \quad \text{no contact} \end{cases} \tag{6.70}$$

In order to render the contact law independent of the mesh density in the contact area, the mean area S_c^* of the element surfaces adjacent to the slave node in contact is

introduced as a multiplication factor in the contact law (Eq. 6.70):

$$S_c^* = \frac{1}{n_n} \sum_{i=1}^{n_n} S_i \tag{6.71}$$

where n_n is the number of nodes of the slave contact faces ($n_n = 3$ for triangular faces), the S_i are the areas of the element faces including the slave node for which the contact force magnitude is determined. Furthermore, the border effects between the contact surface and the connected free surfaces are avoided since only the element faces inside the candidate contact face are accounted for in the computation of the mean area S_c^* (Eq. 6.71). If the deformation of bodies are very small, the mean area S_c^* can be assumed constant, so that it is only computed in the initial configuration at $t = 0$ s and not at the following time steps. If the mesh is regular in the contact zone, the same mean area can be assigned to all contact nodes according to the mesh density.

The parameters k_p and c have the meaning of the contact stiffness and damping coefficient per unit surface area. In this way, these parameters have a constant value when the discretization of the contact surface is refined. These parameters are chosen in such a way that the penetration length is much lower than the elastic deformation. In order to avoid a jump at the beginning of the contact and a tension force at the end, the classical viscous damping term $c\ \dot{\ell}$ has been multiplied by the penetration length.

As for the contact models between rigid bodies (Chapter 4), the damping coefficient can be determined according to an energy restitution coefficient (see Eq. 4.11). Compared to a constant damping coefficient, the advantage of this definition of the damping coefficient lies in its adaptability with the relative velocity at the impact instant. In this way, the amount of damping introduced in the contact law is different for hard or smooth impact.

The penetration length ℓ and the penetration velocity $\dot{\ell}$ in the normal direction are computed as:

$$\ell = \boldsymbol{n}^T(\boldsymbol{x}_{N1} - \boldsymbol{x}_{C_i}) \tag{6.72}$$

$$\dot{\ell} = \boldsymbol{n}^T(\dot{\boldsymbol{x}}_{N1} - \dot{\boldsymbol{x}}_{C_i}) + (\boldsymbol{x}_{N1} - \boldsymbol{x}_{C_i})^T\ \dot{\boldsymbol{n}} \tag{6.73}$$

where $\dot{\boldsymbol{n}}$, the time derivative of $\boldsymbol{n}$ (Eq. 6.61), is given by:

$$\dot{\boldsymbol{n}} = \frac{\boldsymbol{I} - \boldsymbol{n}\boldsymbol{n}^T}{\left\|\widetilde{\boldsymbol{x}}_{N12}\ \boldsymbol{x}_{N13}\right\|}\ \boldsymbol{a}_{\dot{\boldsymbol{n}}} \tag{6.74}$$

with

$$\boldsymbol{a}_{\dot{\boldsymbol{n}}} = \left(\widetilde{\boldsymbol{x}}_{N13} - \widetilde{\boldsymbol{x}}_{N12}\right)\ \dot{\boldsymbol{x}}_{N1} - \widetilde{\boldsymbol{x}}_{N13}\ \dot{\boldsymbol{x}}_{N2} + \widetilde{\boldsymbol{x}}_{N12}\ \dot{\boldsymbol{x}}_{N3} \tag{6.75}$$

In Eqs. 6.73 and 6.75, the time derivative of absolute position vectors of the candidate contact nodes on the slave and master bodies are respectively computed as:

$$\dot{\boldsymbol{x}}_{Ci} = \dot{\boldsymbol{x}}_0^s - \boldsymbol{R}_0^s\widetilde{(\boldsymbol{X}_{C_i} + \overline{\boldsymbol{\Psi}}_{C_i}^s\boldsymbol{\eta}^s)}\ \boldsymbol{\Omega}_0^s + \boldsymbol{R}_0^s\overline{\boldsymbol{\Psi}}_{C_i}^s\boldsymbol{P}^s\ \boldsymbol{v}^s \tag{6.76}$$

$$\dot{\boldsymbol{x}}_{Ni} = \dot{\boldsymbol{x}}_0^m - \boldsymbol{R}_0^m\widetilde{(\boldsymbol{X}_{N_i} + \overline{\boldsymbol{\Psi}}_{Ni}^m\boldsymbol{\eta}^m)}\ \boldsymbol{\Omega}_0^m + \boldsymbol{R}_0^m\overline{\boldsymbol{\Psi}}_{Ni}^m\boldsymbol{P}^m\ \boldsymbol{v}^m \tag{6.77}$$

where the derivative of the tangent matrix $\boldsymbol{P}$ has been neglected.

6.8 Contact force formulation

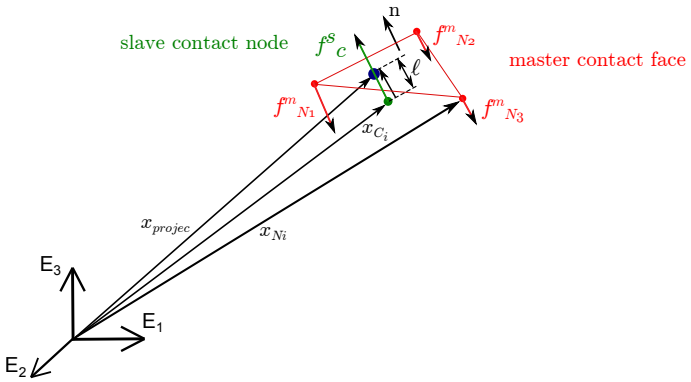

Figure 6.10: Kinematics of contact force.

The contact force (Eq. 6.78) applied on a contact node of the slave or master bodies has its magnitude f defined by the contact law (Eq. 6.70) and its direction given by the normal vector $\boldsymbol{n}$ to the master contact surface involved in the slave-master pair considered. For the master body, the participation factors w permit to distribute the contact force on the master nodes delimiting the master surface (see Fig. 6.10). In case of triangular contact faces, these participation factors are equivalent to the barycentric coordinates already computed in the detection algorithm presented in section 6.6. For the slave body, the parameter w is obviously always equal to one because the contact force amplitude is computed at this node

$$\boldsymbol{f}_c = w\ f\ \boldsymbol{n} \tag{6.78}$$

The contact nodes can be interpreted as virtual nodes since they do not necessarily correspond to the superelement boundary nodes. Therefore, each contact force applied on these virtual nodes has to be transferred to the generalized coordinates vector $\boldsymbol{q}$ of the superelement, loading the retained boundary nodes and the modal variables.

Since the contact force is computed by a penalty method, no kinematic constraint is involved and its contribution to the motion equations (Eq. 2.7) of the multibody system is only contained in the term of internal forces $\boldsymbol{g}^{int}(\boldsymbol{q}, \dot{\boldsymbol{q}})$. The virtual work principle is used in order to get the internal force vector associated with each nodal contact force:

$$\delta \mathcal{W}^{con}_{C_i} = \delta \boldsymbol{x}^T_{C_i}\ \boldsymbol{f}_c \tag{6.79}$$

The virtual displacements $\delta \boldsymbol{x}_{C_i}$ of the contact points are easily obtained by derivation

of Eqs. (6.59 -6.60):

$$\begin{aligned}\delta \boldsymbol{x}_{C_i} &= \delta \boldsymbol{x}_0 - \boldsymbol{R}_0 \widetilde{(\boldsymbol{X}_{C_i} + \boldsymbol{u}_{C_i})}\ \delta \boldsymbol{\Theta}_0 + \boldsymbol{R}_0\ \delta \boldsymbol{u}_{C_i} \\ &= \delta \boldsymbol{x}_0 - \boldsymbol{R}_0 \widetilde{\left(\boldsymbol{X}_{C_i} + \overline{\boldsymbol{\Psi}}_{C_i}\boldsymbol{\eta}\right)}\ \delta \boldsymbol{\Theta}_0 + \boldsymbol{R}_0 \overline{\boldsymbol{\Psi}}_{C_i} \boldsymbol{P}\ \delta \boldsymbol{q}\end{aligned} \tag{6.80}$$

where $\overline{\boldsymbol{\Psi}}_{C_i}$ are the 3 rows of the mode matrix $\overline{\boldsymbol{\Psi}}$ linked to the i^{th} contact node, $\delta\boldsymbol{\Theta}_0$ is the vector of virtual rotation in the corotational frame such that $\widetilde{\delta\boldsymbol{\Theta}_0} = \boldsymbol{R}_0^T\ \delta\boldsymbol{R}_0$ (see Ref. [42]).

The internal force vector $\boldsymbol{g}_{C_i}^{int,con}$ (Eq. 6.81) matching with the contact force $\boldsymbol{f}_c$ applied on the contact point $\boldsymbol{x}_{C_i}$ can be easily obtained by identification of Eq. (6.79) with the classical virtual work expression for a force element: $\delta\mathcal{W} = \delta\boldsymbol{q}^T\ \boldsymbol{g}^{int}$.

$$\boldsymbol{g}_{C_i}^{int,con} = \boldsymbol{P}^T \overline{\boldsymbol{\Psi}}_{C_i}^T \boldsymbol{R}_0^T\ \boldsymbol{f}_c + \left\{ \begin{array}{c} \boldsymbol{f}_c \\ \widetilde{\left(\boldsymbol{X}_{C_i} + \overline{\boldsymbol{\Psi}}_{C_i}\boldsymbol{\eta}\right)} \boldsymbol{R}_0^T\ \boldsymbol{f}_c \\ \boldsymbol{0} \\ \boldsymbol{0} \\ \boldsymbol{0} \end{array} \right\} \tag{6.81}$$

It can be noticed that the contact force vector (Eq. 6.81) has a compact form owing to our choice to add explicitly the corotational frame coordinates $(\boldsymbol{x}_0, \boldsymbol{\alpha}_0)$ in the set of superelement generalized coordinates $(\boldsymbol{q})$. With the corotational frame definition proposed in [42], the contact formulation would be more cumbersome, especially regarding the computation of the iteration matrix detailed below.

Contribution to the iteration matrix

In case of highly discontinuous behaviour such as resulting from unilateral contact, an accurate estimation of the iteration matrix is needed to ensure good convergence. Indeed, unless using extremely small time steps, the approximation of the iteration matrix by the mass matrix is not acceptable because the contribution of the tangent stiffness matrix is dominating.

The method of finite differences offers a simple way to obtain the tangent stiffness and damping matrices. However, this approach increases drastically the CPU time. Indeed, in order to compute the iteration matrix, each generalized coordinate involved in the element definition is successively submitted to a unit variation and the associated residual vector (Eq. 2.9) of the equation system has to be computed. For superelements with a significant number of boundary nodes and internal modes, the determination of the iteration matrix could be very costly. For instance, for the simple benchmark presented in section 6.9 the CPU time is 30 times longer with the finite difference approach than with an iteration matrix computed analytically.

An analytical determination of the tangent matrices ($\boldsymbol{K}_t$, $\boldsymbol{C}_t$) requires an effort to compute the absolute spatial derivative of the internal force vector $\boldsymbol{g}_{C_i}^{int,con}$ (Eq. 6.82) but it has to be computed only once and the CPU time for the full simulation is therefore greatly reduced.

$$\mathrm{d}\boldsymbol{g}_{C_i}^{con}(\boldsymbol{q},\boldsymbol{v}) = \frac{\partial \boldsymbol{g}_{C_i}^{con}}{\partial \boldsymbol{q}}\ \mathrm{d}\boldsymbol{q} + \frac{\partial \boldsymbol{g}_{C_i}^{con}}{\partial \boldsymbol{v}}\ \mathrm{d}\boldsymbol{v} \tag{6.82}$$

$$\text{with} \qquad \mathrm{d}\boldsymbol{q} = \begin{Bmatrix} \mathrm{d}\boldsymbol{q}^s \\ \mathrm{d}\boldsymbol{q}^m \end{Bmatrix} \quad , \quad \mathrm{d}\boldsymbol{v} = \begin{Bmatrix} \mathrm{d}\boldsymbol{v}^s \\ \mathrm{d}\boldsymbol{v}^m \end{Bmatrix} \tag{6.83}$$

In order to simplify some mathematical expressions, the internal contact force vector (Eq. 6.81) is restated as follows:

$$\boldsymbol{g}_{C_i}^{int,con} = f \begin{pmatrix} \boldsymbol{P}^T \overline{\boldsymbol{\Psi}}_{C_i}^T \boldsymbol{R}_0^T\ \boldsymbol{n} + \begin{Bmatrix} \boldsymbol{n} \\ \widetilde{\boldsymbol{z}}_{C_i} \boldsymbol{R}_0^T\ \boldsymbol{n} \\ \boldsymbol{0} \\ \boldsymbol{0} \\ \boldsymbol{0} \end{Bmatrix} \end{pmatrix} \tag{6.84}$$

where $\boldsymbol{z}_{C_i}$ is a compact notation for:

$$\boldsymbol{z}_{C_i} = \boldsymbol{X}_{C_i} + \boldsymbol{u}_{C_i} = \boldsymbol{X}_{C_i} + \overline{\boldsymbol{\Psi}}_{C_i} \boldsymbol{\eta} \tag{6.85}$$

The contact force $\boldsymbol{f}_c$ has been decomposed in its amplitude f and the normal direction $\boldsymbol{n}$ in order to separate the terms depending on the force amplitude from the terms only ruled by geometric effects.

The spatial derivative of $\boldsymbol{g}_{C_i}^{int,con}$ can be now written as:

$$\mathrm{d}\boldsymbol{g}_{C_i}^{con} = \mathrm{d}f\ \frac{1}{f}\boldsymbol{g}_{C_i}^{con} + f\ \mathrm{d} \begin{pmatrix} \boldsymbol{P}^T \overline{\boldsymbol{\Psi}}_{C_i}^T \boldsymbol{R}_0^T\ \boldsymbol{n} + \begin{Bmatrix} \boldsymbol{n} \\ \widetilde{\boldsymbol{z}}_{C_i} \boldsymbol{R}_0^T\ \boldsymbol{n} \\ \boldsymbol{0} \\ \boldsymbol{0} \\ \boldsymbol{0} \end{Bmatrix} \end{pmatrix} \tag{6.86}$$

The derivative of the force amplitude f defined by Equation (6.70) can be expressed as:

$$\mathrm{d}f = \frac{\partial f}{\partial \ell}\ \mathrm{d}\ell + \frac{\partial f}{\partial \dot{\ell}}\ \mathrm{d}\dot{\ell} \tag{6.87}$$

where the partial derivatives are computed as:

$$\frac{\partial f}{\partial \ell} = S_c^* \left(k_p\ n\ \ell^{n-1} + c\ n\ \ell^{n-1}\ \dot{\ell} \right) \quad , \quad \frac{\partial f}{\partial \dot{\ell}} = S_c^*\ c\ \ell^n \tag{6.88}$$

The variation of the penetration length is simply obtained by derivation of Eq. (6.72):

$$\begin{aligned} \mathrm{d}\ell &= \mathrm{d}\left(\boldsymbol{n}^T (\boldsymbol{x}_{N1} - \boldsymbol{x}_{C_i}) \right) \\ &= \boldsymbol{n}^T (\mathrm{d}\boldsymbol{x}_{N1} - \mathrm{d}\boldsymbol{x}_{C_i}) + (\boldsymbol{x}_{N1} - \boldsymbol{x}_{C_i})^T\ \mathrm{d}\boldsymbol{n} \end{aligned} \tag{6.89}$$

where by analogy with Eqs. (6.76-6.77) the total derivatives $\mathrm{d}\boldsymbol{x}_{C_i}$ and $\mathrm{d}\boldsymbol{x}_{N_i}$ are put in the form:

$$\begin{aligned} \mathrm{d}\boldsymbol{x}_{Ci} &= \mathrm{d}\boldsymbol{x}_0^s - \boldsymbol{R}_0^s \widetilde{\boldsymbol{z}}_{C_i}^s \ \mathrm{d}\boldsymbol{\Theta}_0^s + \boldsymbol{R}_0^s \overline{\boldsymbol{\Psi}}_{C_i}^s \boldsymbol{P}^s \ \mathrm{d}\boldsymbol{q}^s \qquad (6.90) \\ \mathrm{d}\boldsymbol{x}_{Ni} &= \mathrm{d}\boldsymbol{x}_0^m - \boldsymbol{R}_0^m \widetilde{\boldsymbol{z}}_{C_{Ni}}^m \ \mathrm{d}\boldsymbol{\Theta}_0^m + \boldsymbol{R}_0^m \overline{\boldsymbol{\Psi}}_{C_i}^m \boldsymbol{P}^m \ \mathrm{d}\boldsymbol{q}^m \qquad (6.91) \end{aligned}$$

In case of triangular-shaped master contact faces, the derivative of the normal vector $\boldsymbol{n}$ (see Eq. 6.61) takes the form:

$$\begin{aligned} \mathrm{d}\boldsymbol{n} &= \frac{\left(\boldsymbol{I} - \boldsymbol{n}\boldsymbol{n}^T\right)}{\left\|\widetilde{\boldsymbol{x}}_{N12} \ \boldsymbol{x}_{N13}\right\|} \ \mathrm{d}\left(\widetilde{\boldsymbol{x}}_{N12} \ \boldsymbol{x}_{N13}\right) \\ &= \frac{\left(\boldsymbol{I} - \boldsymbol{n}\boldsymbol{n}^T\right)}{\left\|\widetilde{\boldsymbol{x}}_{N12} \ \boldsymbol{x}_{N13}\right\|} \ \left(\widetilde{\boldsymbol{x}}_{N12} \ \mathrm{d}\boldsymbol{x}_{N13} - \widetilde{\boldsymbol{x}}_{N13} \ \mathrm{d}\boldsymbol{x}_{N12}\right) \\ &= \frac{\left(\boldsymbol{I} - \boldsymbol{n}\boldsymbol{n}^T\right)}{\left\|\widetilde{\boldsymbol{x}}_{N12} \ \boldsymbol{x}_{N13}\right\|} \left[\left(\widetilde{\boldsymbol{x}}_{N13} - \widetilde{\boldsymbol{x}}_{N12}\right) \ \mathrm{d}\boldsymbol{x}_{N1} - \widetilde{\boldsymbol{x}}_{N13} \ \mathrm{d}\boldsymbol{x}_{N2} + \widetilde{\boldsymbol{x}}_{N12} \ \mathrm{d}\boldsymbol{x}_{N3}\right] \end{aligned} \qquad (6.92)$$

The penetration velocity $\dot{\ell}$ is given by:

$$\begin{aligned} \mathrm{d}\dot{l} &= \mathrm{d}\left[\boldsymbol{n}^T(\dot{\boldsymbol{x}}_{N1} - \dot{\boldsymbol{x}}_{C_i}) + (\boldsymbol{x}_{N1} - \boldsymbol{x}_{C_i})^T \ \dot{\boldsymbol{n}}\right] \\ &= (\dot{\boldsymbol{x}}_{N1} - \dot{\boldsymbol{x}}_{C_i})^T \ \mathrm{d}\boldsymbol{n} + \boldsymbol{n}^T \left(\mathrm{d}\dot{\boldsymbol{x}}_{N1} - \mathrm{d}\dot{\boldsymbol{x}}_{C_i}\right) + \dot{\boldsymbol{n}}^T \left(\mathrm{d}\boldsymbol{x}_{N1} - \mathrm{d}\boldsymbol{x}_{C_i}\right) + (\boldsymbol{x}_{N1} - \boldsymbol{x}_{C_i})^T \ \mathrm{d}\dot{\boldsymbol{n}} \end{aligned} \qquad (6.93)$$

where the various terms not yet defined are given by the following expressions:

$$\begin{aligned} \mathrm{d}\dot{\boldsymbol{x}}_{Ni} = \mathrm{d}\dot{\boldsymbol{x}}_0^m &+ \boldsymbol{R}_0^m \widetilde{\widetilde{\boldsymbol{z}}_{Ni}^m \boldsymbol{\Omega}_0^m} \ \mathrm{d}\boldsymbol{\Theta}_0^m + \boldsymbol{R}_0^m \widetilde{\boldsymbol{\Omega}}_0^m \overline{\boldsymbol{\Psi}}_{Ni}^m \boldsymbol{P}^m \ \mathrm{d}\boldsymbol{q}^m - \boldsymbol{R}_0^m \widetilde{\boldsymbol{z}}_{Ni}^m \ \mathrm{d}\boldsymbol{\Omega}_0^m \\ &- \boldsymbol{R}_0^m \widetilde{(\overline{\boldsymbol{\Psi}}_{Ni}^m \boldsymbol{P}^m \boldsymbol{v}^m)} \ \mathrm{d}\boldsymbol{\Theta}_0^m + \boldsymbol{R}_0^m \overline{\boldsymbol{\Psi}}_{Ni}^m \boldsymbol{P}^m \ \mathrm{d}\boldsymbol{v}^m + \boldsymbol{R}_0^m \overline{\boldsymbol{\Psi}}_{Ni}^m \ \mathrm{d}\boldsymbol{P}^m \ \boldsymbol{v}^m \end{aligned} \qquad (6.94)$$

$$\begin{aligned} \mathrm{d}\dot{\boldsymbol{x}}_{C_i} = \mathrm{d}\dot{\boldsymbol{x}}_0^s &+ \boldsymbol{R}_0^s \widetilde{\widetilde{\boldsymbol{z}}_{C_i}^s \boldsymbol{\Omega}_0^s} \ \mathrm{d}\boldsymbol{\Theta}_0^s + \boldsymbol{R}_0^s \widetilde{\boldsymbol{\Omega}}_0^s \overline{\boldsymbol{\Psi}}_{C_i}^s \boldsymbol{P}^s \ \mathrm{d}\boldsymbol{q}^s - \boldsymbol{R}_0^s \widetilde{\boldsymbol{z}}_{C_i}^s \ \mathrm{d}\boldsymbol{\Omega}_0^s \\ &- \boldsymbol{R}_0^s \widetilde{(\overline{\boldsymbol{\Psi}}_{C_i}^s \boldsymbol{P}^s \boldsymbol{v}^s)} \ \mathrm{d}\boldsymbol{\Theta}_0^s + \boldsymbol{R}_0^s \overline{\boldsymbol{\Psi}}_{C_i}^s \boldsymbol{P}^s \ \mathrm{d}\boldsymbol{v}^s + \boldsymbol{R}_0^s \overline{\boldsymbol{\Psi}}_{C_i}^s \ \mathrm{d}\boldsymbol{P}^s \ \boldsymbol{v}^s \end{aligned} \qquad (6.95)$$

$$\begin{aligned} \mathrm{d}\dot{\boldsymbol{n}} &= \mathrm{d}\left(\frac{\boldsymbol{I} - \boldsymbol{n}\boldsymbol{n}^T}{\left\|\widetilde{\boldsymbol{x}}_{N12} \ \boldsymbol{x}_{N13}\right\|}\right) \ \boldsymbol{a}_{\dot{\boldsymbol{n}}} + \frac{\boldsymbol{I} - \boldsymbol{n}\boldsymbol{n}^T}{\left\|\widetilde{\boldsymbol{x}}_{N12} \ \boldsymbol{x}_{N13}\right\|} \ \mathrm{d}\boldsymbol{a}_{\dot{\boldsymbol{n}}} \\ &= \frac{1}{\left\|\widetilde{\boldsymbol{x}}_{N12} \ \boldsymbol{x}_{N13}\right\|} \left[\left(\widetilde{\widetilde{\boldsymbol{n}} \ \boldsymbol{a}_{\dot{\boldsymbol{n}}}} + \widetilde{\boldsymbol{n}} \ \widetilde{\boldsymbol{a}_{\dot{\boldsymbol{n}}}}\right) \ \mathrm{d}\boldsymbol{n} + \left(\boldsymbol{I} - \boldsymbol{n}\boldsymbol{n}^T\right)\left(\mathrm{d}\boldsymbol{a}_{\dot{\boldsymbol{n}}} - \boldsymbol{a}_{\dot{\boldsymbol{n}}} \ \boldsymbol{n}^T \ \mathrm{d}\left[\widetilde{\boldsymbol{x}}_{N12} \ \boldsymbol{x}_{N13}\right]\right)\right] \end{aligned} \qquad (6.96)$$

with

$$\begin{aligned} \mathrm{d}\boldsymbol{a}_{\dot{\boldsymbol{n}}} = &\left(\widetilde{\boldsymbol{x}}_{N13} - \widetilde{\boldsymbol{x}}_{N12}\right) \ \mathrm{d}\dot{\boldsymbol{x}}_{N1} - \widetilde{\boldsymbol{x}}_{N13} \ \mathrm{d}\dot{\boldsymbol{x}}_{N2} + \widetilde{\boldsymbol{x}}_{N12} \ \mathrm{d}\dot{\boldsymbol{x}}_{N3} \\ &+ \left(\widetilde{\dot{\boldsymbol{x}}}_{N3} - \widetilde{\dot{\boldsymbol{x}}}_{N2}\right) \ \mathrm{d}\boldsymbol{x}_{N1} + \left(\widetilde{\dot{\boldsymbol{x}}}_{N1} - \widetilde{\dot{\boldsymbol{x}}}_{N3}\right) \ \mathrm{d}\boldsymbol{x}_{N2} + \left(\widetilde{\dot{\boldsymbol{x}}}_{N2} - \widetilde{\dot{\boldsymbol{x}}}_{N1}\right) \ \mathrm{d}\boldsymbol{x}_{N3} \end{aligned} \qquad (6.97)$$

and

$$\mathrm{d}\left(\widetilde{\boldsymbol{x}}_{N12}\ \boldsymbol{x}_{N13}\right) = \left(\widetilde{\boldsymbol{x}}_{N13} - \widetilde{\boldsymbol{x}}_{N12}\right)\ \mathrm{d}\boldsymbol{x}_{N1} - \widetilde{\boldsymbol{x}}_{N13}\ \mathrm{d}\boldsymbol{x}_{N2} + \widetilde{\boldsymbol{x}}_{N12}\ \mathrm{d}\boldsymbol{x}_{N3} \tag{6.98}$$

The derivative in the second term of Eq. 6.86 can be easily expanded in:

$$\begin{aligned}\mathrm{d}\left(\boldsymbol{P}^T\overline{\boldsymbol{\Psi}}_{C_i}^T\boldsymbol{R}_0^T\ \boldsymbol{n} + \begin{Bmatrix}\boldsymbol{n}\\ \widetilde{\boldsymbol{z}}_{C_i}\boldsymbol{R}_0^T\ \boldsymbol{n}\\ \boldsymbol{0}\\ \boldsymbol{0}\\ \boldsymbol{0}\end{Bmatrix}\right) &= \boldsymbol{P}^T\ \overline{\boldsymbol{\Psi}}_{C_i}^T\widetilde{\boldsymbol{R}_0^T\boldsymbol{n}}\ \mathrm{d}\boldsymbol{\Theta}_0 + \boldsymbol{P}^T\overline{\boldsymbol{\Psi}}_{C_i}^T\boldsymbol{R}_0^T\ \mathrm{d}\boldsymbol{n}\\ &+ \begin{Bmatrix}\mathrm{d}\boldsymbol{n}\\ -\widetilde{\boldsymbol{R}_0^T\boldsymbol{n}}\overline{\boldsymbol{\Psi}}_{C_i}\boldsymbol{P}\ \mathrm{d}\boldsymbol{q} + \widetilde{\boldsymbol{z}}_{C_i}\widetilde{\boldsymbol{R}_0^T\boldsymbol{n}}\ \mathrm{d}\boldsymbol{\Theta}_0 + \widetilde{\boldsymbol{z}}_{C_i}\boldsymbol{R}_0^T\ \mathrm{d}\boldsymbol{n}\\ \boldsymbol{0}\\ \boldsymbol{0}\\ \boldsymbol{0}\end{Bmatrix}\end{aligned} \tag{6.99}$$

where the terms in $\mathrm{d}\boldsymbol{P}$ have been neglected since they introduce second order contributions.

The development of Equation 6.86 taking into account Equations 6.87-6.99 allows computing the tangent stiffness $\boldsymbol{K}_t^{con}$ and damping $\boldsymbol{C}_t^{con}$ matrices can be computed. Their explicit expression is not given for the sake of conciseness. In order to optimize the computational efficiency, a particular attention has been given to the implementation. For instance, some terms are grouped and the intermediate resulting matrices are saved temporarily to reduce the number of operations. The contribution to the damping matrix $\boldsymbol{C}_t$ is only included in the first term of Eq. 6.86 and is due to the presence of hysteresis damping in the contact law (see Eq. 6.70).

Inasmuch numerous mathematical operations are needed (see Eq. 6.86-6.99), the computation of the iteration matrix could be time consuming. However, since it is not mandatory to have an exact iteration matrix to assure the convergence, some contributions can possibly be omitted. Besides, instead of computing the iteration matrix at each Newton-Raphson iteration, it could be evaluated only once per time step or even kept constant for several time steps. According to the dynamics of the system, the implementation of the tangent damping matrix is perhaps not necessary. Some comparison tests could be performed in the future in order to find the optimal strategy to reduce the CPU time.

6.9 Simple contact example

In order to assess the contact formulation developed in this work, the simulation of a simple contact problem has been performed. The system is composed of two elastic bars

constrained at their center of mass by a hinge joint along the x-axis and the contact is induced by a torque applied along the rotation axis of the bar #2 (see Fig. 6.11).

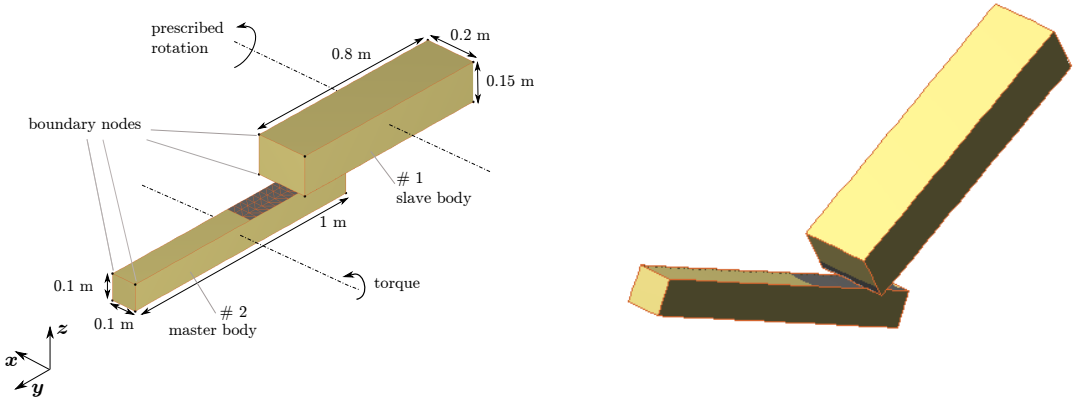

(a) initial configuration ($t = 0$ s) (b) final configuration ($t = 2$ s)

Figure 6.11: Simple contact example: positions of the bars and simulation setup.

Both bars are made of steel (Young's modulus: 210 GPa, Poisson's ratio: 0.3 , mass density: 7800 kg/m^3). Both bars are initially meshed with hexahedral finite elements and their model is then reduced by keeping the 8 vertices as boundary nodes and adding 10 vibration modes. A static mode and an internal vibration mode are depicted in Figure 6.12. The eigen frequencies of the first 10 internal vibration modes are in the range $[603; 3210]$ Hz for bar #1 and in the range $[391; 3008]$ Hz for bar #2. This example aims at verifying that the contact element can work with only a few global shape functions in the reduction basis $\overline{\mathbf{\Psi}}$. The results obtained are acceptable even though the accuracy of system response would improve by increasing the modal basis.

In the initial configuration, the bars are at rest and separated by a very small gap. The torque applied on the additional node linked to the corotational frame of bar #1 is linearly increased from 0 Nm at $t = 0$ s to reach -1000 Nm at $t = 0.6$ s and keeps this value till the end of the simulation. The rotation of bar #2 is prevented during the first second of the simulation and follows a ramp function until $t = 2$ s where the rotation speed keeps a constant value of -1 rad/s.

For both bodies, the candidate contact zone assessed by the contact detection algorithm is depicted in gray in Figure 6.13 and the effective contact area is colored in red at $t = 1.5$ s. The bar deflections at the same time step are represented in Figure 6.14.

This system has also been simulated using the finite element method in the commercial software SAMCEF/MECANO in order to validate the proposed contact formulation. The contact element that is used to model the contact condition between the

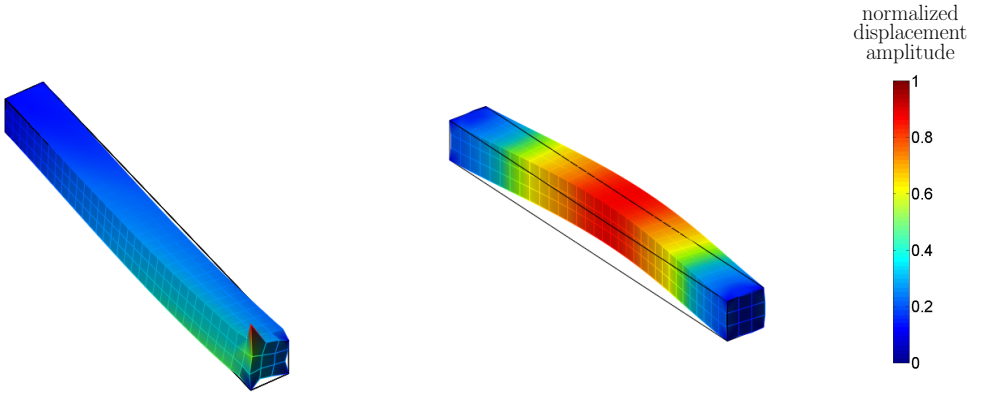

(a) static mode (b) internal vibration mode ($f_1 = 391$ Hz)

Figure 6.12: Examples of retained modes in superelement bar #2.

two bars modelled with finite elements is described in section 3.3.1. Moreover, the system response has been computed with a *non reduced* superelement, i.e., that all nodes of the finite element mesh are retained as boundary nodes such that the superelement matrices have the same size as the initial finite element model. The mesh is identical for the three models and the time step is $h = 0.01$ s. As depicted in Figure 6.15, the total magnitude of the contact force between the two bars is in good agreement for the three methods although the computational effort is greatly reduced with the superelement based model. The decrease of the contact force magnitude observed after about 1.3 s is due to the sliding of the active contact zone along the contact face of the master body. Indeed, for a constant torque applied on the master bar, the total magnitude of the contact force decreases if the the distance from the rotation axis of the master body to the active contact zone increases (Fig. 6.12(b)).

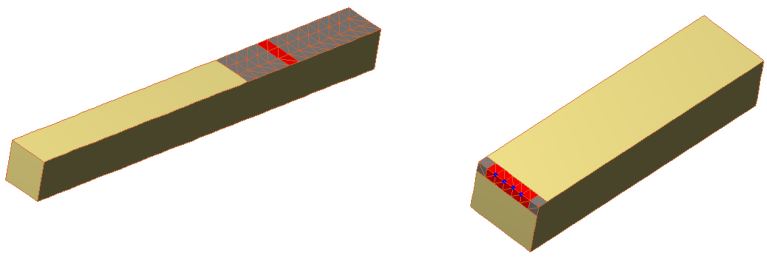

(a) master body (#2) (b) slave body (#1)

Figure 6.13: Candidate contact zones depicted in gray and effective contact zone colored in red ($t = 1.5$ s).

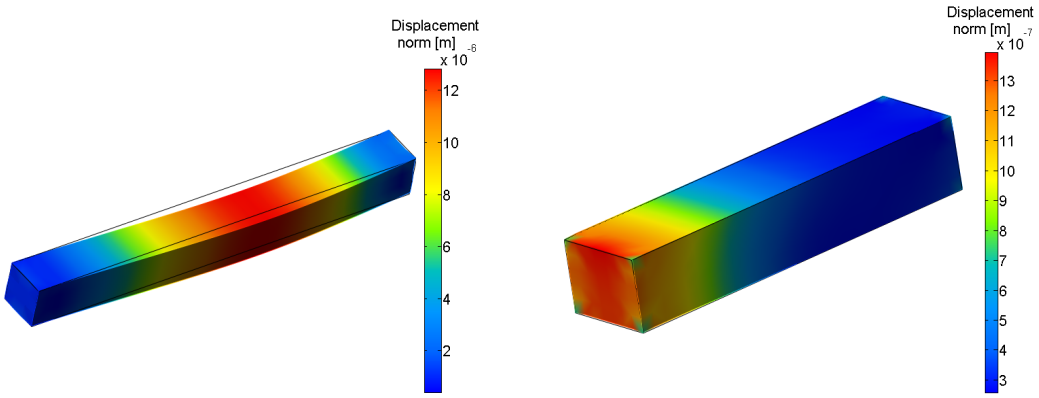

(a) master body (#2) (b) slave body (#1)

Figure 6.14: Bar deflections at $t = 1.5$ s (deformation scaled by factor 2000).

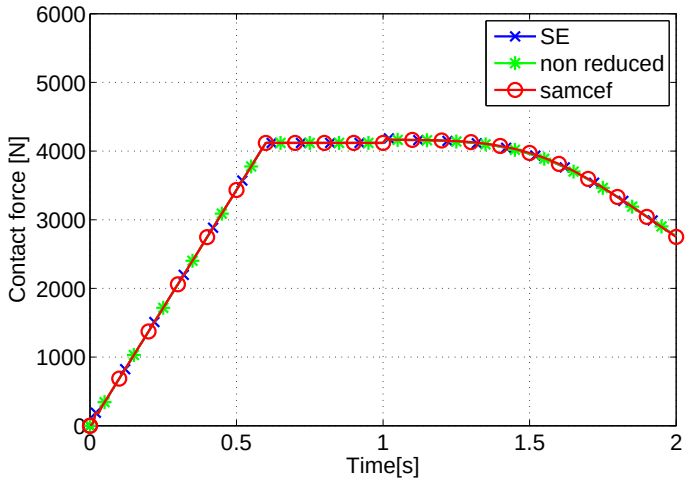

Figure 6.15: Magnitude of the total contact force between the two bars.

6.10 Cam mechanism

The cam system depicted in Figure 6.16 is composed of two superelements (the cam and the roller) and a spring. The material of both flexible bodies is steel. Only a few boundary nodes are retained (18 for the cam and 9 for the roller); they are more or less equally distributed along the vertical edge face. In addition, 20 internal vibration modes are included in each superelement. Therefore, compared with the full finite element model (Fig. 6.17), the number of DOFs of the whole system is greatly reduced: from 107532 DOFs to 142 DOFs. The candidate contact zones are colored in gray in Fig. 6.16. It includes numerous nodes for the cam since all the nodes of the vertical

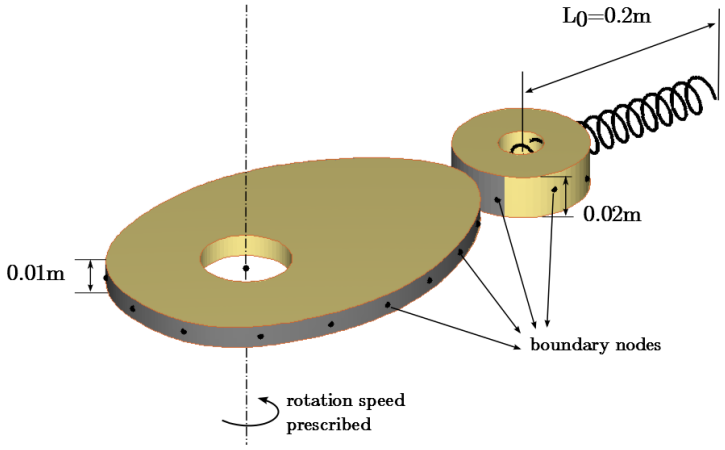

Figure 6.16: Simple cam system.

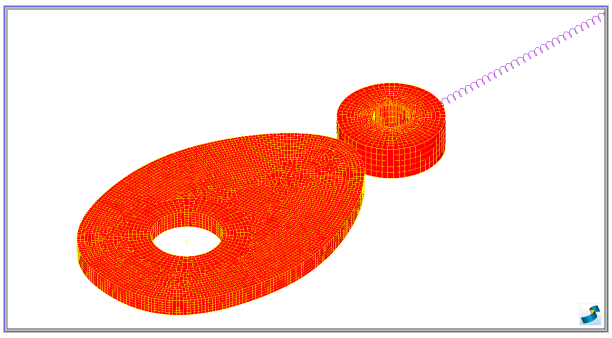

Figure 6.17: Finite Element model of the simple cam system.

edge face can enter in contact during a full revolution. For the roller body, only a reduced section of the cylindrical face is considered.

The rotation speed of the cam is prescribed to 60 rpm whereas the roller can only move in the direction of the spring and cannot rotate. The stiffness of the spring is equal to $k = 1.\text{E}5$ N/m and its undeformed length is $\ell_0 = 0.2$ s. Whatever the angular position of the cam during the revolution, the spring always works under compression.

Figure 6.18(a) shows that the boundary nodes of the cam are alternately loaded according to the angular position: the closest boundary node to the contact points undergoes larger deformations than the others ones. Conversely, on the roller the contact occurs always in the same area. Therefore the deformation is mainly localized around the same boundary node (see Fig. 6.18(b)). As depicted in Figure 6.19, a similar behaviour can be observed for the modal amplitudes of the 20 internal vibration modes.

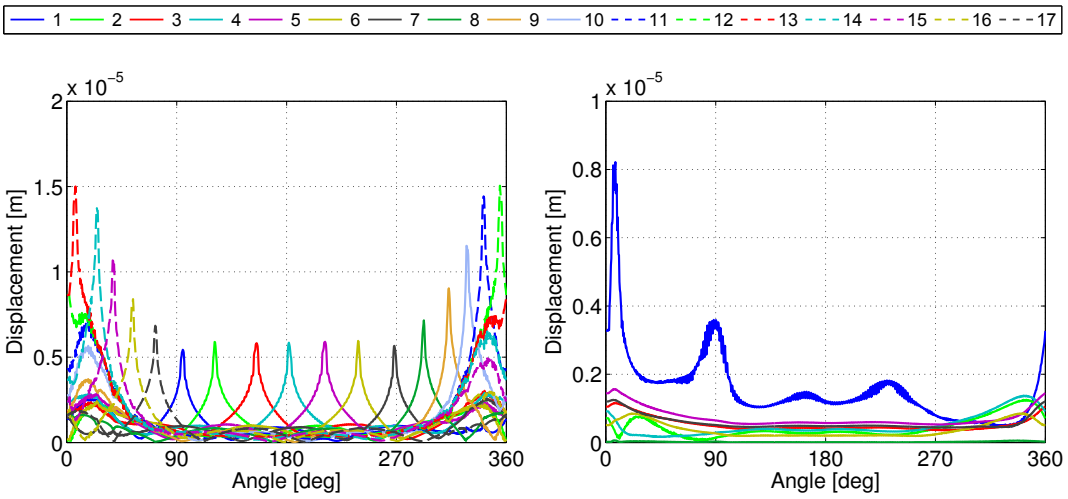

(a) cam (b) roller

Figure 6.18: Displacements of boundary nodes.

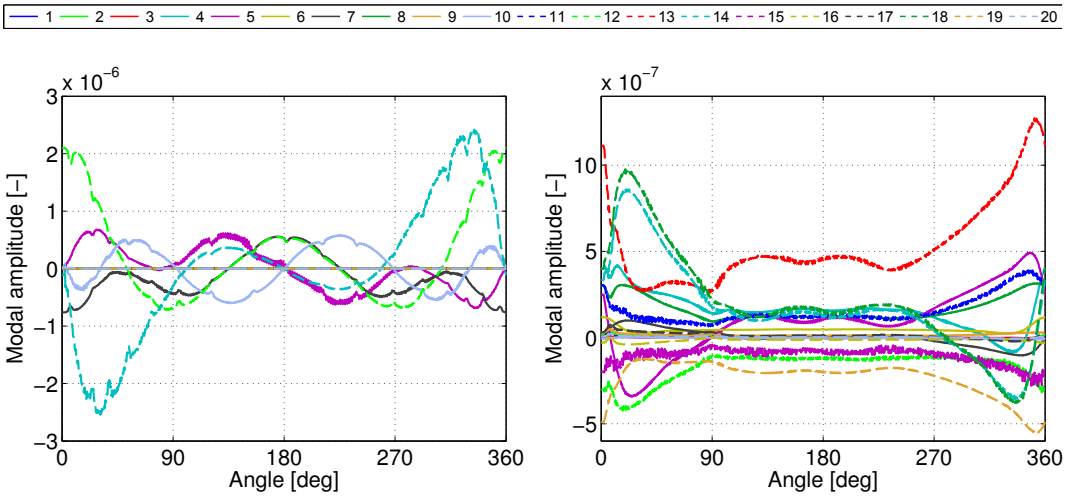

(a) cam (b) roller

Figure 6.19: Magnitude of modal intensities.

The proposed contact formulation defined between two superelements can be used for contacts between rigid bodies too. Indeed, if only one boundary node having 6 DOFs is retained and no vibration mode is included, the superelement model is reduced to a 6 DOFs system. The mode shape matrix is composed of the 6 rigid body modes and the reduced mass matrix is simply given by the global mass and inertia matrix of the whole body. The corotational frame is then equivalent to the unique boundary node.

This kind of *rigid superelement* provides a general approach to model contacts with rigid bodies having a complex geometry. Indeed, the contact area has not been

represented by an analytical expression as for classic contact formulation between rigid bodies, see for instance Ref [47]. At each time, the geometry of the potential contact zone is determined thanks to the modal basis.

The simulation of the cam system has been performed with a full FE model and with the rigid version of the superelement bodies. The parameters are identical to the model presented with superelements including only a small number of modes. The time step size is equal to 1E.-3 s and the contact stiffness is 1E.12 N/m^3. The spatial discretization of the candidate contact zone is exactly the same for the three models.

There is a good agreement for the evolution of the contact force magnitude with respect to the rotation angle of the cam computed with the three different models (Figure 6.20). This result from the fact that the flexible effects are not dominant for the system modelled.

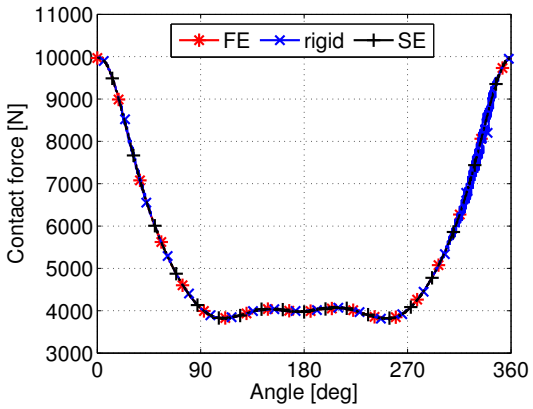

Figure 6.20: Contact force magnitude vs. rotation of the cam. The proposed contact formulation is in accordance with a full FE model performed with SAMCEF/MECANO. In this simulation, the superelements models either include a few modes (SE-curve) or are degenerated to rigid bodies (rigid-curve).

6.11 Gear pair model

Multibody dynamics analysis of gear pairs is often based on the expression of global kinematic joints defined between two rigid bodies representing the gear wheels. These global models make use a spring and damper combination along the normal pressure line in order to represent a unique idealized contact point between teeth (see for instance Ref. [16] and Section 2.6). Such formulation of gear pair models is compact and can be used to simulate complex mechanism systems including gears with relatively low computational time. However, only properly meshing gears can be considered since the disruptive effects are most of the time quite approximately represented. For instance,

transmission devices with misalignment or crossed axes can hardly be accurately modelled.

To model the gear flexibility more accurately and to capture the meshing defects, one can resort to detailed finite element models of the two gear wheels and express the contact conditions between tooth flanks [85]. Such detailed models are without doubt the most reliable technique but they are quite complex to develop and involve a huge computational time.

The modelling of gear wheels as superelements combined with the contact model described previously allows accounting for the tooth flexibility and modelling the misalignment, the gear hammering and the backlash with higher accuracy than classical global models. Moreover, the formulation is more compact and computationally more tractable than with full FE models. The proposed modelling approach takes the actual 3D geometry of the gear wheels (Fig. 6.21) into account and therefore aims at predicting the actual contact points on teeth flanks.

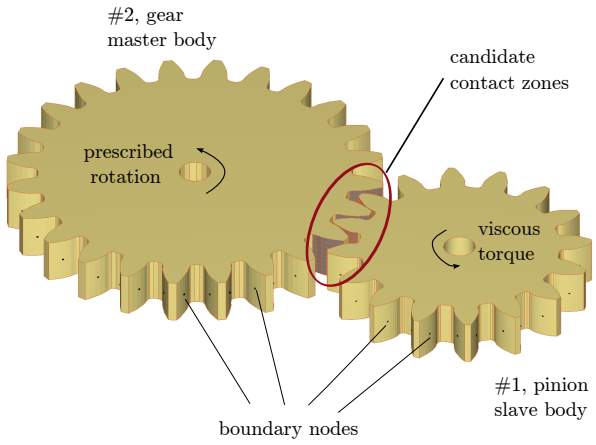

Figure 6.21: Gear pair model.

6.11.1 Selection strategy of slave-master flank pairs

If the candidate contact zone on the skin of bodies under contact is large and includes numerous nodes, the detection procedure can be numerically very costly. Indeed, in this case the projection method of a slave node on a master surface (Section 6.6) has to be repeated a large number of times.

In order to reduce the number of mathematical operations and consequently the computational time, the candidate contact zone can be split in several subareas. A suitable strategy allows determining which contact zones of the two bodies have to be tested by the contact detection algorithm.

For gear pair simulation, each tooth flank can be considered as an individual small candidate contact zone and the several steps described hereafter aim at identifying the couples of slave-master flanks to be supplied to the detection algorithm.

Initial configuration *($t = 0$ s)*

1. Select a reference node on each tooth flank and compute its absolute position.

   A reference node is chosen on each candidate contact zone, i.e., each tooth flank. The absolute position of these reference nodes can be easily determined by means of Equation 6.59. For instance, the reference nodes can be located at the tops of gear teeth as depicted in Figure 6.22.

   The boundary nodes should be used as reference nodes if there is at least one boundary node per tooth as discuss in section 6.11.2. In that case, the position of the reference nodes is available from the vector of generalized coordinates and has not to be computed. One reference node per gear tooth could be sufficient to determine the pairs of slave and master flank for which the presence of contact has to be assessed (see the coarse collision detection presented in Ref. [151]). Nevertheless, in this dissertation thesis with the aim of having a general framework which can be easily extended to other transmission components than the gear pairs, each candidate contact zone can have its own reference node which is not necessarily a boundary node.

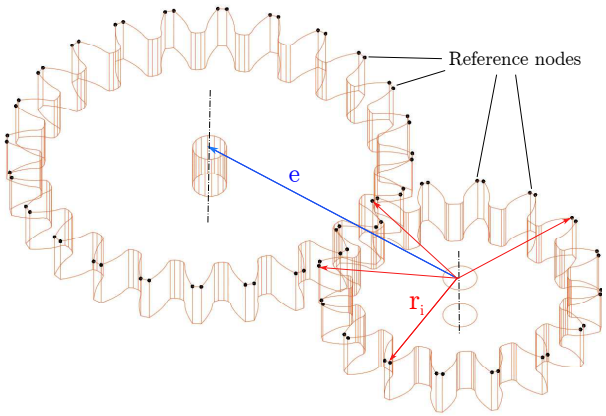

Figure 6.22: A reference node is selected on each tooth flank.

2. Determine the closest slave reference node to the center distance of the gear pair.

   The slave reference node closest to the center distance of the gear pair can be

obtained by solving:

$$\max \left(\frac{\boldsymbol{r}_i \cdot \boldsymbol{e}}{\|\boldsymbol{r}_i\| \ \|\boldsymbol{e}\|} \right) \tag{6.100}$$

where $\boldsymbol{e}$ is the vector between the rotation centers of the two wheels and the $\boldsymbol{r}_i$ are the vectors from the rotation center to the reference nodes of the slave gear wheel.

3. Determine the tooth flank of the master gear wheel which is the nearest to the central slave flank.

   Once the closest slave flank is known, the nearest master flank to this latter slave flank has to be determined. To this end, the minimum distance p_i is looked for (see Fig. 6.23).

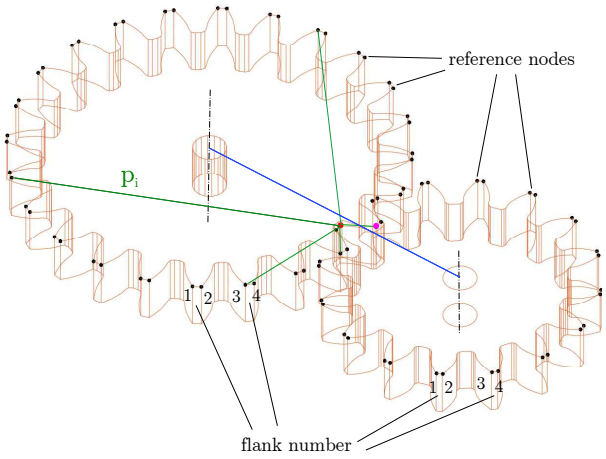

Figure 6.23: Determination of the nearest master flank to the central slave flank.

4. Construct the map with the slave and master tooth flank matched.

   From the knowledge of the slave and master tooth flank ID number around the gear pair center distance, the couple of tooth flanks that could be in contact in a near future are easily determined. Indeed, if the contact zones related to the tooth flanks are numbered consecutively on the two gear wheels (Fig. 6.23), it is only needed to increment the tooth flank ID numbers to get the next tooth flank pairs to be in contact and to construct a map in this way.

Current configuration

1. Compute the position of the slave reference nodes and determine the closest slave tooth flank to the center distance.

At each time step, the position of the reference nodes of the slave wheel are recomputed and the closest node to the center distance has to be determined following the same procedure as in the initial configuration ($t = 0$ s).

2. Update the map of flank couples if necessary and take a few flanks on both sides of the central flank.

   The contact between gear teeth can simultaneously occur between one or several gear tooth pairs. Therefore, the contact detection has also to be performed for a few number of flanks on each side of the central slave-master pair. The total number of flanks which have to be considered depends on the contact ratio of the gear pair (see Ref. [62] for more details). Usually, the number of tooth pairs simultaneously in contact does not exceed three, so that the potential contact zones are often limited to six.

   The ID number of the central slave flank determined at the previous step enables to localize the set of slave-master couples in the table map which are provided to the contact detection algorithm.

   Since the gear wheels often have a prime number of cogs, the same tooth flanks on both wheels rarely enter in contact. Therefore, the map is only constructed for a restricted number of slave-master flanks potentially in contact, for example the smallest number of flanks of the two wheels. Then, the table map is updated from time to time when the selection task of the set of couples tries to exceed the dimension of the table map.

6.11.2 Position of boundary nodes

When developing the model, the number and the location of boundary nodes have to be chosen with great care. Indeed, the system response is significantly influenced by the static modes. Furthermore, the shape functions and the eigen frequencies of vibration modes depend directly on the spatial distribution of superelement boundary nodes.

Keeping one or several static modes for each gear tooth seems a suitable approach in order to describe properly the bending of each tooth. Therefore, at least one boundary node per gear tooth has to be retained in the superelement model. Several configurations have been considered to select the set of boundary nodes (see Fig. 6.24) while keeping a reasonable model size for the resulting superelement.

The most natural choice consists in retaining the closest node to the center of each tooth tip face as a boundary node. However, as depicted in Figure 6.25, the deformed shapes of static modes present huge deformations localized around the boundary nodes. These non-uniform displacements on tooth flanks can lead to partial contact paths along the wheel facewidth.

A solution to circumvent this drawback consists in introducing an additional node

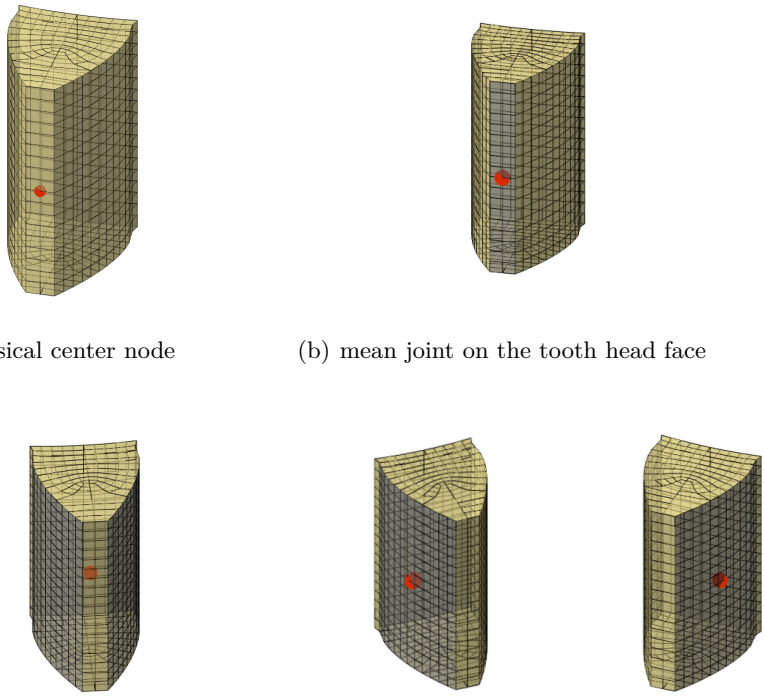

(a) physical center node

(b) mean joint on the tooth head face

(c) mean joint with both flanks

(d) mean joint for each tooth flank

Figure 6.24: Various choices of boundary node configurations on each gear tooth.

near the center of each tooth head face and define this node as the mean frame connected to the nodes on the tooth head. Then, only these extra nodes are retained as boundary nodes of the gear wheel superelement. In this case, there are no longer localized deformations around the boundary nodes for the static modes (see Fig. 6.26).

The 6 DOFs related to the additional node are prescribed by 6 constraints which can be formulated as proposed in [87]:

$$\begin{aligned} \boldsymbol{\Phi}^{tr}(\boldsymbol{q}) &\equiv \sum_{i=1}^{n_G}\left(\frac{1}{n_G}\boldsymbol{u}_{G_i}\right) - \boldsymbol{u}_A + \sum_{i=1}^{n_G}\left(\frac{1}{n_G}(\boldsymbol{x}_{G_i} - \boldsymbol{x}_A)\right) \times \boldsymbol{\Psi}_A = \mathbf{0} \\ \boldsymbol{\Phi}^{rot}(\boldsymbol{q}) &\equiv \sum_{i=1}^{n_G}\left(\frac{1}{n_G}(\boldsymbol{x}_{G_i} - \boldsymbol{x}_A) \times (\boldsymbol{u}_{G_i} - \boldsymbol{u}_A + (\boldsymbol{x}_{G_i} - \boldsymbol{x}_A) \times \boldsymbol{\Psi}_A)\right) = \mathbf{0} \end{aligned} \tag{6.101}$$

where n_G is the number of nodes selected on the FE model and included in the master node group, $\boldsymbol{\Psi}_A$ is the 3×1 vector of rotation parameters associated with the additional node. These constraint equations assume a linear behaviour which is valid since only small displacements are considered in the Craig-Bampton method. The value given to $\boldsymbol{x}_A$ and $\boldsymbol{\Psi}_A$ can be interpreted as the mean position and rotation of the node group located on the tooth head. Each node of the master node group have the same weight $(1/n_G)$ in the constraint formulation. Therefore, if the node group corresponds to a face

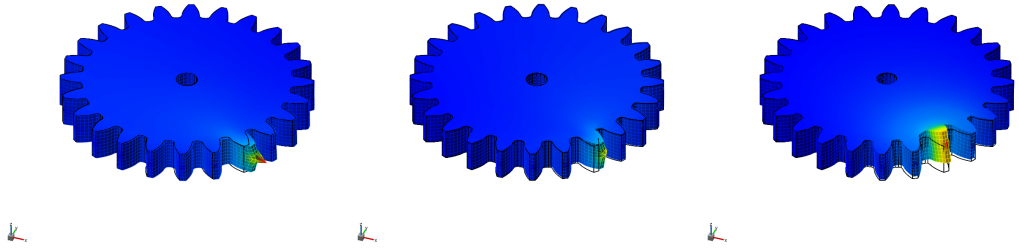

(a) x-direction (b) y-direction (c) z-direction

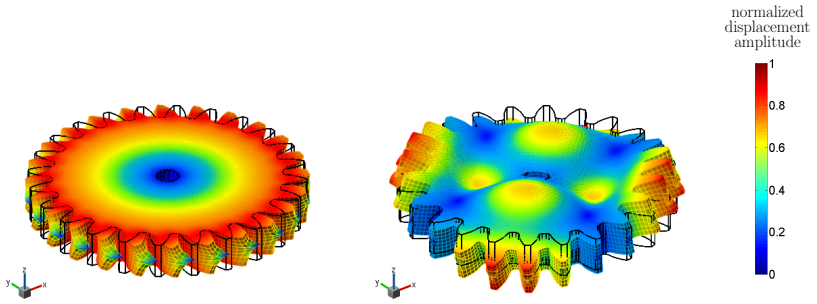

(d) $f_2 = 11789$ Hz (e) $f_{25} = 37261$ Hz

Figure 6.25: Deformation modes of gear wheel superelement when the **center node** of each tooth head face is retained as a boundary node: (a)-(c) static modes; (d)-(e) internal vibration mode.

of the 3D body (e.g. a tooth flank), the nodes on the face boundaries get the same loads as the center face nodes instead of one half load. This fact could explain the non-uniform deformation observe on the top and the bottom of the teeth in Figures 6.26-6.28.

The aim of this *mean* element is similar to that of the corotational frame definition presented in section 6.5 (Eq. 6.50) but the kinematic constraints are not at the same stage of the modelling process. Indeed, the constraints enabling to determine the position and the orientation of the additional node are defined between the nodes of the initial finite element model, whereas the corotational frame constraints are based on the boundary nodes of the reduced model.

In contrast to the previous choice of boundary nodes, the torsion of the gear teeth is represented by static modes (Figs. 6.26(d)-6.26(f)) but this implies that the total number of static modes in the superelement is doubled.

Other choices are possible for the master node group of the mean element. For instance, all the nodes located on the two tooth flanks can be considered as master nodes (see Fig. 6.27). In the latter case the slave node is near the tooth center. Since the contacts in gear pairs occur between the tooth flanks, this choice seems more physical

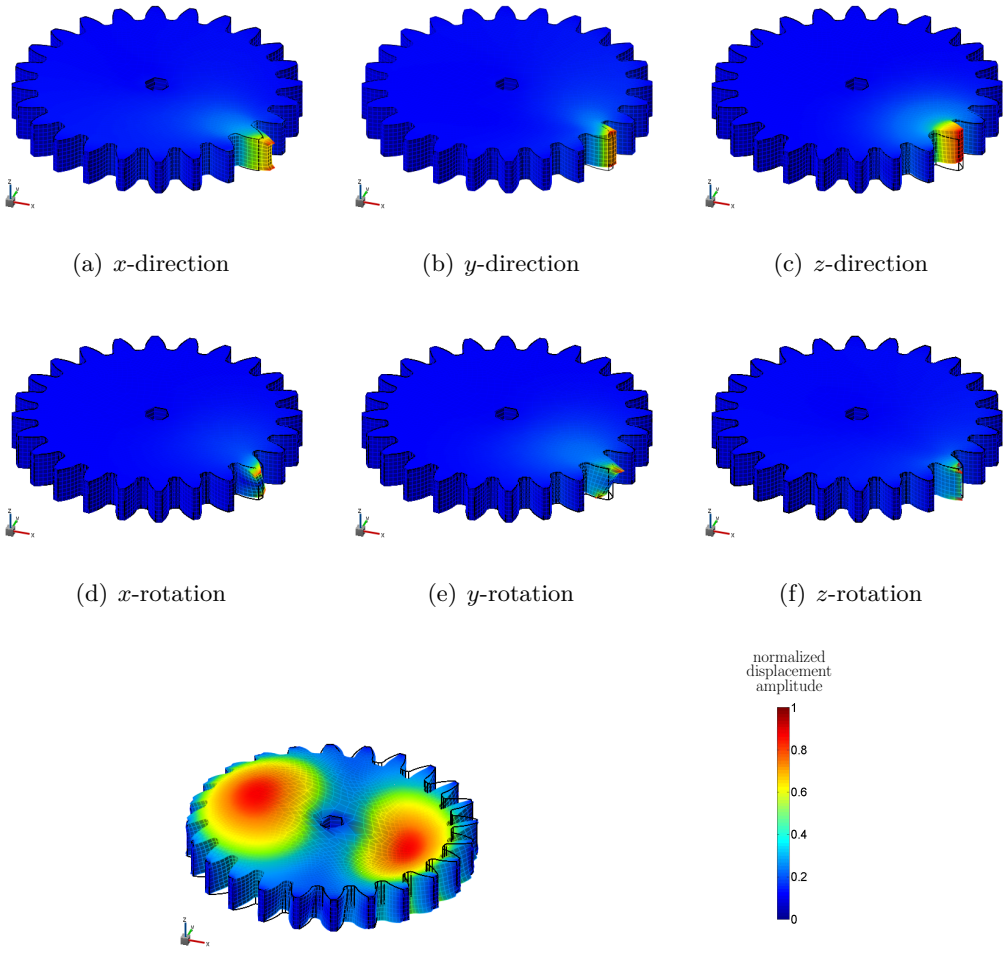

(a) x-direction (b) y-direction (c) z-direction

(d) x-rotation (e) y-rotation (f) z-rotation

(g) $f_2 = 16639$ Hz

Figure 6.26: Deformation modes of gear wheel superelement when the boundary nodes are additional nodes linked to each **tooth head face** by a mean joint: (a)-(f) static modes; (g) internal vibration mode.

than the mean defined on the tooth head face.

In order to capture the compression of the teeth due to the gear meshing, two independent mean elements can be used for each gear tooth, one per tooth flank (Fig. 6.28). Hence, there are two boundary nodes for each tooth and the number of static modes is multiplied by two.

Many others spatial configurations can be imagined for the boundary nodes. Since the deformations due to gear engagement are mainly localized inside the teeth, the modal basis needs to be able to represent accurately the tooth strains.

The node associated with the corotational frame offers a convenient way to pre-

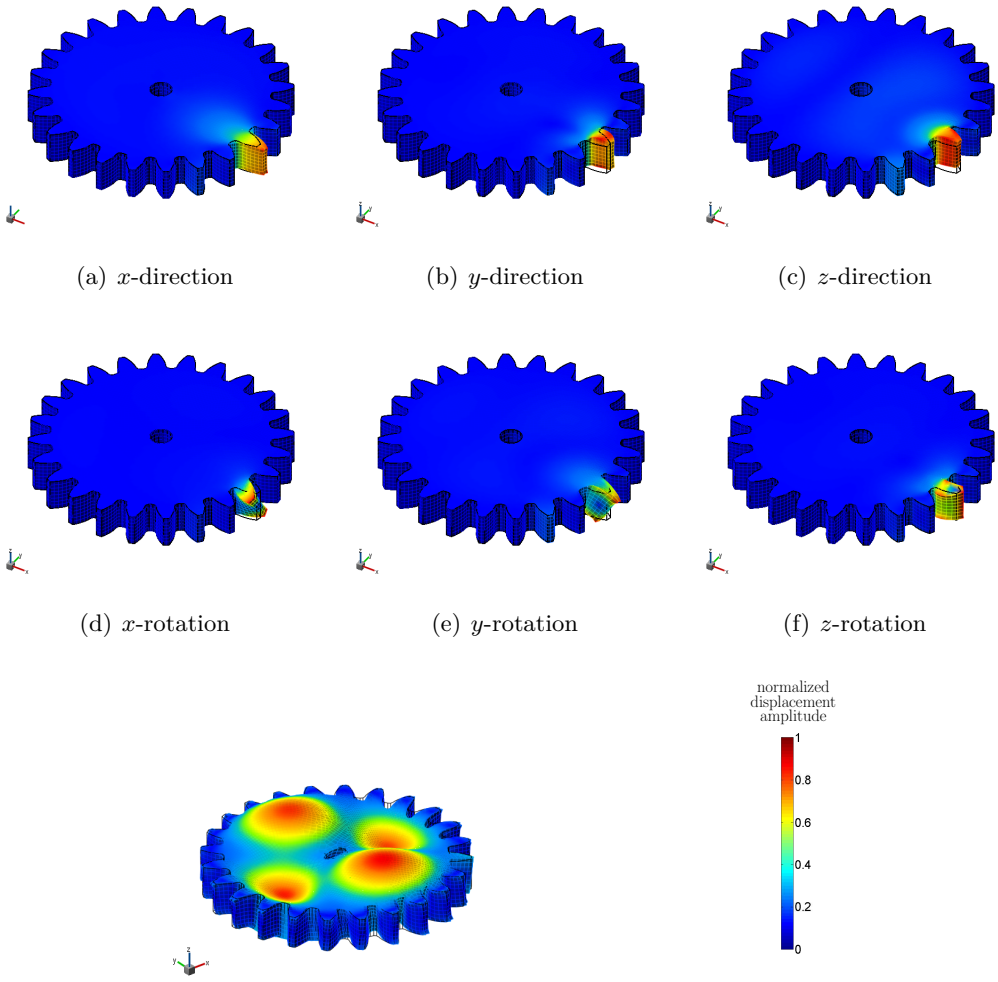

(a) x-direction (b) y-direction (c) z-direction

(d) x-rotation (e) y-rotation (f) z-rotation

(g) $f_2 = 29239$ Hz

Figure 6.27: Deformation modes of gear wheel superelement when the boundary nodes are additional nodes linked to the **two flanks of a same tooth** by a **mean** joint: (a)-(f) static modes; (g) internal vibration mode.

scribe the rotation or to apply a torque onto a gear wheel. This is due to the fact that the corotational frame coordinates have been included in the set of generalized coordinates (Eq. 6.17).

Another solution consists in placing a boundary node on the rotation axis and to apply the loads on this boundary node. Since there is often a bore in the gear web in order to connect the wheel to the driveshaft, a mean element between the cylindrical face of the hole and an additional node located on the rotation axis is also needed. In this way, the deformations of the gear wheel when driven by the driveshaft are represented by a set of six static modes (see Fig. 6.29). With this configuration, the node associated with the corotational frame is not necessarily exactly located on the

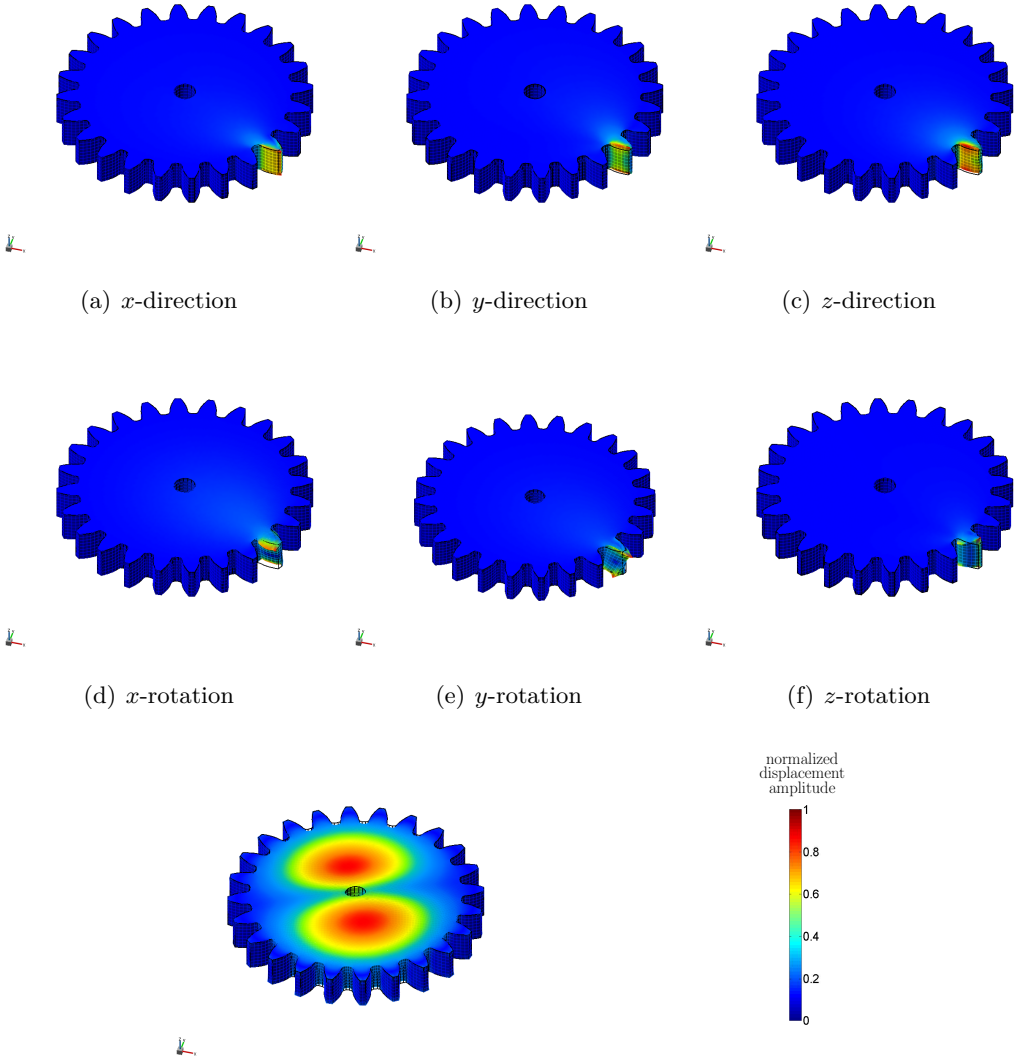

(a) x-direction (b) y-direction (c) z-direction

(d) x-rotation (e) y-rotation (f) z-rotation

(g) $f_2 = 22765$ Hz

Figure 6.28: Deformation modes of gear wheel superelement when the boundary nodes are additional nodes linked to **each tooth flank** by a **mean** joint: (a)-(f) static modes; (g) internal vibration mode.

rotation axis of the gear wheel. Its coordinates depend on the deformation distribution of the boundary nodes and are determined by the constraints defined in Eq. 6.50.

6.11.3 Spur gears

In this section, numerical results are presented for the simulation of a spur gear pair. The geometric data of the pinion and the gear come from Ref. [89] and are summarized

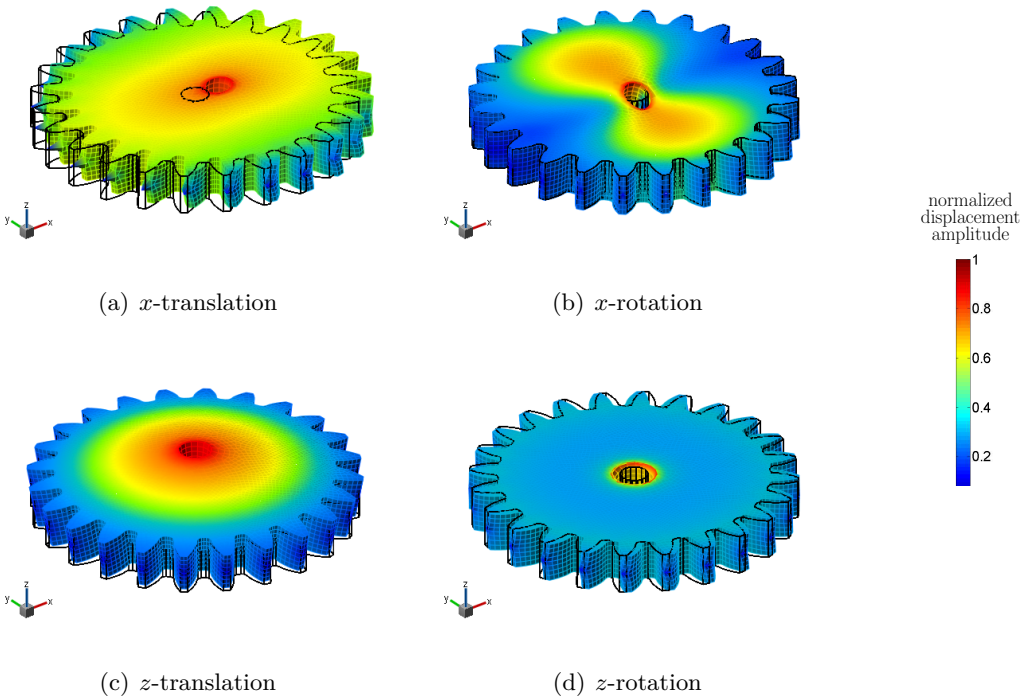

(a) x-translation (b) x-rotation

(c) z-translation (d) z-rotation

Figure 6.29: Static modes for the connection between the gear web and the driveshaft (model with mesh nodes chosen as boundary nodes, Fig. 6.25).

in Table 6.1. As for the two previous test models, the material properties correspond to a standard steel: Young's modulus = 210 GPa, Poisson's ratio = 0.3 , mass density = 7800 kg/m^3.

	Pinion	**Gear**
Number of teeth [-]	16	24
Pitch diameter [mm]	73.2	109.8
Outside diameter [mm]	82.64	118.64
Root diameter [mm]	62.50	98.37
Face width [mm]	15	15
Addendum modification coefficient [-]	0.196	0.125
Pressure angle [deg]	20	20
Module [mm]	4.5	4.5

Table 6.1: Geometric data of spur gear wheels [89].

The configuration of boundary nodes where there is one boundary node per tooth flank has been chosen (see Fig. 6.28). This choice has been made to have the closer model to the dual superelement approach developed in the next chapter (Section 7.6.1) and allow in this way a consistent comparison of numerical results between both superelement formulations.

A boundary node is also located at the center of mass of the gear wheel (see Fig. 6.29). This node is connected to the bore in the gear web by a mean joint (see Eq. 6.101). This last boundary node is used to apply a torque or to prescribe the rotation of the gear wheel.

The superelement of the pinion and the gear wheel have 33 and 49 boundary nodes respectively and also includes 100 vibration modes. Therefore, the size of the reduced models amounts to 298 and 394 DOFs, which is much lower than the initial finite element models (331968 DOFs and 148203 DOFs respectively). The eigen frequencies are in the range $[35331; 146068]$ Hz for the pinion and in the range $[19513; 116664]$ Hz for the gear.

A hinge joint between the ground and the boundary node attached to the gear web bore is introduced to avoid the inclination of the wheel rotation axis. The misalignment will thus not be studied in this simulation. In order to analyze the dynamic response when there is a significant backlash between teeth, the center distance is set to $91,5$ mm.

Analysis of gear wheel deformation

In a first step, in order to assess in a simple way the proposed flexible gear pair model based on contact detection between two superelements, the following load cases have been applied to the system:

- the rotation of the gear wheel #2 is prevented;
- a torque is applied on the pinion gear following a ramp function (20 Nm after $t = 5\ 10^{-3}$ s.

At the initial time, the two gear wheels are separated by a narrow gap and the applied torque induces the contact between teeth. The dynamic simulation is performed using the generalized-α integration scheme with a fixed time step ($h = 10^{-4}$ s) and a spectral radius equal to $\rho_\infty = 0.1$.

The element faces detected in contact on the tooth flanks are depicted in red in Fig. 6.30 for both wheels. They are aligned along a line parallel to the rotation axis and their radial location is consistent with the angular position of the gear pair.

As mentioned in Section 6.6, the spatial discretization on the contacting faces has to be finer for the slave body than for the master body. Figure 6.30 shows that this recommendation is respected: 247 nodes are on each tooth flank of the slave body and 96 faces are on each tooth flank of the master body. This mesh grid enables to capture the meshing irregularities occurring for instance in case of misalignment but is too coarse to compute accurately the stresses. Let us note that since the rotation axes are fixed in the present test case, a smaller number of nodes and element faces could

have been chosen along the gear width direction because the contact always occurs on the full face width. In order to avoid penalizing the computational efficiency, a strategy has been adopted to reduce the number of projections, i.e., the slave nodes close to the upper edge of the gear wheel are not projected onto the lower master faces.

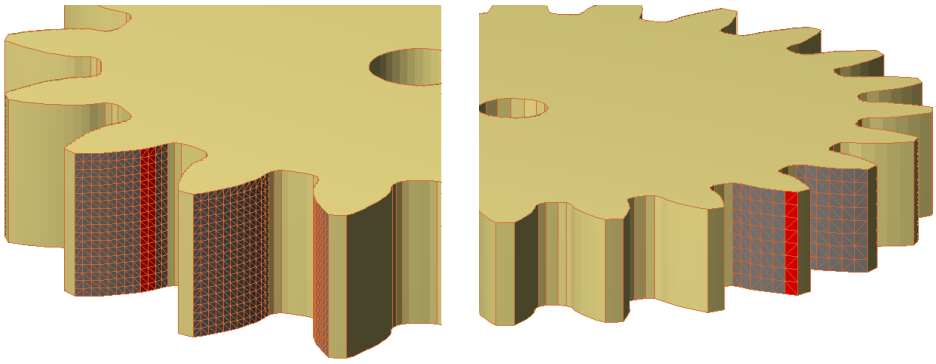

(a) pinion, slave body (b) gear, master body

Figure 6.30: Zone of tooth flanks in contact (in red). The candidate contact zones tested by the contact detection algorithm are the complete tooth flank surfaces (in gray).

The displacement of each point of the gear wheels can be computed from the generalized coordinates and the mode matrix of the superelement models (see Eq. 6.15). The norm of displacements in the three directions is illustrated in Fig. 6.31. As expected, the deformations are mainly concentrated in the gear teeth while the gear wheels undergo almost no deflection. A small deformation is nevertheless observed around the bore in the gear web and is due to the static modes associated with this connection between the gear wheel and the driveshaft. The maximum deformation amplitude is different for the two gear wheels since the thickness at the tooth root varies with the number of teeth. The position of the contact forces along the height of the teeth can also explain the difference of deformation between teeth. The zoom and amplified view in Fig. 6.32 shows the ability of the superelement model to represent the tooth bending.

The modal intensities of all internal vibration modes and the local displacements of all boundary nodes are represented in Figs. 6.33-6.34 for both gear wheels. The two boundary nodes attached to the tooth in contact undergo much larger displacements than the other boundary nodes (see Figs. 6.33(b)-6.34(b)). The displacements are almost null for the teeth at the opposite of the contacting tooth. The constant amplitude of the vibration modes in the steady state phase demonstrates the static contribution of these modes to the response of the superelement.

Figure 6.35 represents the time evolution of the amplitude of the contact force between superelement gear wheels. After some oscillations, a closed contact condition

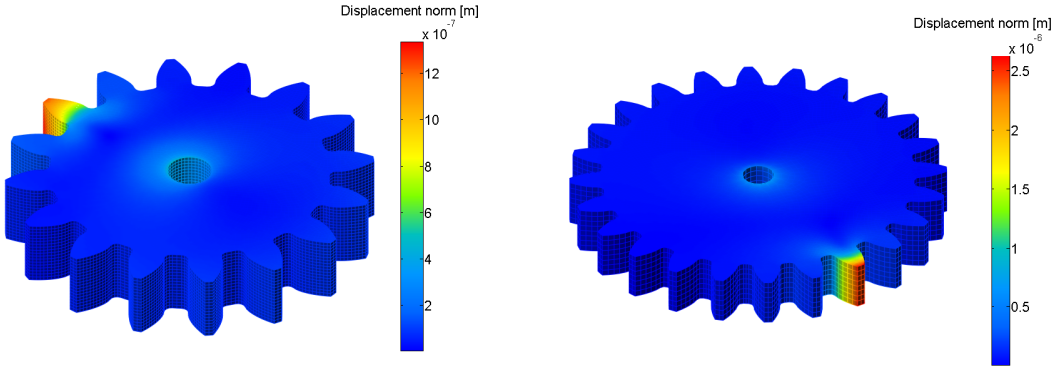

(a) pinion, slave body (b) gear, master body

Figure 6.31: The deformation of gear wheels are mainly concentrated in the teeth.

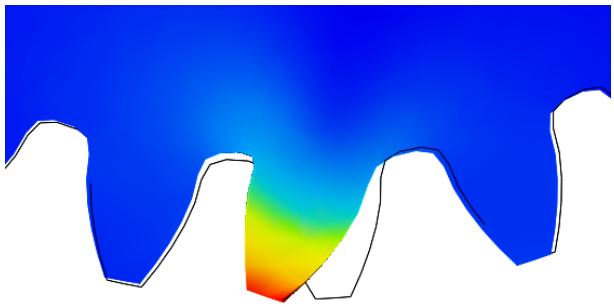

Figure 6.32: The tooth bending produced by gear contact is accounted for by the superelement model (deformation scaled by factor 2000, the wireframe representing the undeformed shape of the gear wheel #2).

is established between the tooth flanks resulting in a constant total contact force applied on the tooth flank. The angular position and the rotation velocity of the gear wheel submitted to the torque are given in Fig. 6.36 where it can observed that after a transient phase the wheel reaches a fixed angular position.

If the initial relative angular position of the two gear wheels is slightly modified and the torque amplitude is increased, the contact simultaneously occurs between two pairs of teeth (see Figs. 6.37-6.38). As depicted in Fig. 6.39, the amplitude of the total contact force is not equitably distributed between the two teeth pairs which explains why the deformations are not equal for both teeth. The tooth #2 enters in contact first and when the tooth has bend the tooth #1 also enters in contact.

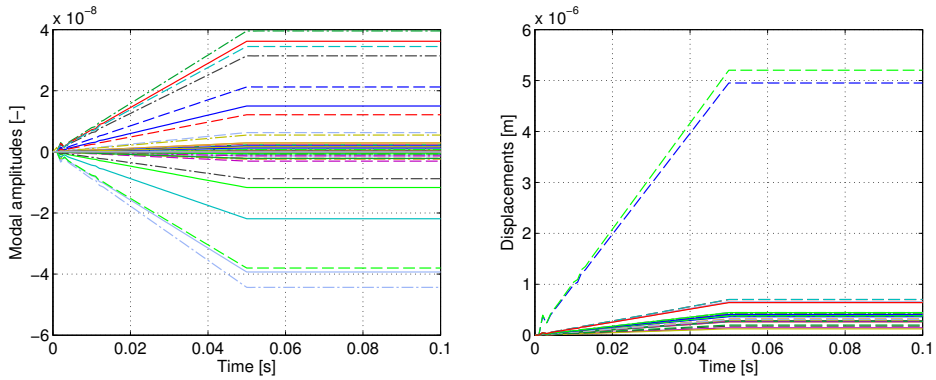

(a) $\boldsymbol{\eta}_I$: internal vibration modes (b) $\boldsymbol{u}_B$: boundary nodes

Figure 6.33: Time evolution of superelement local coordinates (pinion).

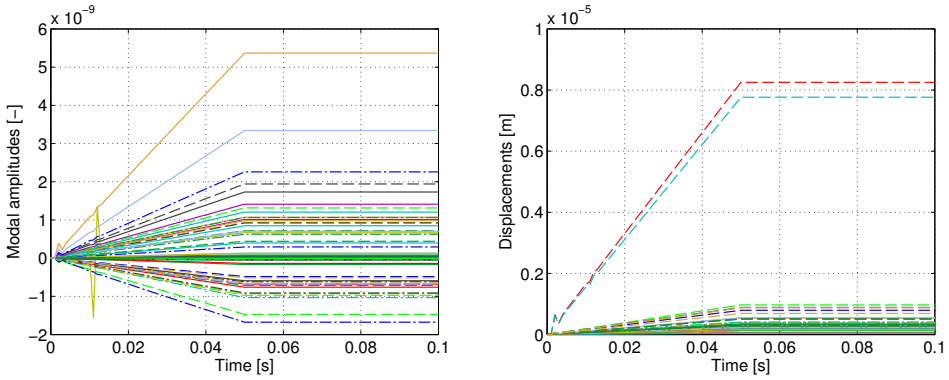

(a) $\boldsymbol{\eta}_I$: internal vibration modes (b) $\boldsymbol{u}_B$: boundary nodes

Figure 6.34: Time evolution of superelement local coordinates (gear).

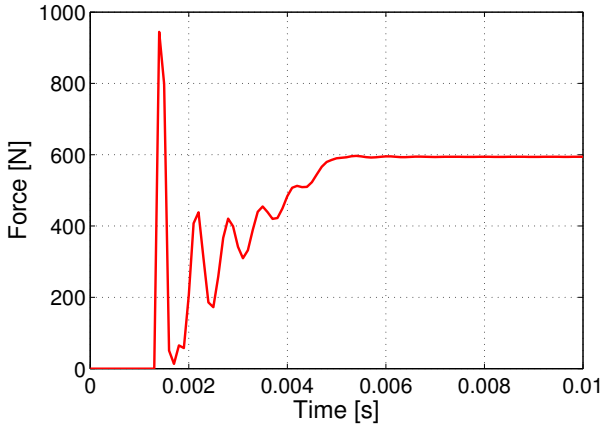

Figure 6.35: Amplitude of the total contact force applied on the tooth flank in contact.

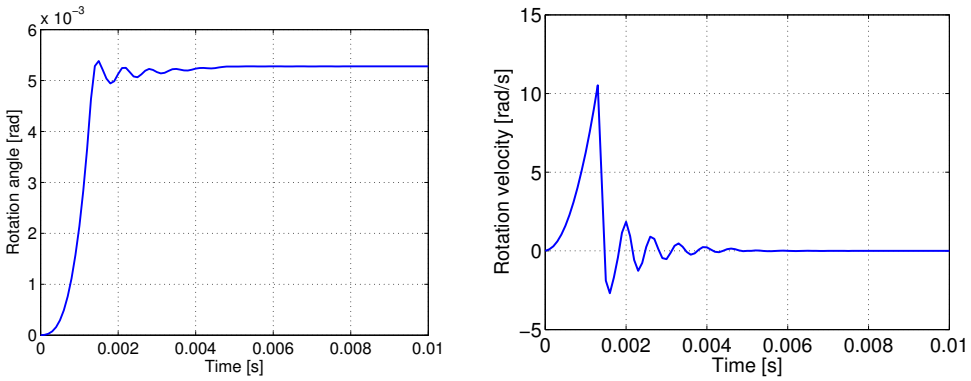

Figure 6.36: Angular position and velocity of the pinion gear #1.

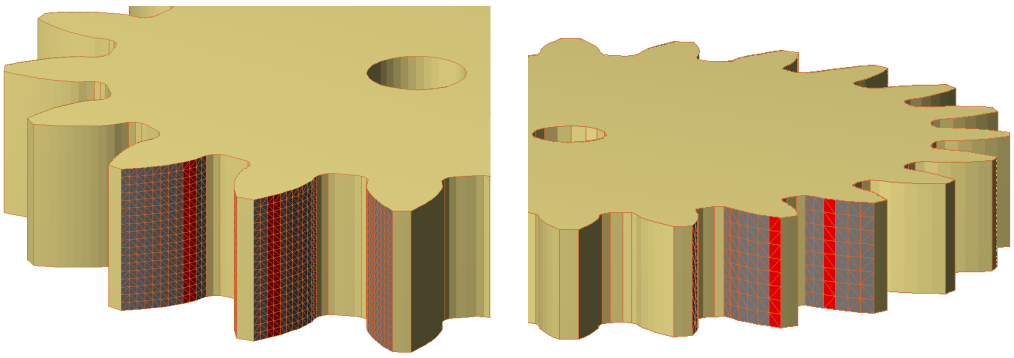

(a) pinion, slave body (b) gear, master body

Figure 6.37: Zone of tooth flanks in contact (in red) when there are two teeth simultaneously in contact. The candidate contact zones are the full tooth flank surfaces (in gray).

Dynamic simulation of gear meshing

In this section, the dynamic response of the spur gear pair is simulated with boundary conditions that mimic classical interactions with the rest of a transmission system.

At the initial time, both gears are not in contact and their rotation velocities are -1000 rpm for the pinion and 667 rpm for the gear according to the transmission ratio. During the whole simulation, the gear rotation is still prescribed at the same velocity whereas a viscous torque ($T = -c\,\omega_{(\mathrm{rad/s})}$) is applied on the pinion. This torque tends to slow down the gear and leads to contact between teeth of the geared wheels. Both gear wheels rotation axis are fixed, so that misalignment effects are not be studied here. The simulation is performed with a fixed time step of 1.E-6 s.

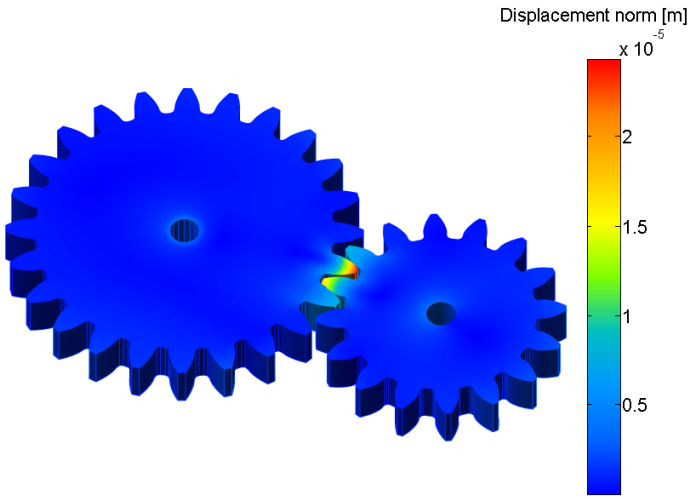

Figure 6.38: Norm of nodal displacements on gear wheels when there are two tooth pairs in contact.

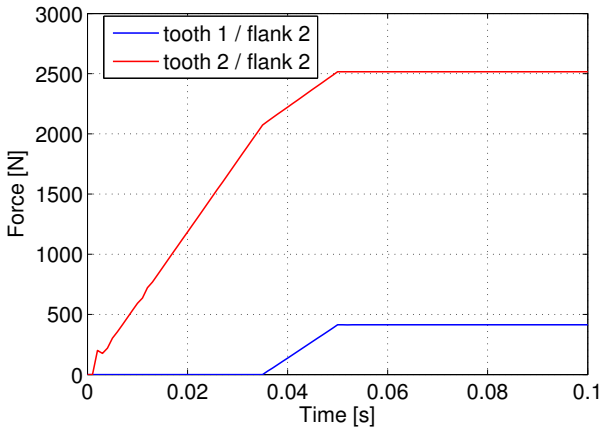

Figure 6.39: Amplitude of the contact force applied on the two tooth flank simultaneously in contact.

The penalty factor k_p of the contact law has been chosen much higher than the tooth stiffness to have a penetration length between the two bodies several orders of magnitude smaller that the tooth deformation. The damping coefficient c has been set to a value allowing to introduce enough dissipation to manage the impacts due to backlash or gear hammering. The values given to these two parameters are $k_p =$ 1E.17 N/m^3 and $c =$ 1E.12 kg/(m^{2}s).

Figure 6.40 displays the amplitude of the accumulated normal contact force applied on tooth flanks of the pinion. It can be observed that during the gear meshing there is

an alternation of time periods with one pair of teeth in contact and periods with two pairs simultaneously in contact. As a consequence of this variation of the mesh stiffness, the rotation of the gear wheels is not uniform during the revolution (Fig. 6.41).

Except during the single-teeth contact stages, the contact forces on tooth flanks vary steeply. Some abrupt changes occur when a second pair of teeth enters in contact or when switching from double to single-teeth contact. Indeed, due to the flexibility of the gear wheel, the applied contact forces give rise to small tooth deflections which result in geometrical improper contacts between gear tooth involutes. The proposed model is able to represent these undesired physical phenomena. For instance, the tooth tip might enter in contact too early (see Fig. 6.42) and produce a shock during the gear meshing. These hard contacts generate gear noise, transmission error and wear. As described in Ref. [89], the deviations from the theoretical geometry of the flank profiles due to the manufacturing process can also lead to similar effects. Reference [106] points out that a flank profile correction by tip relief allows to significantly reduce the discontinuities on contact force curves.

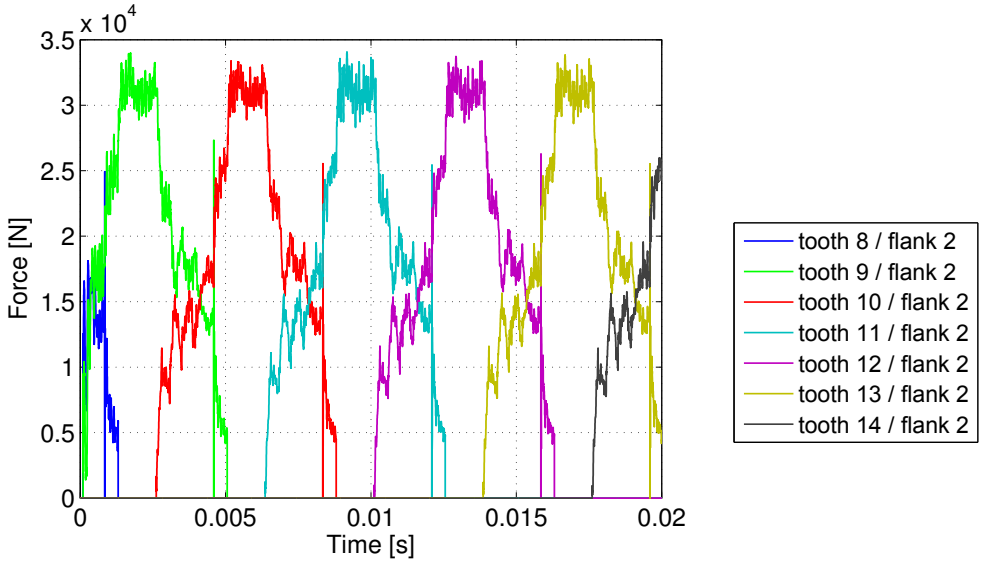

Figure 6.40: Normal contact force applied on tooth flanks of gear #1.

Another contribution to the sudden modifications of the tooth contact forces has a numerical origin and lies in the spatial discretization of the tooth involute. When slave nodes in contact move from one master face to another (see Fig. 6.8), a discontinuity can occur. This is particularly the case with the contact detection algorithm used here (Section 6.6) and the coarse mesh adopted in the present spur gear superelement models (Fig. 6.43).

Even though the contact force on each tooth flank is highly fluctuating, the total force magnitude for all tooth flanks in contact oscillates around the constant value cor-

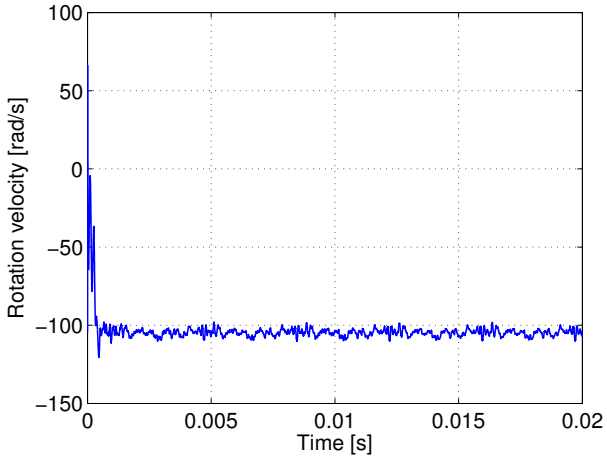

Figure 6.41: Rotation velocity of the gear #1 which is submitted to the viscous torque.

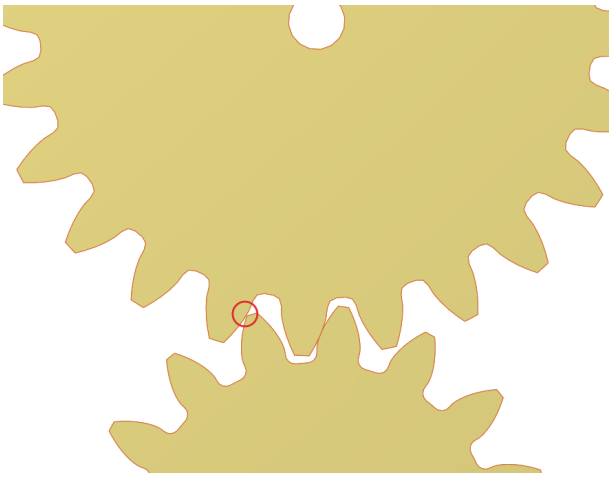

Figure 6.42: The tooth bending leads to inappropriate contact configuration such as too early tip contacts between gear teeth ($t = 0.0046$ s).

responding to a perfectly steady operation (Fig. 6.44(a)). The reaction torque related to the kinematic constraint prescribing the rotation velocity of the gear #2 is depicted in Fig. 6.44(b) and also shows some noise but the mean value verifies the transmission ratio.

The local displacements of the boundary nodes in the corotational frame are given in Fig. 6.45 for the pinion. It can be noted that the global evolution is similar to the distribution of the contact force between tooth flanks. The two boundary nodes attached to each tooth in contact undergo a much higher deformation than the other teeth. When a tooth has left the contact zone, the boundary nodes remains nearly undeformed. The only boundary node loaded during the full revolution is the node lo-

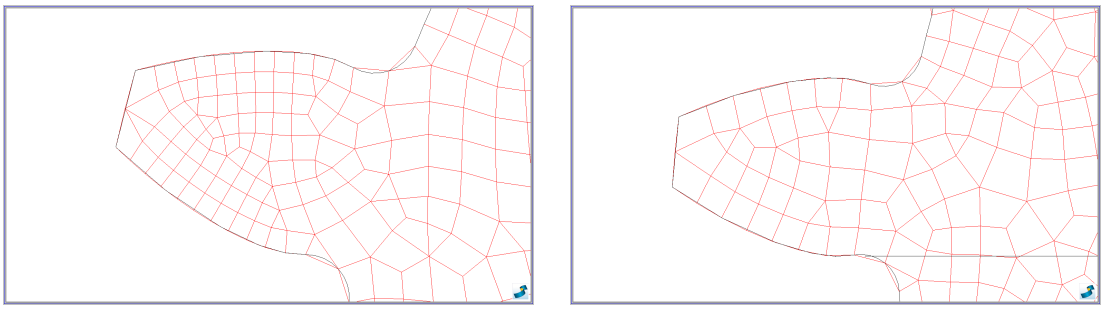

(a) slave body (b) master body

Figure 6.43: Spatial discretization on the flanks of gear teeth.

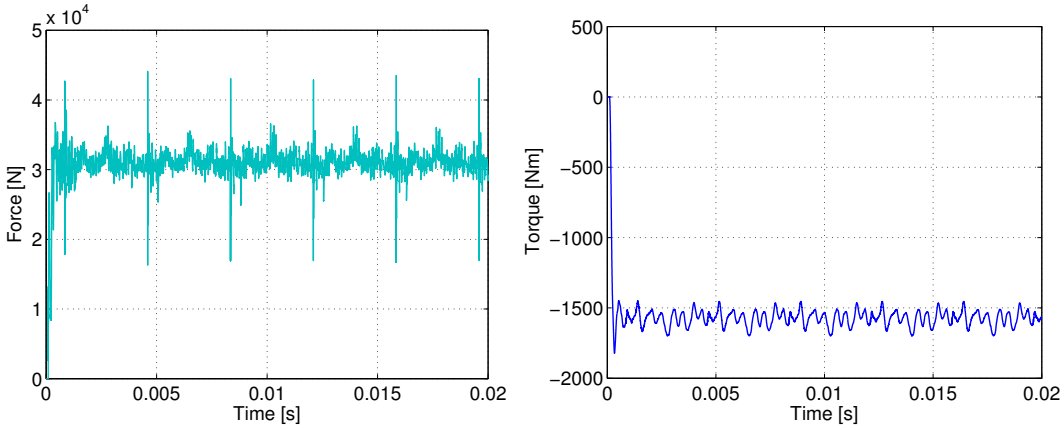

Figure 6.44: Total magnitude of the normal contact force between tooth flanks and reaction torque due to the imposed rotation speed of gear wheel #2.

cated on the rotation axis and used to applied the torque. The red curve on Fig. 6.45(b) with a nearly constant value corresponds to the static mode in torsion of this node.

The modal intensities of the internal vibration modes are illustrated in Fig. 6.46: they exhibit some oscillations when the contact forces present discontinuities.

Figure 6.47 shows that the deformation of teeth is three orders of magnitude higher than the mean penetration between the two bodies. The values given to the penalty parameter and the damping parameter of the contact law are thus appropriate.

The tooth deformation is directly related to the applied torques on the gear wheels. In order to assess the influence of the tooth bending on the contact force distribution between tooth flanks, the same spur gear pair system has been simulated with a smaller and a higher torque on the pinion (see Figs. 6.48-6.49). To this end, the damping parameter c of the viscous torque applied on the pinion ($T = -c\,\omega$) has been multiplied or divided by a factor 10, the other parameters remaining unchanged.

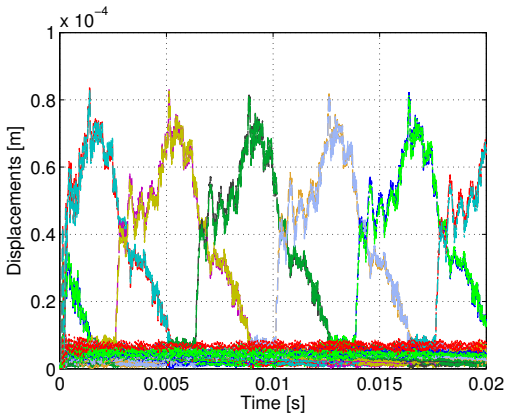

(a) $\boldsymbol{u}_B$: local displacement amplitudes in translation

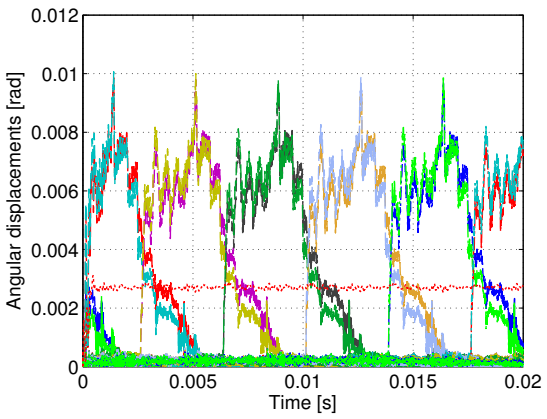

(b) $\boldsymbol{\gamma}_B$: local displacement amplitudes in rotation

Figure 6.45: Boundary node displacements (gear #1).

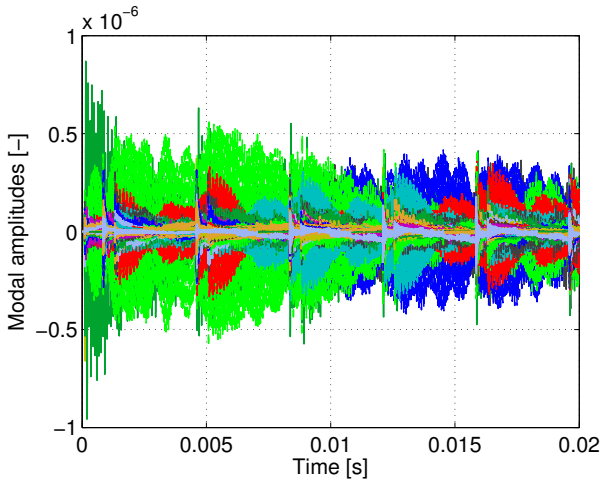

Figure 6.46: Time evolution of the modal intensities of internal vibration modes (gear #2).

The comparison of Figs. 6.40, 6.48(a) and 6.49(a) shows that the tooth flexibility has a huge influence on the distribution of the gear contact force between the various tooth flanks. The duration of the periods when only one pair of teeth is in contact decreases when the applied torque increases since the teeth stay longer in contact due to tooth bending. Indeed, with the high torque value (Fig. 6.48(a)) the deformation is such that there are always two flanks in contact. In contrast, the periods with two tooth pairs simultaneously in contact are very short when a low torque is applied (Fig. 6.49(a)) and instants when the contact is completely lost between the two gear wheels also appear due to the large backlash of the modelled gear pair. Figure 6.50

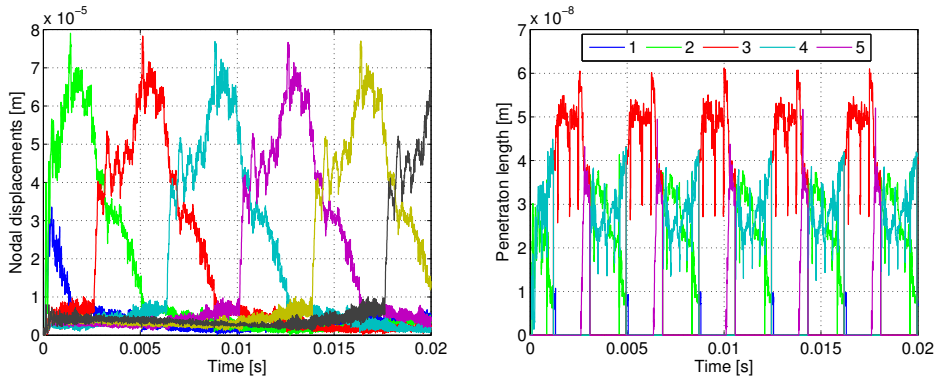

(a) mean deformation of the entire tooth flank face

(b) mean indentation between the slave nodes and the master faces for the five pairs tested by the contact detection algorithm

Figure 6.47: Comparison of the mean deformation of tooth flanks with the mean penetration length of the penalty based contact force formulation.

depicts the impacts occurring at the beginning of the simulation and demonstrates the ability of the model to simulate gear hammering.

The numerical results show that for the gear pair system studied here and the load cases adopted, the flexibility has a significant influence on the dynamic response. In order to assess the advantage of the proposed fully elastic gear pair model compared to fully rigid body models, the same system has been simulated with rigid superelements, i.e., each gear wheel is reduced to a unique boundary node and no internal vibration mode is included.

As represented in Fig. 6.51(a), there are never two tooth pairs simultaneously in contact. This is due to the very high contact stiffness used in the contact law (the same value as for the previous simulations) which leads to contact separation between two flanks as soon as a second tooth pair enters in contact. This phenomenon results in a highly discontinuous behaviour of the gear contact force. Let us note that most rigid body gear pair models (e.g., Ref. [16]) circumvent this drawback by reducing the contact stiffness in order to obtain a smoother response. The non negligible penetration permitted between the gear teeth relaxes the discontinuity and can be interpreted as a global measure the gear wheel deformation. In this way, the variation of the number of teeth in contact can be represented. Nevertheless, this kind of gear model represents the various effects of the flexibility in a more global way than the approach developed in this thesis and can result in a lack of accuracy in some non-standard configurations.

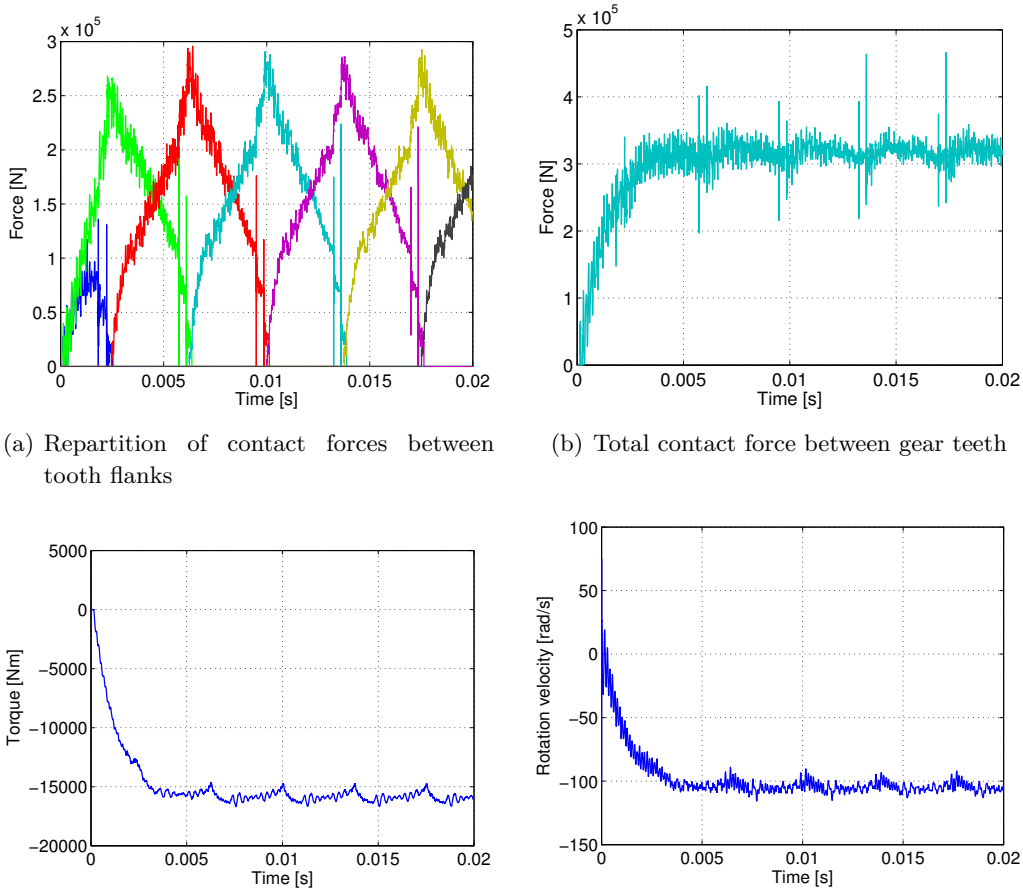

(a) Repartition of contact forces between tooth flanks

(b) Total contact force between gear teeth

(c) Resistant torque on gear #2

(d) Angular velocity of the pinion

Figure 6.48: Influence of tooth bending on the spur gear dynamic response when the viscous torque is 10 times **higher** ($T = -10\ c\ \omega$).

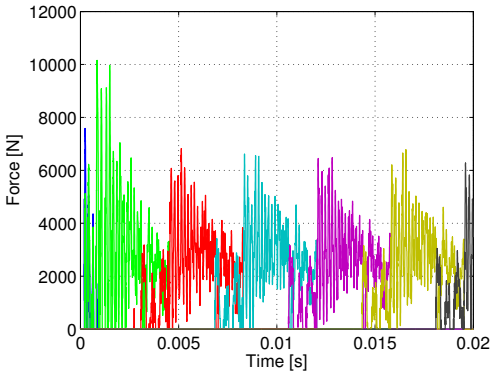

(a) Repartition of contact forces between tooth flanks

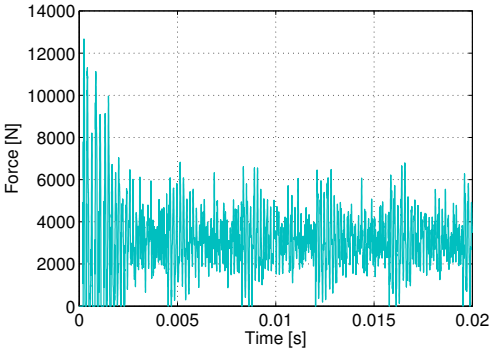

(b) Total contact force between gear teeth

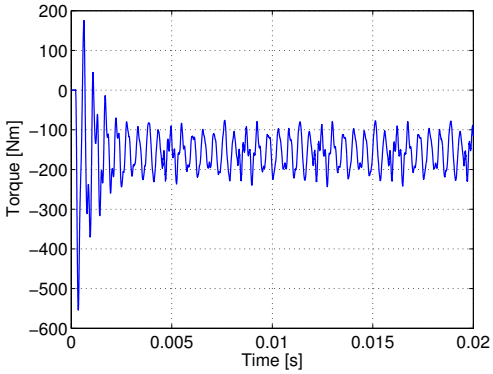

(c) Resistant torque on gear #2

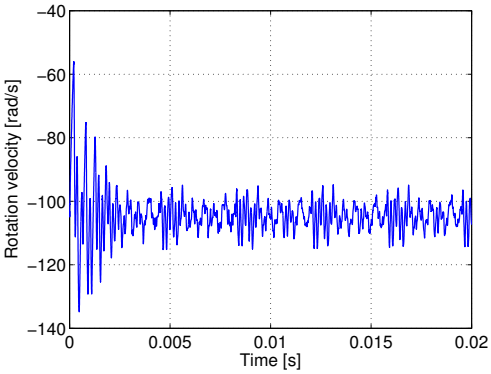

(d) Angular velocity of the pinion

Figure 6.49: Influence of tooth bending on the spur gear dynamic response when the viscous torque is 10 times **lower** ($T = -0.1\ c\ \omega$).

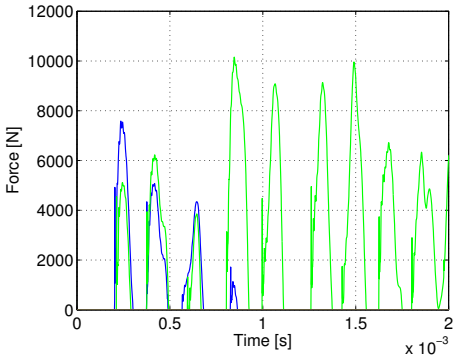

Figure 6.50: Zoom on impacts between tooth flanks at the beginning of the simulation ($T = -0.1\ c\ \omega$).

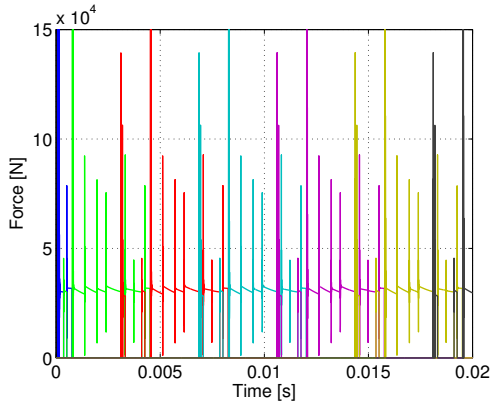

(a) Repartition of contact forces between tooth flanks

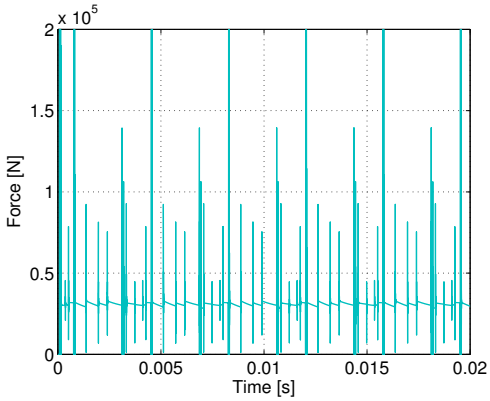

(b) Total contact force between gear teeth

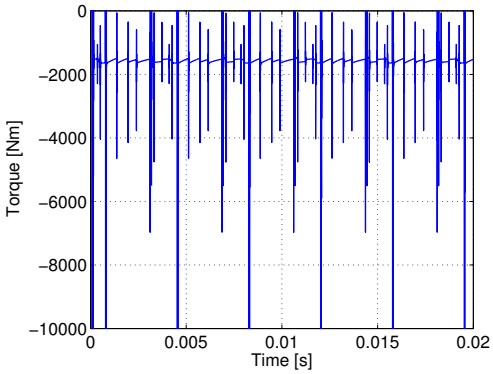

(c) Resistant torque on gear #2

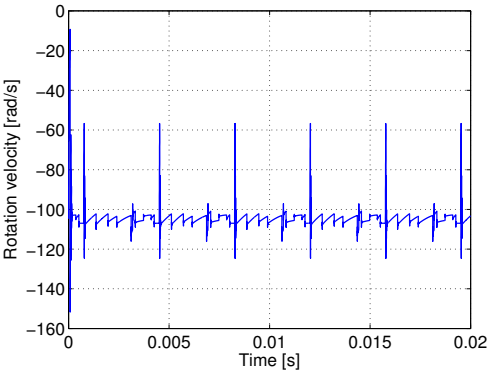

(d) Angular velocity of the pinion

Figure 6.51: Dynamic response of the spur gear pair with rigid gear wheels ($T = -c\,\omega$).

6.12 Concluding remarks

The contact formulation presented in this chapter is defined between two flexible bodies modelled as superelements. One major originality of the proposed approach addresses the determination of the spatial configuration of the potential contact zones from the superelement generalized coordinates. The contact forces computed in the 3D space are reformulated and directly applied upon the superelement generalized coordinates. Such approach allows very compact models of contacting bodies.

For systems with wide potential contact zones or with several sliding contact paths, the size of the reduced model would still be rather large if each potential contact node had to be retained. For instance, in the model of a gear pair, all the nodes on the teeth flanks can enter into contact during the gear mesh. In the formulation developed in this work, in order to keep the model as compact as possible, all the candidate contact nodes do not need to be included in the vector of generalized coordinates, so that a large number of nodes of the skin can still be condensed.

At each time step, the component mode description allows to reconstruct the 3D geometry of the candidate contact zones from the generalized coordinates of the superelement and the global shape functions of both static and dynamic modes. From the absolute positions of the candidate contact node, a node-to-face projection algorithm is used to detect the active contact zone. The contact forces are evaluated by a contact law based on a penalty method with stiffness and damping contributions. Then, these contact forces are mapped to the coordinates of the reduced model using nonlinear kinematic relationships.

The classical Craig-Bampton method has been adopted as the elastic model order reduction technique. It describes the body flexibility by a mixed set of static modes related to the boundary nodes and vibration modes related to the internal nodes. The reduced body matrices are defined in a corotational frame that follows the overall motion of the body, so that one can assume linear elastic behaviour in case of small strains. Only a couple of nodes, not compulsorily located on the contact zone, have to be selected as boundary nodes.

With the implementation achieved in the thesis, the full process to perform the dynamic simulation of contacts between superelements consists of three steps (see Fig. 6.52). The 3D geometry of each body is first constructed in a CAD software (CATIA V5). In a second step, the mesh to obtain the initial finite element model as well as the computation of the reduced matrices ($\overline{\boldsymbol{M}}$, $\overline{\boldsymbol{K}}$, $\overline{\boldsymbol{\Psi}}$) of the superelement are achieved using the SAMCEF FE software [87]. Last, the contact condition is fully implemented in MATLAB and the integration of the DAE-system during the model simulation is also performed in the development code.

The developed contact model between superelements offers a comprise between

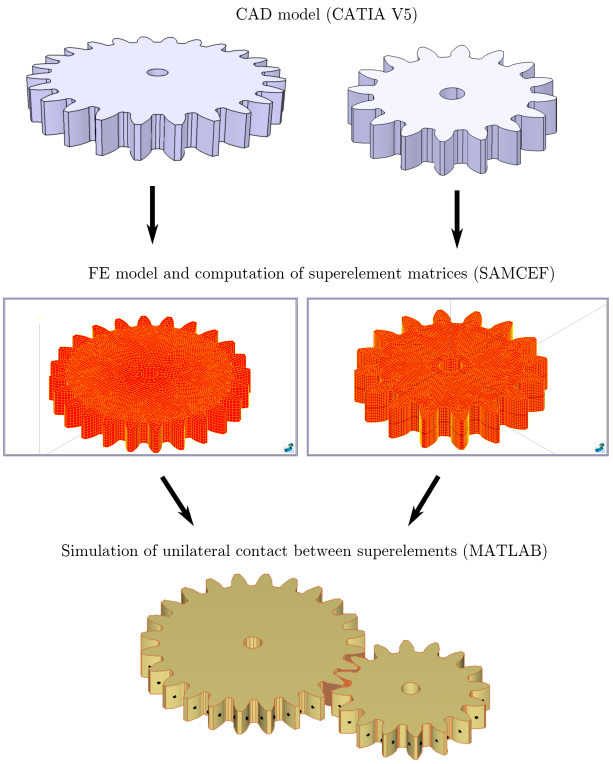

Figure 6.52: Various step of contact model between superelements.

rigid body models and fully elastic FE models. The flexibility effects of contacting bodies are globally represented by keeping a reasonable model size. Besides the contacts between two flexible bodies, rigid/flexible contacts or rigid-rigid contacts can also be represented by the contact formulation detailed in this chapter. In contrast to the rigid-rigid contact models developed in Chapters 4 and 5, no assumption is made for the geometry of the contacting surfaces and complex configurations can be represented.

The relevance of the developed contact approach between superelement models for the dynamic analysis of transmission devices has been assessed through simulation results of two simple benchmarks first, and then on a spur gear pair model.

The general gear pair model presented in this thesis is able to represent tooth bending and meshing defects such as misalignment, backlash or non-standard flank profiles. Since the objective is to obtain global models of transmission components, the number of modes included in each gear wheel superelement model is greatly reduced compared with a full FE model. Only one or two boundary nodes per tooth have been retained in the superelement model in order that the tooth bending is represented by static modes. The full gear pair model includes about 300 coordinates per gear wheel which is much lower than the 1500 modes used in the work described in Ref. [151].

The contact detection algorithm is very simple but comparative tests have shown that a major part of the CPU time is dedicated to the numerous projections of slave nodes on master faces. Some improvements have been introduced to reduce the number of projections, e.g., a selection strategy of tooth flanks around the gear pair center distance.

As a perspective to this work, a more efficient contact detection algorithm could be used before to consider the implementation in a commercial software. In order to avoid numerical oscillations due to a coarse discretization of the contact surface, a smooth detection algorithm based on a parametric curve to represent the actual geometry of the contact surface could be investigated (see Ref. [21]). In order to assess the number of modes needed to obtain a given accuracy, a detailed comparative study could be perform for various gear pair configurations.

Chapter 7

Dual superelement formulation for contact modelling

Contents

As in the previous chapter, this chapter addresses the modelling of contacts between superelements, the gear pairs being the main application system (Section 7.6). Nevertheless, another kind of elastic reduced order model is considered here: the **dual** Craig-Bampton method described in Section 7.2. As a consequence, only small changes appear in the contact force formulation which is summarized in Section 7.5. The expression of the kinematic constraints needed to connect the superelement to its environment are given in Section 7.4. Finally, the chapter ends with the presentation of simulation results (Section 7.6).

7.1 Introduction

The new contact formulation between superelements presented in Chapter 6 has shown satisfying results. Nevertheless, using another basis of deformation modes could improve the accuracy and the reliability of the mechanical response and reduce the CPU time of the simulation. The Craig-Bampton method is an efficient linear reduction

technique for numerous fields of applications but it is perhaps not the best choice when the superelements are connected to its external environment by contact forces.

As described in section 6.3, the Craig-Bampton substructuring technique is based on static modes, which correspond to a unit displacement of one boundary node while the other boundary nodes are clamped. The resulting shape functions present localized deformations around the associated boundary node and nearly no deformation outside this local area. Therefore, they poorly represent the global body deformation involved by contact forces which can occur on large contact zones that are continuously changing with the current configuration. This is particularly the case with the approach adopted previously which is based on a restricted number of boundary nodes to keep the model as compact as possible.

Moreover, the internal vibration modes have the meaning of deformation modes between fixed boundary nodes. The eigenfrequencies and eigenmodes included in the model are then strongly dependent on the number and position of the boundary nodes.

In order to circumvent these drawbacks, this chapter studies a formulation of the superelement using the dual approach. Among the various dual reduction techniques, the dual Craig-Bampton method developed by Rixen is chosen (see [113] for linear structures and [144] for planar co-rotated multibody dynamics). This dynamic substructuring method is based on a set of free interface eigenmodes completed by residual attachment modes. The substructures are assembled through interface forces. This choice is more natural than the MacNeal or Rubin methods [42] which enforce the superelement connectivity through displacements of interface nodes.

7.2 Dual Craig-Bampton method

The dual Craig-Bampton method is a linear reduction method based on the mechanical admittance concept [41, 77]. This latter consists in representing the dynamic response of a structural component by means of its **free-free vibration modes $\boldsymbol{\Psi}_f$** which are obtained by solving the eigenvalue problem:

$$\left(\boldsymbol{K} - \omega^2 \boldsymbol{M}\right) \boldsymbol{\Psi}_f = \mathbf{0}_{n\times n} \tag{7.1}$$

where $\boldsymbol{K}$ and $\boldsymbol{M}$ are the stiffness and mass matrices of the initial finite element model which has n degrees of freedom.

The first free-free vibration modes are the **rigid body modes** and have a zero eigenfrequency. They can be easily expressed as three pure translation modes and three pure rotation modes about the three directions of the reference frame (see the definition of $\boldsymbol{U}_{rig}$, Eqs. 6.51-6.52 in Section 6.5). These rigid body modes are mutually $\boldsymbol{M}$-orthogonal, so that:

$$\boldsymbol{U}_{rig}^T \boldsymbol{M} \boldsymbol{U}_{rig} = \boldsymbol{\mu}_{rig} \tag{7.2}$$

with

$$\boldsymbol{\mu}_{rig} = \begin{bmatrix} \boldsymbol{\mu}_{tr} & \mathbf{0} \\ \mathbf{0} & \boldsymbol{\mu}_{rot} \end{bmatrix} \tag{7.3}$$

where $\boldsymbol{\mu}_{rot}$ is the inertia matrix expressed in the reference frame and $\boldsymbol{\mu}_{tr} = m\boldsymbol{I}$, m being the total mass of the component. If the reference triad is aligned with the principal axes of the structure, $\boldsymbol{\mu}_{rot} = \text{diag}(\boldsymbol{I}_1, \boldsymbol{I}_2, \boldsymbol{I}_3)$ is also a diagonal matrix where the $\boldsymbol{I}_i$ are the principal moments of inertia.

In order to reduce the size of the system matrices, only a subset of eigenmodes are retained in the superelement and consequently the reduction basis includes $\overline{n_f}$ free vibration modes. This **restricted number of vibration modes** $\overline{\boldsymbol{\Psi}}_f$ does not contain the six rigid body modes and verifies the orthogonality properties:

$$\overline{\boldsymbol{\Psi}}_f^T \boldsymbol{K} \overline{\boldsymbol{\Psi}}_f = \boldsymbol{\omega}_f^2 \, \boldsymbol{\mu}_f \tag{7.4}$$

$$\overline{\boldsymbol{\Psi}}_f^T \boldsymbol{M} \overline{\boldsymbol{\Psi}}_f = \boldsymbol{\mu}_f \tag{7.5}$$

$$\overline{\boldsymbol{\Psi}}_f^T \boldsymbol{M} \boldsymbol{U}_{rig} = \mathbf{0} \tag{7.6}$$

where $\boldsymbol{\mu}_f$ and $\boldsymbol{\omega}_f^2$ are diagonal matrices of dimensions $\overline{n_f} \times \overline{n_f}$ with respectively the generalized modal masses and eigenvalues ($\omega_i = 2\pi f_i$ with f_i the eigenfrequencies). The set of free vibration modes retained are often the first eigenmodes with the lowest eigenfrequencies but it is not mandatory, e.g., a set of eigenmodes only in the frequency range of interest can also be selected.

The mechanical admittance principle states that the static response at interface points is correctly represented only if all free-free vibration modes are accounted for. Therefore, when using a truncated set of free-free vibration modes, the superposition of a residual flexibility correction is needed to recover a correct behaviour at attachment nodes.

The static modes, called **attachment modes**, related to the interface connections are collected in $\boldsymbol{Q}$ and are the solutions of

$$\boldsymbol{K} \, \boldsymbol{Q} = \boldsymbol{A}_{rig}^T \, \boldsymbol{G} \tag{7.7}$$

where $\boldsymbol{G}$ is a $n \times n_r$ matrix in which each column describes a **unit load** applied on one of the n_r boundary degrees of freedom. $\boldsymbol{A}_{rig}$ is a projection operator which transforms the set of loads $\boldsymbol{G}$ into self-equilibrated loads so that Equation 7.7 remains solvable for a semi-definite system:

$$\boldsymbol{A}_{rig} = \boldsymbol{I} - \boldsymbol{U}_{rig} \boldsymbol{\mu}_{rig}^{-1} \boldsymbol{U}_{rig}^T \boldsymbol{M} \tag{7.8}$$

This operator allows to filter the rigid body modes $\boldsymbol{U}_{rig}$:

$$\boldsymbol{x}^* = \boldsymbol{A}_{rig} \, \boldsymbol{x} \qquad \rightarrow \qquad \boldsymbol{x}^{*T} \boldsymbol{M} \boldsymbol{U}_{rig} = \mathbf{0} \qquad \forall \boldsymbol{x} \tag{7.9}$$

The attachment modes are often computed by the method of temporary links or by an alternative method which consists in solving a constrained system. Both methods are presented in the following.

Temporary links

The method of temporary links consists in fixing temporarily the structure to avoid the singularity of the stiffness matrix due to rigid body modes or kinematic modes. In this way, a pseudo-inverse of the stiffness matrix can be computed. The full procedure is presented in Ref. [44]. The method can summarized in Eq. 7.10 providing a very compact formulation to compute the static response of a free-free structure.

$$\begin{bmatrix} \boldsymbol{K}_{aa} & \boldsymbol{K}_{al} & \boldsymbol{0} \\ \boldsymbol{K}_{la} & \boldsymbol{K}_{ll} & \boldsymbol{I} \\ \boldsymbol{0} & \boldsymbol{I} & \boldsymbol{0} \end{bmatrix} \begin{bmatrix} \boldsymbol{Q}_{a,1} & \boldsymbol{Q}_{a,2} \\ \boldsymbol{Q}_{l,1} & \boldsymbol{Q}_{l,2} \\ \boldsymbol{\lambda}_1 & \boldsymbol{\lambda}_2 \end{bmatrix} = \begin{bmatrix} \boldsymbol{G}_a & \boldsymbol{M}\boldsymbol{U}_{rig,a} \\ \boldsymbol{G}_l & \boldsymbol{M}\boldsymbol{U}_{rig,l} \\ \boldsymbol{0} & \boldsymbol{0} \end{bmatrix} \tag{7.10}$$

The degrees of freedom of the initial FE model are partitioned into free DOFs $\boldsymbol{q}_a$ and a set of n_l constrained DOFs $\boldsymbol{q}_l$ where n_l is the number of rigid modes. The $n \times n_r$ matrix $\boldsymbol{G}$ is a Boolean matrix in which each column represents the unit external load applied on the DOFs associated with each individual attachment mode. It is partitioned into the $(n - n_l) \times n_r$ and $n_l \times n_r$ matrices $\boldsymbol{G}_a$ and $\boldsymbol{G}_l$; n_r is the number of attachment modes.

The last set of equations in the system 7.10 can be seen as iso-static constraints which allow to lock the structure, $\boldsymbol{Q}_l = \boldsymbol{0}$. The set of Lagrange multipliers $\boldsymbol{\lambda}_1$ $(n_l \times n_r)$ and $\boldsymbol{\lambda}_2$ $(n_l \times n_l)$ can be interpreted as the reaction forces at the locked DOFs.

In order to obtain the static response of the free-free structure, i.e., the attachment modes $\boldsymbol{J}$, the system responses $\boldsymbol{Q}_1$, $\boldsymbol{Q}_2$ have to be combined following Equation 7.11 which leads to have null reaction forces at the DOFs temporarily locked.

$$\boldsymbol{J} = \boldsymbol{Q}_1 - \boldsymbol{Q}_2 \; \boldsymbol{\lambda_2}^{-1} \; \boldsymbol{\lambda_1} \tag{7.11}$$

The implementation of the temporary links method as described by Equations 7.10 and 7.11 is refered to as the inertia relief method. Finally, the attachment modes are filtered with respect to rigid body modes $\boldsymbol{U}_{rig}$ and the vibrations modes $\overline{\boldsymbol{\Psi}}_f$ to give the **residual attachment modes** $\boldsymbol{\Psi}_r$:

$$\boldsymbol{\Psi}_r = \boldsymbol{A}_f \; \boldsymbol{A}_{rig} \; \boldsymbol{J} \tag{7.12}$$

where $\boldsymbol{A}_{rig}$ is the operator filtering the rigid body modes defined in Eq. 7.8 and $\boldsymbol{A}_f$ is the filtering operator enabling to obtain residual attachment modes orthogonal to the elastic modes (see Eq. 7.13). This projection step avoids free vibration modes to be accounted twice.

$$\boldsymbol{A}_f = \boldsymbol{I} - \overline{\boldsymbol{\Psi}}_f \boldsymbol{\mu}_f^{-1} \overline{\boldsymbol{\Psi}}_f^T \boldsymbol{M} \tag{7.13}$$

The location of temporarily locked DOFs can either be chosen by the model analyst or can be automatically determined according to the rule of maximum pivots applied to the initial finite element model.

Constrained system

An alternative method based on the solution of a constrained system (Eq. 7.14) may also be adopted in order to obtain the static response of the free-free system.

$$\begin{bmatrix} \boldsymbol{K} & \boldsymbol{M}\boldsymbol{U}_{rig} \\ \boldsymbol{U}_{rig}^T\boldsymbol{M} & \boldsymbol{0} \end{bmatrix} \begin{bmatrix} \boldsymbol{Q} \\ \boldsymbol{\lambda} \end{bmatrix} = \begin{bmatrix} \boldsymbol{G} \\ \boldsymbol{0} \end{bmatrix} \tag{7.14}$$

$\boldsymbol{G}$ is a $n \times n_r$ matrix with the unit loads applied on the DOFs corresponding to the n_r attachment modes $\boldsymbol{Q}$. The latter ones are already $\boldsymbol{M}$-orthogonal to the rigid body modes. Indeed, the constrained equations, i.e., the second set of equations in the DAE-system 7.14 ($\boldsymbol{U}_{rig}^T\boldsymbol{M}\boldsymbol{Q} = \boldsymbol{0}$), enforce that the attachment modes $\boldsymbol{Q}$ are orthogonalized with respect to the rigid body modes.

The residual attachment modes $\boldsymbol{\Psi}_r$ are simply obtained by filtering the attachment modes with respect to the free vibration modes:

$$\boldsymbol{\Psi}_r = \boldsymbol{A}_f \; \boldsymbol{Q} \tag{7.15}$$

with the filtering operator $\boldsymbol{A}_f$ defined in Eq. 7.13.

Contrarily to the previous method, this method does not require the temporary locking of the structure, which can be seen as an advantage. Therefore, the computation process of attachment modes is fully independent of the choice of the temporary fixations. Nevertheless, the expression of the six constrained equations (in case of a 3D system) is more complex than the iso-static constrained equations in the temporary links method. Indeed, all DOFs of the initial FE model are coupled by the algebraic constraints whereas only the fixed DOFs are explicitly constrained with the first method (see Eq. 7.10).

Whatever the approach adopted to compute the residual attachment modes, the reduction basis of the dual Craig-Bampton reduction technique simply consists in the concatenation of the two kinds of modes:

$$\overline{\boldsymbol{\Psi}} = \begin{bmatrix} \overline{\boldsymbol{\Psi}}_f & \boldsymbol{\Psi}_r \end{bmatrix} \tag{7.16}$$

The elastic displacement field $\boldsymbol{u}$ is approximated in the local frame by adding the contribution of the attachment modes to the contribution of the free vibration modes:

$$\boldsymbol{u} \cong \overline{\boldsymbol{\Psi}}_f \; \boldsymbol{\eta}_f + \boldsymbol{\Psi}_r \; \boldsymbol{r} \tag{7.17}$$

where $\boldsymbol{\eta}_f$ is a vector with the contribution factors of eigenmodes and $\boldsymbol{r}$ are the intensities of loads associated with the residual attachment modes. The latter are interpreted as Lagrange multipliers in Ref. [113] since they have the meaning of a force at interface nodes.

The fact of getting a hybrid set of reduced variables $\left(\boldsymbol{\eta}^T = \{\boldsymbol{\eta}_f^T \ \boldsymbol{r}^T\}\right)$ is the main difference between the dual Craig-Bampton method and the Mac Neal or Rubin reduction techniques. Although they are based on the same ingredients, Mac Neal and Rubin introduce a change of variables such that the resulting superelements can be expressed in terms of interface displacements rather than interface forces. In this way, a primal assembly of the substructure with its external environment can be used, which is common and easy in a finite element framework. In contrast, the dual Craig-Bampton method keeps the interface forces as connection variables in the vector of reduced variables.

An attachment mode often corresponds to the static response of the system when one of its nodes is submitted to a unit force. But attachment modes can also be related to a more global behaviour. For instance, an attachment mode can correspond to a constant pressure applied on an external face of the body modelled as a superelement. That allows having a very restricted number of attachment modes and therefore induces very compact reduced matrices. Moreover, this kind of global static modes avoids the delicate choice of a particular boundary node on a contact face as was the case with the primal Craig-Bampton method for the simulation of gear pairs (see Section 6.11.2).

The part of the reduced stiffness and mass matrices related to the residual attachment modes is obtained by projecting the full FE matrices in the basis formed by the residual attachment modes:

$$\overline{\boldsymbol{K}}_{rr} = \boldsymbol{\Psi}_r^T \boldsymbol{K} \boldsymbol{\Psi}_r \tag{7.18}$$

$$\overline{\boldsymbol{M}}_{rr} = \boldsymbol{\Psi}_r^T \boldsymbol{M} \boldsymbol{\Psi}_r \tag{7.19}$$

The denomination *reduced stiffness matrix* is a misuse of language since the matrix $\overline{\boldsymbol{K}}_{rr}$ has the physical meaning of a **flexibility matrix** because of the nature of the attachment modes.

In the local frame, the whole stiffness and mass matrices of the reduced model are expressed by Equation 7.20.

$$\overline{\boldsymbol{K}} = \begin{bmatrix} \boldsymbol{\omega}_f^2 \ \boldsymbol{\mu}_f & \boldsymbol{0} \\ \boldsymbol{0} & \overline{\boldsymbol{K}}_{rr} \end{bmatrix}, \qquad \overline{\boldsymbol{M}} = \begin{bmatrix} \boldsymbol{\mu}_f & \boldsymbol{0} \\ \boldsymbol{0} & \overline{\boldsymbol{M}}_{rr} \end{bmatrix} \tag{7.20}$$

Unlike the primal Craig-Bampton method (Section 6.3), the reduced stiffness matrix is not singular because the rigid body modes are not accounted for in the free-free vibration modes $\overline{\boldsymbol{\Psi}}_f$. Likewise, the two kinds of modes are fully uncoupled in the reduced matrices contrarily to the primal Craig-Bampton method in which the reduced mass matrix includes coupling terms (see Eq. 6.12).

Since the matrix $\overline{\boldsymbol{K}}_{rr}$ has the physical nature of flexibility matrix, it is needed to scale the attachment modes so that the components of $\overline{\boldsymbol{K}}_{rr}$ have the same order of magnitude as the diagonal terms of $\boldsymbol{\omega}_f^2 \ \boldsymbol{\mu}_f$. In this way, the ill-conditioning of the reduced matrices $\overline{\boldsymbol{K}}$, $\overline{\boldsymbol{M}}$ describing the superelement is avoided.

The reduced stiffness and mass submatrices related to the free-free eigenmodes (i.e. $\boldsymbol{\omega}_f^2\ \boldsymbol{\mu}_f$ and $\boldsymbol{\mu}_f$ respectively in $\overline{\boldsymbol{K}}$ and $\overline{\boldsymbol{M}}$ defined in Eq. 7.20) have a diagonal structure whereas the submatrices $\overline{\boldsymbol{K}}_{rr}$, $\overline{\boldsymbol{M}}_{rr}$ are full matrices. In order to have diagonal reduced matrices $\overline{\boldsymbol{K}}$ and $\overline{\boldsymbol{M}}$, a **mass orthogonalization** of the subsystem formed by the residual attachment modes can be performed. To this end, the eigenvalue problem

$$\overline{\boldsymbol{K}}_{rr}\ \boldsymbol{r}^* = \omega^2\ \overline{\boldsymbol{M}}_{rr}\ \boldsymbol{r}^* \tag{7.21}$$

has to be solved. The vectors $\boldsymbol{r}^*$ are the eigenvectors of the problem 7.21, they should not be confused with the eigenmodes $\overline{\boldsymbol{\Psi}}_f$ of the free-free structure.

Due to this $\boldsymbol{M}$-orthogonalization, the reduction basis (Eq. 7.16) is slightly modified since the residual attachment modes $\boldsymbol{\Psi}_r$ are replaced by $\boldsymbol{\Psi}_{r*}$:

$$\boldsymbol{\Psi}_{r*} = \boldsymbol{\Psi}_r\ \boldsymbol{R}^* \tag{7.22}$$

where $\boldsymbol{R}^*$ is a matrix containing the n_r eigenvectors $\boldsymbol{r}^*$.

The reduced stiffness and mass matrices of the superelement have now the following form:

$$\overline{\boldsymbol{K}} = \begin{bmatrix} \boldsymbol{\omega}_f^2\ \boldsymbol{\mu}_f & \boldsymbol{0} \\ \boldsymbol{0} & \boldsymbol{\omega}_r^2\ \boldsymbol{\mu}_r \end{bmatrix}\ , \qquad \overline{\boldsymbol{M}} = \begin{bmatrix} \boldsymbol{\mu}_f & \boldsymbol{0} \\ \boldsymbol{0} & \boldsymbol{\mu}_r \end{bmatrix} \tag{7.23}$$

where $\boldsymbol{\omega}_r$ is a diagonal matrix with the eigenfrequencies of the *pseudo-eigenmodes* related to the attachment modes. $\boldsymbol{\mu}_r$ includes their generalized modal masses and it is also a diagonal matrix. The lowest eigenfrequency of the orthogonalized attachment modes ($\min f_r$) is always higher than the highest eigenfrequency of the free-free vibration modes ($\max f_f$). The diagonal topology of the matrices is an essential feature since it allows taking advantage of sparse solvers and contributes to CPU time reduction.

In order to illustrate clearly the physical interpretation of the attachment modes, a very simple benchmark is presented in Figs. 7.1-7.5. The elastic bar depicted in Figure 7.1 is meshed with hexahedral volume elements and is made of steel (Young's modulus: 210 GPa, Poisson's ratio: 0.3 , mass density: 7800 kg/m^3).

The first fourtheen free vibrations modes are retained in the superelement reduction basis. The deformed shape of the seventh eigenmode is depicted in Fig. 7.2. For each of the four nodes of the element surface colored in gray (Fig. 7.1), an attachment mode corresponding to a unit load applied along each of the three frame axes x, y, z is considered. Therefore, a total of 12 attachment modes are computed for this system.

The deformed shape of the three attachment modes $\boldsymbol{\Psi}_r$ associated with the node highlighted by a red cross is depicted in Figure 7.3. The residual attachment modes, i.e. after the filtering process of retained eigenmodes, are represented in Fig. 7.4 for the same interface node. Finally, the deformed shapes of these residual attachment modes after $\boldsymbol{M}$-orthogonalization are illustrated in Fig. 7.5. One can observe that the attachment modes and their residual forms can be easily interpreted while the physical meaning is lost after the $\boldsymbol{M}$-orthogonalization.

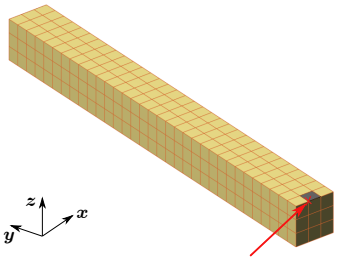

Figure 7.1: Elastic bar meshed with volume elements. Attachment nodes are computed for the nodes of the element surface colored in gray.

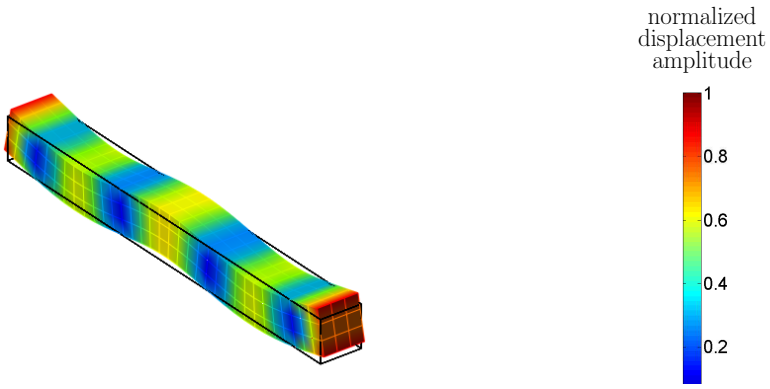

Figure 7.2: Deformed shape of the 7^{th} free vibration mode.

From the description of the principles at the basis of the dual Craig-Bampton method, it appears clearly that this reduction technique is more suitable for contact modelling between massive 3-D elastic structures than the primal Craig-Bampton method. Indeed, the interconnection between bodies submitted to contact conditions is enforced through contact forces. Therefore, a reduction basis where the static modes represent the body deformation when unit loads are applied without clamping the boundary DOFs appears as a better the best way to define the shape functions of superelements submitted to contact conditions. Besides, the vibration modes are related to the free-free structure and are then independent of the number and location of the static boundary nodes.

In the sequel of this dissertation thesis, the basic Craig-Bampton method (Section 6.3) will be denoted as the *primal* Craig-Bampton method in order to avoid the confusion with the *dual* Craig-Bampton approach which has just been introduced.

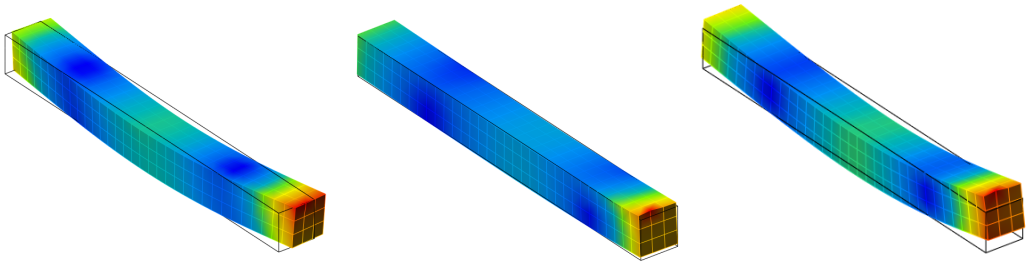

(a) x-direction (b) y-direction (c) z-direction

Figure 7.3: Attachment modes $\boldsymbol{Q}$ (filtered with respect to the rigid body modes but not with respect to the retained free vibration modes).

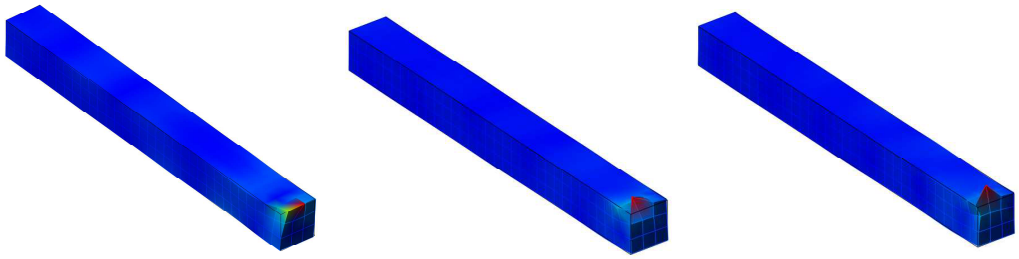

(a) x-direction (b) y-direction (c) z-direction

Figure 7.4: Residual attachment modes $\boldsymbol{\Psi}_r$ (after filtering with respect to the free vibration modes).

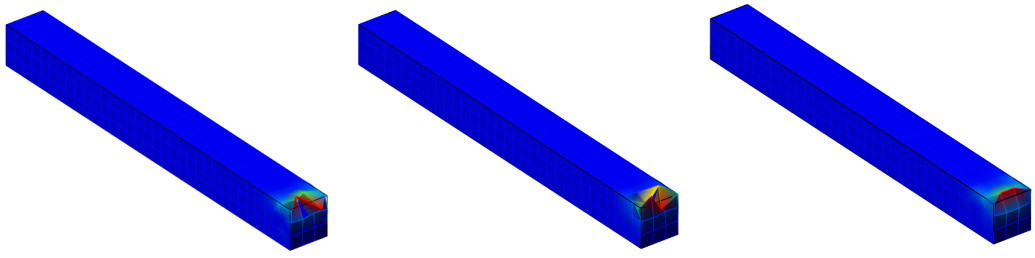

(a) x-direction (b) y-direction (c) z-direction

Figure 7.5: Residual attachment modes $\boldsymbol{\Psi}_{r^*}$ after mass orthogonalization.

7.3 Superelement formulation

In case of large amplitude motion, the linear elasticity assumption can be used in a moving frame following the global motion of the superelement. The **floating frame** approach is used as a local frame in contrast to the primal Craig-Bampton method where a corotational frame has been used (see Section 6.4).

The floating frame enables to separate the rigid body motion from the elastic deformation.

7.3.1 Kinematic description

As for primal Craig-Bampton superelements, the position and rotation matrix of any point of a superelement modelled by the dual Craig-Bampton method can be determined according to Equations 6.13-6.15.

The local coordinates vector $\boldsymbol{\eta}$ (Eq. 7.24) in the floating frame is simply formed by the modal amplitudes of the free eigenmodes ($\boldsymbol{\eta}_f$) and the residual attachment modes ($\boldsymbol{r}$) respectively.

$$\boldsymbol{\eta} = \begin{Bmatrix} \boldsymbol{\eta}_f \\ \boldsymbol{r} \end{Bmatrix} \tag{7.24}$$

In the inertial frame, in addition to the local coordinates $\boldsymbol{\eta}$, the set of generalized coordinates $\boldsymbol{q}$ (Eq. 7.25) includes also the position $\boldsymbol{x}_0$ and rotation $\boldsymbol{\alpha}_0$ variables of the floating frame. The reference node $'0'$ associated with the origin of the floating frame is affected with the total mass and inertia properties of the whole structure.

$$\boldsymbol{q} = \begin{Bmatrix} \boldsymbol{x}_0 \\ \boldsymbol{\alpha}_0 \\ \boldsymbol{\eta} \end{Bmatrix} \tag{7.25}$$

As for the primal Craig-Bampton superelement, the rotation variables are not parametrized but represented by the Lie Group $R^3 \times SO(3)$.

7.3.2 Elastic and inertia forces

The expression of elastic and inertia forces are obtained by applying the Hamilton principle (see Section 2.2.2).

The discretized form of the superelement **kinetic energy** can be computed as a quadratic expression of the absolute velocities rotated in the floating frame even if it is

a non consistent approximation (see Ref. [42]):

$$\mathcal{K} = \frac{1}{2} \sum_i \sum_j \left\{ \left(\boldsymbol{R}_0^T \dot{\boldsymbol{x}}_i \right)^T \quad \boldsymbol{\Omega}_i^T \right\} \boldsymbol{M}_{ij} \left\{ \begin{array}{c} \boldsymbol{R}_0^T \dot{\boldsymbol{x}}_j \\ \boldsymbol{\Omega}_j \end{array} \right\} \tag{7.26}$$

where the $\dot{\boldsymbol{x}}_i$, $\dot{\boldsymbol{x}}_j$ are the absolute nodal velocities in translation of the initial FE model; $\boldsymbol{\Omega}_i$, $\boldsymbol{\Omega}_j$ are the velocities of angular DOFs in the material frame and $\boldsymbol{M}_{ij}$ are the 6×6 blocks of the FE mass matrix coupling the node i and j.

After differentiation with respect to the time, the kinematic description of the absolute position defined in Eq. 6.13 and premultiplying by $\boldsymbol{R}_0^T$, the rotated absolute velocities in translation are expressed as:

$$\boldsymbol{R}_0^T \dot{\boldsymbol{x}}_i = \boldsymbol{R}_0^T \dot{\boldsymbol{x}}_0 + \widetilde{\boldsymbol{\Omega}}_0 \boldsymbol{X}_i + \widetilde{\boldsymbol{\Omega}}_0 \boldsymbol{u}_i + \dot{\boldsymbol{u}}_i \tag{7.27}$$

The first two terms of the last expression can be interpreted as the *rigid part* of the rotated absolute velocity. If the reference node associated with the floating frame is located at the center of mass of the undeformed structure, this rigid part can be reformulated as:

$$\left(\boldsymbol{R}_0^T \dot{\boldsymbol{x}}_i \right)_{rig} = \boldsymbol{U}_{tr,i} \; \boldsymbol{R}_0^T \dot{\boldsymbol{x}}_0 + \boldsymbol{U}_{rot,i} \; \boldsymbol{\Omega}_0 \tag{7.28}$$

where $\boldsymbol{U}_{tr,i}$ and $\boldsymbol{U}_{rot,i}$ are 3×3 matrices representing the contribution of the considered node in the rigid body modes in translation and rotation respectively (see Section 6.52). This expression is valid provided that the rigid body modes are defined as three pure translational and three rotational modes along the three coordinate axes of the material frame in its initial configuration ($\boldsymbol{U}_{tr,i} = \boldsymbol{I}$ and $\boldsymbol{U}_{rot,i} = -\widetilde{\boldsymbol{X}}_i$).

For stiff bodies, the third term of Eq. 7.27 ($\widetilde{\boldsymbol{\Omega}}_0 \boldsymbol{u}_i$) can be omitted which means that the change of the inertia tensor caused by the elastic deformation is not accounted for. This second-order approximation is acceptable for relatively stiff bodies for which the geometric stiffening can be considered as negligible. Furthermore, if the velocity of the local deformation ($\dot{\boldsymbol{u}}_i$) is expanded in terms of the mode shape matrix ($\overline{\boldsymbol{\Psi}}$) and the local coordinates velocity vector ($\dot{\boldsymbol{\eta}}$), the rotated absolute velocities in translation can finally be approximated by:

$$\boldsymbol{R}_0^T \dot{\boldsymbol{x}}_i \simeq \boldsymbol{U}_{tr,i} \; \boldsymbol{R}_0^T \dot{\boldsymbol{x}}_0 + \boldsymbol{U}_{rot,i} \; \boldsymbol{\Omega}_0 + \overline{\boldsymbol{\Psi}}_{tr,i} \; \dot{\boldsymbol{\eta}} \tag{7.29}$$

By replacing $\boldsymbol{R}_0^T \dot{\boldsymbol{x}}_i$ by its approximation Eq. 7.29, the kinetic energy of translational DOFs becomes:

$$\mathcal{K}_{tr} = \frac{1}{2} \left\{ \dot{\boldsymbol{x}}_0^T \quad \boldsymbol{\Omega}_0^T \quad \dot{\boldsymbol{\eta}}^T \right\} \left[\begin{array}{ccc} \boldsymbol{R}_0 \boldsymbol{U}_{tr}^T \boldsymbol{M} \boldsymbol{U}_{tr} \boldsymbol{R}_0^T & \boldsymbol{R}_0 \boldsymbol{U}_{tr}^T \boldsymbol{M} \boldsymbol{U}_{rot} & \boldsymbol{R}_0 \boldsymbol{U}_{tr}^T \boldsymbol{M} \overline{\boldsymbol{\Psi}} \\ \boldsymbol{U}_{rot}^T \boldsymbol{M} \boldsymbol{U}_{tr} \boldsymbol{R}_0^T & \boldsymbol{U}_{rot}^T \boldsymbol{M} \boldsymbol{U}_{rot} & \boldsymbol{U}_{rot}^T \boldsymbol{M} \overline{\boldsymbol{\Psi}} \\ \overline{\boldsymbol{\Psi}}^T \boldsymbol{M} \boldsymbol{U}_{tr} \boldsymbol{R}_0^T & \overline{\boldsymbol{\Psi}}^T \boldsymbol{M} \boldsymbol{U}_{rot} & \overline{\boldsymbol{\Psi}}^T \boldsymbol{M} \overline{\boldsymbol{\Psi}} \end{array} \right] \left\{ \begin{array}{c} \dot{\boldsymbol{x}}_0 \\ \boldsymbol{\Omega}_0 \\ \dot{\boldsymbol{\eta}} \end{array} \right\} \tag{7.30}$$

Because of the orthogonality of the elastic modes with respect to the rigid bodies modes and since the global mass matrix $\boldsymbol{\mu}_{tr} = \boldsymbol{U}_{tr}^T \boldsymbol{M} \boldsymbol{U}_{tr}$ is not affected by a frame rotation ($\boldsymbol{R}_0 \boldsymbol{\mu}_{tr} \boldsymbol{R}_0^T = \boldsymbol{\mu}_{tr}$), the kinetic energy $\mathcal{K}_{tr}$ obeys to block diagonal structure:

$$\mathcal{K}_{tr} = \frac{1}{2} \left\{ \dot{\boldsymbol{x}}_0^T \quad \boldsymbol{\Omega}_0^T \quad \dot{\boldsymbol{\eta}}^T \right\} \begin{bmatrix} \boldsymbol{\mu}_{tr} & \boldsymbol{0} & \boldsymbol{0} \\ \boldsymbol{0} & \boldsymbol{\mu}_{rot} & \boldsymbol{0} \\ \boldsymbol{0} & \boldsymbol{0} & \overline{\boldsymbol{M}} \end{bmatrix} \begin{Bmatrix} \dot{\boldsymbol{x}}_0 \\ \boldsymbol{\Omega}_0 \\ \dot{\boldsymbol{\eta}} \end{Bmatrix} \tag{7.31}$$

with $\boldsymbol{\mu}_{tr} = \boldsymbol{U}_{tr}^T \boldsymbol{M}_{tr} \boldsymbol{U}_{tr}$, $\boldsymbol{\mu}_{rot} = \boldsymbol{U}_{rot}^T \boldsymbol{M}_{rot} \boldsymbol{U}_{rot}$ and $\overline{\boldsymbol{M}} = \boldsymbol{\Psi}^T \boldsymbol{M} \overline{\boldsymbol{\Psi}}$.

The variation of the kinetic energy related to translation DOFs takes the following expression:

$$\delta \mathcal{K}_{tr} = \delta \dot{\boldsymbol{\eta}}^T \overline{\boldsymbol{M}} \dot{\boldsymbol{\eta}} + \delta \dot{\boldsymbol{x}}_0^T \ \boldsymbol{\mu}_{tr} \dot{\boldsymbol{x}}_0 + \delta \boldsymbol{\Omega}_0^T \ \boldsymbol{\mu}_{rot} \boldsymbol{\Omega}_0 \tag{7.32}$$

with

$$\delta \boldsymbol{\Omega}_0 = \widetilde{\boldsymbol{\Omega}}_0 \ \delta \boldsymbol{\Theta}_0 + \delta \dot{\boldsymbol{\Theta}}_0 \tag{7.33}$$

The applications treated in this work include exclusively massive 3D parts which are modelled with volume finite elements. Therefore, in the sequel we will consider the dual formulation of superelements constructed from FE models with translation DOFs only. However, the developments could be extended to systems with both translation and rotation DOFs.

In the floating frame, the variation of the potential **strain energy** is simply expressed as:

$$\delta \mathcal{V} = \delta \boldsymbol{\eta}^T \ \overline{\boldsymbol{K}} \boldsymbol{\eta} \tag{7.34}$$

After having given the detailed expression of the potential and kinetic energy, the Lagrangian $\mathcal{L} = \mathcal{K} - \mathcal{V}$ can be computed and the Hamilton principle applied in order to determined the superelement forces:

$$\int_{t_1}^{t_2} \delta \mathcal{L} \ \mathrm{d}t = \int_{t_1}^{t_2} \delta \dot{\boldsymbol{\eta}}^T \overline{\boldsymbol{M}} \dot{\boldsymbol{\eta}} + \delta \dot{\boldsymbol{x}}_0^T \boldsymbol{\mu}_{tr} \dot{\boldsymbol{x}}_0 + \delta \boldsymbol{\Omega}_0^T \boldsymbol{\mu}_{rot} \boldsymbol{\Omega}_0 - \delta \boldsymbol{\eta}^T \overline{\boldsymbol{K}} \boldsymbol{\eta} \ \mathrm{d}t \tag{7.35}$$

Integrating by parts over a time interval $[t_1, t_2]$ yields:

$$\begin{aligned} \int_{t_1}^{t_2} \delta \mathcal{L} \ \mathrm{d}t = & \left[\delta \boldsymbol{\eta}^T \overline{\boldsymbol{M}} \dot{\boldsymbol{\eta}} + \delta \boldsymbol{x}_0^T \boldsymbol{\mu}_{tr} \dot{\boldsymbol{x}}_0 + \delta \boldsymbol{\Theta}_0^T \boldsymbol{\mu}_{rot} \boldsymbol{\Omega}_0 \right]_{t_1}^{t_2} \\ & - \int_{t_1}^{t_2} \delta \boldsymbol{\eta}^T \overline{\boldsymbol{M}} \ddot{\boldsymbol{\eta}} + \delta \boldsymbol{x}_0^T \boldsymbol{\mu}_{tr} \ddot{\boldsymbol{x}}_0 + \delta \boldsymbol{\Theta}_0^T \left(\boldsymbol{\mu}_{rot} \dot{\boldsymbol{\Omega}}_0 + \widetilde{\boldsymbol{\Omega}}_0 \boldsymbol{\mu}_{rot} \boldsymbol{\Omega}_0 \right) + \delta \boldsymbol{\eta}^T \overline{\boldsymbol{K}} \boldsymbol{\eta} \ \mathrm{d}t \end{aligned} \tag{7.36}$$

Because of the independence and the arbitrary nature of the generalized coordinate variations, the elastic forces $\boldsymbol{g}^{el}$, inertia forces $\boldsymbol{g}^{iner}$ and gyroscopic forces $\boldsymbol{g}^{gyr}$ can be easily identified in Eq. 7.36:

$$\boldsymbol{g}^{el}(\boldsymbol{q}) = \begin{Bmatrix} \boldsymbol{0} \\ \boldsymbol{0} \\ \overline{\boldsymbol{K}} \ \boldsymbol{\eta} \end{Bmatrix} \quad , \quad \boldsymbol{g}^{iner}(\dot{\boldsymbol{v}}) = \begin{Bmatrix} \boldsymbol{\mu}_{tr} \ \ddot{\boldsymbol{x}}_0 \\ \boldsymbol{\mu}_{rot} \ \dot{\boldsymbol{\Omega}}_0 \\ \overline{\boldsymbol{M}} \ \ddot{\boldsymbol{\eta}} \end{Bmatrix} \quad , \quad \boldsymbol{g}^{gyr}(\boldsymbol{v}) = \begin{Bmatrix} \boldsymbol{0} \\ \widetilde{\boldsymbol{\Omega}}_0 \boldsymbol{\mu}_{rot} \boldsymbol{\Omega}_0 \\ \boldsymbol{0} \end{Bmatrix} \tag{7.37}$$

Contribution to the iteration matrix

The tangent stiffness and the tangent damping matrices as well as the mass matrix of the superelement take the following simple forms:

$$\boldsymbol{K}_t^{se} = \begin{bmatrix} \boldsymbol{0} & \boldsymbol{0} & \boldsymbol{0} \\ \boldsymbol{0} & \boldsymbol{0} & \boldsymbol{0} \\ \boldsymbol{0} & \boldsymbol{0} & \overline{\boldsymbol{K}} \end{bmatrix} \quad , \quad \boldsymbol{C}_t^{se} = \begin{bmatrix} \boldsymbol{0} & \boldsymbol{0} & \boldsymbol{0} \\ \boldsymbol{0} & \widetilde{\boldsymbol{\Omega}}_0 \boldsymbol{\mu}_{rot} - \widetilde{\boldsymbol{\mu}_{rot} \boldsymbol{\Omega}_0} & \boldsymbol{0} \\ \boldsymbol{0} & \boldsymbol{0} & \boldsymbol{0} \end{bmatrix}$$
$$\boldsymbol{M}^{se} = \begin{bmatrix} \boldsymbol{\mu}_{tr} & \boldsymbol{0} & \boldsymbol{0} \\ \boldsymbol{0} & \boldsymbol{\mu}_{rot} & \boldsymbol{0} \\ \boldsymbol{0} & \boldsymbol{0} & \overline{\boldsymbol{M}} \end{bmatrix} \tag{7.38}$$

The expression of these tangent matrices taking part in the definition of the iteration matrix (see Eq. 2.27) are much more compact than those generated by the formulation with the primal Craig-Bampton method (see Eqs. 6.46-6.49 in Section 6.4.2). The inertia forces depend only on the accelerations and not on the position of generalized coordinates as it is the case for the superelement inertia forces provided by the primal Craig-Bampton reduction technique (Eq. 6.44). Likewise, the gyroscopic forces of the dual formulation do no longer depend on the generalized coordinates at position level.

7.4 Connectivity constraint

In order to connect the superelement to the other parts of the system, it is often needed that the absolute position $\boldsymbol{x}_B$ and the angular variable $\boldsymbol{\alpha}_B$ of the connection nodes appear explicitly in the vector of generalized coordinates:

$$\boldsymbol{q} = \begin{Bmatrix} \boldsymbol{x}_0 \\ \boldsymbol{\alpha}_0 \\ \boldsymbol{\eta} \\ \boldsymbol{x}_B \\ \boldsymbol{\alpha}_B \end{Bmatrix} \tag{7.39}$$

These connection nodes are submitted to prescribed displacements or connection forces (external forces, contact forces, reactions forces at boundaries, forces at reference nodes of kinematic joints, etc) and can be seen as the analogues of the boundary nodes used by the primal Craig-Bampton method.

The compatibility between these connection nodes and the other superelement variables (floating frame coordinates, static and vibration modal intensities) is expressed a posteriori through kinematic constraints.

A set of three constraints defined in Equation 7.40 is added for each connection node B_i. Their expression is directly inspired from the kinematic equation giving the

absolute position of any superelement point (see Eq. 6.13).

$$\boldsymbol{\Phi}^{tr}(\boldsymbol{q}) \equiv \boldsymbol{x}_{B_i} - \boldsymbol{x}_0 - \boldsymbol{R}_0 \left(\boldsymbol{X}_{B_i} + \overline{\boldsymbol{\Psi}}_{B_i^t} \boldsymbol{\eta} \right) = \boldsymbol{0} \tag{7.40}$$

If the connection nodes have rotational DOFs (for instance if a torque has to be applied on a node), three other constraints per connection node are involved. The formulation of these constraints is based on the composition law of rotation matrices:

$$\boldsymbol{R}_{B_i} = \boldsymbol{R}_0 \boldsymbol{R}(\boldsymbol{\gamma}_{B_i}) \tag{7.41}$$

where $\boldsymbol{R}_{B_i}$ is the rotation matrix of angular DOFs ($\boldsymbol{\alpha}_B$) in the inertial frame, $\boldsymbol{R}_0$ is the rotation matrix of the floating frame and $\boldsymbol{R}(\boldsymbol{\gamma}_{B_i})$ is the rotation matrix associated with the local angular variables $\boldsymbol{\gamma}_{B_i}$ in the reference frame. The constraints can be formulated as the vectorial part of the composition law premultiplied by $\boldsymbol{R}_{B_i}^T$:

$$\boldsymbol{\Phi}^{rot}(\boldsymbol{q}) \equiv \text{vect} \left(-\boldsymbol{R}_{B_i}^T \boldsymbol{R}_0 \boldsymbol{R}(\boldsymbol{\gamma}_{B_i}) \right) = \boldsymbol{0} \tag{7.42}$$

where the local angular variables $\boldsymbol{\gamma}_{B_i}$ can be computed from $\boldsymbol{\gamma}_{B_i} = \overline{\boldsymbol{\Psi}}_{B_i^r}\ \boldsymbol{\eta}$ ($\overline{\boldsymbol{\Psi}}_{B_i^r}$ being the three rows of the mode matrix related to these DOFs).

The constraint gradients involved in the formulation of constraint forces ($\boldsymbol{\Phi}_{\boldsymbol{q}}^T\ \boldsymbol{\lambda}$) as well as in their contribution to the iteration matrix (see Eq. 2.27) are given in Eqs. 7.43-7.44. In order to simplify the expression, the situation at equilibrium is considered for the computation of the constraint gradient of rotations.

$$\boldsymbol{\Phi}_{\boldsymbol{q}}^{tr} = \left[-\boldsymbol{I} \quad \boldsymbol{R}_0 \widetilde{(\boldsymbol{X}_{B_i} + \overline{\boldsymbol{\Psi}}_{B_i^t} \boldsymbol{\eta})} \quad -\boldsymbol{R}_0 \overline{\boldsymbol{\Psi}}_{B_i^t} \quad \boldsymbol{I} \quad \boldsymbol{0} \right] \tag{7.43}$$

$$\boldsymbol{\Phi}_{\boldsymbol{q}}^{rot} = \left[\boldsymbol{0} \quad -\boldsymbol{R}(\boldsymbol{\gamma}_{B_i})^T \quad -\overline{\boldsymbol{\Psi}}_{B_i^r} \quad \boldsymbol{0} \quad \boldsymbol{I} \right] \tag{7.44}$$

In addition to the better representativeness of deformation modes provided by the dual approach, its computational efficiency could also be improved compared to the primal superelement formulation. Indeed, the tangent stiffness and mass matrices (Eq. 7.38) are now constant matrices and exhibit a block diagonal structure and even a full diagonal structure if the residual attachment modes are $\boldsymbol{M}$-orthogonalized (see Eq. 6.44). Only the tangent damping matrix is not constant; it varies with the angular velocity of the floating frame and it has an expression similar to the one of rigid body [42].

The superelement attached to its connection nodes has an almost block-diagonal iteration matrix: only the rows and columns corresponding to the Lagrange multipliers associated with the kinematic constraints generate coupling terms for the modal intensities as well as for the position and rotation variables of the floating frame and for the connection nodes. The nonlinearities are also concentrated on these rows and columns. Therefore, for an equivalent number of boundary nodes, the size of the full equation system is larger with the dual approach than with the primal Craig-Bampton

since a Lagrange multiplier is associated to each attachment mode. Nevertheless, the introduction of a set of extra variables is compensated by the sparse structure of system matrices which enables to take advantage of sparse solvers and thus to reduce the computational time.

7.5 Contact force formulation

The contact between superelements can be considered as a particular interconnection between two substructures. In this case, the position of each node potentially in contact is embedded in the vector of generalized coordinates like any other connection node and the associated connectivity constraints (Eqs. 7.40-7.42) are introduced in the DAE-system. However, as already mentioned in section 6.6, if the candidate contact zone is large and contains numerous contact nodes, the model matrices could still be cumbersome and they could not be significantly reduced compared to the FE model.

In this work, to have a superelement model as compact as possible, the numerous candidate contact nodes are not considered as connection nodes. Therefore, as in the approach adopted for the contact formulation between primal superelements (Section 6.8), the absolute positions of contact nodes are not available in the generalized coordinate vector and need to be computed from the floating frame coordinates ($\boldsymbol{x}_0$, $\boldsymbol{\alpha}_0$) and the modal amplitudes ($\boldsymbol{\eta}$):

$$\boldsymbol{x}_{C_i} = \boldsymbol{x}_0^s + \boldsymbol{R}_0^s(\boldsymbol{X}_{C_i} + \overline{\boldsymbol{\Psi}}_{C_i}\boldsymbol{\eta}^s) \tag{7.45}$$

$$\boldsymbol{x}_{N_i} = \boldsymbol{x}_0^m + \boldsymbol{R}_0^m(\boldsymbol{X}_{N_i} + \overline{\boldsymbol{\Psi}}_{N_i}\boldsymbol{\eta}^m) \tag{7.46}$$

where the superscripts s and m denote the slave and the master body respectively. The connectivity constraints (Eqs. 7.40-7.42) are not introduced since the contact forces are transformed to load directly the modal variables and the floating frame coordinates. This specific contact formulation can be seen as a constraint elimination method of connectivity constraints related to the contact nodes. If the contact node positions were explicitly available in the generalized coordinate vector, the contact force expression and, especially, its contribution to the iteration matrix would be simplified but the model would be larger and more complex due to the presence of algebraic constraints.

As a conclusion, the contact formulation is almost unchanged compared to the contact between primal superelements described in section 6.8. The magnitude of contact forces is determined by means of a penalty method whose nonlinear contact law is defined in Eq. 6.70. The main simplifications in the formulation are due to the fact that the local coordinates $\boldsymbol{\eta}$ in the reference frame are also a subset of the generalized coordinates vector $\boldsymbol{q}$, so that it is not needed to define a kinematic tangent operator $\boldsymbol{P}$ to convert the variations of the local coordinates into absolute generalized coordinates (see Eq. 6.26).

The expression of the absolute velocities of the candidate contact nodes on the slave ($\dot{\boldsymbol{x}}_{C_i}$) and the master body ($\dot{\boldsymbol{x}}_{N_i}$) are slightly simplified and are given by:

$$\dot{\boldsymbol{x}}_{C_i} = \dot{\boldsymbol{x}}_0^s - \boldsymbol{R}_0^s \widetilde{(\boldsymbol{X}_{C_i} + \overline{\boldsymbol{\Psi}}_{C_i}^s \boldsymbol{\eta}^s)}\ \boldsymbol{\Omega}_0^s + \boldsymbol{R}_0^s \overline{\boldsymbol{\Psi}}_{C_i}^s\ \dot{\boldsymbol{\eta}}^s \tag{7.47}$$

$$\dot{\boldsymbol{x}}_{N_i} = \dot{\boldsymbol{x}}_0^m - \boldsymbol{R}_0^m \widetilde{(\boldsymbol{X}_{N_i} + \overline{\boldsymbol{\Psi}}_{Ni}^m \boldsymbol{\eta}^m)}\ \boldsymbol{\Omega}_0^m + \boldsymbol{R}_0^m \overline{\boldsymbol{\Psi}}_{Ni}^m\ \dot{\boldsymbol{\eta}}^m \tag{7.48}$$

The virtual work principle is used to compute the internal force vector (Eq. 7.49) applied onto the full set of superelement generalized coordinates due to a 3D contact force $\boldsymbol{f}_c$ detected for any contact node. It comes

$$\boldsymbol{g}_{C_i}^{int,con} = \begin{Bmatrix} \boldsymbol{f}_c \\ \widetilde{\left(\boldsymbol{X}_{C_i} + \overline{\boldsymbol{\Psi}}_{C_i}\boldsymbol{\eta}\right)}\ \boldsymbol{R}_0^T\ \boldsymbol{f}_c \\ \overline{\boldsymbol{\Psi}}_{C_i}^T \boldsymbol{R}_0^T\ \boldsymbol{f}_c \end{Bmatrix} \tag{7.49}$$

It can be noticed that the formulation of the load vector (Eq. 7.49) is slightly more compact than for the primal superelement version (see Eq. 6.81). This expression of the internal force vector can be easily retrieved by developing the virtual displacement of the contact point:

$$\begin{aligned} \delta\boldsymbol{x}_{C_i} &= \delta\boldsymbol{x}_0 - \boldsymbol{R}_0 \widetilde{(\boldsymbol{X}_{C_i} + \boldsymbol{u}_{C_i})}\ \delta\boldsymbol{\Theta}_0 + \boldsymbol{R}_0\ \delta\boldsymbol{u}_{C_i} \\ &= \delta\boldsymbol{x}_0 - \boldsymbol{R}_0 \widetilde{\left(\boldsymbol{X}_{C_i} + \overline{\boldsymbol{\Psi}}_{C_i}\boldsymbol{\eta}\right)}\ \delta\boldsymbol{\Theta}_0 + \boldsymbol{R}_0 \overline{\boldsymbol{\Psi}}_{C_i}\ \delta\boldsymbol{\eta} \end{aligned} \tag{7.50}$$

Contribution to the iteration matrix

Following the same procedure as previously, the contribution of each contact force to the iteration matrix is computed analytically. The spatial derivative of $\boldsymbol{g}_{C_i}^{con}$ is then expressed as:

$$\mathrm{d}\boldsymbol{g}_{C_i}^{con} = \mathrm{d}f\ \frac{1}{f}\boldsymbol{g}_{C_i}^{con} + f\ \mathrm{d}\begin{Bmatrix} \boldsymbol{n} \\ \widetilde{\boldsymbol{z}}_{C_i}\boldsymbol{R}_0^T\ \boldsymbol{n} \\ \overline{\boldsymbol{\Psi}}_{C_i}^T \boldsymbol{R}_0^T\ \boldsymbol{n} \end{Bmatrix} \tag{7.51}$$

The derivative of the force amplitude f defined by Equation (6.70) can be expressed as:

$$\mathrm{d}f = \frac{\partial f}{\partial \ell}\ \mathrm{d}\ell + \frac{\partial f}{\partial \dot{\ell}}\ \mathrm{d}\dot{\ell} \tag{7.52}$$

where the partial derivatives are equal to:

$$\frac{\partial f}{\partial \ell} = S_c^* \left(k_p\ n\ \ell^{n-1} + c\ n\ \ell^{n-1}\ \dot{\ell}\right) \qquad , \qquad \frac{\partial f}{\partial \dot{\ell}} = S_c^*\ c\ \ell^n \tag{7.53}$$

The variation of the penetration length is simply obtained by derivative of Equation (6.72):

$$\mathrm{d}\ell = \mathrm{d}\left(\boldsymbol{n}^T(\boldsymbol{x}_{N1} - \boldsymbol{x}_{C_i})\right) \tag{7.54}$$

$$= \boldsymbol{n}^T(\mathrm{d}\boldsymbol{x}_{N1} - \mathrm{d}\boldsymbol{x}_{C_i}) + (\boldsymbol{x}_{N1} - \boldsymbol{x}_{C_i})^T\ \mathrm{d}\boldsymbol{n} \tag{7.55}$$

where by analogy with Equations (6.76-6.77) the total derivatives $\mathrm{d}\boldsymbol{x}_{C_i}$,$\mathrm{d}\boldsymbol{x}_{N_i}$ are put in the form:

$$\begin{aligned} \mathrm{d}\boldsymbol{x}_{Ci} &= \mathrm{d}\boldsymbol{x}_0^s - \boldsymbol{R}_0^s \widetilde{\boldsymbol{z}}_{C_i}^s \, \mathrm{d}\boldsymbol{\Theta}_0^s + \boldsymbol{R}_0^s \overline{\boldsymbol{\Psi}}_{C_i}^s \, \mathrm{d}\boldsymbol{\eta}^s && (7.56) \\ \mathrm{d}\boldsymbol{x}_{Ni} &= \mathrm{d}\boldsymbol{x}_0^m - \boldsymbol{R}_0^m \widetilde{\boldsymbol{z}}_{C_{Ni}}^m \, \mathrm{d}\boldsymbol{\Theta}_0^m + \boldsymbol{R}_0^m \overline{\boldsymbol{\Psi}}_{C_i}^m \, \mathrm{d}\boldsymbol{\eta}^m && (7.57) \end{aligned}$$

In case of triangular-shaped master contact faces, the derivative of the normal vector $\boldsymbol{n}$ (see Eq. 6.61) takes the form:

$$\begin{aligned} \mathrm{d}\boldsymbol{n} &= \frac{\left(\boldsymbol{I} - \boldsymbol{n}\boldsymbol{n}^T\right)}{\left\|\widetilde{\boldsymbol{x}}_{N12} \, \boldsymbol{x}_{N13}\right\|} \, \mathrm{d}\left(\widetilde{\boldsymbol{x}}_{N12} \, \boldsymbol{x}_{N13}\right) && (7.58) \\ &= \frac{\left(\boldsymbol{I} - \boldsymbol{n}\boldsymbol{n}^T\right)}{\left\|\widetilde{\boldsymbol{x}}_{N12} \, \boldsymbol{x}_{N13}\right\|} \, \left(\widetilde{\boldsymbol{x}}_{N12} \, \mathrm{d}\boldsymbol{x}_{N13} - \widetilde{\boldsymbol{x}}_{N13} \, \mathrm{d}\boldsymbol{x}_{N12}\right) && (7.59) \\ &= \frac{\left(\boldsymbol{I} - \boldsymbol{n}\boldsymbol{n}^T\right)}{\left\|\widetilde{\boldsymbol{x}}_{N12} \, \boldsymbol{x}_{N13}\right\|} \, \left[\left(\widetilde{\boldsymbol{x}}_{N13} - \widetilde{\boldsymbol{x}}_{N12}\right) \, \mathrm{d}\boldsymbol{x}_{N1} - \widetilde{\boldsymbol{x}}_{N13} \, \mathrm{d}\boldsymbol{x}_{N2} + \widetilde{\boldsymbol{x}}_{N12} \, \mathrm{d}\boldsymbol{x}_{N3}\right] && (7.60) \end{aligned}$$

The derivative of the penetration length $\dot{\ell}$ is developed as:

$$\begin{aligned} \mathrm{d}\dot{l} &= \mathrm{d}\left[\boldsymbol{n}^T(\dot{\boldsymbol{x}}_{N1} - \dot{\boldsymbol{x}}_{C_i}) + (\boldsymbol{x}_{N1} - \boldsymbol{x}_{C_i})^T \, \dot{\boldsymbol{n}}\right] \\ &= (\dot{\boldsymbol{x}}_{N1} - \dot{\boldsymbol{x}}_{C_i})^T \, \mathrm{d}\boldsymbol{n} + \boldsymbol{n}^T \left(\mathrm{d}\dot{\boldsymbol{x}}_{N1} - \mathrm{d}\dot{\boldsymbol{x}}_{C_i}\right) + \dot{\boldsymbol{n}}^T \left(\mathrm{d}\boldsymbol{x}_{N1} - \mathrm{d}\boldsymbol{x}_{C_i}\right) + (\boldsymbol{x}_{N1} - \boldsymbol{x}_{C_i})^T \, \mathrm{d}\dot{\boldsymbol{n}} \end{aligned} \tag{7.61}$$

where the various terms that are not yet defined can be formulated by the following expressions:

$$\begin{aligned} \mathrm{d}\dot{\boldsymbol{x}}_{Ni} = \mathrm{d}\dot{\boldsymbol{x}}_0^m &+ \boldsymbol{R}_0^m \widetilde{\widetilde{\boldsymbol{z}}_{Ni}^m \boldsymbol{\Omega}_0^m} \, \mathrm{d}\boldsymbol{\Theta}_0^m + \boldsymbol{R}_0^m \widetilde{\boldsymbol{\Omega}}_0^m \overline{\boldsymbol{\Psi}}_{Ni}^m \, \mathrm{d}\boldsymbol{\eta}^m - \boldsymbol{R}_0^m \widetilde{\boldsymbol{z}}_{Ni}^m \, \mathrm{d}\boldsymbol{\Omega}_0^m \\ &- \boldsymbol{R}_0^m \widetilde{(\overline{\boldsymbol{\Psi}}_{Ni}^m \dot{\boldsymbol{\eta}}^m)} \, \mathrm{d}\boldsymbol{\Theta}_0^m + \boldsymbol{R}_0^m \overline{\boldsymbol{\Psi}}_{Ni}^m \, \mathrm{d}\dot{\boldsymbol{\eta}}^m \end{aligned} \tag{7.62}$$

$$\begin{aligned} \mathrm{d}\dot{\boldsymbol{x}}_{C_i} = \mathrm{d}\dot{\boldsymbol{x}}_0^s &+ \boldsymbol{R}_0^s \widetilde{\widetilde{\boldsymbol{z}}_{C_i}^s \boldsymbol{\Omega}_0^s} \, \mathrm{d}\boldsymbol{\Theta}_0^s + \boldsymbol{R}_0^s \widetilde{\boldsymbol{\Omega}}_0^s \overline{\boldsymbol{\Psi}}_{C_i}^s \, \mathrm{d}\boldsymbol{\eta}^s - \boldsymbol{R}_0^s \widetilde{\boldsymbol{z}}_{C_i}^s \, \mathrm{d}\boldsymbol{\Omega}_0^s \\ &- \boldsymbol{R}_0^s \widetilde{(\overline{\boldsymbol{\Psi}}_{C_i}^s \dot{\boldsymbol{\eta}}^s)} \, \mathrm{d}\boldsymbol{\Theta}_0^s + \boldsymbol{R}_0^s \overline{\boldsymbol{\Psi}}_{C_i}^s \, \mathrm{d}\dot{\boldsymbol{\eta}}^s \end{aligned} \tag{7.63}$$

$$\begin{aligned} \mathrm{d}\dot{\boldsymbol{n}} &= \mathrm{d}\left(\frac{\boldsymbol{I} - \boldsymbol{n}\boldsymbol{n}^T}{\left\|\widetilde{\boldsymbol{x}}_{N12} \, \boldsymbol{x}_{N13}\right\|}\right) \, \boldsymbol{a}_{\dot{\boldsymbol{n}}} + \frac{\boldsymbol{I} - \boldsymbol{n}\boldsymbol{n}^T}{\left\|\widetilde{\boldsymbol{x}}_{N12} \, \boldsymbol{x}_{N13}\right\|} \, \mathrm{d}\boldsymbol{a}_{\dot{\boldsymbol{n}}} && (7.64) \\ &= \frac{1}{\left\|\widetilde{\boldsymbol{x}}_{N12} \, \boldsymbol{x}_{N13}\right\|} \left[\left(\widetilde{\widetilde{\boldsymbol{n}} \, \boldsymbol{a}_{\dot{\boldsymbol{n}}}} + \widetilde{\boldsymbol{n}} \, \widetilde{\boldsymbol{a}_{\dot{\boldsymbol{n}}}}\right) \, \mathrm{d}\boldsymbol{n} + \left(\boldsymbol{I} - \boldsymbol{n}\boldsymbol{n}^T\right) \left(\mathrm{d}\boldsymbol{a}_{\dot{\boldsymbol{n}}} - \boldsymbol{a}_{\dot{\boldsymbol{n}}} \, \boldsymbol{n}^T \, \mathrm{d}\left[\widetilde{\boldsymbol{x}}_{N12} \, \boldsymbol{x}_{N13}\right]\right)\right] && (7.65) \end{aligned}$$

with

$$\begin{aligned} \mathrm{d}\boldsymbol{a}_{\dot{\boldsymbol{n}}} = &\left(\widetilde{\boldsymbol{x}}_{N13} - \widetilde{\boldsymbol{x}}_{N12}\right) \, \mathrm{d}\dot{\boldsymbol{x}}_{N1} - \widetilde{\boldsymbol{x}}_{N13} \, \mathrm{d}\dot{\boldsymbol{x}}_{N2} + \widetilde{\boldsymbol{x}}_{N12} \, \mathrm{d}\dot{\boldsymbol{x}}_{N3} \\ &+ \left(\widetilde{\dot{\boldsymbol{x}}}_{N3} - \widetilde{\dot{\boldsymbol{x}}}_{N2}\right) \, \mathrm{d}\boldsymbol{x}_{N1} + \left(\widetilde{\dot{\boldsymbol{x}}}_{N1} - \widetilde{\dot{\boldsymbol{x}}}_{N3}\right) \, \mathrm{d}\boldsymbol{x}_{N2} + \left(\widetilde{\dot{\boldsymbol{x}}}_{N2} - \widetilde{\dot{\boldsymbol{x}}}_{N1}\right) \, \mathrm{d}\boldsymbol{x}_{N3} \end{aligned} \tag{7.66}$$

and

$$\mathrm{d}\left(\widetilde{\boldsymbol{x}}_{N12}\ \boldsymbol{x}_{N13}\right) = \left(\widetilde{\boldsymbol{x}}_{N13} - \widetilde{\boldsymbol{x}}_{N12}\right)\ \mathrm{d}\boldsymbol{x}_{N1} - \widetilde{\boldsymbol{x}}_{N13}\ \mathrm{d}\boldsymbol{x}_{N2} + \widetilde{\boldsymbol{x}}_{N12}\ \mathrm{d}\boldsymbol{x}_{N3} \tag{7.67}$$

Finally, the derivative in the second term of Equation 6.86 can be easily expanded in:

$$\mathrm{d}\begin{Bmatrix} \boldsymbol{n} \\ \widetilde{\boldsymbol{z}}_{C_i}\boldsymbol{R}_0^T\ \boldsymbol{n} \\ \overline{\boldsymbol{\Psi}}_{C_i}^T\boldsymbol{R}_0^T\ \boldsymbol{n} \end{Bmatrix} = \begin{Bmatrix} \mathrm{d}\boldsymbol{n} \\ -\widetilde{\boldsymbol{R}_0^T\boldsymbol{n}}\overline{\boldsymbol{\Psi}}_{C_i}\ \mathrm{d}\boldsymbol{\eta} + \widetilde{\boldsymbol{z}}_{C_i}\widetilde{\boldsymbol{R}_0^T\boldsymbol{n}}\ \mathrm{d}\boldsymbol{\Theta}_0 + \widetilde{\boldsymbol{z}}_{C_i}\boldsymbol{R}_0^T\ \mathrm{d}\boldsymbol{n} \\ \overline{\boldsymbol{\Psi}}_{C_i}^T\widetilde{\boldsymbol{R}_0^T\boldsymbol{n}}\ \mathrm{d}\boldsymbol{\Theta}_0 + \overline{\boldsymbol{\Psi}}_{C_i}^T\boldsymbol{R}_0^T\ \mathrm{d}\boldsymbol{n} \end{Bmatrix} \tag{7.68}$$

7.6 Gear pair model

During the meshing between two gear wheels, each node on the tooth flanks can potentially enter in contact. If an attachment mode is associated with each node of this group, the superelement model becomes cumbersome. Indeed, in this case the set of generalized coordinates should be large since a modal variable is introduced for each attachment mode (see vector $\boldsymbol{r}$ in Eq. 7.24). Moreover, a large number of connectivity constraints would be added to the system unless a activation/deactivation strategy would be used.

In order to circumvent these drawbacks, the static mode switching and static mode sliding have been investigated in Refs. [131, 133, 134] to simulate the dynamics of gear pairs too. These recent works consist in including in the modal basis only the attachment modes related to the modes detected in effective contact. In this way, the model of each gear wheel keeps a reasonable dimension. Nevertheless, on the one hand the static mode switching approach suffers from discontinuities when the static modes are added or removed of the modal basis and an explicit Runge-Kutta integrator without numerical damping has been used. On the other hand, the static mode sliding approaches requires a configuration dependent modal basis which significantly complicates the formulation and the implementation.

In this work, we prefer to keep a constant mode matrix which contains a restricted number of attachment modes in order to have a compact superelement model. These attachment modes correspond in this case to more global loadings than a force applied on an individual node. For instance, a normal pressure applied to a part or to the whole tooth flank can reproduce the global bending behaviour of the teeth when they are engaged. Since, the contact points are not included in the generalized coordinates vector, the mapping of contact forces to load directly the full set of modal variables is mandatory as detailed in Section 7.5.

The developed gear pair model is perhaps less suited to capture local effects near the contact points than the models proposed in [134] or [150] but seems more computationally efficient in a global system approach. Indeed, the objective followed since

the beginning of this thesis is to develop integrated simulations of complex industrial systems. A standard implicit integration scheme of the generalized-α family can be used to simulate the MBS model including not only the proposed gear pair model but also other flexible bodies such as beam elements to model the driveshafts. Our gear pair model considers a damping contribution in the contact law and also numerical damping but no structural damping unlike Ref. [134].

In order to limit the number of projections of slave nodes on master faces of the contact detection process, the strategy to select the paired tooth flanks described in Section 6.11.1 is also used here with the dual version of the superelement model.

7.6.1 Spur gears

In this section, the spur gear pair system presented in Section 6.11.3 will be simulated with the dual formulation of the superelement. The geometric data of two gear wheels are given in Tab. 6.1. The simulation is performed during 0.02 s with a fixed time step of 1.E-6 s. The load case can be summarized as follows: the rotation of the biggest wheel is prescribed to keep a constant velocity; the smallest wheel has an initial velocity equals to -1000 rpm and is braked by a viscous torque ($T = -10\ \omega$). The rotation axis cannot tilt so that there is no misalignment. The center distance is such that a significant backlash occurs.

The most natural choice to select the attachment modes of a spur gear pair consists in considering lines of uniform loads parallel to the axial direction. A normal pressure offers a convenient approach to accurately represent the loads due to teeth contact. In the presence of meshing defaults such as misalignment, non symmetric static modes can be added to account for these effects.

In order to model the tooth bending due to the gear engagement in a global way, a normal pressure applied on the entire flank face is used to introduce only one attachment mode per tooth flank (Figs. 7.6-7.7). The same philosophy of global static modes related to each tooth flank was already used in Section 6.11.2 for the selection of boundary nodes linked with the mean joint.

Figure 7.6 shows the superelement modes when only the first eigenmode of the free-free structure is retained whereas Fig. 7.7 draws a few mode shapes when the 100-first vibration modes are included in the gear wheel model. The residual attachment mode illustrated in Fig. 7.6(b) highlights the good ability of this mode to represent the tooth bending. The comparison with Fig. 7.7(b) enables to notice that if numerous eigenmodes are retained, the tooth bending is already represented by these modes and the residual attachment only corresponds to local deformation effects. Therefore, in order to capture the global tooth bending, it is not necessary to include a huge number of eigenmodes in the mode matrix of the superelement.

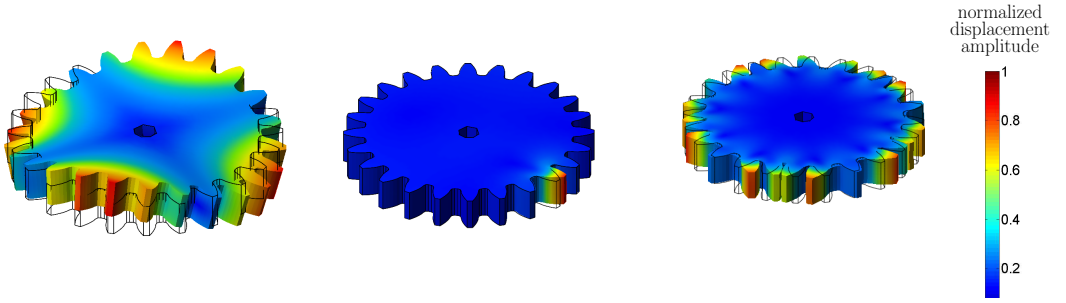

(a) unique elastic eigen mode ($f = 5857$ Hz) (b) residual attachment mode (c) 12^{th} mode of the system composed of the set of residual attachment modes

Figure 7.6: Dual superelement of a gear wheel including the first free-free eigen mode and a normal pressure attachment mode for each tooth flank as well as 6 attachment modes to connect the gear web to the propeller shaft.

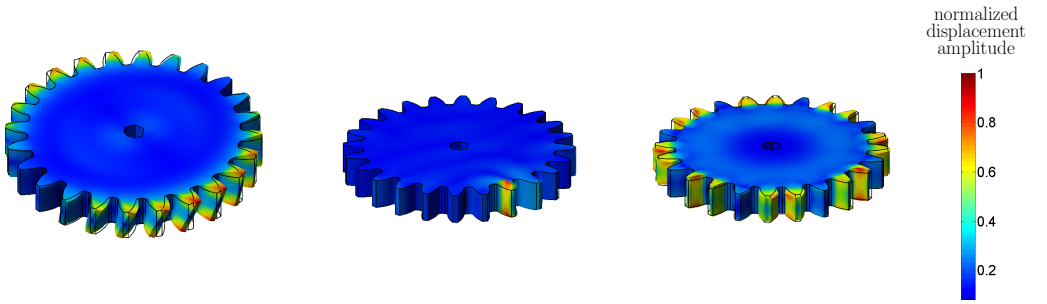

(a) 90^{th} elastic eigen mode ($f = 126819$ Hz) (b) residual attachment mode (c) 30^{th} mode of the system composed of the set of residual attachment modes

Figure 7.7: Dual superelement of a gear wheel including 100 free-free eigen mode and a normal pressure attachment mode for each tooth flank as well as 6 attachment modes to connect the gear web to the propeller shaft.

Similarly to the gear wheel superelement based on the primal Craig-Bampton method presented in Section 6.11 (see Fig. 6.29), six attachment modes (3 in translation and 3 in rotation) are introduced to represent the deformation due to the connection between the gear web and the propeller shaft. This set of attachment modes is related to a unit force or a torque applied on an additional node linked to the cylindrical face of the gear web bore by a mean joint (see Eq. 6.101). The mode shapes related to the x-axis are depicted in Fig. 7.8.

The numerical results presented below have been obtained with superelement models including the 30-first free-free eigenmodes and one global pressure attachment per

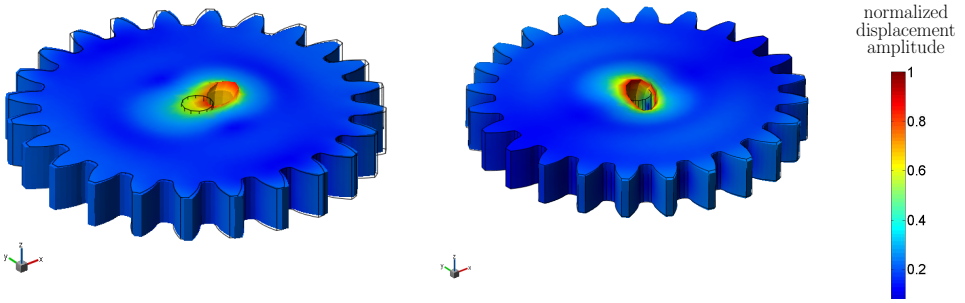

(a) x-translation (b) x-rotation

Figure 7.8: Residual attachment modes for the connection between the gear web and the driveshaft (before mass orthogonalisation with the others attachement modes).

tooth flank. The model size of the two superelements amounts to 74 DOFs for the pinion and 90 DOFs for the gear wheel, which is much lower than the initial finite element models (331968 DOFs and 148203 DOFs respectively) and also significantly lower than in the primal Craig-Bampton superelement (298 DOFs and 394 DOFs respectively) . The eigen frequencies are in the range $[12545; 42360]$ Hz for the pinion and in the range $[5839; 37766]$ Hz for the big gear.

The time evolution of the normal contact forces applied to the various tooth flanks is illustrated in Fig . 7.9. It presents the same global aspect as in Fig. 6.40 where the primal superelement models were used. We observe a periodic variation of the number of tooth flanks in contact. The duration of the single-teeth contact periods are inversely proportional to the transmitted torque and this a consequence of the elastic deformation of gear teeth. Indeed, when the forces applied on the tooth increase, the tooth bending also increases and results in a longer contact period for this tooth.

The sudden changes in the contact forces are due to non-conformal contacts between the flank profiles produce by tooth deflection. The coarse spatial discretization of the tooth flanks (see Fig. 6.43) as well as the assumptions introduced in the simple contact detection algorithm also contribute to the steep variations of the contact forces.

The amplitude of the total contact force between gear wheels and the resistant torque needed to preserve the constant velocity of the gear wheel #2 are represented in Fig. 7.10. Their mean value is constant but some noise is superimposed owing to the oscillations of the elastic displacements. The nonuniform rotation of the pinion during the revolution (see Fig. 7.11) is also a consequence of this not perfectly steady operation.

This gear pair simulation allows us to validate the use of the dual superelement formulation with the proposed contact approach. The numerical results are close to those obtained in Chapter 6 but the simulation is more efficient since the model size is

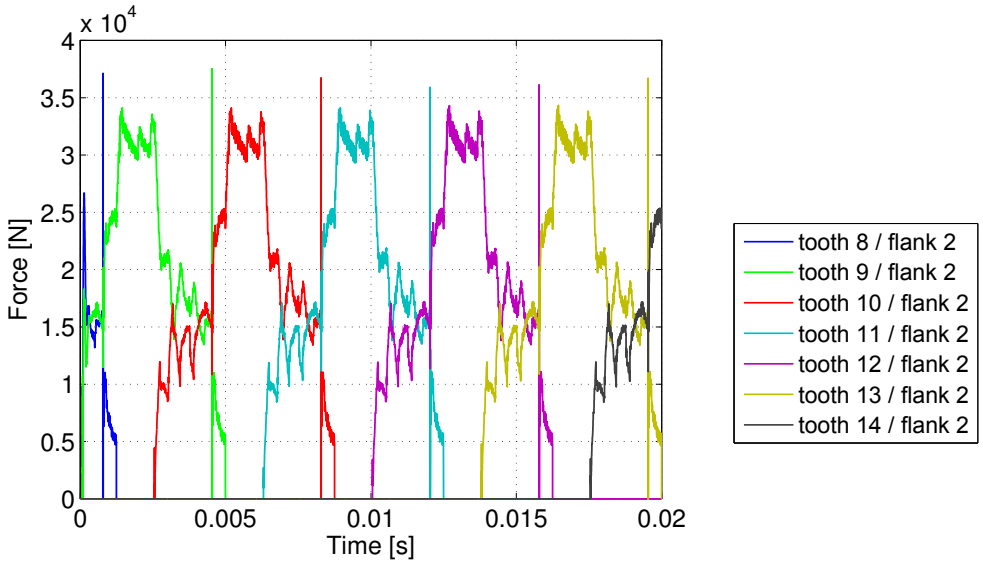

Figure 7.9: Normal contact force applied on tooth flanks of wheel #1.

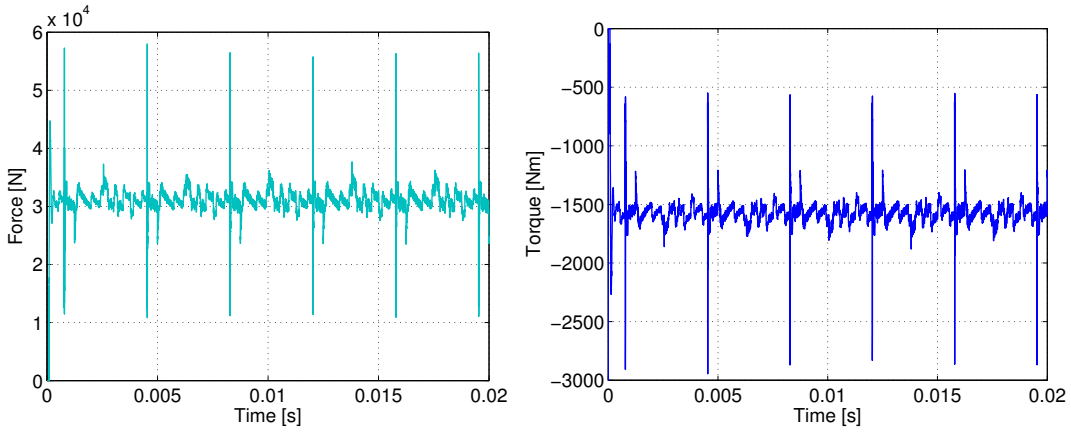

Figure 7.10: Total magnitude of the normal contact force between tooth flanks and reaction torque due to the imposed rotation speed of gear wheel #2.

lower and the system matrices present a better sparsity.

7.6.2 Helical gears

The developed gear pair model is very general with respect to the geometry of the gear wheels. The formulation remains the same for all kinds of gear pairs, e.g., helical gear, bevel gear, rack and pinion. In this section, simulation results of the meshing of an helical gear coming from an energy production system pair are presented. Both

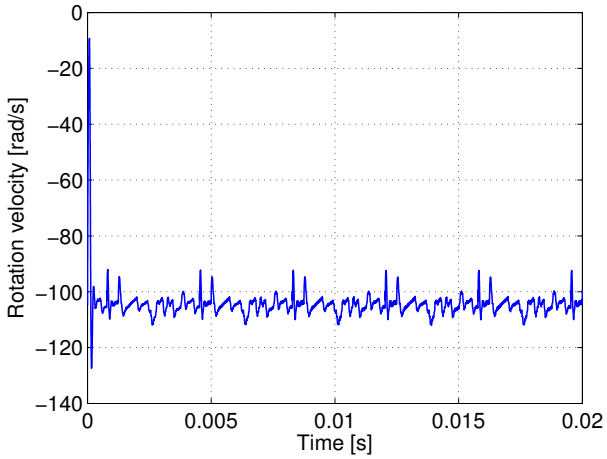

Figure 7.11: Rotation speed of the pinion.

gear wheels have the same number of teeth (see Fig. 7.12). They have a large radius ($R_m \approx 0.42$ m), a large face width ($b = 0.6$ m) and have the particularity to present a very wide bore in the gear web. The shafts are not modelled but would certainly stiffen the wheels in a practical setup.

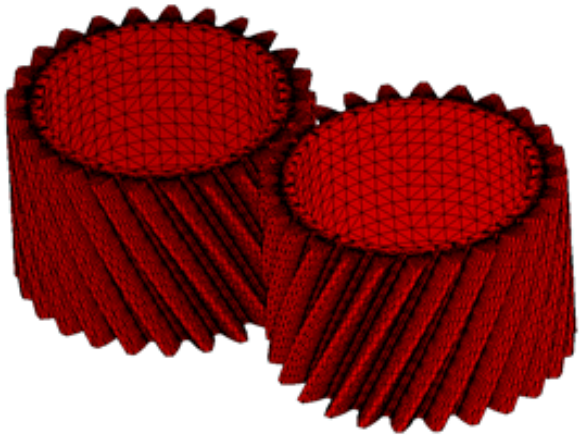

Figure 7.12: Finite element model of an helical gear pair.

Figure 7.13 illustrates the deformed shapes of the gear wheel superelement model based on the *primal* Craig-Bampton method if the same choice is adopted to select the boundary nodes as for the spur gear pair model described in Section 6.11.3, namely one boundary node linked to each flank face by a mean joint. It can be observed that the static modes do not correctly represent the loading applied to the gear teeth.

For the dual superelement formulation, the deformation modes are depicted in Fig. 7.14 if the same load case is used to computed the attachment modes as the spur

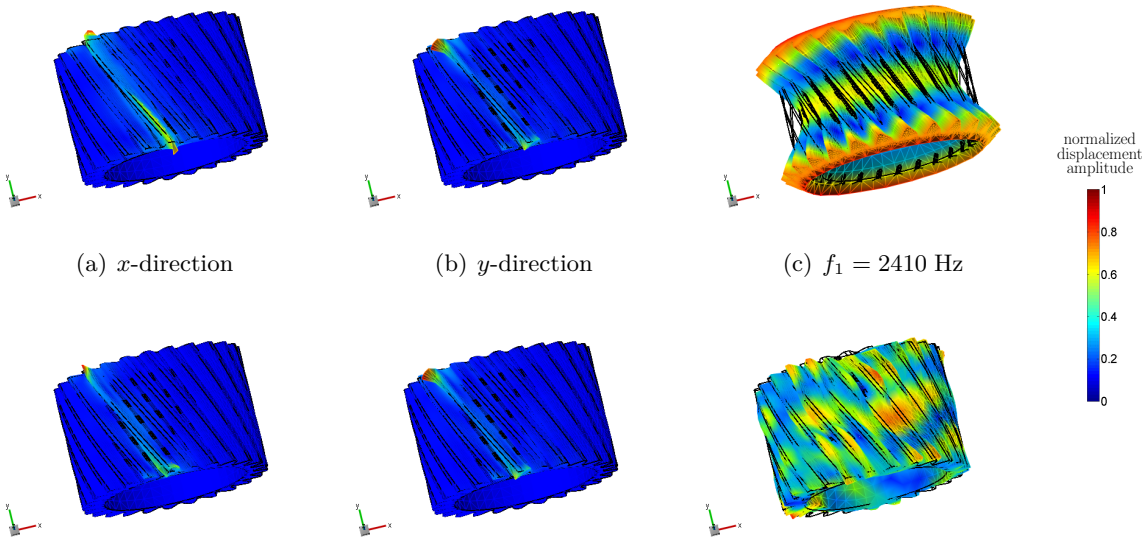

(a) x-direction (b) y-direction (c) $f_1 = 2410$ Hz

(d) x-rotation (e) y-rotation (f) $f_{50} = 6.691$ Hz

Figure 7.13: Deformation modes of the helical gear wheel superelement when the boundary nodes are additional nodes linked to each tooth flank by a mean joint: (a),(b),(d),(e) are static modes; (c),(f) are two of the 100 retained internal vibration modes.

gear model (Section 7.6.1), i.e., a uniform normal pressure applied on the whole tooth flank face. Figure 7.14(e) shows that the residual attachment mode better represents the tooth bending than the static modes of the superelement based on the *primal* Craig-Bampton method (Fig. 7.13).

Nevertheless, the attachment modes are still far from the true loading applied by the gear contacts. Indeed, the tooth flanks of helical gears get into contact at single points instead of occurring along a line for normal operation of spur gears. Therefore, the selection of a unique static mode per tooth flank cannot accurately represent the actual behaviour even from a global point of view. Thus, compared to spur gears, the choice of static modes has to be adapted to have a reliable helical gear pair model.

A better choice consists in considering several attachment modes according to the position of the contact point on the tooth flank face. For instance, the teeth can be split in several zones along the axial direction of the gear wheel (Fig. 7.15) and a pressure attachment mode is associated with each zone. Obviously, the accuracy of the superelement model increases with the number of zones but we choose to keep a small number of zones (5) in order that the model size remains reasonable and much smaller than the initial FE model.

In the proposed model, the 16171 DOFs of each helical gear wheel have been reduced to 292 DOFs in the superelement model. Only the first 30 free-free vibration modes are included in the reduced model and have an eigenfrequency between 2410 Hz

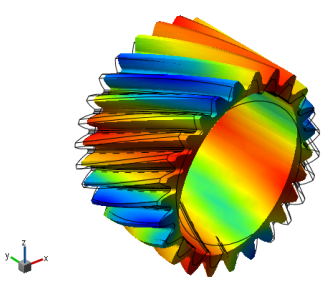

(a) 1^{st} elastic eigen mode ($f = 260$ Hz)

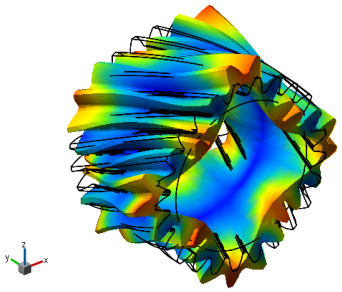

(b) 15^{th} elastic eigen mode ($f = 1785$ Hz)

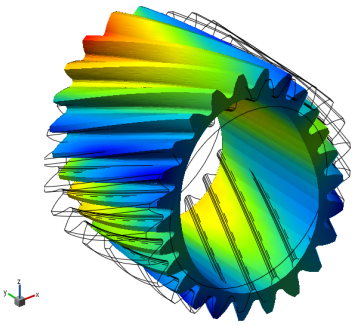

(c) attachment mode for a unit pressure on a tooth flank

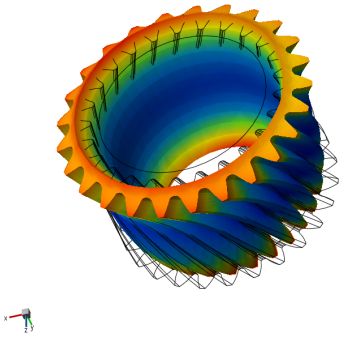

(d) attachment mode of a unit force in y-direction on the node linked to the gear web

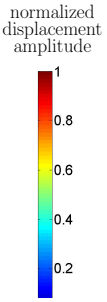

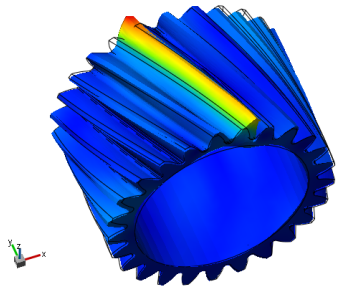

(e) residual attachment mode for a unit pressure on a tooth flank

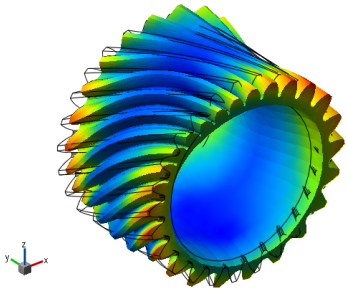

(f) 5^{th} mode of the system composed of the set of residual attachment modes

Figure 7.14: Dual superelement of the helical gear wheel including 30 free-free eigen mode and a normal pressure attachment mode for each tooth flank as well as 6 attachment modes to connect the gear web to the propeller shaft.

and 5797 Hz. The boundary conditions are illustrated in Fig. 7.16: a constant torque is applied on the left-handed gear wheel while the rotation speed of the right-handed gear wheel is prescribed. A fixed time step size of 1E.-3 s is used.

The active contact zones at the last time step of the simulation are depicted in

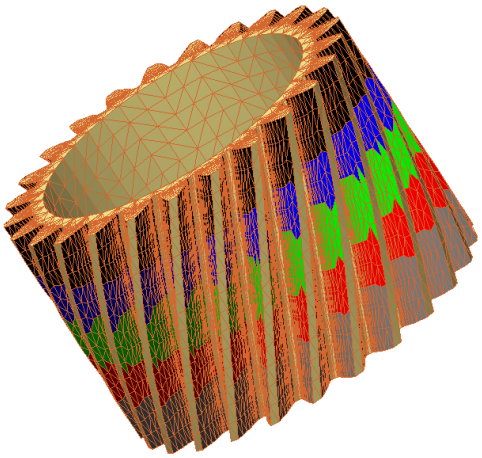

Figure 7.15: The tooth flanks are divided in five zones of equal width along the axial direction; a pressure attachment mode is associated with each zone.

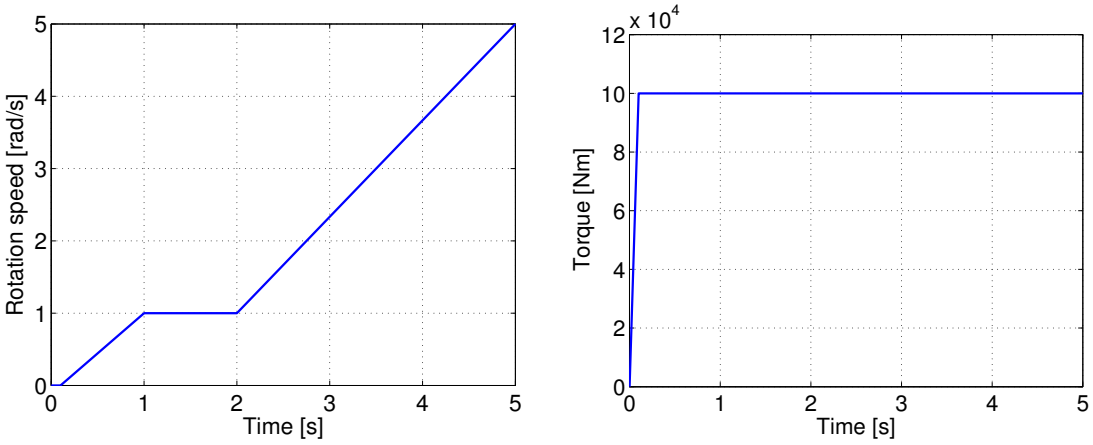

(a) rotation speed prescribed on the right-handed helical gear

(b) torque applied on left-handed helical gear

Figure 7.16: Total magnitude of the normal contact force between tooth flanks and reaction torque due to the imposed rotation speed of gear wheel #2.

Fig. 7.17. At this instant, three pairs of tooth flanks are in contact and it can be checked that the contact zones are inside a band parallel to the gear wheel axis.

Figure 7.18 illustrates the deformation of both gear wheels. Contrarily to the spur gear pair model, the deformation of the superelement is not only limited to the gear teeth. Indeed, the gear web is quite thin for the gear wheels studied here which results in an ovalisation of the overall gear structure under the load applied by tooth contact. The first eigenmodes of the gear wheels are mainly excited as represented in Fig. 7.19.

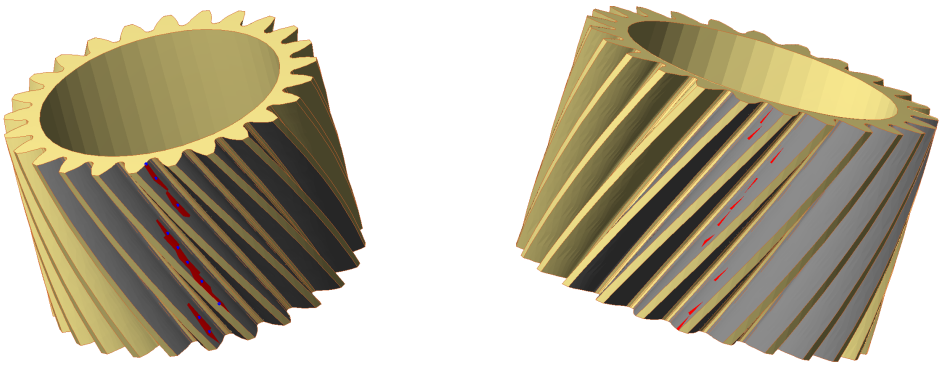

(a) slave body (b) master body

Figure 7.17: Active contact zone on both gear wheels. The blue points represent the slave nodes detected in contact and all adjacent faces are colored in red. For the master body, only the master faces considered in contact are collored.

The deformed shapes of these modes correspond to an ovalisation of the gear body (see Fig. 7.14(a)).

Moreover, owing to the helix angle of teeth, the deformation is not uniform along the axis of the wheel. This kind of behaviour cannot be represented by a rigid body gear pair model since only the tooth bending is accounted for in these global models.

The normal contact forces applied on several tooth flanks are depicted in Fig. 7.21(a). The number of teeth simultaneously in contact varies between three and four because the helical shape of the teeth leads to a significant increase of the contact ratio of the gear meshing compared to spur gear pairs. Since the rotation velocity of the right-handed gear wheel is increased after $t = 2$ s, the contact duration for each tooth flank decreases in the second part of the simulation when the gear wheel has a covered a full revolution. As for the spur gear pairs, these contact forces are affected by oscillations owing either to the elastic deformation of the teeth or to the numerical discontinuities introduced by a note-to-surface contact detection algorithm combined with a coarse discretization of tooth flanks.

Even though the magnitude of the contact forces applied on individual tooth flanks is highly fluctuating, the total gear contact force, the transmitted torque and the rotation speed have nearly a steady behaviour as shown in Figs. 7.21-7.22. It can observed that the noise superimposed to the mean value increases with the rotation velocity after $t = 2$ s.

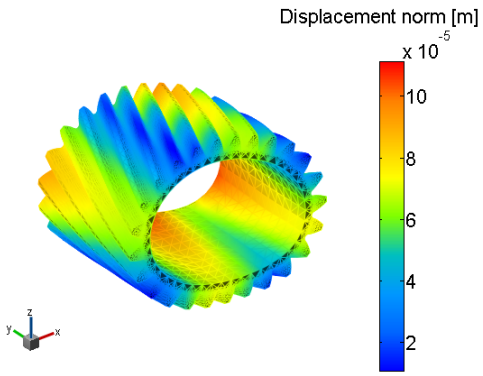

(a) left-handed gear

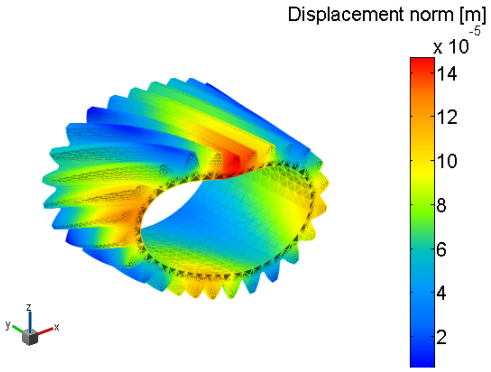

(b) right-handed gear

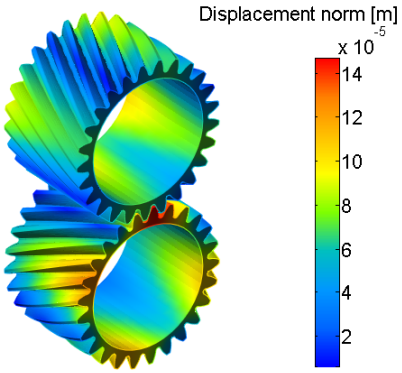

(c)

Figure 7.18: Deformation of the two helical gear wheels at $t = 0.6$ s ((a)-(b): deformation scaled by factor 1000, (c): no amplification).

7.7 Concluding remarks

This chapter deals with the **dual** Craig-Bampton method to formulate superelements submitted to unilateral contact conditions. The basic principle of this substructuring technique is to enrich the modal basis initially composed of a reduced number of eigenmodes of the free-free structure by a set of attachment modes related to the possible loads exerted by the other components of the system, e.g., at the contact interface. This association of modes enables to represent both the local linear deformation due to the forces applied on any node and the global deformations involved by the dynamic behaviour of the flexible body. The floating frame of reference approach is used to represent the rigid body motion of the structure and the set of elastic coordinates defines the deformation in this moving frame. The connection of the superelement with the rest of the system requires the explicit appearance of connection nodes in the set of generalized coordinates of the superelement. The introduction of kinematic constraints enables to express a posteriori the connection between these nodes and the

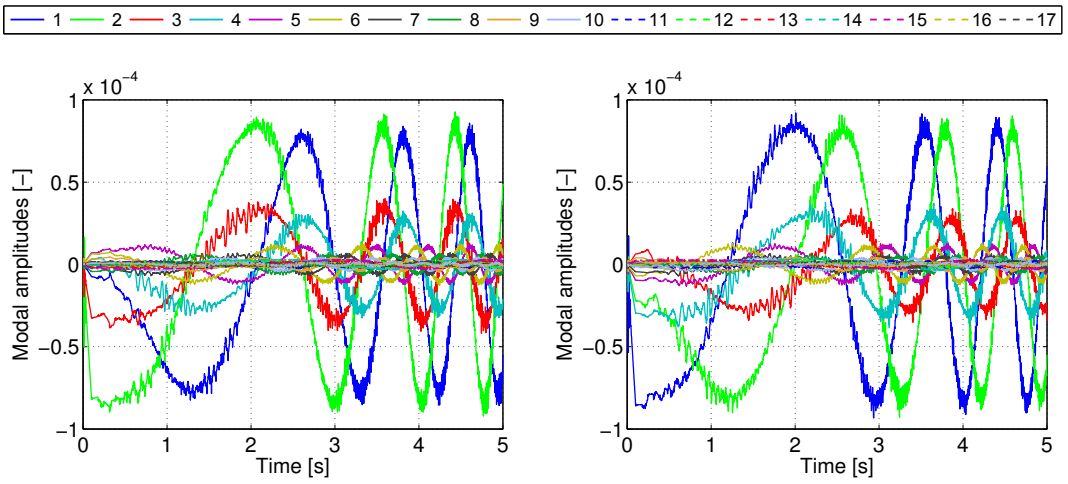

(a) left-handed wheel (b) right-handed wheel

Figure 7.19: Modal participation factors of the free-free eigenmodes included in the gear wheel superelement model.

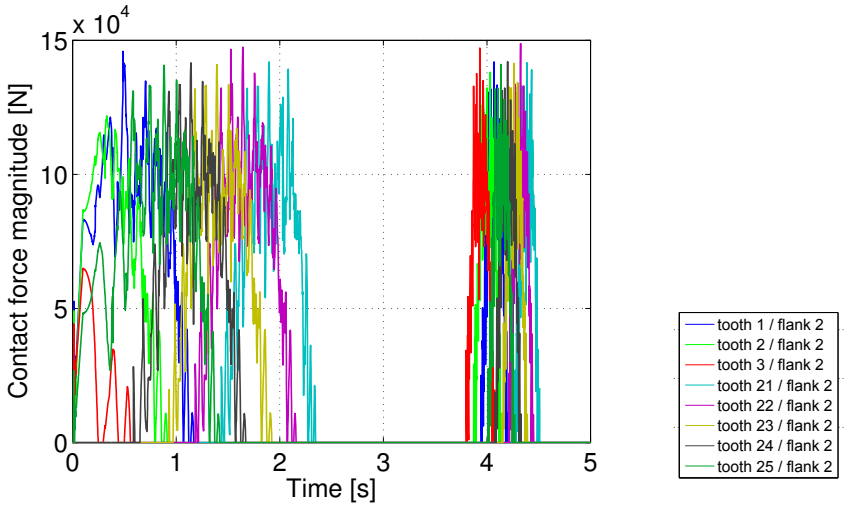

Figure 7.20: Magnitude of the contact force per tooth flank.

superelement modes.

The approach developed in Chapter 6 to express the contact between two superelements is conserved. In order to keep the model compact, the candidate contact nodes are not necessarily included in the set of boundary nodes. Therefore, a large number of nodes of the skin can be condensed. At each time step, the absolute positions of the candidate contact nodes are computed in terms of the position and the rotation matrix of the floating frame together with the modal intensities of the superelement modes. A node-to-surface projection method is used to detect the effective contact zones and compute the local penetration length of the penalty-based contact force law. Finally,

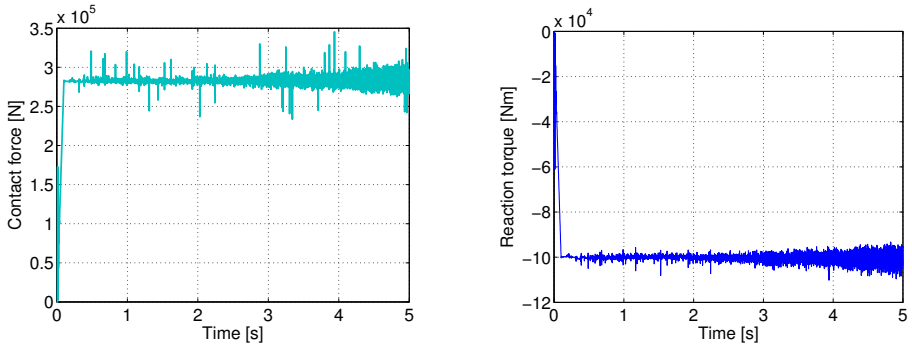

(a) total gear contact force (b) transmitted torque

Figure 7.21: Magnitude of the the total contact force between gear wheels and the transmitted torque.

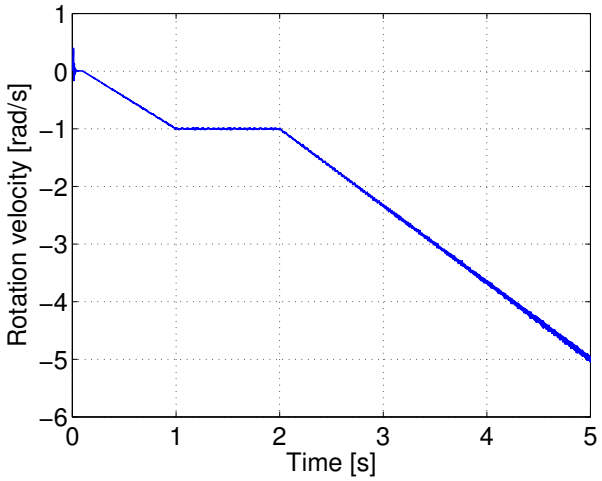

Figure 7.22: Rotation speed of the left-handed gear wheel submitted to the torque.

each individual 3D contact force is transferred to the generalized coordinate vector, loading thus the floating frame coordinates and the modal coordinates. The various steps of this contact approach are summarized in Fig. 7.23.

The relevance of the dual superelement formulation to simulate unilateral contact has been assessed by the simulation of a spur gear model and an helical gear pair model. The numerical results show that the static modes of the dual Craig-Bampton method have a better capability to represent the deformations undergone by contact forces than the static modes of the primal Craig-Bampton method. As a consequence, the number of modes included in the superelement model is lowered and results in an improvement of the computational efficiency.

In this work, in order to include a reasonable number of attachment modes in the superelement, the latter are selected to represent the global loading applied on

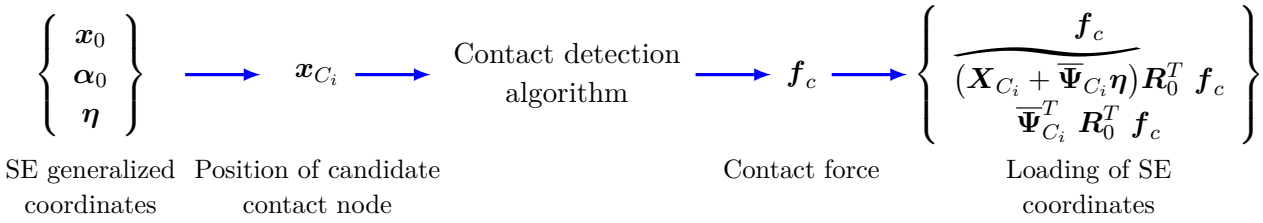

Figure 7.23: Summary of contact formulation between superelements.

the contact face, e.g., a normal pressure applied on the entire tooth flank face. Thus, the number of dedicated attachment modes is kept much lower than the number of candidate contact nodes.

For future work, the dynamic updating of the modal basis and of the connection nodes during the analysis according to the location of the active contact area could be another solution to reduce the size of the model and to improve the computational efficiency, e.g. based on the static mode switching or on the static mode sliding techniques [56, 133, 134]. These methods are usually dedicated to more detailed analysis than those performed in the present thesis. For instance, the stress distribution in gear teeth is studied in [132].

Chapter 8

Conclusion

8.1 Summary of the work

The objective of this doctoral thesis was to contribute to the dynamic modelling of mechanical transmission systems. The various developments have been carried out in the field of automotive drivetrain components where the need for such dynamic models is particularly strong. Reliable driveline models would allow to fully model the vehicle from the engine to the suspension systems.

As a representative industrial application, the methodological developments are demonstrated by the modelling of TORSEN differentials. In a first part of the thesis, global models of the TORSEN differential have been constructed in the flexible multibody software SAMCEF/MECANO and have been be validated with experimental data. In order to find the best correlation with the experimental data, the friction coefficient in the joint between the planet gears and the housing has been fitted. The main difficulties encountered had concerned the contact modelling in presence of impact and friction as well as the lack of capability to model contact between rigid bodies.

Indeed, the unilateral contact conditions employed in the initial differential models require that at least one of the two contacting bodies is a flexible body discretized with finite elements. Besides the high computational cost induced by the large model size, this contact formulation can hardly support the shocks produced by contact establishments at high velocities.

In order to circumvent these drawbacks, several contact models have been developed in the second part of the thesis which enable to remove some of the assumptions introduced in the first models of the differential. The proposed formulations are based on a penalty method, so that a continuous integration scheme of the generalized-α family can be adopted. The first developments considered that the two supports of the contact condition are rigid bodies whereas the last works address the contact modelling

between two flexible structures represented by means of superelements.

The proposed contact models are formulated in the framework of the nonlinear finite element method for flexible multibody systems. They have different levels of details and accuracy and they can be combined in the same model in order to simulate complex and full drivetrain components with a reasonable computational efficiency. For instance, the contacting bodies for which the attention is put can be represented by superelements while the other contact conditions of minor importance are modelled between rigid bodies.

8.2 Claimed contributions

The main achievements of the present PhD thesis can be listed as follows.

- Development of a methodology to model automotive differentials. Thanks to a detailed analysis of the working principle of TORSEN differentials, the elements which significantly contribute to the global locking effect of this kind of limited slip differential have been identified. In contrast, some effects of minor importance have been neglected and a set of modelling assumptions have been introduced. The differentials in test bed as well as in vehicle configuration have been reproduced in the numerical simulations. These models have been globally validated by comparison with experimental data of the torque distribution ratios for the four working modes of the TORSEN differentials.

- Formulation of a 3D frictional contact element between two rigid bodies in a finite element framework. A general kinematic description is proposed to model the contact between two nodes rigidly attached to the contact surfaces. The magnitude of the contact forces is computed by a continuous impact law which uses a restitution coefficient to represent the loss of kinetic energy inherent to each impact. The geometric shapes of the contacting surfaces have been particularized to planar rings for the implementation.

- Modelling of a cylindrical joint with operation defects. The clearance, the tilting and the friction forces are taken into account in this kinematic joint model based on the contact detection between the pin and the hollow cylinder considered as rigid bodies.

- Enhancement of contact models by introducing the effects of the lubricating oil. Thanks to a set of physical and geometrical hypotheses, a simple and compact squeeze film model has been developed to account for the damping force produced by the film of lubricant between two planar discs or rings.

- Integrated simulation of the interactions between differentials and the vehicle dynamics. The TORSEN differential models have been included in global vehicle

models in order to analyse the dynamics response of the vehicle in case of manoeuvres or slippery ground surfaces. These global models could be very useful in the design phase of an automotive differential by significantly reducing the number of physical prototypes. For instance, the influence of the modification of the friction coefficient of one thrust washer can be investigated.

- Development of a new contact formulation defined between flexible components modelled as superelements. The proposed contact model accounts for the global flexible behaviour of the contacting bodies but with a model size of one to several order of magnitude smaller than a full finite element mesh. Therefore, the CPU time needed for the simulation is significantly reduced. The main distinctive feature of this contact formulation lies in the direct loading of the modal generalized variables. Two different superelement formulations have been investigated: the primal and the dual Craig-Bampton methods.
- Use of two different types of superelement formulations to represent the global flexibility by a mixed of static modes and vibration modes.
- Modelling of flexible gear pairs with accurate representation of geometric and meshing defects. Each gear wheel is represented by an independent superelement. The unilateral contact conditions prescribed between both superelements offer a convenient approach to account for the gear teeth flexibility. The formulation is very general and can be easily applied to any kind of gear pair since the actual 3D geometry of each gear wheel is embedded in the superelement model.

Excepted the contact model between superelements which has been implemented in a MATLAB development code, the other contributions of this thesis have been implemented the FEM-based flexible multibody commercial software SAMCEF/MECANO.

8.3 Directions for future work

Some perspectives for future developments in the various research domains tackled in this thesis are now proposed. Firstly, the outlooks directly related to the contributions achieved in this work will be exposed. Afterwards, more general outcomes will be addressed.

The proposed rigid-rigid contact elements could be **extended to support other geometries** of the contacting surfaces. Only planar discs or rings are available with the current implementation of the rigid contact model and the squeeze film model. Likewise, the non-ideal cylindrical joint model considers that the extremities of the inner cylinder have a spherical shape.

The regularized friction model adopted for each contact condition should be enhanced in order to be able to represent the transient behaviour between sticking and

sliding friction. Indeed, the locking of TORSEN differentials corresponds to the situation where there is no relative motion between the gear wheels and the thrust washers. Owing to the regularization of the friction coefficient in the friction law used in this work, the sticking situation cannot be represented strictly speaking. Moreover, the **stick and slip** phenomena due to the variation of the friction coefficient between the static and the kinematic friction coefficients can be a source of noise and vibration.

The TORSEN differential models could be improved by introducing the **flexibility** of several parts. For instance, the housing or the case could be easily modelled by a finite element model or a superelement. The flexible behaviour of the driveshafts could be easily represented by means of FE beam elements and so that the propagation of the vibrations generated by the differential towards the others subsystems of the vehicle can be studied. For instance, impacts or the variation of the number of gear teeth simultaneously in contact can be at the origin of vibrations.

In order to improve the **computational efficiency of the developed contact formalism between superelements**, the implementation should be performed in a compiled code such as SAMCEF for example. In the current implementation, a large CPU time time is devoted to the projection of the slave nodes on the master faces. Thus, a more efficient contact detection algorithm would be beneficial.

The flexible gear pair model based on the contact modelling between superelements could be tested to model a gear train system such as the TORSEN differentials. In addition to the gear pairs, the other contact conditions could also be represented by the contact element defined between superelements. In this way the global flexibility of many bodies could be accounted for with a reasonable model size and many defects could be represented. The influence of the lubrication on the gear meshing could also be included in the gear pair model as proposed in Refs. [120, 121].

A new avenue of research consists in formulating the unilateral contact conditions between superelements with kinematic constraints instead of a continuous contact force law. In this way, impact phenomena should be represented by using larger time steps and no penetration occurs between the contacting bodies. To this end, the nonsmooth generalized-α integration scheme proposed in [20] could be tested.

An other issue for the contact model with superelements is the addition of the friction forces in the model. The stresses and wear index in bodies in contact would also be interesting to simulate.

Concerning the perspectives at a more general point of view, let us first mention the structural optimization of components by accounting of the dynamic response of the system, see for instance Ref. [140].

List of Publications

First author

- G. Virlez, O. Brüls, and P. Duysinx. Modeling of contact between stiff bodies in automotive transmission systems. In J. Samin and P. Fisette, editors, *Proceedings of Multibody Dynamics 2011, ECCOMAS Thematic Conference, 4-7 July 2011, Brussels, Belgium.*

- G. Virlez, O. Brüls, N. Poulet, and P. Duysinx. Multibody dynamics analysis of differentials in vehicle drivetrains. In *The First Joint International Conference on Multibody System Dynamics, May 25-27, 2010, Lappeenranta, Finland.*

- G. Virlez, O. Brüls, N. Poulet, and P. Duysinx. Simulation of differentials in four-wheel drive vehicles using multibody dynamics. In *Proceedings of the ASME 2011 International Design Engineering Technical Conferences Computers and Information in Engineering Conference IDETC/CIE 2011, August 29-31, 2011, Washington, DC, USA.*

- G. Virlez, O. Brüls, V. Sonneville, E. Tromme, P. Duysinx, and M. Géradin. Contact model between superelements in dynamic multibody systems. In *Proceedings of the ASME 2013 International Design Engineering Technical Conferences Computers and Information in Engineering Conference IDETC/CIE 2013, August 04-07, 2013, Portland, Oregon, USA.*

- G. Virlez, O. Brüls, E. Tromme, and P. Duysinx. Analysis of stresses in vehicle driveline systems using a flexible multibody approach. In G. A. Holzapfel and R. W. Ogden, editors, *Proceedings of the 8th European Solid Mechanics Conference, 9-13 July 2012, Graz, Austria.*

- G. Virlez, O. Brüls, E. Tromme, and P. Duysinx. Modelling of joints with clearance and friction in multibody dynamic simulation of automotive differentials. In *Proceedings of the 6th Asian Conference on Multibody Dynamics, 26-30 August, 2012, Shanghai, China.*

- G. Virlez, A. Cardona, O. Brüls, and P. Duysinx. Modelling of frictional unilateral contact in automotive differentials. In *Proceedings of the Fifth International*

Conference on Advanced Computational Methods in Engineering (ACOMEN), 14-17 November 2011, Liège, Belgium.

- G. Virlez, O. Brüls, N. Poulet, E. Tromme, and P. Duysinx. *Computational Methods in Applied Sciences*, volume Multibody Dynamics: Computational Methods and Applications, chapter Modelling of contact between stiff bodies in automotive transmission systems, pages 193–214. Springer, 2013.

- G. Virlez, O. Brüls, N. Poulet, E. Tromme, and P. Duysinx. Modeling of joints with clearance and friction in multibody dynamic simulation of automotive differentials. *Theoretical and Applied Mechanics Letters*, 3:013003, 2013.

Co-author

- Q.-Z. Chen, V. Acary, G. Virlez, and O. Brüls. A Newmark-type integrator for flexible systems considering nonsmooth unilateral constraints. In *Proceedings of The Second Joint International Conference on Multibody System Dynamics, May 29-June 1, 2012, Stuttgart, Germany.*

- P. Duysinx, J. Emonds-Alt, G. Virlez, O. Brüls, and M. Bruyneel. Advances in optimization of flexible components in multibody systems: application to robot-arms design. In *5th Asian Conference on Multibody Dynamics 2010, August 23-26,2010, Kyoto, Japan.*

- P. Duysinx, J. Emonds-Alt, G. Virlez, O. Brüls, and M. Bruyneel. Recent developments in optimization of flexible components of multibody systems. In *IV European Conference on Computational Mechanics, Palais des Congrés, May 16-21, 2010, Paris, France.*

- Q.-Z. Chen, V. Acary, G. Virlez, and O. Brüls. A nonsmooth generalized-α scheme for flexible multibody systems with unilateral constraints. *International Journal for Numerical Methods in Engineering*, 96(8):487–511, 2013.

- E. Tromme, O. Brüls, J. Emonds-Alt, M. Bruyneel, G. Virlez, and P. Duysinx. Discussion on the optimization problem formulation of flexible components in multibody systems. *Structural and Multidisciplinary Optimization*, 48(6):1189–1206, 2013.

Bibliography

[1] V. Acary and B. Brogliato. Numerical methods for nonsmooth dynamical systems. *Lecture Notes in Applied and Computational Mechanics*, 2008.

[2] P. Alart and A. Curnier. A mixed formulation for frictional contact problems prone to Newton like solution method. *Computer Methods in Applied Mechanics and Engineering*, 92(3):353–375, 1991.

[3] J. Ambrósio and P. Versissimo. Improved bushing models for general multibody systems and vehicle dynamics. *Multibody System Dynamics*, 22:341–365, 2009.

[4] M. Arnold. Numerical methods for simulation in applied dynamics. In Martin Arnold and Werner Schiehlen, editors, *Simulation Techniques for Applied Dynamics*, volume 507 of *CISM International Centre for Mechanical Sciences*, pages 191–246. Springer Vienna, 2009.

[5] M. Arnold and O. Brüls. Convergence of the generalized-α scheme for constrained mechanical systems. *Multibody System Dynamics*, 18(2):185–202, 2007.

[6] G. Bastos, R. Seifried, and O. Brüls. Inverse dynamics of serial and parallel underactuated multibody systems using a DAE optimal control approach. *Multibody System Dynamics*, 30(3):359–376, 2013.

[7] O. Bauchau. *Flexible Multibody Dynamics*, volume 176. Springer Science+ Business Media, 2011.

[8] O. Bauchau and J.-Y. Choi. The vector parameterization of motion. *Nonlinear Dynamics*, 33(2):165–188, 2003.

[9] O. Bauchau and J. Rodriguez. Modeling of joints with clearance in flexible multibody systems. *International Journal of Solids and Structures*, 39:41–63, 2002.

[10] P. Benner, S. Gugercin, and K. Willcox. A survey of model reduction methods for parametric systems. Technical Report MPIMD/13-14, August.

[11] M. Blundell and D. Harty. *The Multibody Systems Approach to Vehicle Dynamics*. Elsevier Butterworth-Heinemann Publications, 2004.

[12] R. Bravo, J. L. Pèrez-Aparicio, and T. A. Laursen. An enhanced energy conserving time stepping algorithm for frictionless particle contacts. *International Journal for Numerical Methods in Engineering*, 85(11):1415–1435, 2011.

[13] O. Brüls. *Lecture Notes in Kinematics and Dynamics of Mechanisms, 2011, University of Liège.*

[14] O. Brüls, V. Acary, and A. Cardona. Simultaneous enforcement of constraints at position and velocity levels in the nonsmooth generalized-α scheme. Submitted in *Computer Methods in Applied Mechanics and Engineering*, 2014.

[15] O. Brüls, A. Cardona, and M. Arnold. Lie group generalized-α time integration of constrained flexible multibody systems. *Mechanism and Machine Theory*, 48:121–137, 2012.

[16] A. Cardona. Flexible three dimensional gear modelling. *European Journal of Computational Mechanics*, 268(5-6):663–691, 1995.

[17] A. Cardona. Three-dimensional gears modelling in multibody systems analysis. *International Journal for Numerical Methods in Engineering*, 40:357–381, 1997.

[18] A. Cardona. Superelements modelling in flexible multibody dynamics. *Multibody System Dynamics*, 4:245–266, 2000.

[19] F. J. Cavalieri and A. Cardona. An augmented Lagrangian technique combined with a mortar algorithm for modelling mechanical contact problems. *International Journal for Numerical Methods in Engineering*, 93(4):420–442, 2012.

[20] Q.-Z. Chen, V. Acary, G. Virlez, and O. Brüls. A nonsmooth generalized-α scheme for flexible multibody systems with unilateral constraints. *International Journal for Numerical Methods in Engineering*, 96(8):487–511, 2013.

[21] J. Choi and J. H. Choi. A smooth contact algorithm using cubic spline surface interpolation for rigid flexible bodies. In *Proceedings of the ASME 2013 International Design Engineering Technical Conferences Computers and Information in Engineering Conference IDETC/CIE 2013, August 04-07, 2013, Portland, Oregon, USA.*

[22] P.W. Christensen, A. Klarbring, J.S. Pang, and N. Strömberg. Formulation and comparison of algorithms for frictional contact problems. *International Journal for Numerical Methods in Engineering.*, 42:145–173, 1998.

[23] J. Chung and G. M. Hulbert. A time integration algorithm for structural dynamics with improved numerical dissipation: The generalized-α method. *ASME Journal of Applied Mechanics*, 60:371–375, 1993.

[24] R. Craig. Coupling of substructures for dynamic analyses: an overview. In *Structures, Structural Dynamics and Material Conferences, 41st AIAA/ASME/ASCE/AHS/ASC, Atlanta,2000, AIAA-2000-1573.*

[25] C. B. Drab, H. W. Engl, J. R. Haslinger, and G. Offner. Dynamic simulation of crankshaft multibody systems. *Multibody System Dynamics*, 22:133–144, 2009.

[26] Y. Dumont and L. Paoli. Numerical simulation of a model of vibrations with joint clearance. *International Journal of Computer Applications in Technology*, 33:41–53, 2008.

[27] S. K. Dwivedy and P. Eberhard. Dynamic analysis of flexible manipulators, a literature review. *Mechanism and Machine Theory*, 41:749–777, 2006.

[28] S. Ebrahimi and P. Eberhard. Rigid-elastic modeling of meshing gear wheels in multibody systems. *Multibody System Dynamics*, 16(1):55–71, 2006.

[29] E. A. Estupinan and I. F. Santos. Modelling hermetic compressors using different constraint equations to accommodate multibody dynamics and hydrodynamic lubrication. *Journal of the Brazilian Society of Mechanical Sciences and Engineering*.

[30] G. Fichera, M. Lacagnina, and F. Petrone. Modelling of torsion beam rear suspension by using multibody method. *Mulibody System Dynamics*, 12:303–313, 2004.

[31] P. Fisette, D. A. Johnson, and J.-C. Samin. A fully symbolic generation of the equations of motion of multibody systems containing flexible beams. *Computer Methods in Applied Mechanics and Engineering*, 142(1–2):123 – 152, 1997.

[32] P. Flores. A parametric study on the dynamic response of planar multibody systems with multiple clearance joints. *Nonlinear Dynamics*, 61:633–653, 2010.

[33] P. Flores, J. Ambrósio, J.-C. Claro, and H. Lankarani. Kinematics and dynamics of multibody systems with imperfect joints: Models and case studies. *Lecture Notes in Applied and Computational Mechanics*, 2008.

[34] P. Flores, J. Ambrósio, J. C. P. Claro, and H. M. Lankarani. Influence of the contact-impact force model on the dynamic response of multi-body systems. *Proc. IMechE Vol. 220 Part K: J. Multi-body Dynamics*, 2006.

[35] P. Flores and H. Lankarani. Spatial rigid-multibody systems with lubricated spherical clearance joints: modeling and simulation. *Nonlinear Dynamics*, 60(1-2):99–114, 2010.

[36] P. Flores, R. Leine, and C. Glocker. Modeling and analysis of planar rigid multibody systems with translational clearance joints based on the non-smooth dynamics approach. *Multibody System Dynamics*, 23:165–190, 2009.

[37] P. Flores, M. Machado, M. T. Silva, and J. M. Martins. On the continuous contact force models for soft materials in multibody dynamics. *Multibody System Dynamics*, 25:357–375, 2011.

[38] D. García-Vallejo, J. Mayo, J. L. Escalona, and J. Domínguez. Three-dimensional formulation of rigid-flexible multibody systems with flexible beam elements. *Multibody System Dynamics*, 20(1):1–28, 2008.

[39] J. García de Jalón. Twenty-five years of natural coordinates. *Multibody System Dynamics*, 18(1):15–33, 2007.

[40] J. García de Jalón and E. Bayo. *Kinematic and Dynamic Simulation of Multibody Systems: The Real-Time Challenge*. Springer-Verlag, 1994.

[41] M. Géradin. A dual superelement formulation for 3-D elastic models in multibody dynamics. Research report, DS^+ SPRL, 2013.

[42] M. Géradin and A. Cardona. *Flexible Multibody Dynamics: A Finite Element Approach*. John Wiley & Sons, New York, 2001.

[43] M. Géradin and D. Rixen. Parametrization of finite rotations in computational dynamics: a review. *Revue Europénne des Éléments Finis*, 4(5-6):497–553, 1995.

[44] M. Géradin and D. Rixen. *Mechanical Vibrations - Theory and Apllication to Structural Dynamics*. John Wiley & Sons, New York, 2 edition, 2001.

[45] G. Gilardi and I. Sharf. Literature survey of contact dynamics modelling. *Mechanism and Machine Theory*, 37(10):1213 – 1239, 2002.

[46] V. E. Gleasman. Differential gear mechanism, November 11 1958. US Patent 2,859,641.

[47] C. Glocker. Formulation of spatial contact situations in rigid multibody systems. *Computer Methods in Applied Mechanics and Engineering*, 177:199–214, 1999.

[48] W. Goldsmith. *Impact: The Theory and Physical Behavior of Colliding Solids*. Edward Arnold, 1964.

[49] J. Gonçalves and J. Ambrósio. Optimization of vehicle suspension systems for improved comfort of road vehicles using flexible multibody dynamics. *Nonlinear Dynamics*, 34:113–131, 2003.

[50] Y. Gonthier, J. McPhee, C. Lange, and J.-C. Piedboeuf. A regularized contact model with asymmetric damping and dwell-time dependent friction. *Multibody System Dynamics*, 11:209–233, 2004.

[51] E. J. Grimme. *Krylov projection methods for model reduction*. PhD thesis, 1997.

[52] J. Happian-Smith. *An introduction to modern vehicle design*. Elsevier, 2001.

[53] S. Hartmann and E. Ramm. A mortar based contact formulation for non-linear dynamics using dual lagrange multipliers. *Finite Elements in Analysis and Design*, 44:245–258, 2008.

[54] E. J. Haug. *Computer aided kinematics and dynamics of mechanical systems*, volume 1. Allyn and Bacon Boston, 1989.

[55] A. Heege, J. Betran, and Y. Radovic. Fatigue load computation of wind turbine gearboxes by coupled finite element, multi-body system and aerodynamic analysis. *Wind Energy*, 10(5):395–413, 2007.

[56] G. Heirman, T. Tamarozzi, and W. Desmet. Static modes switching for more efficient flexible multibody simulation. *International Journal for Numerical Methods in Engineering*, 87(11):1025–1045, 2011.

[57] H. Heisler. *Advanced vehicle technology*. Elsevier, 2002.

[58] M. Hiller and A. Kecskeméthy. Dynamics of multibody systems with minimal coordinates. In Manuel F.O. Seabra Pereira and Jorge A.C. Ambrósio, editors, *Computer-Aided Analysis of Rigid and Flexible Mechanical Systems*, volume 268 of *NATO ASI Series*, pages 61–100. Springer Netherlands, 1994.

[59] M. Hjiaj, Z-Q. Feng, G. De la Saxcé, and Z. Mróz. Three-dimensional finite element computations for frictional contact problems with non-associated sliding rule. *International Journal for Numerical Methods in Engineering*, 60:2045–2076, 2004.

[60] K. Hunt and F. Crossley. Coefficient of restitution interpreted as damping in vibroimpact. *Journal of Applied Mechanics*, 42(2):440–445, 1975.

[61] B. Irons. Structural eigenvalue problems-elimination of unwanted variables. *AIAA Journal*, 3(5):961–962, 1965.

[62] ISO6336-1. Calculation of load capacity of spur and helical gears - part 1. International Organisation for Standardisation, 2000.

[63] M. Jean. The non-smooth contact dynamics method. *Computer Methods in Applied Mechanics and Engineering*, 177:235–257, 1999.

[64] P. Jetteur. Contact between flexible bodies in nonlinear analysis, using lagrange multipliers. In *International Conference on Engineering Computational Technology*, pages 257–261, 2000.

[65] P. Johansen, D. Rømer, Torben O. Andersen, and H. C. Pedersen. A modelling approach to multibody dynamics of fluid power machinery with hydrodynamic lubrication. In *8th International Conference on Fluid Power Transmission and Control, ICFP 2013*.

[66] R Jones, K Mao, A Phang, and B Allen. Effects of linear and angular misalignment on a spur gear pair. *Insight - Non-Destructive Testing and Condition Monitoring*, 53(8):420–425, 2011-08-01T00:00:00.

[67] A. Kahraman. Planetary gear train dynamics. *Journal of Mechanical Design*, 116(3):713–720, 1994.

[68] A. Kahraman and R. Singh. Non-linear dynamics of a spur gear pair. *Journal of sound and vibration*, 142(1):49–75, 1990.

[69] A. Kahraman and R. Singh. Interactions between time-varying mesh stiffness and clearance non-linearities in a geared system. *Journal of Sound and Vibration*, 146(1):135 – 156, 1991.

[70] I. Karagiannis, S. Theodossiades, and H. Rahnejat. On the dynamics of lubricated hypoid gears. *Mechanism and Machine Theory*, 48:94–120, 2012.

[71] G. Kerschen, J.-C. Golinval, A. Vakakis, and L. Bergman. The method of proper orthogonal decomposition for dynamical characterization and order reduction of mechanical systems: an overview. *Nonlinear Dynamics*, 41(1-3):147–169, 2005.

[72] M.M. Khonsari. On the modeling of multi-body interaction problems in tribology. *Wear*, 207(1–2):55 – 62, 1997.

[73] Y. Khulief and A. Shabana. A continuous force model for the impact analysis of flexible multibody systems. *Mechanism and Machine Theory*, 22(3):213–224, 1987.

[74] S.-S. Kim and E. J. Haug. A recursive formulation for flexible multibody dynamics, part i: open-loop systems. *Computer Methods in Applied Mechanics and Engineering*, 71(3):293–314, 1988.

[75] L. Kogut and I. Etsion. Elastic-plastic contact analysis of a sphere and a rigid flat. *Journal of Applied Mechanics*, 69:657–662, 2002.

[76] W. Kortüm. Review of multibody computer, codes for vehicle system dynamics. *Vehicle System Dynamics*, 22(sup1):3–31, 1993.

[77] P. Koutsovasilis. *Model order reduction in structural mechanics. Coupling the rigid and elastic multi body dynamics.* PhD thesis, Technische Universität Dresden, Germany, 2009.

[78] W. Krüger, I. Besselink, D. Cowling, D. B. Doan, W. Kortüm, and W. Krabacher. Aircraft landing gear dynamics: simulation and control. *Vehicle System Dynamics: International Journal of Vehicle Mechanics and Mobility*, 28:119–158, 1997.

[79] H. Lankarani. *Canonical equations of motion and estimation of parameters in the analysis of impact problems.* PhD thesis, University of Arizona, USA, 1988.

[80] H. Lankarani and P. Nikravesh. Continuous contact force models for impact analysis in multibody analysis. *Nonlinear Dynamics*, 5:193–207, 1994.

[81] A. Laub, M. Heath, C. Paige, and R. Ward. Computation of system balancing transformations and other applications of simultaneous diagonalization algorithms. *Automatic Control, IEEE Transactions on*, 32(2):115–122, 1987.

[82] K. Lee. A short note for numerical analysis of dynamic contact considering impact and a very stiff spring-damper constraint on the contact point. *Multibody System Dynamics*, 26(4):425–439, 2011.

[83] E. Lens and A. Cardona. A nonlinear beam element formulation in the framework of an energy preserving time integration scheme for constrained multibody systems dynamics. *Computers and Structures*, 86:47–63, 2008.

[84] T. Li and Y. Wang. Deployment dynamic analysis of deployable antennas considering thermal effect. *Aerospace Science and Technology*, 13:210–215, 2009.

[85] T. Lin, H. Ou, and R. Li. A finite element method for 3D static and dynamic contact/impact analysis of gear drives. *Computer Methods in Applied Mechanics and Engineering*, 196:1716–1728, 2007.

[86] LMS-SAMTECH S.A. *BOSS QUATTRO V6.1 - User's and Installation Manuel*.

[87] LMS-SAMTECH S.A. *SAMCEF/DYNAM V13 - User's and Installation Manuel*.

[88] LMS-SAMTECH S.A. *SAMCEF/MECANO V13 - User's and Installation Manuel*.

[89] O. Lundvall, N. Strömberg, and A. Klarbring. A flexible multi-body approach for frictional contact in spur gears. *Journal of Sound and Vibration*, 278:479–499, 2004.

[90] Z.-D. Ma and N. Perkins. An efficient multibody dynamics model for internal combustion engine systems. *Multibody Systems Dynamics*, 10:363–391, 2003.

[91] M. Machado, P. Moreira, P. Flores, and H. M. Lankarani. Compliant contact force models in multibody dynamics: Evolution of the Hertz contact theory. *Mechanism and Machine Theory*, 53(0):99 – 121, 2012.

[92] R. H. MacNeal. A hybrid method of component mode synthesis. *Computers & Structures*, 1(4):581 – 601, 1971. Special Issue on Structural Dynamics.

[93] G. Mantriota and E. Pennestrì. Theoretical and experimental efficiency analysis of multi-degrees-of-freedom epicyclic gear trains. *Multibody system dynamics*, 9(4):389–408, 2003.

[94] E. Meli, M. Malvezzi, S. Papini, L. Pugi, M. Rinchi, and A. Rindi. A railway vehicle multibody model for real-time applications. *Vehicle System Dynamics: International Journal of Vehicle Mechanics and Mobility*, 46(12):1083–1105, 2008.

[95] L. Menhour, D. Lechner, and A. Charara. Two degrees of freedom PID multi-controllers to design a mathematical driver model: experimental validation and robustness tests. *Vehicle System Dynamics*, 49(4):595–624, 2011.

[96] D. Negrut, E. J. Haug, and H. C. German. An implicit runge-kutta method for integration of differential algebraic equations of multibody dynamics. *Multibody System Dynamics*, 9:121–142, 2003.

[97] D. Negrut, D. Melanz, H. Mazhar, D. Lamb, P. Jayakumar, and M. Letherwood. Investigating through simulation the mobility of light tracked vehicles operating on discrete granular terrain. *SAE International Journal of Passenger Cars-Mechanical Systems*, 6(1):369–381, 2013.

[98] N. M. Newmark. A method for computation for structural dyanmics. *ASCE Journal of the Engineering Mechanics Division*, 85(3):67–94, 1959.

[99] G. Niemann and A. A. Massanet. *Tratado teórico-práctico de elementos de máquinas: cálculo, diseño y construcción*. Labor, 1973.

[100] P. E. Nikravesh. An overview of several formulations for multibody dynamics. In *Product Engineering*, pages 189–226. Springer, 2005.

[101] P. E. Nikravesh and Y.-S. Lin. Use of principal axes as the floating reference frame for a moving deformable body. *Multibody System Dynamics*, 13(2):211–231, 2005.

[102] A. Palermo, D. Mundo, R. Hadjit, and W. Desmet. Multibody element for spur and helical gear meshing based on detailed three-dimensional contact calculations. *Mechanism and Machine Theory*, 62(0):13 – 30, 2013.

[103] L. Paoli and M. Schatzman. A numerical scheme for impact problems II: The multidimensional case. *SIAM Journal on Numerical Analysis*, 40(2):734–768, 2003.

[104] M. S. M. Perera, S. Theodossiades, and H. Rahnejat. Elasto-multi-body dynamics of internal combustion engines with tribological conjunctions. *Proceedings of the Institution of Mechanical Engineers, Part K: Journal of Multi-body Dynamics*, 224(3):261–277, 2010.

[105] F. Pfeiffer. On non-smooth dynamics. *Meccanica*, 43:533–554, 2008.

[106] T. Phu Do, P. Ziegler, and P. Eberhard. Simulation of elastic gears with non-standard flank profiles. *Archive of Mechanical Engineering*, 60(1):55–73, 2013.

[107] R. Potenza, J.F. Dunne, S. Vulli, and D. Richardson. A model for simulating the instantaneous crank kinematics and total mechanical losses in a multicylinder in-line engine. *International Journal of Engine Research*, 8(4):379–397, 2007.

[108] M. Puso. A 3D mortar method for solid mechanics. *International Journal for Numerical Methods in Engineering*, 69:657–662, 2004.

[109] M. J. Puttock and E. G. Thwaite. Elastic compression of spheres and cylinders at point and line contact. Research Report 25, Commonwealth Scientific and Industrial Research Organization, Australia, 1969.

[110] C. Quental, J. Folgado, J. Ambrósio, and J. Monteiro. A multibody biomechanical model of the upper limb uncluding the schoulder girdle. *Multibody System Dynamics*, 28:83–108, 2012.

[111] P. Ravn. A continuous analysis method for planar multibody systems with joint clearance. *Multibody System Dynamics*, 2:1–24, 1998.

[112] J. Reimpell and H. Stoll. *The automotive chassis: engineering principles*. Society of Automotive Engineers Warrendale„ PA, USA, 1996.

[113] D. J. Rixen. A dual Craig-Bampton method for dynamic substructuring. *Journal of Computational and Applied Mathematics*, 168:383–391, 2004.

[114] I. Romero. A comparison of finite elements for nonlinear beams: the absolute nodal coordinate and geometrically exact formulations. *Multibody System Dynamics*, 20(1):51–68, 2008.

[115] W. J. Roux, N. Stander, and R. T. Haftka. Response surface approximations for structural optimization. *International Journal for Numerical Methods in Engineering*, 42(3):517–534, 1998.

[116] S. Rubin. Improved component-mode representation for structural dynamic analysis. *AIAA journal*, 13(8):995–1006, 1975.

[117] C. Rustin. *Physiological Modelling and Dynamic Simulation of Human Walking*. PhD thesis, Université de Mons, Faculté Polytechnique, Belgium, December 2010.

[118] J.-C. Samin and P. Fisette. *Symbolic modeling of multibody systems*. Kluwer Academic Publishers, Dordrecht, 2003.

[119] W. Schiehlen. Multibody system dynamics: Roots and perspectives. *Multibody System Dynamics*, 1(2):149–188, 1997.

[120] S. Seetharaman and A. Kahraman. Load-independent spin power losses of a spur gear pair: model formulation. *Journal of tribology*, 131(2), 2009.

[121] S. Seetharaman, A. Kahraman, M.D. Moorhead, and T.T. Petry-Johnson. Oil churning power losses of a gear pair: experiments and model validation. *Journal of tribology*, 131(2), 2009.

[122] R. Seifried, W. Schiehlen, and P. Eberhard. The role of the coefficient of restitution on impact problems in multi-body dynamics. *Proc. IMechE, Part K:J. Multi-body Dynamics*, 224:279–306, 2010.

[123] A. A. Shabana. *Dynamics of Multibody Systems.* Cambridge University Press, New York, 3 edition, 2005.

[124] A. A. Shabana and R. A. Wehage. A coordinate reduction technique for dynamic analysis of spatial substructures with angular rotations. *Journal of Structural Mechanics*, 11:401–431, 1983.

[125] J. C. Simo. A finite strain beam formulation. the three-dimensional dynamic problem. part I. *Computer Methods in Applied Mechanics and Engineering*, 49(1):55 – 70, 1985.

[126] J. C. Simo and N. Tarnow. The discrete energy-momentum method. conserving algorithms for nonlinear elastodynamics. *Zeitschrift für angewandte Mathematik und Physik ZAMP*, 43(5):757–792, 1992.

[127] J. C. Simo and L. Vu-Quoc. A three-dimensional finite-strain rod model. part II: Computational aspects. *Computer Methods in Applied Mechanics and Engineering*, 58(1):79–116, 1986.

[128] V. Sonneville, A. Cardona, and O. Brüls. Geometrically exact beam finite element formulated on the Special Euclidean group $SE(3)$. *Computer Methods in Applied Mechanics and Engineering*, 268:451–474, 2014.

[129] W. J. Stronge. *Impact Mechanics.* Cambridge University Press, 2004.

[130] J. A. Szivek, P. L. Anderson, and J. B. Benjamin. Average and peak contact stress distribution evaluation of total knee arthroplasties. *The Journal of arthroplasty*, 11(8):952–963, 1996.

[131] T. Tamarozzi. *Efficient numerical simulation strategies for flexible multibody systems with variable topology.* PhD thesis, KU Leuven, Belgium, 2014.

[132] T. Tamarozzi, G.H.K. Heirman, and W. Desmet. An on-line time dependent parametric model order reduction scheme with focus on dynamic stress recovery. *Computer Methods in Applied Mechanics and Engineering*, 268(0):336–358, 2014.

[133] T. Tamarozzi, P. Ziegler, P. Eberhard, and W. Desmet. On the applicability of static modes switching in gear contact applications. *Multibody System Dynamics*, pages 1–11, 2013.

[134] T. Tamarozzi, P. Ziegler, P. Eberhard, and W. Desmet. Static modes switching in gear contact simulation. *Mechanism and Machine Theory*, 63(0):89 – 106, 2013.

[135] Y. Tezuka, H. Ishii, and S. Kiyota. Application of the magic formula tire model to motorcycle maneuverability analysis. *JSAE Review*, 22(3):305 – 310, 2001.

[136] S. Theodossiades, O. Tangasawi, and H. Rahnejat. Gear teeth impacts in hydrodynamic conjunctions promoting idle gear rattle. *Journal of sound and vibration*, 303(3):632–658, 2007.

[137] Q. Tian, C. Liu, M. Machado, and P. Flores. A new model for dry and lubricated cylindrical joints with clearance in spatial flexible multibody systems. *Nonlinear Dynamics*, 64(1):25–47, 2011.

[138] Q. Tian, Y. Zhang, L. Chen, and P. Flores. Dynamics of spatial flexible multibody systems with clearance and lubricated spherical joints. *Computers & Structures*, 87(13-14):913 – 929, 2009.

[139] S. Timoshenko and J. N. Goodier. *Theory of Elasticity*. McGraw-Hill Book Company, 1951.

[140] E. Tromme, O. Brüls, J. Emonds-Alt, M. Bruyneel, G. Virlez, and P. Duysinx. Discussion on the optimization problem formulation of flexible components in multibody systems. *Structural and Multidisciplinary Optimization*, 48(6):1189–1206, 2013.

[141] H. True and P. G. Thomsen. *Non-smooth Problems in Vehicle Systems Dynamics, Proceedings of the Euromech 500 Colloquium*. Springer, Berlin, Wien, New York, 2010.

[142] B. Fraeijs De Veubeke. The dynamics of flexible bodies. *International Journal of Engineering Science*, 14(10):895 – 913, 1976.

[143] T. M. Wasfy and A. K. Noor. Computational strategies for flexible multibody systems. *Applied Mechanics Review*, 56(6):553–613, 2003.

[144] S. T. Weerathunge Kadawathagedara and D. J. Rixen. Model reduction in corotated multi-body dynamics based on the dual Craig-Bampton method. In *Proceedings of* 52^{nd} *AIAA/ASME/ASCE/AHS/ASC Structures, Structural Dynamics and Material Conference. 4-7 April 2011, Denver, Colorado, USA.*

[145] J. Williams. *Engineering tribology*, volume 10. Cambridge University Press, 2005.

[146] J. Wittenburg. *Dynamics of multibody systems*. Springer, 2007.

[147] B. Yang and T. A. Laursen. A mortar-finite element approach to lubricated contact problems. *Computer Methods in Applied Mechanics and Engineering*, 198(47–48):3656 – 3669, 2009.

[148] M. Zaeh and D. Siedl. A new method for simulation of machining performance by integrating finite element and multi-body simulation for machine tools. *Annals of the CIRP - Manufacturing Technology*, 56(1):383–386, 2007.

[149] R. Zander. *Flexible multi-body systems with set-valued force laws*. PhD thesis, Teschnischen Universität München, 2008.

[150] P. Ziegler and P. Eberhard. Simulative and experimental investigation of impacts on gear wheels. *Computer Methods for Applied mechanics and engineering*, 197(51-52):4653–4662, 2008.

[151] P. Ziegler and P. Eberhard. Investigation of gears using an elastic multibody model with contact. *Multibody Dynamics: Computational Methods and Applications, Computational Methods in Applied Sciences*, 23:309–327, 2011.

[152] P. Ziegler, P. Eberhard, and B. Schweizer. Simulation of impacts in geartrains using different approaches. *Arch Appl Mech*, 76:537–548, 2006.

Appendices

Appendix A

Iteration matrix of rigid contact models

For nonsmooth behaviours such as those introduced by unilateral and frictional contacts, a reliable estimation of the iteration matrix is required in order to limit the number of Newton iterations to reach the convergence. An iteration matrix not sufficiently accurate can even prevent the convergence of the numerical integration. An analytical computation of the iteration matrix needs an effort to determine the various matrix components but enables to reduce significantly the CPU time of the entire multibody simulation compared with the finite difference approach.

In this appendix, the iteration matrices of the three contact models between rigid bodies presented in Chapter 4 are detailed.

A.1 Contact element between two plane rings

This section presents the fully analytical computation of the iteration matrix related to the contact element between two plane rings detailed in Section 4.3. The expressions given hereabove are the same if the contact force is determined by a continuous impact law (Section 4.2.1) or the squeeze film model (Section 5.2.5) since they are both based on the same kinematic description. Only the derivative of the magnitude of the contact force and the friction force is different for the two methods, but these simple expressions are not detailed in the sequel of this section.

The derivative of the virtual work principle (Eq. 4.25) takes the form:

$$\begin{aligned}\delta \mathrm{d}W = {} & \delta \boldsymbol{u}^T \, \frac{\partial \boldsymbol{f}_t(\boldsymbol{u}, \dot{\boldsymbol{u}})}{\partial \boldsymbol{u}} \, \mathrm{d}\boldsymbol{u} + \delta \boldsymbol{u}^T \, \frac{\partial \boldsymbol{f}_t(\boldsymbol{u}, \dot{\boldsymbol{u}})}{\partial \dot{\boldsymbol{u}}} \, \mathrm{d}\dot{\boldsymbol{u}} + \delta \mathrm{d}\boldsymbol{u}^T \, \boldsymbol{f}_t \\ & + \delta \boldsymbol{\Theta}_{rel}^T \, \frac{\partial \boldsymbol{f}_r(\boldsymbol{\Theta}_{rel}, \dot{\boldsymbol{\Theta}}_{rel})}{\partial \boldsymbol{\Theta}_{rel}} \, \mathrm{d}\boldsymbol{\Theta}_{rel} + \delta \boldsymbol{\Theta}_{rel}^T \, \frac{\partial \boldsymbol{f}_r(\boldsymbol{\Theta}_{rel}, \dot{\boldsymbol{\Theta}}_{rel})}{\partial \dot{\boldsymbol{\Theta}}_{rel}} \, \mathrm{d}\dot{\boldsymbol{\Theta}}_{rel} + \delta \mathrm{d}\boldsymbol{\Theta}_{rel}^T \, \boldsymbol{f}_r\end{aligned} \tag{A.1}$$

This expression A.1 has to be transformed in order that the following structure appears:

$$\delta \mathrm{d}W = \delta \boldsymbol{q}^T \, \frac{\partial \boldsymbol{g}^{int}(\boldsymbol{q}, \dot{\boldsymbol{q}})}{\partial \boldsymbol{q}} \, \mathrm{d}\boldsymbol{q} + \delta \boldsymbol{q}^T \, \frac{\partial \boldsymbol{g}^{int}(\boldsymbol{q}, \dot{\boldsymbol{q}})}{\partial \dot{\boldsymbol{q}}} \, \mathrm{d}\dot{\boldsymbol{q}} \tag{A.2}$$

To this end, the various terms of Eq. A.1 have to be expanded in terms of the generalized coordinates ($\boldsymbol{q}$).

The spatial and time derivative of the relative position vector $\boldsymbol{u}$ are obtained by analogy with $\delta\boldsymbol{u}$ (see Eq. 4.26):

$$\mathrm{d}\boldsymbol{u} = \widetilde{\boldsymbol{u}} \boldsymbol{R}_1^T \boldsymbol{T}(\boldsymbol{\Psi}_{A\ inc}) \, \mathrm{d}\boldsymbol{\Psi}_{A\ inc} + \boldsymbol{R}_1^T \boldsymbol{R}_A^T \left(\mathrm{d}\boldsymbol{x}_B - \mathrm{d}\boldsymbol{x}_A\right) \tag{A.3}$$

$$\dot{\boldsymbol{u}} = \widetilde{\boldsymbol{u}} \boldsymbol{R}_1^T \boldsymbol{T}(\boldsymbol{\Psi}_{A\ inc}) \dot{\boldsymbol{\Psi}}_{A\ inc} + \boldsymbol{R}_1^T \boldsymbol{R}_A^T \left(\dot{\boldsymbol{x}}_B - \dot{\boldsymbol{x}}_A\right) \tag{A.4}$$

One more derivative enables to computes $\mathrm{d}\dot{\boldsymbol{u}}$. It comes

$$\begin{aligned}\mathrm{d}\dot{\boldsymbol{u}} = {} & - \overbrace{\left(\boldsymbol{R}_1^T \boldsymbol{T}(\boldsymbol{\Psi}_{A\ inc}) \dot{\boldsymbol{\Psi}}_{A\ inc}\right)}^{\sim} \boldsymbol{R}_1^T \boldsymbol{R}_A^T (\mathrm{d}\boldsymbol{x}_B - \mathrm{d}\boldsymbol{x}_A) \\ & - \Big[\overbrace{\left(\boldsymbol{R}_1^T \boldsymbol{T}(\boldsymbol{\Psi}_{A\ inc}) \dot{\boldsymbol{\Psi}}_{A\ inc}\right)}^{\sim} \widetilde{\boldsymbol{u}} \boldsymbol{R}_1^T \boldsymbol{T}(\boldsymbol{\Psi}_{A\ inc}) - \widetilde{\boldsymbol{u}} \boldsymbol{R}_1^T \boldsymbol{G}(\boldsymbol{\Psi}_{A\ inc}, \dot{\boldsymbol{\Psi}}_{A\ inc}) \\ & \qquad + \boldsymbol{R}_1^T \overbrace{\left(\boldsymbol{R}_A^T (\dot{\boldsymbol{x}}_B - \dot{\boldsymbol{x}}_A)\right)}^{\sim} \boldsymbol{T}(\boldsymbol{\Psi}_{A\ inc}) \Big] \, \mathrm{d}\boldsymbol{\Psi}_{A\ inc} \\ & + \boldsymbol{R}_1^T \boldsymbol{R}_A^T (\mathrm{d}\dot{\boldsymbol{x}}_B - \mathrm{d}\dot{\boldsymbol{x}}_B) + \widetilde{\boldsymbol{u}} \boldsymbol{R}_1^T \boldsymbol{T}(\boldsymbol{\Psi}_{A\ inc}) \mathrm{d}\dot{\boldsymbol{\Psi}}_{A\ inc}\end{aligned} \tag{A.5}$$

where the matrix $\boldsymbol{G}$ comes from:

$$\mathrm{d}\boldsymbol{T}(\boldsymbol{\Psi}_{A\ inc}) \dot{\boldsymbol{\Psi}}_{A\ inc} = \boldsymbol{G}(\boldsymbol{\Psi}_{A\ inc}, \dot{\boldsymbol{\Psi}}_{A\ inc}) \, \mathrm{d}\boldsymbol{\Psi}_{A\ inc} \tag{A.6}$$

By means of the previous developed vectors, the various terms of the virtual work expression (Eq.A.1) can be reformulated. The first term becomes:

$$\begin{aligned}\delta \boldsymbol{u}^T \, \frac{\partial \boldsymbol{f}_t(\boldsymbol{u}, \dot{\boldsymbol{u}})}{\partial \boldsymbol{u}} \, \mathrm{d}\boldsymbol{u} = {} & \left\{ -\delta \boldsymbol{\Psi}_{A\ inc}^T \boldsymbol{T}^T(\boldsymbol{\Psi}_{A\ inc}) \boldsymbol{R}_1 \widetilde{\boldsymbol{u}} + \left(\delta \boldsymbol{x}_B^T - \delta \boldsymbol{x}_A^T\right) \boldsymbol{R}_A \boldsymbol{R}_1 \right\} \, \frac{\partial \boldsymbol{f}_t(\boldsymbol{u}, \dot{\boldsymbol{u}})}{\partial \boldsymbol{u}} \\ & \left\{ \widetilde{\boldsymbol{u}} \boldsymbol{R}_1^T \boldsymbol{T}(\boldsymbol{\Psi}_{A\ inc}) \mathrm{d}\boldsymbol{\Psi}_{A\ inc} + \boldsymbol{R}_1^T \boldsymbol{R}_A^T \left(\mathrm{d}\boldsymbol{x}_B - \mathrm{d}\boldsymbol{x}_A\right) \right\}\end{aligned} \tag{A.7}$$

If the two first terms of $\mathrm{d}\dot{\boldsymbol{u}}$ are neglected, the second term takes the form:

$$\begin{aligned}\delta \boldsymbol{u}^T \, \frac{\partial \boldsymbol{f}_t(\boldsymbol{u}, \dot{\boldsymbol{u}})}{\partial \dot{\boldsymbol{u}}} \, \mathrm{d}\dot{\boldsymbol{u}} = {} & \left\{ (\delta \boldsymbol{x}_B^T - \delta \boldsymbol{x}_A^T) \boldsymbol{R}_A \boldsymbol{R}_1 - \delta \boldsymbol{\Psi}_{A\ inc}^T \, \boldsymbol{T}^T(\boldsymbol{\Psi}_{A\ inc}) \boldsymbol{R}_1 \widetilde{\boldsymbol{u}} \right\} \\ & \frac{\partial \boldsymbol{f}_t(\boldsymbol{u}, \dot{\boldsymbol{u}})}{\partial \dot{\boldsymbol{u}}} \left\{ \boldsymbol{R}_1^T \boldsymbol{R}_A^T (\mathrm{d}\boldsymbol{x}_B - \mathrm{d}\boldsymbol{x}_A) + \widetilde{\boldsymbol{u}} \boldsymbol{R}_1^T \boldsymbol{T}(\boldsymbol{\Psi}_{A\ inc}) \mathrm{d}\boldsymbol{\Psi}_{A\ inc} \right\}\end{aligned} \tag{A.8}$$

The third term of the variation of the virtual work (Eq. A.1) can be approximated by:

$$\begin{aligned}\delta \mathrm{d}\boldsymbol{u}^T \boldsymbol{f}_t \cong &- \left(\delta \boldsymbol{x}_B^T - \delta \boldsymbol{x}_A^T\right) \boldsymbol{R}_A \boldsymbol{R}_1 \widetilde{\boldsymbol{f}}_t \boldsymbol{R}_1^T \boldsymbol{T}(\boldsymbol{\Psi}_{A\ inc}) \mathrm{d}\boldsymbol{\Psi}_{A\ inc} \\ &+ \delta \boldsymbol{\Psi}_{A\ inc}^T \left[\frac{1}{2}\widetilde{\left(\boldsymbol{R}_1 \widetilde{\boldsymbol{u}} \boldsymbol{f}_t\right)} + \boldsymbol{R}_1 \widetilde{\boldsymbol{f}}_t \widetilde{\boldsymbol{u}} \boldsymbol{R}_1^T\right] \mathrm{d}\boldsymbol{\Psi}_{A\ inc}\end{aligned} \tag{A.9}$$

For the fourth term of Eq. A.1, it is needed to compute the absolute spatial derivative of relative rotation vector $\boldsymbol{\Theta}_{rel}$.

$$\mathrm{d}\boldsymbol{\Theta}_{rel} = -\boldsymbol{R}_1^T \boldsymbol{R}_B^T \boldsymbol{R}_A \boldsymbol{T}(\boldsymbol{\Psi}_{A\ inc}) \mathrm{d}\boldsymbol{\Psi}_{A\ inc} + \boldsymbol{R}_1^T \boldsymbol{T}(\boldsymbol{\Psi}_{B\ inc}) \mathrm{d}\boldsymbol{\Psi}_{B\ inc} \tag{A.10}$$

$$\begin{aligned}\delta \boldsymbol{\Theta}_{rel}^T \frac{\partial \boldsymbol{f}_r(\boldsymbol{\Theta}_{rel}, \dot{\boldsymbol{\Theta}}_{rel})}{\partial \boldsymbol{\Theta}_{rel}} \mathrm{d}\boldsymbol{\Theta}_{rel} = &\left\{-\delta \boldsymbol{\Psi}_{A\ inc}^T \boldsymbol{T}^T(\boldsymbol{\Psi}_{A\ inc}) \boldsymbol{R}_A^T \boldsymbol{R}_B \boldsymbol{R}_1\right. \\ &\left. + \delta \boldsymbol{\Psi}_{B\ inc}^T \boldsymbol{T}^T(\boldsymbol{\Psi}_{B\ inc}) \boldsymbol{R}_1\right\} \frac{\partial \boldsymbol{f}_r(\boldsymbol{\Theta}_{rel}, \dot{\boldsymbol{\Theta}}_{rel})}{\partial \boldsymbol{\Theta}_{rel}} \\ &\left\{-\boldsymbol{R}_1^T \boldsymbol{R}_B^T \boldsymbol{R}_A \boldsymbol{T}(\boldsymbol{\Psi}_{A\ inc}) \mathrm{d}\boldsymbol{\Psi}_{A\ inc} + \boldsymbol{R}_1^T \boldsymbol{T}(\boldsymbol{\Psi}_{B\ inc}) \mathrm{d}\boldsymbol{\Psi}_{B\ inc}\right\}\end{aligned} \tag{A.11}$$

In order to compute $\mathrm{d}\dot{\boldsymbol{\Theta}}_{rel}$, we start from the derivative of:

$$\boldsymbol{\Omega}_{rel} = \boldsymbol{R}_1^T\ \boldsymbol{\Omega}_B - \boldsymbol{R}_1^T \boldsymbol{R}_B^T \boldsymbol{R}_A\ \boldsymbol{\Omega}_A \tag{A.12}$$

and after some mathematical manipulations, we get:

$$\begin{aligned}\mathrm{d}\dot{\boldsymbol{\Theta}}_{rel} = &\boldsymbol{R}_1^T \boldsymbol{R}_B^T \boldsymbol{R}_A \left[\widetilde{\left(\boldsymbol{T}(\boldsymbol{\Psi}_{A\ inc}) \dot{\boldsymbol{\Psi}}_{A\ inc}\right)} \boldsymbol{T}(\boldsymbol{\Psi}_{A\ inc}) - \boldsymbol{G}(\boldsymbol{\Psi}_{A\ inc}, \dot{\boldsymbol{\Psi}}_{A\ inc})\right] \mathrm{d}\boldsymbol{\Psi}_{A\ inc} \\ &- \boldsymbol{R}_1^T \left[\widetilde{\left(\boldsymbol{R}_B^T \boldsymbol{R}_A \boldsymbol{T}(\boldsymbol{\Psi}_{A\ inc}) \dot{\boldsymbol{\Psi}}_{A\ inc}\right)} \boldsymbol{T}(\boldsymbol{\Psi}_{B\ inc}) - \boldsymbol{G}(\boldsymbol{\Psi}_{B\ inc}, \dot{\boldsymbol{\Psi}}_{B\ inc})\right] \mathrm{d}\boldsymbol{\Psi}_{B\ inc} \\ &- \boldsymbol{R}_1^T \boldsymbol{R}_B^T \boldsymbol{R}_A \boldsymbol{T}(\boldsymbol{\Psi}_{A\ inc}) \mathrm{d}\dot{\boldsymbol{\Psi}}_{A\ inc} + \boldsymbol{R}_1^T \boldsymbol{T}(\boldsymbol{\Psi}_{B\ inc}) \mathrm{d}\dot{\boldsymbol{\Psi}}_{B\ inc} \\ &- \boldsymbol{G}(\boldsymbol{\Theta}_{rel}, \dot{\boldsymbol{\Theta}}_{rel})\ \mathrm{d}\boldsymbol{\Theta}_{rel}\end{aligned} \tag{A.13}$$

By omitting the terms in $\mathrm{d}\boldsymbol{\Psi}_{A\ inc}$ and $\mathrm{d}\boldsymbol{\Psi}_{B\ inc}$, the fifth term of Eq. A.1 can be reduced to:

$$\begin{aligned}\delta \boldsymbol{\Theta}_{rel}^T \frac{\partial \boldsymbol{f}_r(\boldsymbol{\Theta}_{rel}, \dot{\boldsymbol{\Theta}}_{rel})}{\partial \dot{\boldsymbol{\Theta}}_{rel}} \mathrm{d}\dot{\boldsymbol{\Theta}}_{rel} = &\left\{-\delta \boldsymbol{\Psi}_{A\ inc}^T \boldsymbol{T}^T(\boldsymbol{\Psi}_{A\ inc}) \boldsymbol{R}_A^T \boldsymbol{R}_B \boldsymbol{R}_1\right. \\ &\left. + \delta \boldsymbol{\Psi}_{B\ inc}^T \boldsymbol{T}^T(\boldsymbol{\Psi}_{B\ inc}) \boldsymbol{R}_1\right\} \frac{\partial \boldsymbol{f}_r(\boldsymbol{\Theta}_{rel}, \dot{\boldsymbol{\Theta}}_{rel})}{\partial \dot{\boldsymbol{\Theta}}_{rel}} \\ &\left\{-\boldsymbol{R}_1^T \boldsymbol{R}_B^T \boldsymbol{R}_A \boldsymbol{T}(\boldsymbol{\Psi}_{A\ inc}) \mathrm{d}\dot{\boldsymbol{\Psi}}_{A\ inc} + \boldsymbol{R}_1^T \boldsymbol{T}(\boldsymbol{\Psi}_{B\ inc}) \mathrm{d}\dot{\boldsymbol{\Psi}}_{B\ inc}\right\}\end{aligned} \tag{A.14}$$

Finally, the last term of Equation A.1 can be neglected in first approximation:

$$\delta \mathrm{d}\boldsymbol{\Theta}_{rel}^T\ \boldsymbol{f}_r \cong 0 \tag{A.15}$$

Owing to the few terms neglected, the tangent stiffness and tangent damping matrices can be put in a compact matrix form (Eq. A.16-A.17).

$$\boldsymbol{K}_t^{con} = \frac{\partial \boldsymbol{g}^{int}(\boldsymbol{q},\dot{\boldsymbol{q}})}{\partial \boldsymbol{q}} = \boldsymbol{B}^T \begin{bmatrix} \frac{\partial \boldsymbol{f}_t(\boldsymbol{u},\dot{\boldsymbol{u}})}{\partial \boldsymbol{u}} & \boldsymbol{0} \\ \boldsymbol{0} & \frac{\partial \boldsymbol{f}_r(\boldsymbol{\Theta}_{rel},\dot{\boldsymbol{\Theta}}_{rel})}{\partial \boldsymbol{\Theta}_{rel}} \end{bmatrix} \boldsymbol{B} + \begin{bmatrix} \boldsymbol{0} & \boldsymbol{R}_A \boldsymbol{R}_1 \widetilde{f}_t \boldsymbol{R}_1^T \boldsymbol{T}(\boldsymbol{\Psi}_{A\ inc}) & \boldsymbol{0} & \boldsymbol{0} \\ \boldsymbol{0} & \frac{1}{2}\widetilde{\left(\boldsymbol{R}_1 \widetilde{\boldsymbol{u}} \boldsymbol{f}_t\right)} + \boldsymbol{R}_1 \widetilde{f}_t \widetilde{\boldsymbol{u}} \boldsymbol{R}_1^T & \boldsymbol{0} & \boldsymbol{0} \\ \boldsymbol{0} & -\boldsymbol{R}_A \boldsymbol{R}_1 \widetilde{f}_t \boldsymbol{R}_1^T \boldsymbol{T}(\boldsymbol{\Psi}_{A\ inc}) & \boldsymbol{0} & \boldsymbol{0} \\ \boldsymbol{0} & \boldsymbol{0} & \boldsymbol{0} & \boldsymbol{0} \end{bmatrix} \tag{A.16}$$

$$\boldsymbol{C}_t^{con} = \frac{\partial \boldsymbol{g}^{int}(\boldsymbol{q},\dot{\boldsymbol{q}})}{\partial \dot{\boldsymbol{q}}} = \boldsymbol{B}^T \begin{bmatrix} \frac{\partial \boldsymbol{f}_t(\boldsymbol{u},\dot{\boldsymbol{u}})}{\partial \dot{\boldsymbol{u}}} & \boldsymbol{0} \\ \boldsymbol{0} & \frac{\partial \boldsymbol{f}_r(\boldsymbol{\Theta}_{rel},\dot{\boldsymbol{\Theta}}_{rel})}{\partial \dot{\boldsymbol{\Theta}}_{rel}} \end{bmatrix} \boldsymbol{B} \tag{A.17}$$

The contribution of the contact element to the iteration matrix of the full MBS is given by:

$$\boldsymbol{S}_t^{con} = \boldsymbol{K}_t^{con} + \frac{\gamma}{\beta h}\, \boldsymbol{C}_t^{con} \tag{A.18}$$

A.2 Cylindrical joint with clearance and friction

The iteration matrix of the cylindrical joint with clearance and friction described in section 4.5 is detailled in the following of this appendix. Owing to the huge number of mathematical operations involved, the computation of the full iteration matrix could be time consuming. Some terms given herebelow provide probably a insignificant contribution to the full iteration matrix and could be omitted. A detailed study could be carried out in order to determine which terms should be neglected.in order to optimize the CPU time.

The contribution to the iteration matrix of any force element can be obtained by deriving the virtual work expression (Eq. 4.61):

$$\delta \mathrm{d}\mathcal{W} = \delta \boldsymbol{q}^T\ \mathrm{d}\boldsymbol{g}^{int}(\boldsymbol{q},\dot{\boldsymbol{q}}) \tag{A.19}$$

A.2.1 Contact Force

In order to separate explicitly the contributions due to purely geometric effects and the contributions due to the contact force magnitude, it has be chosen to decompose the internal force vector $\boldsymbol{g}_n^{int}$ (Eq. 4.63) in two parts. Therefore, the absolute derivative of

this force vector is made of two terms:

$$\mathrm{d}\boldsymbol{g}^{int}(\boldsymbol{q},\dot{\boldsymbol{q}}) = \mathrm{d}f \begin{Bmatrix} -\boldsymbol{n} \\ -\boldsymbol{T}^T(\boldsymbol{\Psi}_{A\ inc})\boldsymbol{R}_A^T\boldsymbol{R}_1^T\widetilde{\boldsymbol{x}}_{AB}\ \boldsymbol{n} \\ \boldsymbol{n} \\ \boldsymbol{0} \end{Bmatrix} + f\ \mathrm{d} \begin{Bmatrix} -\boldsymbol{n} \\ -\boldsymbol{T}^T(\boldsymbol{\Psi}_{A\ inc})\boldsymbol{R}_A^T\boldsymbol{R}_1^T\widetilde{\boldsymbol{x}}_{AB}\ \boldsymbol{n} \\ \boldsymbol{n} \\ \boldsymbol{0} \end{Bmatrix} \tag{A.20}$$

Spatial derivation of the contact law

The contact force depends on the penetration length ℓ and the penetration velocity $\dot{\ell}$. This dependence will be used to express the spatial derivative of f:

$$\mathrm{d}f = \frac{\partial f}{\partial \ell}\ \mathrm{d}\ell + \frac{\partial f}{\partial \dot{\ell}}\ \mathrm{d}\dot{\ell} \tag{A.21}$$

where the spatial derivative are defined by:

$$\frac{\partial f}{\partial \ell} = k\ n\ \ell^{n-1} + c\ n\ \ell^{n-1}\ \dot{\ell} \tag{A.22}$$

$$\frac{\partial f}{\partial \dot{\ell}} = c\ \ell^n \tag{A.23}$$

The derivative of the penetration length takes the form:

$$\mathrm{d}\ell = \mathrm{d}\left(\boldsymbol{x}_{PQ}^T\ \boldsymbol{n}\right) = \boldsymbol{n}^T\mathrm{d}\boldsymbol{x}_{PQ} + \boldsymbol{x}_{PQ}^T\ \mathrm{d}\boldsymbol{n} \tag{A.24}$$

$$= \boldsymbol{n}^T\ \mathrm{d}\boldsymbol{x}_{AB} + \boldsymbol{A}_2\ \mathrm{d}\boldsymbol{\Psi}_{A\ inc} \tag{A.25}$$

with:

$$\mathrm{d}\boldsymbol{x}_{PQ} = \mathrm{d}\boldsymbol{x}_{AB} - \widetilde{\boldsymbol{x}}_{BQ}\boldsymbol{R}_1\boldsymbol{R}_B\boldsymbol{T}(\boldsymbol{\Psi}_{B\ inc})\mathrm{d}\boldsymbol{\Psi}_{B\ inc} + \widetilde{\boldsymbol{x}}_{AP}\boldsymbol{R}_1\boldsymbol{R}_A\boldsymbol{T}(\boldsymbol{\Psi}_{A\ inc})\mathrm{d}\boldsymbol{\Psi}_{A\ inc}$$

$$\boldsymbol{A}_2 = \boldsymbol{n}^T\ \widetilde{\boldsymbol{x}}_{AP}\boldsymbol{R}_1\boldsymbol{R}_A\boldsymbol{T}(\boldsymbol{\Psi}_{A\ inc}) = \boldsymbol{n}^T\ \widetilde{\boldsymbol{x}}_{AB}\boldsymbol{R}_1\boldsymbol{R}_A\boldsymbol{T}(\boldsymbol{\Psi}_{A\ inc}) \tag{A.26}$$

The derivative of the penetration velocity can be formulated as:

$$\mathrm{d}\dot{\ell} = \mathrm{d}\left(\dot{\boldsymbol{x}}_{PQ}^T\ \boldsymbol{n} + \boldsymbol{x}_{PQ}^T\ \dot{\boldsymbol{n}}\right) \tag{A.27}$$

$$= \boldsymbol{n}^T\mathrm{d}\dot{\boldsymbol{x}}_{PQ} + \dot{\boldsymbol{x}}_{PQ}^T\ \mathrm{d}\boldsymbol{n} \tag{A.28}$$

The vector $\mathrm{d}\boldsymbol{n}$ appearing in Eq. A.28 can be expanded in:

$$\mathrm{d}\boldsymbol{n} = \left(\boldsymbol{I} - \boldsymbol{n}\boldsymbol{n}^T\right)\frac{\mathrm{d}\left[\left(\boldsymbol{I} - \boldsymbol{e}''_{A_1}{\boldsymbol{e}''_{A_1}}^T\right)\boldsymbol{x}_{AB}\right]}{\left\|\left(\boldsymbol{I} - \boldsymbol{e}''_{A_1}{\boldsymbol{e}''_{A_1}}^T\right)\boldsymbol{x}_{AB}\right\|} \tag{A.29}$$

with:

$$\mathrm{d}\left[\left(\boldsymbol{I} - \boldsymbol{e}''_{A_1}{\boldsymbol{e}''_{A_1}}^T\right)\boldsymbol{x}_{AB}\right] = \mathrm{d}\left(\boldsymbol{I} - \boldsymbol{e}''_{A_1}{\boldsymbol{e}''_{A_1}}^T\right)\boldsymbol{x}_{AB} + \left(\boldsymbol{I} - \boldsymbol{e}''_{A_1}{\boldsymbol{e}''_{A_1}}^T\right)\mathrm{d}\boldsymbol{x}_{AB} \tag{A.30}$$

The first term is developed in:

$$\begin{aligned} \mathrm{d}\left(\boldsymbol{I}-\boldsymbol{e}''_{A_1}{\boldsymbol{e}''_{A_1}}^{T}\right)\boldsymbol{x}_{AB} &= \mathrm{d}\left(-\widetilde{\boldsymbol{e}''_{A_1}}\widetilde{\boldsymbol{e}''_{A_1}}\right)\boldsymbol{x}_{AB} \\ &= -\left(\widetilde{\widetilde{\boldsymbol{e}''_{A_1}}\boldsymbol{x}_{AB}}+\widetilde{\boldsymbol{e}''_{A_1}}\widetilde{\boldsymbol{x}_{AB}}\right)\boldsymbol{R}_A\widetilde{\boldsymbol{e}}_{A_1}\boldsymbol{T}(\boldsymbol{\Psi}_{A\ inc})\mathrm{d}\boldsymbol{\Psi}_{A\ inc} \end{aligned} \tag{A.31}$$

In summary, the derivative of the normal vector is restated in a compact form:

$$\mathrm{d}\boldsymbol{n}=\boldsymbol{A}_3\ \mathrm{d}\boldsymbol{x}_{AB}+\boldsymbol{A}_4\ \mathrm{d}\boldsymbol{\Psi}_{A\ inc} \tag{A.32}$$

where

$$\boldsymbol{A}_3 = \frac{1}{\left\|\left(\boldsymbol{I}-\boldsymbol{e}''_{A_1}{\boldsymbol{e}''_{A_1}}^{T}\right)\boldsymbol{x}_{AB}\right\|}\left(\boldsymbol{I}-\boldsymbol{n}\boldsymbol{n}^T\right)\left(\boldsymbol{I}-\boldsymbol{e}''_{A_1}{\boldsymbol{e}''_{A_1}}^{T}\right) \tag{A.33}$$

$$\boldsymbol{A}_4 = -\frac{1}{\left\|\left(\boldsymbol{I}-\boldsymbol{e}''_{A_1}{\boldsymbol{e}''_{A_1}}^{T}\right)\boldsymbol{x}_{AB}\right\|}\left(\boldsymbol{I}-\boldsymbol{n}\boldsymbol{n}^T\right)\left(\widetilde{\widetilde{\boldsymbol{e}''_{A_1}}\boldsymbol{x}_{AB}}+\widetilde{\boldsymbol{e}''_{A_1}}\widetilde{\boldsymbol{x}_{AB}}\right)\boldsymbol{R}_A\widetilde{\boldsymbol{e}}_{A_1}\boldsymbol{T}(\boldsymbol{\Psi}_{A\ inc})$$

In addition to the term in $\mathrm{d}\boldsymbol{n}$, Eq. A.28 requires also computing $\mathrm{d}\dot{\boldsymbol{x}}_{PQ}$:

$$\begin{aligned} \mathrm{d}\dot{\boldsymbol{x}}_{PQ} = \mathrm{d}\dot{\boldsymbol{x}}_{AB} &+ \widetilde{\left(\boldsymbol{R}_1\boldsymbol{R}_B\boldsymbol{T}(\boldsymbol{\Psi}_{B\ inc})\dot{\boldsymbol{\Psi}}_{B\ inc}\right)}\ \mathrm{d}\boldsymbol{x}_{BQ}-\widetilde{\left(\boldsymbol{R}_1\boldsymbol{R}_A\boldsymbol{T}(\boldsymbol{\Psi}_{A\ inc})\dot{\boldsymbol{\Psi}}_{A\ inc}\right)}\ \mathrm{d}\boldsymbol{x}_{AP} \\ &+\widetilde{\boldsymbol{x}}_{BQ}\boldsymbol{R}_1\boldsymbol{R}_B\widetilde{\left(\boldsymbol{T}(\boldsymbol{\Psi}_{B\ inc})\dot{\boldsymbol{\Psi}}_{B\ inc}\right)}\boldsymbol{T}(\boldsymbol{\Psi}_{B\ inc})\ \mathrm{d}\boldsymbol{\Psi}_{B\ inc} \\ &-\widetilde{\boldsymbol{x}}_{AP}\boldsymbol{R}_1\boldsymbol{R}_A\widetilde{\left(\boldsymbol{T}(\boldsymbol{\Psi}_{A\ inc})\dot{\boldsymbol{\Psi}}_{A\ inc}\right)}\boldsymbol{T}(\boldsymbol{\Psi}_{A\ inc})\ \mathrm{d}\boldsymbol{\Psi}_{A\ inc} \\ &-\widetilde{\boldsymbol{x}}_{BQ}\boldsymbol{R}_1\boldsymbol{R}_B\boldsymbol{T}(\boldsymbol{\Psi}_{B\ inc})\ \mathrm{d}\dot{\boldsymbol{\Psi}}_{B\ inc}+\widetilde{\boldsymbol{x}}_{AP}\boldsymbol{R}_1\boldsymbol{R}_A\boldsymbol{T}(\boldsymbol{\Psi}_{A\ inc})\ \mathrm{d}\dot{\boldsymbol{\Psi}}_{A\ inc} \end{aligned} \tag{A.34}$$

Finally, $\mathrm{d}\ell$ is composed of four terms:

$$\mathrm{d}\dot{\ell}=\boldsymbol{A}_5\ \mathrm{d}\boldsymbol{x}_{AB}+\boldsymbol{A}_6\ \mathrm{d}\boldsymbol{\Psi}_{A\ inc}+\boldsymbol{n}^T\mathrm{d}\dot{\boldsymbol{x}}_{AB}+\boldsymbol{A}_7\ \mathrm{d}\dot{\boldsymbol{\Psi}}_{A\ inc} \tag{A.35}$$

where:

$$\boldsymbol{A}_5 = \boldsymbol{n}^T\widetilde{\boldsymbol{\omega}}_B\ r_B\ \boldsymbol{A}_3-\boldsymbol{n}^T\widetilde{\boldsymbol{\omega}}_A\left[\boldsymbol{I}+(r_b-l)\boldsymbol{A}_3\right]+\dot{\boldsymbol{x}}_{PQ}^T\ \boldsymbol{A}_3 \tag{A.36}$$

$$\boldsymbol{A}_6 = \boldsymbol{n}^T\widetilde{\boldsymbol{\omega}}_B\ r_B\ \boldsymbol{A}_4-\boldsymbol{n}^T\widetilde{\boldsymbol{\omega}}_A(r_b-l)\boldsymbol{A}_4 \tag{A.37}$$

$$+\boldsymbol{n}^T\ \widetilde{\boldsymbol{x}}_{AP}\boldsymbol{R}_1\boldsymbol{R}_A\widetilde{\left(\boldsymbol{T}(\boldsymbol{\Psi}_{A\ inc})\dot{\boldsymbol{\Psi}}_{A\ inc}\right)}\boldsymbol{T}(\boldsymbol{\Psi}_{A\ inc})+\dot{\boldsymbol{x}}_{PQ}^T\ \boldsymbol{A}_4 \tag{A.38}$$

$$\boldsymbol{A}_7 = \boldsymbol{n}^T\widetilde{\boldsymbol{x}}_{AP}\boldsymbol{R}_1\boldsymbol{R}_A\boldsymbol{T}(\boldsymbol{\Psi}_{A\ inc}) \tag{A.39}$$

The tangent stiffness matrix and the tangent damping matrix of the first term of Equation A.20 can be reduced to:

$$\boldsymbol{K}_{t_{/1}} = \boldsymbol{A}_1\{-\boldsymbol{G}\ \boldsymbol{H}\ \boldsymbol{G}\ \boldsymbol{0}\} \tag{A.40}$$

$$\boldsymbol{C}_{t_{/1}} = \boldsymbol{A}_1\{-\boldsymbol{L}\ \boldsymbol{J}\ \boldsymbol{L}\ \boldsymbol{0}\} \tag{A.41}$$

with:

$$\boldsymbol{A}_1 = \begin{Bmatrix} -\boldsymbol{n} \\ -\boldsymbol{T}^T(\boldsymbol{\Psi}_{A\ inc})\boldsymbol{R}_A^T\boldsymbol{R}_1^T\widetilde{\boldsymbol{x}}_{AB}\ \boldsymbol{n} \\ \boldsymbol{n} \\ \boldsymbol{0} \end{Bmatrix} \tag{A.42}$$

$$\boldsymbol{G} = \frac{\partial f}{\partial \ell}\boldsymbol{n}^T + \frac{\partial f}{\partial \dot{\ell}}\boldsymbol{A}_5 \tag{A.43}$$

$$\boldsymbol{H} = \frac{\partial f}{\partial \ell}\boldsymbol{A}_2 + \frac{\partial f}{\partial \dot{\ell}}\boldsymbol{A}_6 \tag{A.44}$$

$$\boldsymbol{L} = \frac{\partial f}{\partial \dot{\ell}}\boldsymbol{n}^T \tag{A.45}$$

$$\boldsymbol{J} = \frac{\partial f}{\partial \dot{\ell}}\boldsymbol{A}_7 \tag{A.46}$$

Let us note that in the case where the contact law does not include a damping contribution, this tangent stiffness matrix is symmetric.

Spatial derivation of the geometric term of the internal force vector

The second term of Equation A.20 can be reformulated as:

$$f\ \mathrm{d}\begin{Bmatrix} -\boldsymbol{n} \\ -\boldsymbol{T}^T(\boldsymbol{\Psi}_{A\ inc})\boldsymbol{R}_A^T\boldsymbol{R}_1^T\widetilde{\boldsymbol{x}}_{AB}\ \boldsymbol{n} \\ \boldsymbol{n} \\ \boldsymbol{0} \end{Bmatrix} = f\ \begin{Bmatrix} -\mathrm{d}\boldsymbol{n} \\ -\boldsymbol{A}_8 \\ \mathrm{d}\boldsymbol{n} \\ \boldsymbol{0} \end{Bmatrix} \tag{A.47}$$

with:

$$\begin{aligned} \boldsymbol{A}_8 = {} & \boldsymbol{T}^T(\boldsymbol{\Psi}_{A\ inc})\widetilde{\left(\boldsymbol{R}_A^T\boldsymbol{R}_1^T\widetilde{\boldsymbol{x}}_{AB}\ \boldsymbol{n}\right)}\ \boldsymbol{T}(\boldsymbol{\Psi}_{A\ inc})\ \mathrm{d}\boldsymbol{\Psi}_{A\ inc} \\ & - \boldsymbol{T}^T(\boldsymbol{\Psi}_{A\ inc})\boldsymbol{R}_A^T\boldsymbol{R}_1^T\ \widetilde{\boldsymbol{n}}\ \mathrm{d}\boldsymbol{x}_{AB} \\ & + \boldsymbol{T}^T(\boldsymbol{\Psi}_{A\ inc})\boldsymbol{R}_A^T\boldsymbol{R}_1^T\ \widetilde{\boldsymbol{x}}_{AB}\ \mathrm{d}\boldsymbol{n} \end{aligned} \tag{A.48}$$

By replacing $\mathrm{d}\boldsymbol{n}$ by his expression (Eq. A.32), this last matrix can be merged in only two terms:

$$\boldsymbol{A}_8 = \boldsymbol{A}_9\ \mathrm{d}\boldsymbol{x}_{AB} + \boldsymbol{A}_{10}\ \mathrm{d}\boldsymbol{\Psi}_{A\ inc} \tag{A.49}$$

with:

$$\boldsymbol{A}_9 = -\boldsymbol{T}^T(\boldsymbol{\Psi}_{A\ inc})\boldsymbol{R}_A^T\boldsymbol{R}_1^T\ \widetilde{\boldsymbol{n}} + \boldsymbol{T}^T(\boldsymbol{\Psi}_{A\ inc})\boldsymbol{R}_A^T\boldsymbol{R}_1^T\ \widetilde{\boldsymbol{x}}_{AB}\ \boldsymbol{A}_3 \tag{A.50}$$

$$= \boldsymbol{T}^T(\boldsymbol{\Psi}_{A\ inc})\boldsymbol{R}_A^T\boldsymbol{R}_1^T\left(-\widetilde{\boldsymbol{n}} + \widetilde{\boldsymbol{x}}_{AB}\ \boldsymbol{A}_3\right) \tag{A.51}$$

$$\begin{aligned} \boldsymbol{A}_{10} = {} & \boldsymbol{T}^T(\boldsymbol{\Psi}_{A\ inc})\widetilde{\left(\boldsymbol{R}_A^T\boldsymbol{R}_1^T\widetilde{\boldsymbol{x}}_{AB}\ \boldsymbol{n}\right)}\ \boldsymbol{T}(\boldsymbol{\Psi}_{A\ inc}) \\ & + \boldsymbol{T}^T(\boldsymbol{\Psi}_{A\ inc})\boldsymbol{R}_A^T\boldsymbol{R}_1^T\ \widetilde{\boldsymbol{x}}_{AB}\boldsymbol{A}_4 \end{aligned} \tag{A.52}$$

In a matrix form, the contribution of the geometric term of $\boldsymbol{g}^{int}$ to the tangent stiffness matrix is:

$$\boldsymbol{K}_{t_{/2}} = f \begin{bmatrix} \boldsymbol{A}_3 & -\boldsymbol{A}_4 & -\boldsymbol{A}_3 & \boldsymbol{0} \\ \boldsymbol{A}_9 & -\boldsymbol{A}_{10} & -\boldsymbol{A}_9 & \boldsymbol{0} \\ -\boldsymbol{A}_3 & \boldsymbol{A}_4 & \boldsymbol{A}_3 & \boldsymbol{0} \\ \boldsymbol{0} & \boldsymbol{0} & \boldsymbol{0} & \boldsymbol{0} \end{bmatrix} \tag{A.53}$$

A.2.2 Friction forces

The derivative of the internal force vector due to friction (Eq. 4.76) is defined by:

$$\mathrm{d}\boldsymbol{g}_{fr}^{int}(\boldsymbol{q},\dot{\boldsymbol{q}}) = \mathrm{d} \begin{Bmatrix} -\boldsymbol{f}_{fr} \\ -\boldsymbol{T}^T(\boldsymbol{\Psi}_{A\ inc})\boldsymbol{R}_A^T\boldsymbol{R}_1^T\widetilde{\boldsymbol{x}}_{AM}\ \boldsymbol{f}_{fr} \\ \boldsymbol{f}_{fr} \\ \boldsymbol{T}^T(\boldsymbol{\Psi}_{B\ inc})\boldsymbol{R}_B^T\boldsymbol{R}_1^T\widetilde{\boldsymbol{x}}_{BM}\ \boldsymbol{f}_{fr} \end{Bmatrix} = \begin{Bmatrix} -\mathrm{d}\boldsymbol{f}_{fr} \\ -\boldsymbol{A}_{11} \\ \mathrm{d}\boldsymbol{f}_{fr} \\ \boldsymbol{A}_{12} \end{Bmatrix} \tag{A.54}$$

The derivative of the friction force can be split in three terms. The expression of each vector or matrix involved in these three terms is given in the set of Equations A.56 to A.76 .

$$\mathrm{d}\boldsymbol{f}_{fr} = -\left[\ \mathrm{d}\mu_R(v_t)\ f\ \boldsymbol{t} + \mu_R(v_t)\ \mathrm{d}f\ \boldsymbol{t} + \mu_R(v_t)\ f\ \mathrm{d}\boldsymbol{t}\ \right] \tag{A.55}$$

1^{st} **term**

$$\mathrm{d}\mu_r(v_t) = \frac{\partial \mu_R}{\partial v_t}\ \mathrm{d}v_t \tag{A.56}$$

with

$$\frac{\partial \mu_r}{\partial v_t} = \begin{cases} \mu\left(\frac{2}{\epsilon_v} - \frac{2}{\epsilon_v^2}\ v_t\right) & v_t < \epsilon_v \\ 0 & v_t \geq \epsilon_v \end{cases} \tag{A.57}$$

$$\mathrm{d}v_t = \boldsymbol{v}_t^T\mathrm{d}\boldsymbol{t} + \boldsymbol{t}^T\mathrm{d}\boldsymbol{v}_t \tag{A.58}$$

$$\mathrm{d}\boldsymbol{t} = \left(\boldsymbol{I} - \boldsymbol{t}\ \boldsymbol{t}^T\right)\frac{\mathrm{d}\boldsymbol{v}_t}{v_t} \tag{A.59}$$

$$\mathrm{d}\boldsymbol{v}_t = \mathrm{d}\left[\left(\boldsymbol{I} - \boldsymbol{n}\boldsymbol{n}^T\right)\left(\dot{\boldsymbol{x}}_M^B - \dot{\boldsymbol{x}}_M^A\right)\right] \tag{A.60}$$

$$= \left(\overbrace{\left[\widetilde{\boldsymbol{n}}\left(\dot{\boldsymbol{x}}_M^B - \dot{\boldsymbol{x}}_M^A\right)\right]} + \widetilde{\boldsymbol{n}}\overbrace{\left(\dot{\boldsymbol{x}}_M^B - \dot{\boldsymbol{x}}_M^A\right)}\right)\mathrm{d}\boldsymbol{n} + \left(\boldsymbol{I} - \boldsymbol{n}\ \boldsymbol{n}^T\right)\mathrm{d}\left(\dot{\boldsymbol{x}}_M^B - \dot{\boldsymbol{x}}_M^A\right) \tag{A.61}$$

$$\begin{aligned} \mathrm{d}\dot{\boldsymbol{x}}_M^B = {} & \mathrm{d}\dot{\boldsymbol{x}}_B - \mathrm{d}\widetilde{\boldsymbol{x}}_{BM}\ \boldsymbol{\omega}_B \\ & - \widetilde{\boldsymbol{x}}_{BM}\boldsymbol{R}_1\ \mathrm{d}\boldsymbol{R}_B\ \boldsymbol{T}(\boldsymbol{\Psi}_{B\ inc})\dot{\boldsymbol{\Psi}}_{B\ inc} \\ & - \widetilde{\boldsymbol{x}}_{BM}\boldsymbol{R}_1\boldsymbol{R}_B\ \boldsymbol{T}(\boldsymbol{\Psi}_{B\ inc})\ \mathrm{d}\dot{\boldsymbol{\Psi}}_{B\ inc} \end{aligned} \tag{A.62}$$

$$\begin{aligned}\mathrm{d}\dot{\boldsymbol{x}}_M^B = \mathrm{d}\dot{\boldsymbol{x}}_B + \widetilde{\boldsymbol{\omega}}_B \left(r_b - \frac{l}{2}\right) \mathrm{d}\boldsymbol{n} \\ + \widetilde{\boldsymbol{x}}_{BM} \boldsymbol{R}_1 \boldsymbol{R}_B \overbrace{\left(\boldsymbol{T}(\boldsymbol{\Psi}_{B\ inc}) \dot{\boldsymbol{\Psi}}_{B\ inc}\right)}^{} \boldsymbol{T}(\boldsymbol{\Psi}_{B\ inc})\ \mathrm{d}\boldsymbol{\Psi}_{B\ inc} \\ - \widetilde{\boldsymbol{x}}_{BM} \boldsymbol{R}_1 \boldsymbol{R}_B\ \boldsymbol{T}(\boldsymbol{\Psi}_{B\ inc})\ \mathrm{d}\dot{\boldsymbol{\Psi}}_{B\ inc}\end{aligned} \tag{A.63}$$

$$\begin{aligned}\mathrm{d}\dot{\boldsymbol{x}}_M^A = \mathrm{d}\dot{\boldsymbol{x}}_A + \widetilde{\boldsymbol{\omega}}_A \left[\mathrm{d}\boldsymbol{x}_{AB} + \left(r_B - \frac{l}{2}\right) \mathrm{d}\boldsymbol{n}\right] \\ + \widetilde{\boldsymbol{x}}_{AM} \boldsymbol{R}_1 \boldsymbol{R}_A \overbrace{\left(\boldsymbol{T}(\boldsymbol{\Psi}_{A\ inc}) \dot{\boldsymbol{\Psi}}_{A\ inc}\right)}^{} \boldsymbol{T}(\boldsymbol{\Psi}_{A\ inc})\ \mathrm{d}\boldsymbol{\Psi}_{A\ inc} \\ - \widetilde{\boldsymbol{x}}_{AM} \boldsymbol{R}_1 \boldsymbol{R}_A\ \boldsymbol{T}(\boldsymbol{\Psi}_{A\ inc})\ \mathrm{d}\dot{\boldsymbol{\Psi}}_{A\ inc}\end{aligned} \tag{A.64}$$

$$\begin{aligned}\mathrm{d}\boldsymbol{v}_t = \boldsymbol{A}_{13}\ \mathrm{d}\boldsymbol{x}_{AB} + \boldsymbol{A}_{14}\ \mathrm{d}\boldsymbol{\Psi}_{A\ inc} + \boldsymbol{A}_{15}\ \mathrm{d}\boldsymbol{\Psi}_{B\ inc} \\ + \boldsymbol{A}_{16}\ \mathrm{d}\dot{\boldsymbol{x}}_{AB} + \boldsymbol{A}_{17}\ \mathrm{d}\dot{\boldsymbol{\Psi}}_{A\ inc} + \boldsymbol{A}_{18}\ \mathrm{d}\dot{\boldsymbol{\Psi}}_{B\ inc}\end{aligned} \tag{A.65}$$

$$\begin{aligned}\boldsymbol{A}_{13} = \left(\overbrace{\left[\widetilde{\boldsymbol{n}}\left(\dot{\boldsymbol{x}}_M^B - \dot{\boldsymbol{x}}_M^A\right)\right]}^{} + \widetilde{\boldsymbol{n}}\overbrace{\left(\dot{\boldsymbol{x}}_M^B - \dot{\boldsymbol{x}}_M^A\right)}^{}\right) \boldsymbol{A}_3 \\ + \left(\boldsymbol{I} - \boldsymbol{n}\ \boldsymbol{n}^T\right) \widetilde{\boldsymbol{\omega}}_B \left(r_b - \frac{l}{2}\right) \boldsymbol{A}_3 \\ - \left(\boldsymbol{I} - \boldsymbol{n}\ \boldsymbol{n}^T\right) \widetilde{\boldsymbol{\omega}}_A \left[\boldsymbol{I} + \left(r_b - \frac{l}{2}\right) \boldsymbol{A}_3\right]\end{aligned} \tag{A.66}$$

$$\begin{aligned}\boldsymbol{A}_{14} = \left(\overbrace{\left[\widetilde{\boldsymbol{n}}\left(\dot{\boldsymbol{x}}_M^B - \dot{\boldsymbol{x}}_M^A\right)\right]}^{} + \widetilde{\boldsymbol{n}}\overbrace{\left(\dot{\boldsymbol{x}}_M^B - \dot{\boldsymbol{x}}_M^A\right)}^{}\right) \boldsymbol{A}_4 \\ + \left(\boldsymbol{I} - \boldsymbol{n}\ \boldsymbol{n}^T\right) \widetilde{\boldsymbol{\omega}}_B \left(r_b - \frac{l}{2}\right) \boldsymbol{A}_4 \\ - \left(\boldsymbol{I} - \boldsymbol{n}\ \boldsymbol{n}^T\right) \widetilde{\boldsymbol{\omega}}_A \left[\boldsymbol{I} + \left(r_b - \frac{l}{2}\right) \boldsymbol{A}_4\right] \\ - \left(\boldsymbol{I} - \boldsymbol{n}\ \boldsymbol{n}^T\right) \widetilde{\boldsymbol{x}}_{AM} \boldsymbol{R}_1 \boldsymbol{R}_A \overbrace{\left(\boldsymbol{T}(\boldsymbol{\Psi}_{A\ inc}) \dot{\boldsymbol{\Psi}}_{A\ inc}\right)}^{} \boldsymbol{T}(\boldsymbol{\Psi}_{A\ inc})\end{aligned} \tag{A.67}$$

$$\boldsymbol{A}_{15} = \left(\boldsymbol{I} - \boldsymbol{n}\ \boldsymbol{n}^T\right) \widetilde{\boldsymbol{x}}_{BM} \boldsymbol{R}_1 \boldsymbol{R}_B \overbrace{\left(\boldsymbol{T}(\boldsymbol{\Psi}_{B\ inc}) \dot{\boldsymbol{\Psi}}_{B\ inc}\right)}^{} \boldsymbol{T}(\boldsymbol{\Psi}_{B\ inc}) \tag{A.68}$$

$$\boldsymbol{A}_{16} = \left(\boldsymbol{I} - \boldsymbol{n}\ \boldsymbol{n}^T\right) \tag{A.69}$$

$$\boldsymbol{A}_{17} = \left(\boldsymbol{I} - \boldsymbol{n}\ \boldsymbol{n}^T\right) \widetilde{\boldsymbol{x}}_{AM} \boldsymbol{R}_1 \boldsymbol{R}_A\ \boldsymbol{T}(\boldsymbol{\Psi}_{A\ inc}) \tag{A.70}$$

$$\boldsymbol{A}_{18} = -\left(\boldsymbol{I} - \boldsymbol{n}\ \boldsymbol{n}^T\right) \widetilde{\boldsymbol{x}}_{BM} \boldsymbol{R}_1 \boldsymbol{R}_B\ \boldsymbol{T}(\boldsymbol{\Psi}_{B\ inc}) \tag{A.71}$$

$$\begin{aligned}\mathrm{d}\boldsymbol{t} = \frac{1}{v_t} \left(\boldsymbol{I} - \boldsymbol{t}\ \boldsymbol{t}^T\right) \big(\ \boldsymbol{A}_{13}\ \mathrm{d}\boldsymbol{x}_{AB} + \boldsymbol{A}_{14}\ \mathrm{d}\boldsymbol{\Psi}_{A\ inc} + \boldsymbol{A}_{15}\ \mathrm{d}\boldsymbol{\Psi}_{B\ inc} + \boldsymbol{A}_{16}\ \mathrm{d}\dot{\boldsymbol{x}}_{AB} \\ + \boldsymbol{A}_{17}\ \mathrm{d}\dot{\boldsymbol{\Psi}}_{A\ inc} + \boldsymbol{A}_{18}\ \mathrm{d}\dot{\boldsymbol{\Psi}}_{B\ inc}\big)\end{aligned} \tag{A.72}$$

In summary, we have:

$$\mathrm{d}\mu_r(v_t)\ f\ \boldsymbol{t} = f\ \frac{\partial \mu_R}{\partial v_t} \left[\left(\boldsymbol{t}\ \boldsymbol{v}_t^T\right) \frac{1}{v_t} \left(\boldsymbol{I} - \boldsymbol{t}\ \boldsymbol{t}^T\right) + \boldsymbol{t}\ \boldsymbol{t}^T\right] \mathrm{d}\boldsymbol{v}_t \tag{A.73}$$

2^{nd} term

By analogy with Eqs. A.40-A.41, the contribution of the second term to the tangent stiffness matrix has the following form

$$\mu_r(v_t)\ \mathrm{d}f\ \boldsymbol{t} = \mu_r(v_t)\ \boldsymbol{t}\ \{-\boldsymbol{G}\ \boldsymbol{H}\ \boldsymbol{G}\ \boldsymbol{0}\} \tag{A.74}$$

and the contribution to the tangent damping matrix has the form:

$$\mu_r(v_t)\ \mathrm{d}f\ \boldsymbol{t} = \mu_r(v_t)\ \boldsymbol{t}\ \{-\boldsymbol{L}\ \boldsymbol{J}\ \boldsymbol{L}\ \boldsymbol{0}\} \tag{A.75}$$

3^{rd} term

$$\mu_r(v_t)\ f\ \mathrm{d}\boldsymbol{t} = \mu_r(v_t)\ \frac{f}{v_t}\ \left(\boldsymbol{I} - \boldsymbol{t}\ \boldsymbol{t}^T\right)\ \mathrm{d}\boldsymbol{v}_t \tag{A.76}$$

$\mathrm{d}\boldsymbol{f}_{fr}$ can be now expressed as:

$$\mathrm{d}\boldsymbol{f}_{fr} = \boldsymbol{A}_{19}\,\mathrm{d}\boldsymbol{x}_{AB} + \boldsymbol{A}_{20}\,\mathrm{d}\boldsymbol{\Psi}_{A\ inc} + \boldsymbol{A}_{21}\,\mathrm{d}\boldsymbol{\Psi}_{B\ inc} + \boldsymbol{A}_{22}\,\mathrm{d}\dot{\boldsymbol{x}}_{AB} + \boldsymbol{A}_{23}\,\mathrm{d}\dot{\boldsymbol{\Psi}}_{A\ inc} + \boldsymbol{A}_{24}\,\mathrm{d}\dot{\boldsymbol{\Psi}}_{B\ inc} \tag{A.77}$$

The intermediate matrix $\boldsymbol{A}_{11}$ appearing in Eq. A.54 is expanded in:

$$\begin{aligned}\boldsymbol{A}_{11} = {} & \boldsymbol{T}^T(\boldsymbol{\Psi}_{A\ inc})\widetilde{\left(\boldsymbol{R}_A^T\boldsymbol{R}_1^T\widetilde{\boldsymbol{x}}_{AM}\boldsymbol{f}_{fr}\right)}\boldsymbol{T}(\boldsymbol{\Psi}_{A\ inc})\ \mathrm{d}\boldsymbol{\Psi}_{A\ inc} \\ & - \boldsymbol{T}^T(\boldsymbol{\Psi}_{A\ inc})\boldsymbol{R}_A^T\boldsymbol{R}_1^T\ \widetilde{\boldsymbol{f}}_{fr}\ \left[\mathrm{d}\boldsymbol{x}_{AB} + \left(r_B - \frac{l}{2}\right)\mathrm{d}\boldsymbol{n}\right] \\ & + \boldsymbol{T}^T(\boldsymbol{\Psi}_{A\ inc})\boldsymbol{R}_A^T\boldsymbol{R}_1^T\widetilde{\boldsymbol{x}}_{AM}\ \mathrm{d}\boldsymbol{f}_{fr}\end{aligned} \tag{A.78}$$

$$\boldsymbol{A}_{11} = \boldsymbol{A}_{27}\,\mathrm{d}\boldsymbol{x}_{AB} + \boldsymbol{A}_{28}\,\mathrm{d}\boldsymbol{\Psi}_{A\ inc} + \boldsymbol{A}_{29}\,\mathrm{d}\boldsymbol{\Psi}_{B\ inc} + \boldsymbol{A}_{30}\,\mathrm{d}\dot{\boldsymbol{x}}_{AB} + \boldsymbol{A}_{31}\,\mathrm{d}\dot{\boldsymbol{\Psi}}_{A\ inc} + \boldsymbol{A}_{32}\,\mathrm{d}\dot{\boldsymbol{\Psi}}_{B\ inc} \tag{A.79}$$

with:

$$\boldsymbol{A}_{27} = \boldsymbol{A}_{25} + \boldsymbol{T}^T(\boldsymbol{\Psi}_{A\ inc})\boldsymbol{R}_A^T\boldsymbol{R}_1^T\widetilde{\boldsymbol{x}}_{AM}\boldsymbol{A}_{19} \tag{A.80}$$

$$\boldsymbol{A}_{28} = \boldsymbol{A}_{26} + \boldsymbol{T}^T(\boldsymbol{\Psi}_{A\ inc})\boldsymbol{R}_A^T\boldsymbol{R}_1^T\widetilde{\boldsymbol{x}}_{AM}\boldsymbol{A}_{20} \tag{A.81}$$

$$\boldsymbol{A}_{29} = \boldsymbol{T}^T(\boldsymbol{\Psi}_{A\ inc})\boldsymbol{R}_A^T\boldsymbol{R}_1^T\widetilde{\boldsymbol{x}}_{AM}\boldsymbol{A}_{21} \tag{A.82}$$

$$\boldsymbol{A}_{30} = \boldsymbol{T}^T(\boldsymbol{\Psi}_{A\ inc})\boldsymbol{R}_A^T\boldsymbol{R}_1^T\widetilde{\boldsymbol{x}}_{AM}\boldsymbol{A}_{22} \tag{A.83}$$

$$\boldsymbol{A}_{31} = \boldsymbol{T}^T(\boldsymbol{\Psi}_{A\ inc})\boldsymbol{R}_A^T\boldsymbol{R}_1^T\widetilde{\boldsymbol{x}}_{AM}\boldsymbol{A}_{23} \tag{A.84}$$

$$\boldsymbol{A}_{32} = \boldsymbol{T}^T(\boldsymbol{\Psi}_{A\ inc})\boldsymbol{R}_A^T\boldsymbol{R}_1^T\widetilde{\boldsymbol{x}}_{AM}\boldsymbol{A}_{24} \tag{A.85}$$

$$\boldsymbol{A}_{25} = -\boldsymbol{T}^T(\boldsymbol{\Psi}_{A\ inc})\boldsymbol{R}_A^T\boldsymbol{R}_1^T\ \widetilde{\boldsymbol{f}}_{fr}\ \left[\boldsymbol{I} + \left(r_B - \frac{l}{2}\right)\boldsymbol{A}_3\right] \tag{A.86}$$

$$\boldsymbol{A}_{26} = \boldsymbol{T}^T(\boldsymbol{\Psi}_{A\ inc})\widetilde{\left(\boldsymbol{R}_A^T\boldsymbol{R}_1^T\widetilde{\boldsymbol{x}}_{AM}\boldsymbol{f}_{fr}\right)}\boldsymbol{T}(\boldsymbol{\Psi}_{A\ inc}) - \boldsymbol{T}^T(\boldsymbol{\Psi}_{A\ inc})\boldsymbol{R}_A^T\boldsymbol{R}_1^T\ \widetilde{\boldsymbol{f}}_{fr}\ \left(r_B - \frac{l}{2}\right)\boldsymbol{A}_4$$

The intermediate matrix $\boldsymbol{A}_{12}$ of Eq. A.54 can be developed as:

$$\begin{aligned}\boldsymbol{A}_{12} = {} & \boldsymbol{T}^T(\boldsymbol{\Psi}_{B\ inc})\overbrace{\left(\boldsymbol{R}_B^T\boldsymbol{R}_1^T\widetilde{\boldsymbol{x}}_{BM}\ \boldsymbol{f}_{fr}\right)}\boldsymbol{T}(\boldsymbol{\Psi}_{B\ inc})\ \mathrm{d}\boldsymbol{\Psi}_{B\ inc} \\ & - \boldsymbol{T}^T(\boldsymbol{\Psi}_{B\ inc})\boldsymbol{R}_B^T\boldsymbol{R}_1^T\ \widetilde{\boldsymbol{f}}_{fr}\ \left(r_B - \frac{l}{2}\right)\mathrm{d}\boldsymbol{n} \\ & + \boldsymbol{T}^T(\boldsymbol{\Psi}_{B\ inc})\boldsymbol{R}_B^T\boldsymbol{R}_1^T\widetilde{\boldsymbol{x}}_{BM}\ \mathrm{d}\boldsymbol{f}_{fr}\end{aligned} \tag{A.87}$$

$$\boldsymbol{A}_{12} = \boldsymbol{A}_{33}\ \mathrm{d}\boldsymbol{x}_{AB} + \boldsymbol{A}_{34}\ \mathrm{d}\boldsymbol{\Psi}_{A\ inc} + \boldsymbol{A}_{35}\ \mathrm{d}\boldsymbol{\Psi}_{B\ inc} + \boldsymbol{T}^T(\boldsymbol{\Psi}_{B\ inc})\boldsymbol{R}_B^T\boldsymbol{R}_1^T\widetilde{\boldsymbol{x}}_{BM}\ \mathrm{d}\boldsymbol{f}_{fr} \tag{A.88}$$

with:

$$\boldsymbol{A}_{33} = -\boldsymbol{T}^T(\boldsymbol{\Psi}_{B\ inc})\boldsymbol{R}_B^T\boldsymbol{R}_1^T\ \widetilde{\boldsymbol{f}}_{fr}\ \left(r_B - \frac{l}{2}\right)\boldsymbol{A}_3 \tag{A.89}$$

$$\boldsymbol{A}_{34} = -\boldsymbol{T}^T(\boldsymbol{\Psi}_{B\ inc})\boldsymbol{R}_B^T\boldsymbol{R}_1^T\ \widetilde{\boldsymbol{f}}_{fr}\ \left(r_B - \frac{l}{2}\right)\boldsymbol{A}_4 \tag{A.90}$$

$$\boldsymbol{A}_{35} = \boldsymbol{T}^T(\boldsymbol{\Psi}_{B\ inc})\overbrace{\left(\boldsymbol{R}_B^T\boldsymbol{R}_1^T\widetilde{\boldsymbol{x}}_{BM}\boldsymbol{f}_{fr}\right)}\boldsymbol{T}(\boldsymbol{\Psi}_{B\ inc}) \tag{A.91}$$

After reformulation, we get:

$$\boldsymbol{A}_{12} = \boldsymbol{A}_{36}\ \mathrm{d}\boldsymbol{x}_{AB} + \boldsymbol{A}_{37}\ \mathrm{d}\boldsymbol{\Psi}_{A\ inc} + \boldsymbol{A}_{38}\ \mathrm{d}\boldsymbol{\Psi}_{B\ inc} + \boldsymbol{A}_{39}\ \mathrm{d}\dot{\boldsymbol{x}}_{AB} + \boldsymbol{A}_{40}\ \mathrm{d}\dot{\boldsymbol{\Psi}}_{A\ inc} + \boldsymbol{A}_{41}\ \mathrm{d}\dot{\boldsymbol{\Psi}}_{B\ inc} \tag{A.92}$$

with:

$$\boldsymbol{A}_{36} = \boldsymbol{A}_{33} + \boldsymbol{T}^T(\boldsymbol{\Psi}_{B\ inc})\boldsymbol{R}_B^T\boldsymbol{R}_1^T\widetilde{\boldsymbol{x}}_{BM}\ \boldsymbol{A}_{19} \tag{A.93}$$

$$\boldsymbol{A}_{37} = \boldsymbol{A}_{34} + \boldsymbol{T}^T(\boldsymbol{\Psi}_{B\ inc})\boldsymbol{R}_B^T\boldsymbol{R}_1^T\widetilde{\boldsymbol{x}}_{BM}\ \boldsymbol{A}_{20} \tag{A.94}$$

$$\boldsymbol{A}_{38} = \boldsymbol{A}_{35} + \boldsymbol{T}^T(\boldsymbol{\Psi}_{B\ inc})\boldsymbol{R}_B^T\boldsymbol{R}_1^T\widetilde{\boldsymbol{x}}_{BM}\ \boldsymbol{A}_{21} \tag{A.95}$$

$$\boldsymbol{A}_{39} = \boldsymbol{T}^T(\boldsymbol{\Psi}_{B\ inc})\boldsymbol{R}_B^T\boldsymbol{R}_1^T\widetilde{\boldsymbol{x}}_{BM}\ \boldsymbol{A}_{22} \tag{A.96}$$

$$\boldsymbol{A}_{40} = \boldsymbol{T}^T(\boldsymbol{\Psi}_{B\ inc})\boldsymbol{R}_B^T\boldsymbol{R}_1^T\widetilde{\boldsymbol{x}}_{BM}\ \boldsymbol{A}_{23} \tag{A.97}$$

$$\boldsymbol{A}_{41} = \boldsymbol{T}^T(\boldsymbol{\Psi}_{B\ inc})\boldsymbol{R}_B^T\boldsymbol{R}_1^T\widetilde{\boldsymbol{x}}_{BM}\ \boldsymbol{A}_{24} \tag{A.98}$$

Finally, the contributions of $\boldsymbol{A}_{11}$ and $\boldsymbol{A}_{12}$ to the tangent stiffness and damping matrix become:

$$\boldsymbol{K}_{t_{/3}} = \begin{bmatrix} \boldsymbol{A}_{19} & -\boldsymbol{A}_{20} & -\boldsymbol{A}_{19} & -\boldsymbol{A}_{21} \\ \boldsymbol{A}_{27} & -\boldsymbol{A}_{28} & -\boldsymbol{A}_{27} & -\boldsymbol{A}_{29} \\ -\boldsymbol{A}_{19} & \boldsymbol{A}_{20} & \boldsymbol{A}_{19} & \boldsymbol{A}_{21} \\ -\boldsymbol{A}_{36} & \boldsymbol{A}_{37} & \boldsymbol{A}_{36} & \boldsymbol{A}_{38} \end{bmatrix} \tag{A.99}$$

$$\boldsymbol{C}_{t_{/3}} = \begin{bmatrix} \boldsymbol{A}_{22} & -\boldsymbol{A}_{23} & -\boldsymbol{A}_{22} & -\boldsymbol{A}_{24} \\ \boldsymbol{A}_{30} & -\boldsymbol{A}_{31} & -\boldsymbol{A}_{30} & -\boldsymbol{A}_{32} \\ -\boldsymbol{A}_{22} & \boldsymbol{A}_{23} & \boldsymbol{A}_{22} & \boldsymbol{A}_{24} \\ -\boldsymbol{A}_{39} & \boldsymbol{A}_{40} & \boldsymbol{A}_{39} & \boldsymbol{A}_{41} \end{bmatrix} \tag{A.100}$$

List of Tables

List of Figures